



MONASH University

**Structural and geochemical evolution of the
Yalgoo Dome, Yilgarn Craton (Western Australia)**

Frediano Clos
MSc

A thesis submitted for the degree of Doctor of Philosophy
at Monash University in 2018
School of Earth, Atmosphere and Environment



Cover Image: view of the Yalgoo Dome near its core.

Copyright

© Frediano Clos 2018. Except as provided in the Copyright Act 1968, this thesis may not be reproduced in any form without the written permission of the author.

I certify that I have made all reasonable efforts to secure copyright permissions for thirdparty content included in this thesis and have not knowingly added copyright content to my work without the owner's permission.

ABSTRACT

This thesis investigates the tectono-magmatic evolution of the Late-Archean Yalgoo Dome, exposed in the granite–greenstone terranes of the Yilgarn Craton (Western Australia). The Yalgoo Dome is a broad elliptical granitic structure with a concentric core-rim distribution of granitoid intrusions, wrapped by a composite greenstone belt that resulted from a long-lived volcanic and plutonic activity. Three phases of mantle-derived mafic–ultramafic magmatism induced crustal reworking and generated a variety of granitic rocks. Phase one (2970–2900 Ma) includes greenstones accompanied by rocks of the tonalite-trondhjemite-granodiorite series (TTG). Phase two commenced with the deposition of mafic-ultramafic greenstones between 2825–2760 Ma. This caused a thermal perturbation of the crust that triggered an array of cascading reactions starting with partial melting of the mafic lower crust and the underlying metasomatized mantle, which lead to the formation of transitional TTGs (2760–2740 Ma) and high-Mg granitoids (c. 2750 Ma; Archean sanukitoid suite). These magmas rose, intruded and melted the older middle crust comprising the first phase rocks that are now exposed in the core of the Yalgoo Dome as migmatitic bodies. The third phase started with a renewed phase of mafic-ultramafic greenstones (2730–2710 Ma) and crustal reworking which involved the intrusion of K-rich granitic intrusions of transitional TTGs dykes at c. 2707 Ma and post-tectonic A-type and Low-Ca granites at 2640–2600 Ma.

The initial conditions leading to crustal reworking and diapirism during phase two were investigated in the old migmatitic core. This area defines multi-scale domes-and-basins, formerly interpreted as the result of superposed folding. Structural data show that the observed geometries result from vertical sheath folds developed in a single syn-anatectic deformation event (D_1) and were locally re-folded by D_2 folds during the last phase of diapirism. Phase equilibria modelling and thermobarometry indicate that D_1 – D_2 melting and reworking of the migmatitic rocks record water-excess partial melting at mid-crustal conditions (3–9 kbar, 700–800 °C), induced by the emplacement of transitional TTGs at 2760–2740 Ma. In essence, Phase two magmatism reflects the upward migration of a wave of heat and fluids mediated by crustal anatexis and magma migration, which weakened the strong mid-crustal levels, allowing for sagduction of the cold greenstone overburden and diapirism of hot migmatitic and magmatic bodies.

The Yalgoo Dome offers a unique view not only on the dome-forming mechanisms, but also on the fundamental processes necessary to generate an Archean felsic continental crust because all five granitoid suites that typify late Archean terranes outcrop in the dome and its surroundings. These granitoids are normally distributed throughout cratons and are rarely found in the same crustal section. Thus, the Yalgoo Dome records the magmatic evolution of the same lithospheric column through a time span of more than 300 Myr and support a stepwise growth of the crust, in response to major phases of mantle-derived mafic-ultramafic magmatism accompanied by crustal reworking at 2970–2900 Ma, 2760–2740 Ma and 2707–2600 Ma. Granitic magmatism records the secular shift from sodic (i.e. TTG) to increasingly potassic compositions (transitional TTG and low-Ca suites), including the appearance of high-Mg granitoids (Archean sanukitoids) at c. 2750 Ma during diapirism. Comparable processes and chemical evolution of granitic rocks were recorded in the older domes of the East Pilbara Terrane (3550–2850 Ma), except for the absence of A-type and high-Mg granitoids (Archean sanukitoids).

Thesis including published works declaration

I hereby declare that this thesis contains no material which has been accepted for the award of any other degree or diploma at any university or equivalent institution and that, to the best of my knowledge and belief, this thesis contains no material previously published or written by another person, except where due reference is made in the text of the thesis.

This thesis includes three original papers published in peer reviewed journals. The core theme of the thesis is the crustal evolution of the Yalgoo Dome in the Yilgarn Craton of Western Australia. The ideas, development and writing up of all the papers in the thesis were the principal responsibility of myself, the student, working within the School of Earth, Atmosphere and Environment under the supervision of Professor Roberto Weinberg and Ivan Zibra from the Geological Survey of Western Australia.

(The inclusion of co-authors reflects the fact that the work came from active collaboration between researchers and acknowledges input into team-based research.)

In the case of each chapter my contribution to the work involved the following:

Thesis Chapter	Publication Title	Status	Nature and % of student contribution	Co-author name(s) Nature and % of Co-author's contribution*	Co-author(s), Monash student Y/N*
2	Archean diapirism recorded by vertical sheath folds in the core of the Yalgoo Dome, Yilgarn Craton	Submitted	85%. Field work, sample preparation, data analyses, preparation of manuscript	1) Roberto Weinberg (5%): manuscript preparation, idea development 2) Ivan Zibra (5%): sample collection, manuscript preparation, idea development 3) Michael Fenwick (5%): mapping and data collection	Ivan Zibra Michael Fenwick
3	Diapirism assisted by water-present melting: insights from the migmatitic core of the Archean Yalgoo Dome, Yilgarn Craton	To be submitted	90%. Field work, sample preparation, petrographic and mineral, data analyses, preparation of manuscript	1) Roberto Weinberg (4%): manuscript preparation, idea development 2) Ivan Zibra (4%): sample collection, manuscript preparation, idea development 3) Martin Schwindinger (2%): idea development	Ivan Zibra Martin Schwindinger
4	Building the Archean continental crust: 300 Myr of felsic magmatism in the Yalgoo Dome (Yilgarn Craton)	Submitted	90%. Field work, sample preparation, data analyses, preparation of manuscript	1) Roberto Weinberg (5%): manuscript preparation, idea development 2) Ivan Zibra (5%): sample collection, manuscript preparation, idea development	Ivan Zibra

*If no co-authors, leave fields blank

I have renumbered sections of submitted or published papers in order to generate a consistent presentation within the thesis.

Student signature:



Date: 9/02/2018

The undersigned hereby certify that the above declaration correctly reflects the nature and extent of the student's and co-authors' contributions to this work. In instances where I am not the responsible author I have consulted with the responsible author to agree on the respective contributions of the authors.

Main Supervisor signature:



Date: 9/02/2018

TABLE OF CONTENTS

Copyright.....	IV
Abstract.....	VI
Thesis including published works declaration.....	VIII
Acknowledgments.....	XVI
CHAPTER 1: Introduction.....	18
Part 1: The rise of continents.....	20
Part 2: Methods.....	24
Part 3: Thesis structure.....	24
References.....	26
CHAPTER 2: Archean diapirism recorded by vertical sheath folds in the core of the Yalgoo Dome, Yilgarn Craton.....	30
Abstract.....	32
1 Introduction.....	33
2 Geological setting.....	34
3 Migmatitic Domain.....	35
4 Structures of the Migmatitic Domain.....	39
4.1 Central Domain.....	39
4.1.1 Early structures (D_1): sheath folds.....	39
4.1.2 Second deformation event and anatexis (D_2).....	41
4.1.3 Shearing of granitic dyke swarm (D_3).....	42
4.2 Western Domain.....	43
4.3 Eastern Domain.....	45
5 Discussion.....	45
5.1 Refolded sheath folds.....	45
5.2 Diapirism during anatexis: the origin of sheath folds (D_1).....	46
5.3 EW shortening (D_2 and D_3).....	49
5.4 From vertical to horizontal tectonics.....	50
6 Conclusion.....	50
Acknowledgments.....	51
References.....	51
CHAPTER 3: Diapirism assisted by water-present melting: insights from the migmatitic core of the Archean Yalgoo Dome, Yilgarn Craton.....	56
Abstract.....	58
1 Introduction.....	59
2 Geological setting.....	60
2.1 Yalgoo Dome.....	60

2.1 Migmatitic Domain	62
3 Petrography and mineral chemistry	64
3.1 Migmatitic tonalite (sample 155879)	64
3.2 Migmatitic amphibolite (sample 214403c)	67
3.3 Amphibolite (sample 209690)	72
4 Melting conditions	72
4.1 Migmatitic tonalite	72
4.1.1 Melting reactions	72
4.1.2 Pseudosection modelling	73
4.2 Amphibolite	76
4.2.1 Melting reactions	76
4.2.2 P–T estimates	77
5 Discussion	79
5.1 Reworking of middle crust	79
5.2 Origin of the Goonetarra Granodiorite	80
5.3 Source of fluids	81
5.4 Role of fluids during diapirism	83
6 Conclusion	85
Acknowledgments	86
References	86
Supplementary material	92

CHAPTER 4: Building the Archean continental crust: 300 Myr of felsic magmatism in the Yalgoo dome (Yilgarn Craton) 94

Abstract	96
1 Introduction	97
2 Geological setting	98
3 Late Archean granitic rocks	100
3.1 TTG	101
3.2 Transitional TTG	101
3.3 High-Mg granitic rocks	101
3.4 A-type granites	102
3.5 Low-Ca granites	102
4 Granitic groups in the Yalgoo dome	102
4.1 TTG	104
4.1.1 Field relationships, age and petrography	104
4.1.2 Geochemistry	104
4.2 Transitional TTG	105
4.2.1 Field relationships, age and petrography	105
4.2.2 Geochemistry	107
4.3 High-Mg group: Cagacaroon pluton	107
4.3.1 Field relationships, age and petrography	107
4.3.2 Geochemistry	109

4.4 A-type group: Damperwah and Seelingson monzogranite	109
4.4.1 Field relationships, age and petrography.	109
4.4.2 Geochemistry	110
4.5 Low-Ca granites	113
4.5.1 Field relationships, age and petrography.	113
4.5.2 Geochemistry	114
5 Discussion	114
5.1 STAGE 1: TTG magmatism (2970–2900 Ma)	115
5.2 STAGE 2: high-Mg granitic rocks and transitional TTGs (2760–2740 Ma)	116
5.2.1 Origin of the high-Mg granitic rocks: Cagacaroon Syenogranite.	116
5.2.2 Origin of the transitional TTGs.	117
5.2.3 Lithospheric reworking	119
5.3 STAGE 3: transitional TTGs dykes (c. 2700 Ma).	120
5.4 STAGE 4: Post-tectonic granites (2640–2600 Ma): A-type and low-Ca granites	121
5.4.1 Origin of the A-type granites	121
5.4.2 Origin of the low-Ca granites	123
5.4.3 Lower crust delamination	123
5.5 Implications for incremental formation of Archean continental crust	124
6 Conclusion	127
Acknowledgments	128
References	128
Supplementary material	132
CHAPTER 5: Conclusion	134
1 Introduction	136
2 Reworking of crustal rocks and diapirism	136
3 Intermittent crustal reworking and development of continental crust.	137
4 Future outlook	141
4.1 Origin of the high-Mg granitoids	141
4.2 Archean crust and depleted mantle coupling?	142
4.3 Which came first, subduction or continental crust?	143
4 Conclusion	144
References	145
APPENDICES	149
APPENDIX A: Geological setting and literature review	150
1 Murchison Domain	151
1.1 Greenstones	151
1.2 Granitic rocks	152
1.2.1 Geochemical classification	152
1.2.2 Composite classification	153
1.3 Crustal evolution.	155

2 Yalgoo Dome	158
2.1 Greenstones.....	159
2.2 Granitic rocks.....	160
2.3 Structural Geology.....	160
2.4 Tectonic models.....	161
References	165

APPENDIX B: Tectono-magmatic evolution of the Neoproterozoic Yalgoo Dome (Yilgarn Craton). Diapirism in a pre-orogenic setting.	167
--	------------

APPENDIX C: Badja 1:100,000 Geological Map	167
---	------------

APPENDIX D: The ~2730 Ma onset of the Neoproterozoic Yilgarn Orogeny	167
---	------------

List of figures

CHAPTER 1

Figure 1: Crustal growth models.	21
Figure 2: Map of worldwide Archean crust	22
Figure 3: Map of the Archean Yilgarn Craton.	23

CHAPTER 2

Figure 1: Geological map of the Yalgoo Dome.	34
Figure 2: Structural map of three key areas of the core	36
Figure 3: Representative lithologies in the Central Domain.	37
Figure 4: Structures in the Central Domain	41
Figure 5: Summary outcrop	43
Figure 6: Structures in the Western and Estearn Domain	44
Figure 7: Summary of D_1 and D_2 in the Migmatitic Domain	47
Figure 8: Internal dynamics of the Migmatitic Domain	48

CHAPTER 3

Figure 1: Geological map of the Yalgoo Dome	61
Figure 2: Field appearance of the migmatitic tonalites and amphibolites	65
Figure 3: Minerals and microstructures in migmatite tonalite	67
Figure 4: Minerals and textures in the migmatitic amphibolite	69
Figure 5: Mineral composition of amphibolites.	70
Figure 6: Minerals and textures in amphibolite	71
Figure 7: Perple_X P–T phase diagram modelling.	74
Figure 8: Perple_X T–H ₂ O phase diagram modelling	75
Figure 9: Tonalite and amphibolite comparison	78
Figure 10: Chemical diagrams	82
Figure 11: Cartoon of the dome-forming episode (2760–2740 Ma).	85

CHAPTER 4

Figure 1: Geological map of the Yalgoo dome	99
Figure 2: Granitic groups in the Yalgoo Dome.	103
Figure 3: Photographs of granitic groups	106
Figure 4: Trace elements plots	111
Figure 5: Major and trace elements plots	112
Figure 6: Chondrite normalized REE spider plots	113
Figure 7: Comparative time-space diagram of the Yalgoo Dome.	114
Figure 8: Comparison diagram.	118
Figure 9: Cartoon illustrating the scenario at 2760–2740 Ma.	119
Figure 10: Cartoon showing the scenario at 2730–2660 Ma	120
Figure 11: A-type discrimination diagram	122

Figure 12: Cartoon showing the scenario at 2640–2600 Ma	124
Figure 13: Three phases of crustal reworking in Youanmi Terrane	126

CHAPTER 5

Figure 1: Geology of the Yalgoo and Mt. Edgar domes	139
Figure 2: Chemical evolution of the Yalgoo and Pilbara domes	140

List of tables

CHAPTER 3

Table 1: Plagioclase analyses	67
Table 2: Biotite and amphibole analyses.	68
Table 3: Hbl-Pl thermobarometry	78

CHAPTER 4

Table 1: Nomenclature comparison.	100
Table 2: Average composition of granitic groups	108

Acknowledgments

First and foremost, I would like to thank my supervisor, Prof. Roberto Weinberg, for the patient encouragement, advice and guidance he has provided during my time as his student. I have been extremely lucky to have a supervisor who responded to my questions and queries so promptly and vastly helped me to improve my scientific and communication skills.

A major thanks also to my external supervisor, Dr. Ivan Zibra, who introduced me to the “gioie e dolori” of mapping in the Yilgarn Craton and answered with infinite calmness to thousands of questions.

Thanks to Martin as our discussions were critical to the success of my thesis because we reciprocally improved each other, sharing and testing new ideas and methods. Thanks to Massimo Raveggi and Junnel Alegado for the help with sample preparation at the Monash University and the Staff at the Carlisle laboratories in Perth for their sample handling. Shachar Lazar is thanked for his assistance during the fieldwork and for the long philosophical conversations under the stars. I would also like to thank the Geological Survey of Western Australia for providing the resources to conduct successful and safe fieldtrips.

I would like to thank my family for their love and patience trying to communicate with me, while I was so far from home.

Finally, the most important thanks goes to the person that holds my heart, my wife Christina. Words cannot express how grateful I am that we persisted through all difficulties and we managed to complete this chapter of our journey together and with so much love. You kept me grounded and focused on the essential aspects of life with your passionate love. These last four years wouldn't have been the same without you to support me and hold my hand.

CHAPTER 1

Introduction



Part 1: The rise of continents

One of the Earth's extraordinary aspects when compared with inner rocky planets in the Solar system is its distribution of the crust into two modes: oceanic and continental crusts. In contrast to the thin oceanic crust (<10 km), which is largely basaltic and young (<200 Ma), the continental crust is thicker (average 35–40 km; Li and Mooney, 1998) and with a wider age range (Rudnick, 1995; Cawood et al., 2013), starting from the 4000–4030 Ma Acasta Gneiss in Canada (Bowring and Williams, 1999). The continental crust comprises 70% of the crust by volume, but covers only 41% of the Earth's surface area (Cogley, 1984; Cawood et al., 2013). To the best of our current knowledge, Earth is the only rocky planet with chemically “evolved” continents and large masses of liquid water. These two features are genetically linked because only a planet with oceans could generate continents by prolonged accumulation of buoyant felsic melts generated by partial melting of sea-floor hydrated basalts (Campbell and Taylor, 1983).

During the first billion years of Earth's history, the crust was dominated by basaltic magmatism. Higher Archean mantle temperature would have caused more extensive melting of mantle rocks and would have developed a primary Mg-rich crust on top of a highly depleted residual mantle (Herzberg et al., 2010; Herzberg and Rudnick, 2012; Griffin et al., 2014). Thermodynamic modelling by Johnson et al. (2014) demonstrated that fully hydrated and anhydrous Mg-rich rocks at the base of a 45 km thick crust are denser than the underlying residual mantle. Delamination and recycling of this MgO-rich basalts in negatively buoyant drips caused more melting and could form hydrated Mg-poor basalts, the ideal protolith to generate the rocks of the tonalite–trondhjemite–granodiorite series (TTG) (Barker and Arth, 1976; Moyen and Martin, 2012; Johnson et al., 2017). TTGs are sodic granitoids found in all Archean cratons and represent the building blocks of the first continental crust.

The continental crust developed throughout the Archean, but with different growth rates and mechanisms with respect modern settings (Cawood et al., 2013). Early models for the rate of continental crust growth were divided in two end-members (Fig. 1). On the one hand advocates of continuous crustal growth from Archean to present-day based their inferences on the geographic distribution

of Rb-Sr and K-Ar isotope ages (Hurley and Rand, 1969; Goodwin, 1996). These models showed an increase in production rate from the Mesoproterozoic onwards (c. 1500 Ma), but this was biased by low preservation of older terranes and by overprinting of old rocks by younger orogenies (Cawood et al., 2013). On the other hand, Armstrong (1981) proposed that the large majority of the continental crust formed early and was then reworked, but at constant volume (Fig. 1). More recent models based on large compilations of Hf (Belousova et al., 2010) and Hf and oxygen isotopes on detrital and magmatic zircons (Dhuime et al., 2012) shows that the growth of continental crust was a continuous process that generated c. 70% of the total volume of the crust before 2500 Ma (Fig. 1). These authors claim the decrease in rate production at the end of the Archean eon (3000–2500 Ma) reflects a period of fundamental change in many aspects of the geological record on a planetary scale.

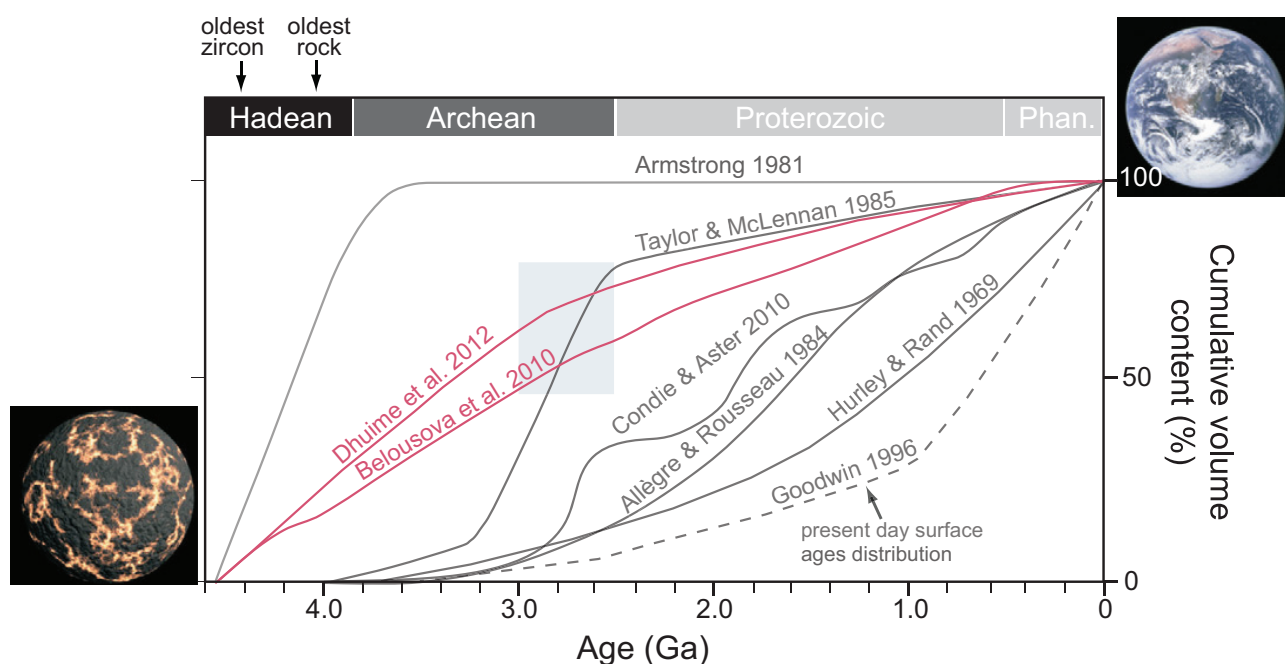


Figure 1: Crustal growth models of Hurley and Rand (1969), Armstrong (1981), Allègre and Rousseau (1984), Taylor and McLennan (1985), Condie and Aster (2010), and Dhuime et al. (2012) and Goodwin (1996). Modified after Cawood et al. (2013)

The upper crust matured from a highly mafic bulk composition before 3000 Ma, to a felsic bulk composition by 2500 Ma (Dhuime et al., 2012; 2015; Keller and Schoene, 2012; Tang et al., 2016). This late Archean change arose from a five-fold increase in the mass of the upper continental crust due to addition of granitic rocks (Tang et al., 2016) and corresponds to the transition from dominant TTG magmatism to potassic magmatism (Moyen, 2011). Laurent et al. (2014) showed that the chronology of granitoid intrusion varies from craton to craton, but can be generalized in a two-stage

sequence: a protracted period of TTG magmatism, that lasts 200 to 500 Ma, is followed by 20 to 150 Ma period of potassic, sanukitoid (high-Mg granitoids in this thesis) and hybrid magmatism (Laurent et al., 2014) (Fig. 2). The diversification of granitic rocks at the end of the Archean is explained by the shift from a >3000 Ma in-situ crustal reworking regime, dominated by body forces, to the onset of modern-style plate tectonics, between 3000 and 2500 Ma (Laurent et al., 2014). This timing is consistent with the secular changes in: i) Hf and O isotopes in zircon (Valley et al., 2005; Belousova et al., 2010; Dhuime et al., 2012) (Fig. 1), ii) chemistry of continental basalts (Condie 1989; Smithies et al., 2004), iii) the observation that inclusions in diamonds changed from peridotitic only to peridotitic and eclogitic after 3000 Ma (Shirey and Richardson, 2011), and iv) style of deformation in orogenic belts (Chardon et al., 2009). In a nutshell, the end of the Archean eon

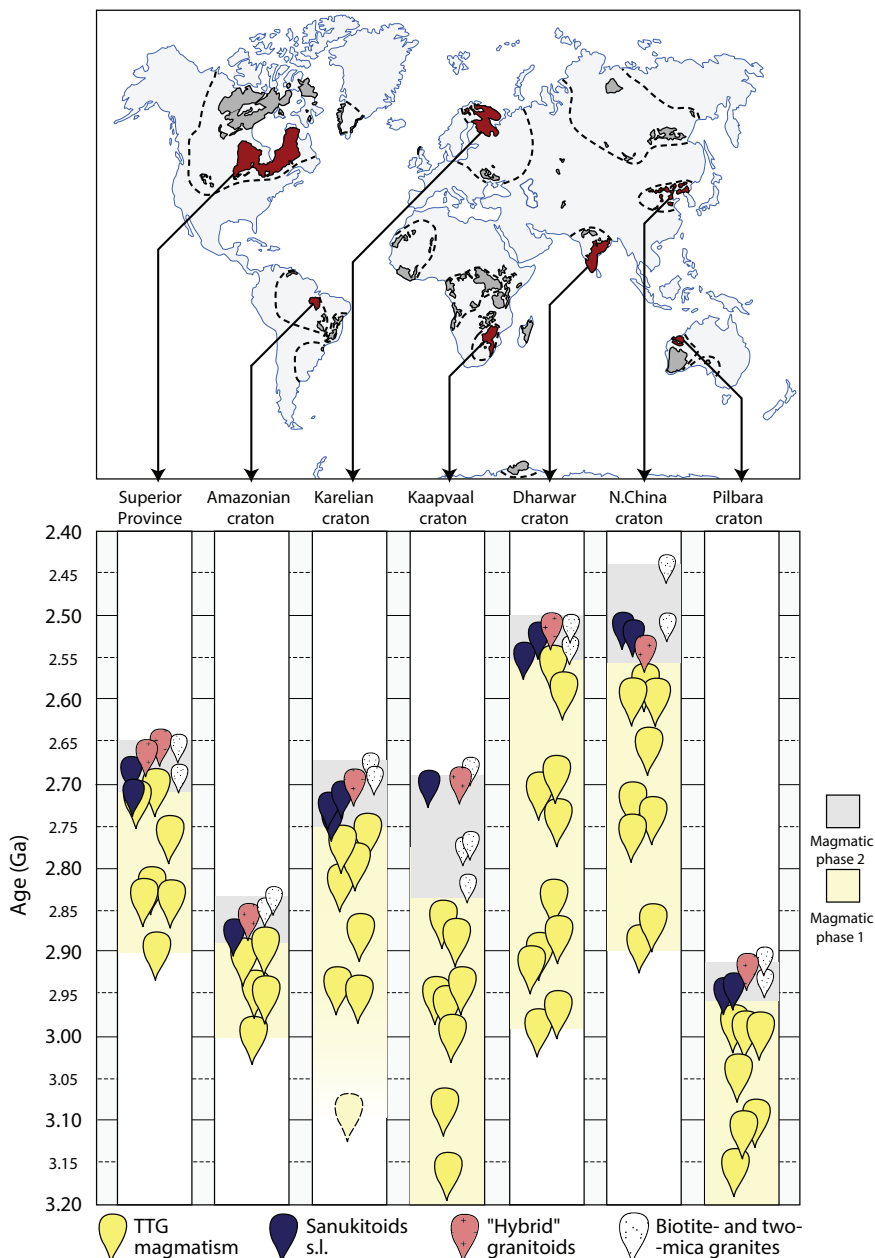


Figure 2: Map of exposed Archean crust and age distribution for some of the major cratons (in red) showing the evolution from TTG-dominated magmatism to a shorter period dominated by more diversified granitoid magmatism including sanukitoids (high-Mg), hybrids and biotite- and two mica (potassic) granites (diagram after Laurent et al., 2014).

marked a major shift in the equilibrium between crustal growth, recycling and destruction, marking the stabilization of large volumes of continental crust.

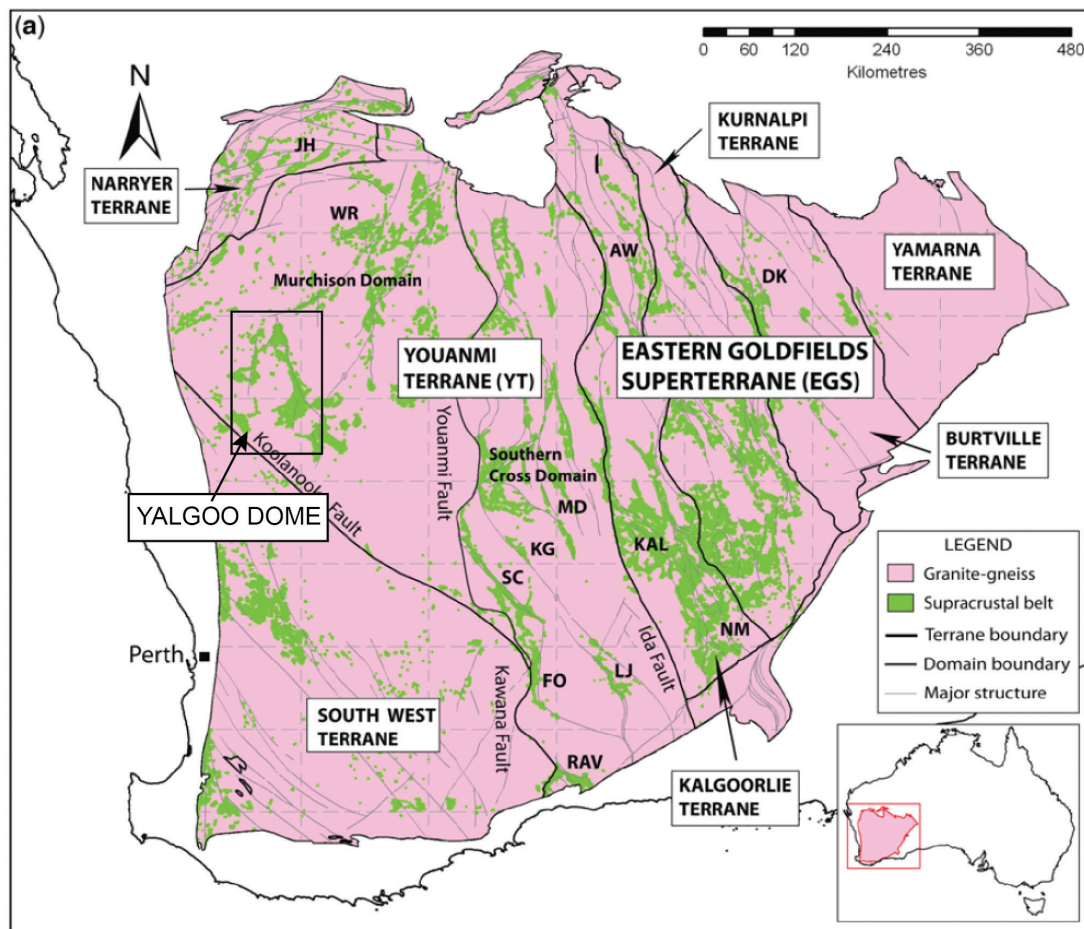


Figure 3: Map of the Archaean Yilgarn Craton showing the distribution of granite (pink) and greenstone (green) and tectonic division in four major terranes. Rectangle shows location of the Yalgoo Dome in the SW part of the Murchison Domain of the Youanmi Terrane (map after Mole et al., 2013).

This thesis investigates structural, metamorphic and magmatic characteristics of the Late Archean Yalgoo Dome (2970–2600 Ma) of the Yilgarn Craton (Western Australia; Fig. 3) with the purpose of improving our understanding of the fundamental processes that contribute to the genesis of continental crust at the end of the Archean. The project has been developed in collaboration with the Geological Survey of Western Australia (GSWA), which started a new mapping project in the Yalgoo area in 2012. This thesis builds on previous research in the Yalgoo Dome (Myers and Watkins, 1985; Watkins and Wiedenbeck, 1993; Foley, 1997; Caudery, 2013; Fenwick, 2014; review in Appendix A) and uses recent geochronology results from the GSWA as a framework to support data and interpretations (Zibra et al., 2018; Appendix B).

Part 2: Methods

A number of methods were employed during this work. They are briefly introduced here, and described in detail in the relevant chapters. Mapping and sampling of migmatitic and granitic rocks in the Yalgoo Dome was conducted in collaboration with (and under supervision of) Dr. Ivan Zibra of the Geological Survey of Western Australia (GSWA). Mapping and sampling in different parts of the dome was conducted according to the standards of the GSWA and provided the basis of understanding for the whole project. Collected samples were used for geochemical, geochronological and petrographic analyses.

More than 50 samples were collected for whole-rock geochemistry and processed in the GSWA laboratory in Carlisle (Perth). The samples were analysed according to their internal standards and published online with free access at <https://dasc.dmp.wa.gov.au/dasc/>. Thin sections were prepared at Monash University for petrography and study with optical and scanning electron microscopy. Petrography was the basis for selection of key samples to be analysed for mineral composition with the electron microprobe (EMP) at the University of Melbourne. Pressure, temperature and fluid conditions of metamorphism were estimated for selected samples using both phase equilibria modelling (Perple_X version 6.7.9; Connolly, 2009) and Hbl-P1 geothermobarometry (Schmidt, 1992; Holland and Blundy, 1994; Anderson, 1995; Ernst and Liu, 1998; Bhadra and Bhattacharya, 2007; Molina et al., 2015).

Part 3: Thesis structure

The findings of this thesis are presented in three main research chapters (Chapters 2–4), with an introductory (Chapter 1) and a conclusions chapter (Chapter 5). Each research chapter is formatted as a stand-alone journal article, and is either submitted or in preparation for submission. This is an accepted thesis format for Monash University that leads to some unavoidable repetition. Formatting of the research chapters has been altered here to maintain consistent layout and referencing style throughout the thesis.

CHAPTER 2 ‘Archean diapirism recorded by vertical sheath folds in the core of the Yalgoo

Dome, Yilgarn Craton’.

This chapter aims to determine the structural evolution of the migmatitic core of the dome, revisiting an old fold interference model (Myers and Watkins, 1985; Appendix A) and provides insight into the early evolution of the dome. This chapter was submitted to Precambrian Research.

CHAPTER 3: ‘Diapirism assisted by water-present melting: insights from the migmatitic core of the Archean Yalgoo Dome, Yilgarn Craton’.

In the Yilgarn Craton there is a dearth of P–T determinations because mineral assemblages in both greenstones and granites are in many cases unsuitable to application of classic geothermobarometry and thermodynamic modelling. Metamorphic grade is generally inferred exclusively from quantitative field observations rather than quantitative and precise estimates. This chapter aims to define the P-T and fluids conditions during melting in the migmatitic core, to better understand dynamics of crustal recycling in Archean domes.

CHAPTER 4 ‘Building the Archean continental crust: 300 Myr of felsic magmatism in the Yalgoo Dome (Yilgarn Craton)’.

In this contribution, I examine the geochemical evolution recorded in five granitic suites and introduce a four-stage tectono-magmatic evolution that correlate with three major pulses of mafic–ultramafic juvenile mantle inputs. Over 300 Myr of felsic magmatism in the Yalgoo Dome provides insights into the key processes responsible for the production of an Archean continental crust. This chapter is accepted for publication as a GSWA report.

CHAPTER 5: Conclusion

This final chapter summarizes and integrates the findings of the three research chapters, provide

insights into the tectono-magmatic evolution of the Yalgoo Dome and formation of continental crust at the of the Archean eon. Then I compare the history of the Yalgoo dome with a much older dome from the East Pilbara Terrane to show that even tough processes of crustal formation are remarkably similar, sanukitoids/high-Mg granitoids can be found only in the Yalgoo Dome and might have profound geodynamic implications.

Supplementary material referred to chapters 2–4 are directly related to and follows each chapter. Additional appendices are provided at the end of the thesis. These include the regional geology based on the literature (Appendix A). The other appendices B, C and D present a series of collaborative works with Dr. Zibra, a geoscientist at the GSWA and external supervisor. Appendix B is a GSWA report that summarizes the structural evolution of the Yalgoo Dome and builds the foundations for Chapter 2. Appendix C shows the [Badja 1:100,000 Geological Map](#), to which I contributed with the geological map presented in figure 2 of Chapter 2. Appendix D is a paper recently published in *Tectonics* entitled “[The ~2730 Ma onset of the Neoproterozoic Yilgarn Orogeny](#)”, which I co-authored.

References

- Allègre, C.J. and Rousseau, D., 1984. The growth of the continent through geological time studied by Nd isotope analysis of shales. *Earth and Planetary Science Letters*, 67(1), pp.19–34.
- Anderson, D.L., 1995. Lithosphere, asthenosphere, and perisphere. *Reviews of Geophysics*, 33(1), pp.125–149.
- Taylor, S.R., McLennan, S.M., Armstrong, R.L. and Tarney, J., 1981. The composition and evolution of the continental crust: rare earth element evidence from sedimentary rocks. *Philosophical Transactions of the Royal Society of London A: Mathematical, Physical and Engineering Sciences*, 301(1461), pp.381–399.
- Barker, F. and Arth, J.G., 1976. Generation of trondhjemitic-tonalitic liquids and Archean bimodal trondhjemite-basalt suites. *Geology*, 4(10), pp.596–600.
- Belousova, E.A., Kostitsyn, Y.A., Griffin, W.L., Begg, G.C., O'Reilly, S.Y. and Pearson, N.J., 2010. The growth of the continental crust: constraints from zircon Hf-isotope data. *Lithos*, 119(3), pp.457–466.
- Bhadra, S. and Bhattacharya, A., 2007. The barometer tremolite+ tschermakite+ 2 albite= 2 pargasite+ 8 quartz: constraints from experimental data at unit silica activity, with application to garnet-free natural assemblages. *American Mineralogist*, 92(4), pp.491–502.
- Bowring, S.A. and Williams, I.S., 1999. Proterozoic (4.00–4.03 Ga) orthogneisses from northwestern Canada. *Contributions to Mineralogy and Petrology*, 134(1), pp.3–16.

- Campbell, I.H. and Taylor, S.R., 1983. No water, no granites-No oceans, no continents. *Geophysical Research Letters*, 10(11), pp.1061–1064.
- Caudery, J.N. 2014. Structural evolution of the Yalgoo Dome, Yilgarn Craton, Western Australia. *Geological Survey of Western Australia, Record 2014/4*, pp.89.
- Cawood, P.A., Hawkesworth, C.J. and Dhuime, B., 2013. The continental record and the generation of continental crust. *Geological Society of America Bulletin*, 125(1–2), pp.14–32.
- Chardon, D., Gapais, D. and Cagnard, F., 2009. Flow of ultra-hot orogens: a view from the Precambrian, clues for the Phanerozoic. *Tectonophysics*, 477(3), pp.105–118.
- Cogley, J.G., 1984. Continental margins and the extent and number of the continents. *Reviews of Geophysics*, 22(2), pp.101–122.
- Condie, K.C., 1989. Geochemical changes in basalts and andesites across the Archean-Proterozoic boundary: Identification and significance. *Lithos*, 23(1–2), pp.1–18.
- Condie, K.C. and Aster, R.C., 2010. Episodic zircon age spectra of orogenic granitoids: the supercontinent connection and continental growth. *Precambrian Research*, 180(3), pp.227–236.
- Connolly, J.A.D., 2009. The geodynamic equation of state: what and how. *Geochemistry, Geophysics, Geosystems*, 10(10), 19.
- Dhuime, B., Hawkesworth, C.J., Cawood, P.A. and Storey, C.D., 2012. A change in the geodynamics of continental growth 3 billion years ago. *Science*, 335(6074), pp.1334–1336.
- Dhuime, B., Wuestefeld, A. and Hawkesworth, C.J., 2015. Emergence of modern continental crust about 3 billion years ago. *Nature Geoscience*, 8(7), pp.552–555.
- Ernst, W.G. and Liu, J., 1998. Experimental phase-equilibrium study of Al- and Ti-contents of calcic amphibole in MORB—a semi-quantitative thermobarometer. *American Mineralogist*, 83(9–10), pp.952–969.
- Fenwick, M.J., 2014. Structural evolution of the Yalgoo Dome, Yilgarn Craton, Western Australia: a core perspective. *Geological Survey of Western Australia, record 2015/1016*.
- Foley, B.J., 1997. Reassessment of Archaean tectonics in the Yalgoo District, Murchison Province, Western Australia. Unpublished Thesis. Monash University, Melbourne, Australia.
- Goodwin, A.M., 1996. Principles of Precambrian geology. Academic Press, 327 p.
- Griffin, W.L., Belousova, E.A., O'Neill, C.O.S.Y., O'Reilly, S.Y., Malkovets, V., Pearson, N.J., Spetsius, S. and Wilde, S.A., 2014. The world turns over: Hadean–Archean crust–mantle evolution. *Lithos*, 189, pp.2–15.
- Herzberg, C. and Rudnick, R., 2012. Formation of cratonic lithosphere: an integrated thermal and petrological model. *Lithos*, 149, pp.4–15.
- Herzberg, C., Condie, K. and Korenaga, J., 2010. Thermal history of the Earth and its petrological expression. *Earth and Planetary Science Letters*, 292(1), pp.79–88.
- Holland, T. and Blundy, J., 1994. Non-ideal interactions in calcic amphiboles and their bearing on amphibole-plagioclase thermometry. *Contributions to Mineralogy and Petrology*, 116(4), pp.433–447.
- Hurley, P.M. and Rand, J.R., 1969. Pre-drift continental nuclei. *Science*, 164(3885), pp.1229–1242.

- Johnson, T.E., Brown, M., Kaus, B.J. and VanTongeren, J.A., 2014. Delamination and recycling of Archaean crust caused by gravitational instabilities. *Nature Geoscience*, 7(1), pp.47–52.
- Johnson, T.E., Brown, M., Gardiner, N.J., Kirkland, C.L. and Smithies, R.H., 2017. Earth's first stable continents did not form by subduction. *Nature*, 543, pp. 239–242.
- Keller, C.B. and Schoene, B., 2012. Statistical geochemistry reveals disruption in secular lithospheric evolution about 2.5 Gyr ago. *Nature*, 485(7399), pp.490–493.
- Laurent, O., Martin, H., Moyen, J.F. and Doucelance, R., 2014. The diversity and evolution of late-Archaean granitoids: evidence for the onset of “modern-style” plate tectonics between 3.0 and 2.5 Ga. *Lithos*, 205, pp.208–235.
- Molina, J.F., Moreno, J.A., Castro, A., Rodríguez, C. and Fershtater, G.B., 2015. Calcic amphibole thermobarometry in metamorphic and igneous rocks: new calibrations based on plagioclase/amphibole Al-Si partitioning and amphibole/liquid Mg partitioning. *Lithos*, 232, pp.286–305.
- Li, S. and Mooney, W.D., 1998. Crustal structure of China from deep seismic sounding profiles. *Tectonophysics*, 288(1), pp.105–113.
- Moyen, J.F. and Martin, H., 2012. Forty years of TTG research. *Lithos*, 148, pp.312–336.
- Moyen, J.F., 2011. The composite Archaean grey gneisses: petrological significance, and evidence for a non-unique tectonic setting for Archaean crustal growth. *Lithos*, 123(1), pp.21–36.
- Myers, J.S. and Watkins, K.P., 1985. Origin of granite-greenstone patterns, Yilgarn block, Western Australia. *Geology*, 13(11), pp.778–780.
- Rudnick, R.L., 1995. Making continental crust. *Nature*, 378(6557), pp.571–577.
- Schmidt, M.W., 1992. Amphibole composition in tonalite as a function of pressure: an experimental calibration of the Al-in-hornblende barometer. *Contributions to Mineralogy and Petrology*, 110(2–3), pp.304–310.
- Shirey, S.B. and Richardson, S.H., 2011. Start of the Wilson cycle at 3 Ga shown by diamonds from subcontinental mantle. *Science*, 333(6041), pp.434–436.
- Smithies, R.H., Champion, D.C. and Sun, S.S., 2004. Evidence for early LREE-enriched mantle source regions: diverse magmas from the c. 3.0 Ga Mallina Basin, Pilbara Craton, NW Australia. *Journal of Petrology*, 45(8), pp.1515–1537.
- Tang, M., Chen, K. and Rudnick, R.L., 2016. Archean upper crust transition from mafic to felsic marks the onset of plate tectonics. *Science*, 351(6271), pp.372–375.
- Taylor, S.R. and McLennan, S.M., 1985. *The continental crust: its composition and evolution*. Oxford, England, Blackwell, 321 p.
- Valley, J.W., Lackey, J.S., Cavosie, A.J., Clechenko, C.C., Spicuzza, M.J., Basei, M.A.S., Bindeman, I.N., Ferreira, V.P., Sial, A.N., King, E.M. and Peck, W.H., 2005. 4.4 billion years of crustal maturation: oxygen isotope ratios of magmatic zircon. *Contributions to Mineralogy and Petrology*, 150(6), pp.561–580.
- Wiedenbeck, M. and Watkins, K.P., 1993. A time scale for granitoid emplacement in the Archaean Murchison Province, Western Australia, by single zircon geochronology. *Precambrian Research*, 61(1–2), pp.1–26.
- Zibra, I., Peternell, M., Schiller, M., Wingate, M.T.D., Lu, Y., Clos, F., 2018. Tectono-magmatic evolution of the Neoproterozoic Yalgoo Dome (Yilgarn Craton). Diapirism in a pre-orogenic setting. *Geological Survey of Western Australia, Report 176*.

CHAPTER 2

Archean diapirism recorded by vertical sheath folds in the core of the Yalgoo Dome, Yilgarn Craton

Frediano Clos^a, Roberto F. Weinberg^a and Ivan Zibra^{a,b}

^a School of Earth, Atmosphere & Environment, Monash University, Clayton, 3800 VIC, Australia

^b Geological Survey of Western Australia, Perth, WA 6004, Australia



Abstract

In Archean granite-greenstone terrains, both vertical and horizontal tectonic processes can generate the typical dome-and-keel structural geometries. One of the classic Archean domes interpreted to result from a horizontal tectonic regime is the Yalgoo Dome in the Yilgarn Craton of Western Australia. In this contribution, we reassess the structural evolution of the Yalgoo Dome by detailing the structures exposed in the migmatitic core. The core contains multi-scale domes-and-basins. These structures were previously interpreted as the result of superposed folding. Our structural mapping shows that the dome-and-basin patterns result from vertical sheath folds developed in a single, progressive deformation event (D_1). This first event most likely resulted from diapiric ascent of a buoyant partially molten tonalitic crust and was overprinted by two contractional episodes (D_2 - D_3) both reflecting bulk EW shortening. The structural evolution proposed here points towards a shift from an early history of vertical tectonics dominated by diapirism to a regional regime dominated by horizontal tectonics.

Keywords: Archean, Yilgarn Craton, gneiss dome, sheath fold, migmatites, diapirism

1 Introduction

Granitic domes separated by narrow keels of metamorphosed greenstones characterize most Archean terranes (Bouhallier et al., 1995; Chardon et al., 1998; Collins, 1989; Ramsay, 1989). The genesis of these dome-and-keel geometries remain controversial and debated amongst proponents of uniformitarian and non-uniformitarian paradigms. In non-uniformitarian models, doming is driven by gravitational instabilities generated by density inversion following the deposition of thick packages of dense greenstones above lower density continental crust and its granitoids (Chardon et al., 1998; Choukroune et al., 1995; Collins, 1989; Hickman, 2004; Van Kranendonk et al., 2004; Weinberg and van der Borgh, 2008). Burial of radiogenic continental crust coupled with the blanketing effect from the greenstone cover, increased the temperature and decreased the integrated strength of the middle-to-lower crust (Bodorkos and Sandiford, 2013; Rey et al., 2003). Thermal and mechanical crustal softening was enhanced by partial melting and promoted diapirism of buoyant granitoids and migmatitic terranes into denser supracrustal rocks (Campbell and Hill, 1988; Van Kranendonk et al., 2014).

By contrast, uniformitarian models are consistent with today's view of plate tectonics dominated by horizontal tectonic forces in a stiff and strong lithosphere. In this scenario, Archean domes are interpreted as metamorphic core complexes (Boulter et al., 1987; Hofmann et al., 2015; Kloppenburg et al., 2001; Lana et al., 2010; Zegers et al., 1996) or resulting from superposition of multiple folding events (Drury et al., 1984; Fyson, 1984; Myers and Watkins, 1985; Snowden, 1984; Yin, 2004). One of the examples used to support the formation of large-scale Archean domes by two superposed fold is the Yalgoo Dome in the Yilgarn Craton of Western Australia (Fig. 1) (Myers and Watkins (1985).

This contribution reassesses the structural evolution of the Yalgoo Dome's core (Fig. 1) and show that dome-and-basin patterns result from vertical sheath fold development in a single, progressive deformation event (D_1) related to diapiric ascent. These structures were subsequently overprinted by two EW contractional episodes (D_2 – D_3) suggesting a shift from vertical to horizontal tectonics.

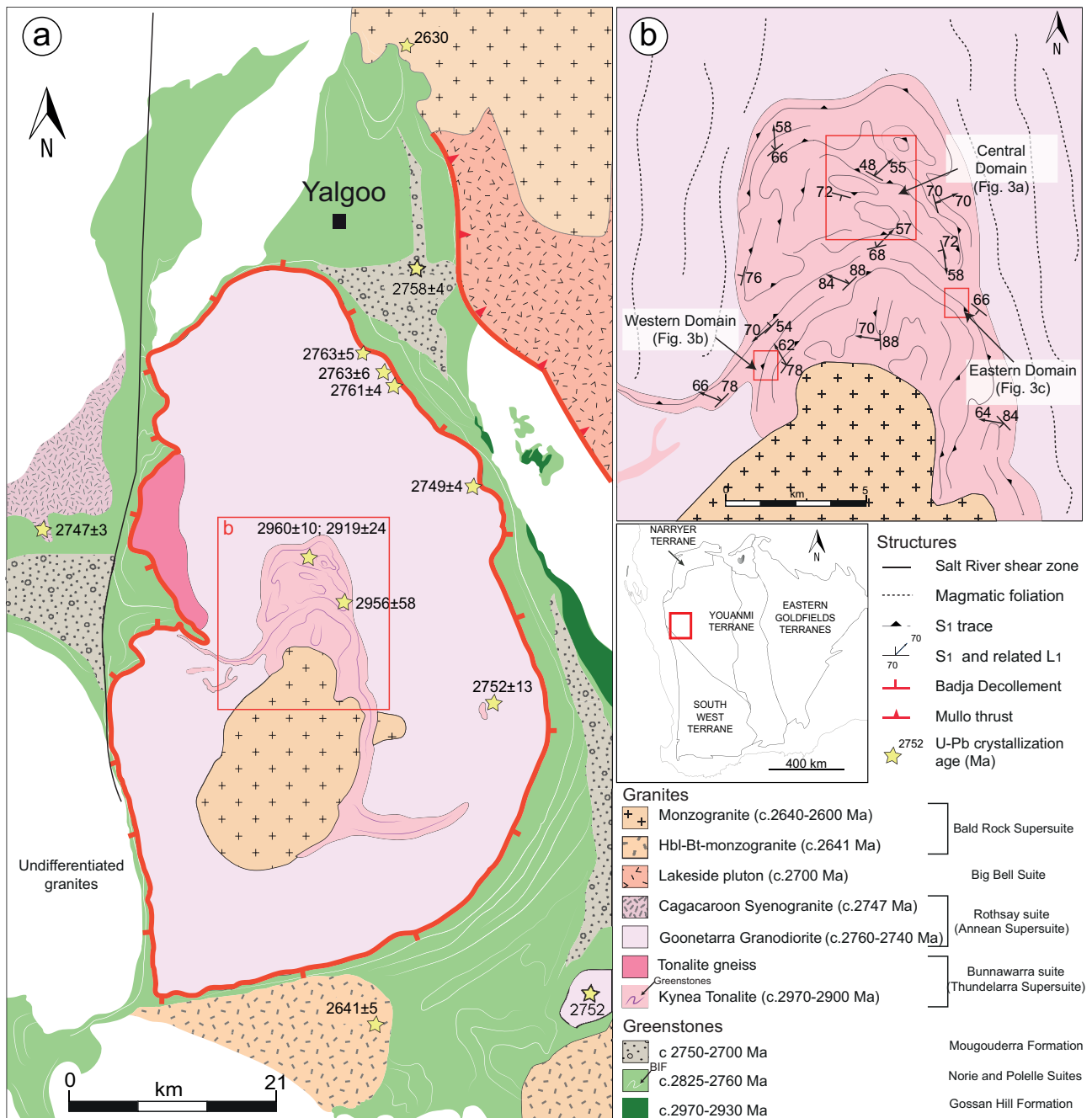


Figure 1: Geological map of the Yalgoo Dome and greenstone envelope combining field and geophysical data. The inset on upper right shows location of the studied area in the Murchison Domain, Yilgarn Craton (a). The batholith comprises multiple generations of granites intruded over a time span >300 m.yr: in the core, the Migmatitic Domain comprises 2970-2900 Ma Kynea Tonalite and narrow greenstone layers. This complex is surrounded by the voluminous intrusions of 2760–2740 Ma Goonetarra Granodiorite. b) Structural map of the Migmatitic Domain shows D₁ foliation patterns outlining inner F₁ circular folds and large-scale F₂ subvertical folds, which define the contour of the entire domain. Red rectangles indicate location of detailed maps in Fig. 2 and yellow star indicates U-Pb zircon crystallization ages (Zibra et al., 2018).

2 Geological setting

In the western half of the Archean Yilgarn Craton, the Youanmi Terrane includes a 2960–2720 Ma greenstone sequence intruded by 2970–2600 Ma granitoids (Ivanic et al., 2012; Van Kranendonk et al., 2013). A craton-scale network of transpressive shear zones that accommodated EW regional

shortening during the Neoproterozoic orogeny 2730 and 2660 Ma (Zibra et al., 2017) dissects most of the terrane. In map view, these shear zones form anastomosing lenses broadly N-trending and continuous over hundreds of kilometers along strike (Zibra et al., 2014a). In the westernmost part of the terrane, these large-scale shear zones are lacking and coincides with the region where the Yalgoo dome and its surrounding keels are exposed. This is a prominent, 100 km long, elliptical granitic dome surrounded by greenstones, comparable to the broad domes of the East Pilbara Craton (Collins, 1989). A suite of granitic rocks known as the Bald Rock Suite (2640–2600 Ma; Ivanic et al., 2012; Van Kranendonk et al., 2013) intruded both the Yalgoo Dome and the transpressive shear zones to the east.

Greenstone sequences wrapping around the Yalgoo Dome include the 2963–2958 Ma Gossan Hill Formation of felsic volcanic and volcanoclastic rocks. These sequences are unconformably overlain by mafic volcanic rocks, felsic volcanoclastic sandstones and banded iron-formation of the 2825–2805 Ma Norie Group and the 2800–2760 Ma Polelle group, a >8 km thick volcanic sequence evolving from komatiitic basalts to tholeiitic basalts and andesites (Ivanic et al., 2015). On top of these sequences, unconformably, lies the Mougooderra Formation, a siliciclastic sequence whose maximum depositional age is 2758 ± 4 Ma (Zibra et al., 2018). A 1–2 km wide high-strain zone, the Badja décollement (Fig. 1; Zibra et al., 2018), juxtaposes the greenstones against the granitic dome. Multiple kinematic indicators along the Badja décollement indicates granite-up and greenstone-down sense of movement (Foley, 1997; Zibra et al., 2018). This dome is composed of multiple granitoids (2760–2740 Ma Goonetarra Granodiorite of the Rothsay Suite) and a migmatitic core, where the oldest rocks are well-exposed in a region of $\sim 8 \times 12$ km (Fig. 1) and are here defined as the Migmatitic Domain.

3 Migmatitic Domain

The Migmatitic Domain comprises the Kynea Tonalite (Figs 1, 2), a migmatitic tonalite intruded into amphibolite and banded iron formation (BIF) sequences (Zibra et al., 2018). The Kynea Tonalite underwent migmatization and Wiedenbeck and Watkins (1993) reported zircon core U-Pb ages of 2912 ± 12 Ma, and rim ages of 2700–2800 Ma, interpreted as the crystallization age of the

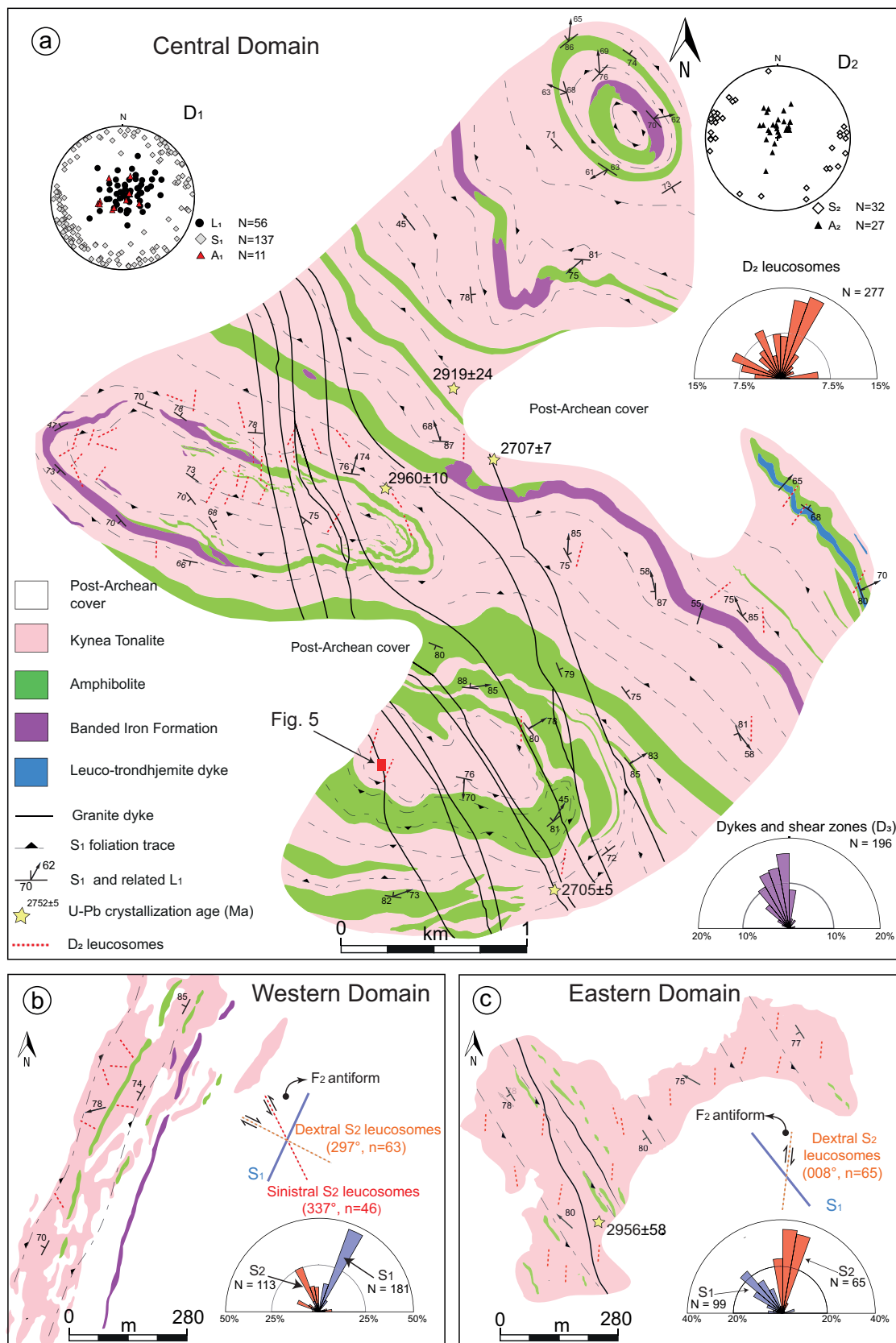


Figure 2: Structural map of three key areas of the core (Fig. 1a): a) Central Domain representing the hinge zone of a large-scale F_2 fold. This is the same area mapped by Myers and Watkins (1985). The Western (b) and Eastern Domain (c) represent instead opposite limbs of large-scale subvertical folds. In each domain insets show equal area, lower hemisphere stereonet and rose diagram of the orientation of structures associated with major deformation phases (D_1 – D_3). D_1 – D_2 structures are cut by c. 2707 Ma granitic dykes. L_1 = mineral lineation, S_1 – S_2 = foliation planes, A_1 – A_2 = fold axes. S_1 and S_2 foliation traces show the vergence of D_2 and the arrow indicates the direction of fold closure.

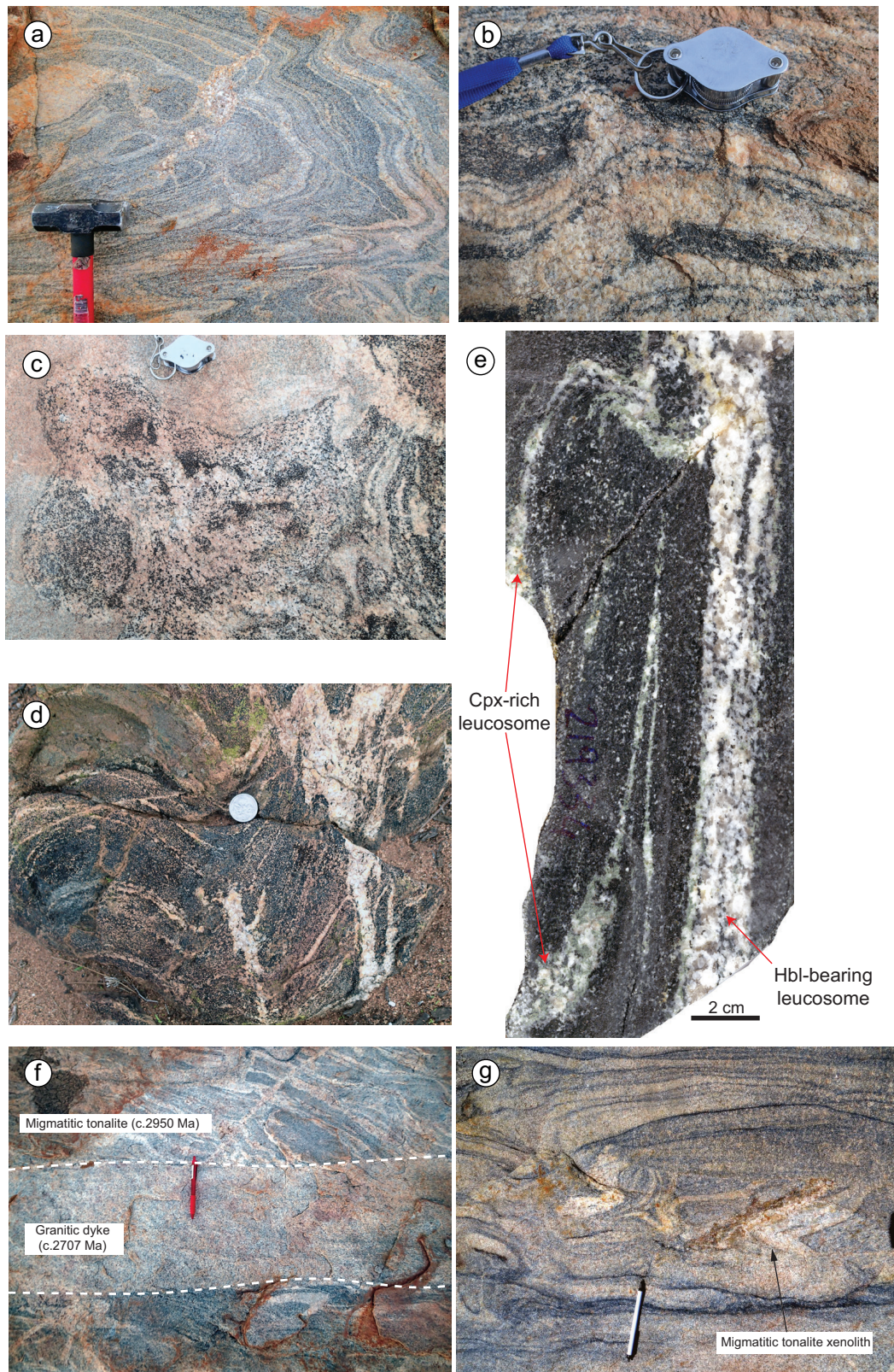


Figure 3: Representative lithologies in the Central Domain of the Migmatitic Domain. a) Folded layering in migmatitic tonalites marked by irregular repetition of leucocratic, mesocratic and melanocratic layers; b) typical interlayering of leucocratic migmatitic tonalite and amphibolite parallel to dominant foliation S_1 ; c) disaggregated amphibolite in migmatitic tonalite showing Hbl-bearing tonalitic patches surrounding Hbl-rich restites, indicative of D_1 migmatitisation in amphibolites; d) second anatectic event in amphibolite, showing S_1 -parallel leucosomes cut by larger discordant leucosomes parallel to the axial plane of F_2 folds; e) polished hand-specimen of amphibolite migmatite showing deformed D_2 leucosomes. Small bottle green clinopyroxene-rich leucosomes (< 1 cm) connect with wider hornblende-bearing leucosomes; f) cross-cutting relationships between migmatitic tonalite and granitic dyke (c. 2707 Ma), and (g) schlieren granite in dykes, including mm-to-metric migmatitic tonalite xenoliths.

tonalitic gneiss protolith and an overgrowth linked to its migmatization, respectively. More recent investigations further constrain the emplacement of the tonalitic protolith at 2960 ± 10 Ma and 2956 ± 58 Ma (Zibra et al., 2018; Fig. 2a). In map-view, the Migmatitic Domain show complex geometries (Figs 1, 2) that were interpreted by Myers and Watkins (1985) as fold interference patterns. Their model was supported by field observations of large- and small-scale dome-and-basin patterns in the Migmatitic Domain. These map-scale dome-and-basin structures were interpreted as the superimposition of two orthogonal sets of folds with steep axial surfaces and subhorizontal fold axes. Migmatitic tonalites show a pervasive gneissic foliation, delineated by preferential alignment of biotite and subparallel to a well-developed compositional layering. This layering comprises melanosome, mesosome and leucosomes (metatexites, Figs 3a, 4a–c) and is therefore interpreted as migmatitic. The melanosome and mesosome are dominated by biotite. The mesosome comprises abundant plagioclase, quartz and interstitial K-feldspar with rare muscovite. Leucosomes exhibit the same mineralogy, but with a net decrease in biotite and increase in K-feldspar content. Where leucosomes are more abundant, they develop an interconnected network in which layer-parallel leucosomes are truncated by discordant leucosomes (Figs 3d, 4c).

Amphibolite and BIF form 20–300 m wide layers within the migmatitic tonalite and represent remnants of an older greenstone sequence. In map view, the greenstone layers are continuous for hundreds of meters along strike, defining large-scale elliptical structures (Fig. 2a). Amphibolites are medium- to coarse-grained SL-tectonites consisting of hornblende, plagioclase, titanite, quartz and rare biotite, with accessory magnetite and apatite. In places, amphibolites have evidence for in situ melting forming stromatic metatexites (Figs 3c–d). Leucosomes contain dominant euhedral hornblende and bottle green clinopyroxene as peritectic minerals (Fig. 3e). BIFs comprise Fe- and Si-rich layers with thickness ranging between 1 and 4 mm. Ferruginous domains contain Fe-rich amphibole (cummingtonite-grunerite series) and clinopyroxene alongside magnetite, while Si-rich layers have abundant quartz and small, equant crystals of magnetite. This mineral paragenesis indicates low to medium amphibolite facies conditions (Klein, 2005).

The migmatitic tonalite were intruded by a ~NS trending, subvertical swarm of granitic dykes (Fig.

2a). Zircons from the late granite dykes have been recently dated by U-Pb SHRIMP at 2700 ± 7 Ma and 2705 ± 6 Ma with zircon cores yielding inheritance ages at 2958 ± 20 and 2943 ± 9 Ma (Zibra et al., 2018). Contacts with host rocks are sharp and lack chilled margins. These dykes differ from the host migmatitic tonalite not only in composition, but also by the presence of biotite-rich schlieren. Most dykes are granitic, with equigranular to porphyritic magmatic fabric. A diffuse schlieren layering (Figs 3f–g) is highlighted by biotite-rich layers approximately parallel to the dykes' margins (Fig. 3f). The gradual disaggregation of migmatitic tonalite xenoliths into the dyke (Fig. 3g) indicates that schlieren layering might represent the melanocratic residuum left after digestion of the host migmatitic tonalite.

4 Structures of the Migmatitic Domain

We have identified three major deformation phases (D_1 – D_3) in the Migmatitic Domain. The dominant pervasive foliation (S_1) is parallel to the lithological contacts and compositional layering in migmatitic tonalite. D_1 structures have been refolded into a series of km-scale F_2 vertical folds with NS striking axial planes (Fig. 1b). NS shear zones (D_3) postdate D_1 – D_2 structures and developed only within the granitic dykes (Fig. 2a). We describe below the three distinct structural domains of the dome's core, (Fig. 1b): (i) the Central Domain, (ii) the Western and (iii) the Eastern Domain (Fig. 2).

4.1 Central Domain

The Central Domain is a region characterized by structural domes comprising a well-exposed area of ~ 20 km² in the center of the Migmatitic Domain (Fig. 1).

4.1.1 Early structures (D_1): sheath folds

In the central part of the complex, concentric S_1 trajectories define domes elongated WNW–ESE (Figs 1, 2a), with long axes up to 1 km in length. Foliation is parallel to lithological contacts and define elliptical rings in map view (Fig. 2a). These structures are characterized by radial down-dip L_1 lineations, changing in orientation in harmony with changes in the circumcentric foliation (Fig. 2a). Elliptical patterns are also evident at outcrop scale, where they are defined by the leucosome-mel-

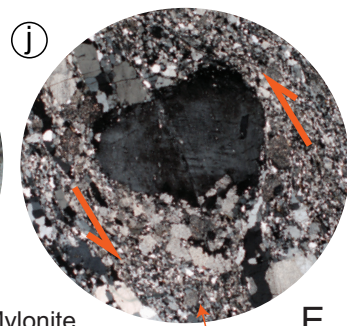
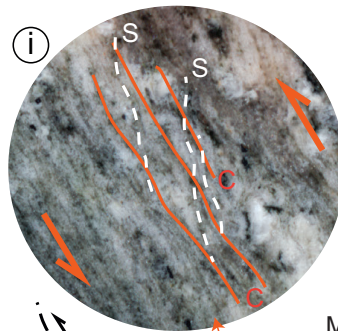
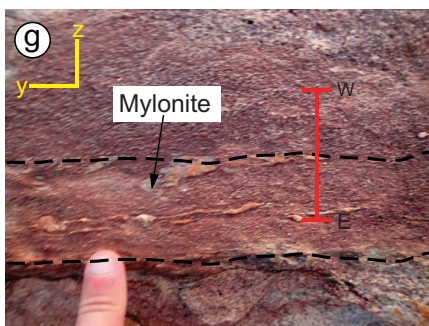
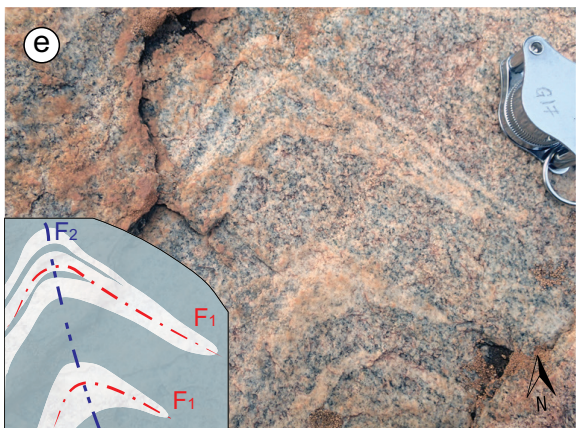
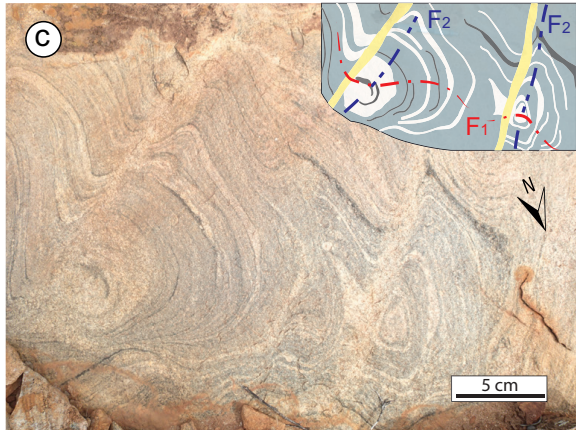
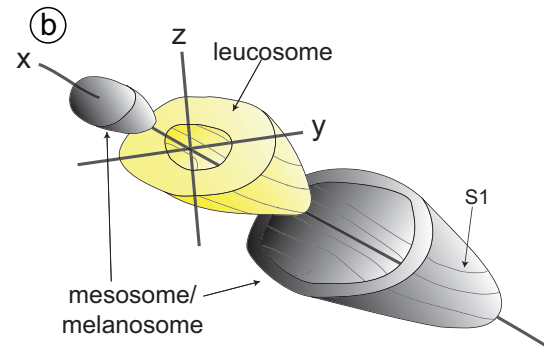
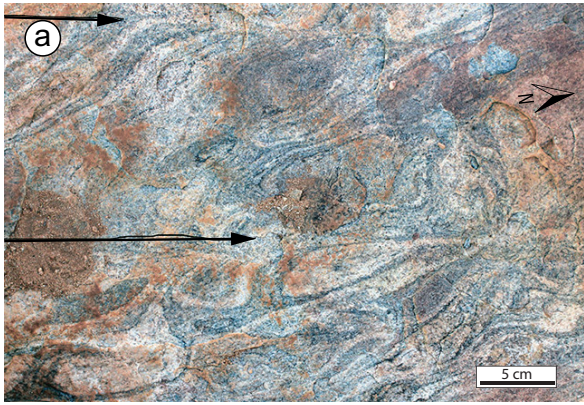


Figure 4: Representative outcrop-scale structures in the Central Domain of the Migmatitic Domain: a) F_1 sheath folds in migmatitic tonalite with “analogous-eye-fold” (lower part of photograph) and “bulls-eye-folds” geometry (upper part of photograph) (Alsop and Holdsworth, 2006) overprinted by D_2 leucosomes, locally associated with dextral dragging of the F_1 folds. Leucosome position and direction are indicated by pair of arrows; b) 3D drawing of F_1 sheath folds defined by repetition of leucosomes in yellow and mesosome in grey. This was constructed from a series of parallel cuts on a large specimen (from Fenwick, 2014); c) S_1 schistosity defining F_1 sheath folds elongated ~EW, refolded by open F_2 folds and cross-cut by S_2 axial planar leucosomes trending NNE–SSW at high angles to S_1 (for a more complete description see “Photo of the month” in *Journal of Structural Geology*, [https://doi.org/10.1016/S0191-8141\(16\)30146-8](https://doi.org/10.1016/S0191-8141(16)30146-8)); d) two S_2 shear bands filled with leucosome dragging F_1 isoclinal fold defined by cm-interlayering of amphibolite and migmatitic tonalite; e) F_1 isoclinal folds defined by leucosomes, refolded by ~NS subvertical F_2 open folds, resulting in “Type-3” fold interference (Ramsay, 1962); f) S_1 compositional layering cut at high angle by D_2 axial planar leucosome, trending NNE–SSW, and with a sinistral strike-slip component indicated by drag folding; (g) transition to D_3 mylonite within c. 2707 Ma granitic dykes. Note quartz ribbons parallel to the shear zone, which is also parallel to the dike margin. EW red line mark the position of the sample in figure h; (h) hand-sample cut parallel to the lineation L_3 and perpendicular to foliation S_3 (XZ finite strain plane) showing the contact between magmatic foliation (left) and the mylonitic D_3 shear zone (right). Mylonite shows grain-size reduction by dynamic recrystallization. Relics of K-feldspar are surrounded by a fine-grained matrix composed of plagioclase, K-feldspar, quartz and biotite. S/C fabric (i) and mantled K-feldspar porphyroclast (j) indicate reverse sense of shear.

anosome layering in migmatites (Fig. 4a) and reflect 3D sheath fold geometries (Fig. 4b; Fenwick, 2014) or isoclinal folds defined by amphibolite-tonalite interlayering (Fig. 4d). In this contribution, we use the term “sheath fold” as a descriptive term, with no genetic connotation. Most F_1 sheath folds resemble the “analogous-eye-folds” with subordinate occurrence of “bulls-eye-folds” (Fig. 4a; Alsop and Holdsworth, 2006).

The boundaries between migmatitic tonalite and greenstones show a cm-scale interlayering of amphibolite and banded iron formation with leucocratic migmatitic tonalite. These layers show a layer-parallel foliation (S_1), with a spacing of 1 mm. The intensity of S_1 and the percentage of leucosomes in the migmatitic tonalite decrease gradually away from the contacts. D_1 anatexis of amphibolites is localized along the granite-greenstone interface, where the more competent amphibolites were boudinaged and disaggregated during deformation.

4.1.2 Second deformation event and anatexis (D_2)

The D_2 event comprises gentle to open folds with subvertical axial plane striking ~NNE–SSW and steeply-N plunging fold axis (Fig. 2a). These folds vary in scale from kilometric to decimetric.

Superposition of F_2 on F_1 folds produced Type-3 patterns (Ramsay (1962) (Figs 4c–d–e). Refolding of S_1 and F_1 sheath folds is associated with a second anatexis event, evidenced by leucosomes parallel to F_2 axial planes in both migmatitic tonalite (Fig. 4c) and amphibolite (Fig. 3d). D_2 leucosomes assist F_2 folding by accommodating shearing on fold limbs (Figs 4c–f, 5e–f; Symington et

al., 2014). Most outcrops in the region are subhorizontal, with rare vertical exposures. This outcrop bias has hampered documentation of vertical displacement. On horizontal outcrops, axial planar leucosomes deflect pre-existing subvertical foliation with a dominant dextral shear sense, and less commonly with a sinistral sense (Fig. 4c) with horizontal offsets of 1–40 cm. Locally, these axial planar foliations show dextral horizontal shearing on the right limb of F_2 folds and sinistral on the left (Fig. 5e–f). D_2 leucosomes in the migmatitic tonalite lack peritectic minerals and are compositionally identical to S_1 leucosomes. In amphibolite, D_2 leucosomes comprise anhedral clinopyroxene and amphibole (Fig. 3e).

In summary, F_2 folds overprint earlier D_1 leucosomes (Fig. 5) and F_1 sheath and isoclinal folds trending EW (Figs 4c–d). F_2 folds had melt-filled axial planar trending ~NNE–SSW foliations, now preserved as D_2 leucosomes.

4.1.3 Shearing of granitic dyke swarm (D_3)

The ~NS trending, c. 2707 Ma granitic dyke swarm has not been deformed by D_1 – D_2 structures (Figs 3f, 5). These dykes generally preserve primary magmatic foliation parallel to dyke margins, concordant with schlieren layering (Fig. 5d), and are overprinted only by D_3 shear zones subparallel to dyke boundaries and localized within the dykes (Figs 4h, 5). E-dipping shear zones, commonly <10 cm wide, occur at the interface between dykes < 1 m thick and migmatitic tonalite (Fig. 5c), but shear zones wider than 1 m are present within thicker dykes (>5 m). S_3 is a well-developed mylonitic foliation, defined by an anastomosed network of millimeter-size layers of recrystallized biotite, feldspars and quartz grains wrapping around less deformed microlithons (Fig. 4h). These shear zones have steeply-plunging mineral stretching lineation L_3 . Ultramylonites occur in the center of the shear zones, where rare K-feldspar porphyroclasts (Fig. 4j) and elongated quartz aggregates (Fig. 4i) are immersed in a fine-grained mylonitic matrix. On sections perpendicular to mylonitic foliation S_3 and parallel to mylonitic lineation L_3 (i.e. XZ plane of the finite strain ellipsoid; Fig. 4h), mantled K-feldspar porphyroclasts and S/C fabric indicate top-to-the-W reverse sense of shear (Fig. 4h–j).

4.2 Western Domain

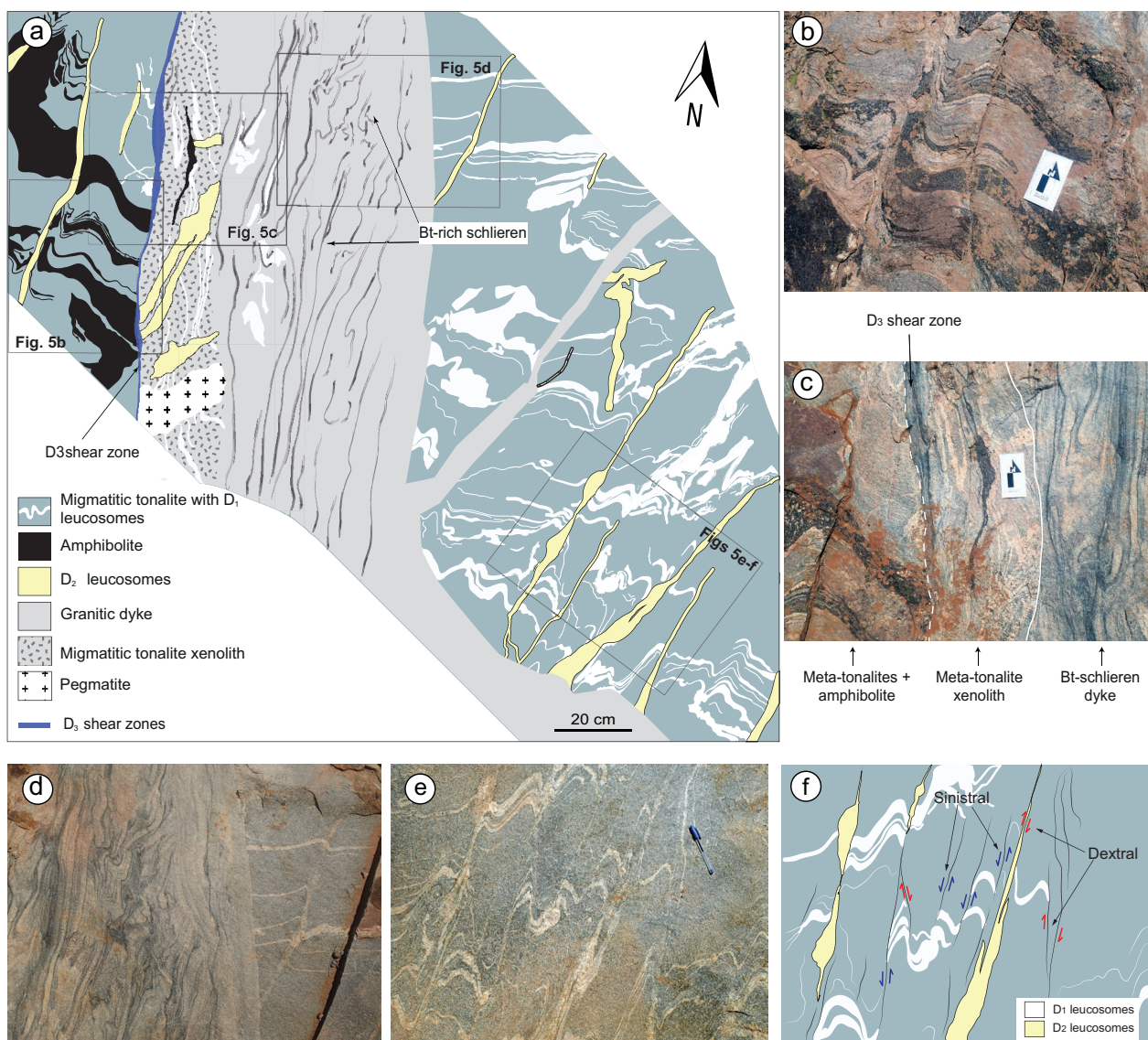


Figure 5: a) Key outcrop marked in Fig. 2a illustrating relationships between D_1 – D_2 – D_3 and dykes. Migmatitic tonalite shows compositional banding parallel to S_1 schistosity defined by repetitive melanosome, mesosome and leucosomes and interlayered with amphibolite (b). D_2 define open folds (F_2) associated with S_2 axial planar leucosomes trending ~NNE–SSW. D_1 – D_2 structures are cut by the c. 2707 Ma granitic dykes rich in biotite-schlieren; c) The contact between the dyke and host migmatitic tonalite is marked by a steeply-dipping D_3 shear zone and a transposed migmatitic tonalite enclave grading into the granitic dyke, d) Bt-schlieren granite dyke cutting both S_1 and S_2 ; e-f) photograph and line drawing of parallel array of D_2 axial planar leucosomes with dextral horizontal shear sense on the right flank and sinistral on the left flank of a mesoscale F_2 fold.

The Western Domain outcrops nearly 1km east of the contact between the Migmatitic Domain and the Goonetarra Granodiorite (Fig. 1b). The study area encompasses a semi-continuous 1.5 km² flat exposure of migmatitic tonalite and two layers of greenstone 5–20 m wide (Fig. 2b). D_1 – D_2 structures are similar to the Central Domain, but here S_1 trends NNE–SSW (average strike 024°; Fig. 2b) rather than defining the WNW–ESE-elongated domes. The absence of three-dimensional exposures prevents a systematic collection of linear fabrics, although Fenwick (2014) reports a few

steeply-plunging mineral lineations (L_1). D_2 consists of a gentle to open folds (F_2) associated with a dominant axial planar foliation trending NW-SE and commonly filled with leucosomes defining shear bands (S_2) similar to the Central Domain (Figs 6a–b). S_2 leucosomes trend NW–SE, at an angle to S_1 and display both sinistral (Fig. 6a) and dextral (Fig. 6b) horizontal shear components, with an average orientation of 337° ($n=46$) and 297° ($n=63$), respectively (Fig. 2b; Fenwick (2014)). We have no information regarding the vertical component of motion due to the flat nature of the outcrop. Relationships between D_1 and D_2 are well preserved in the NW portion of this outcrop, where their vergence suggests the occurrence of a F_2 fold closure to the east, towards the hinge zone in the Central Domain (Fig. 2b).

4.3 Eastern Domain

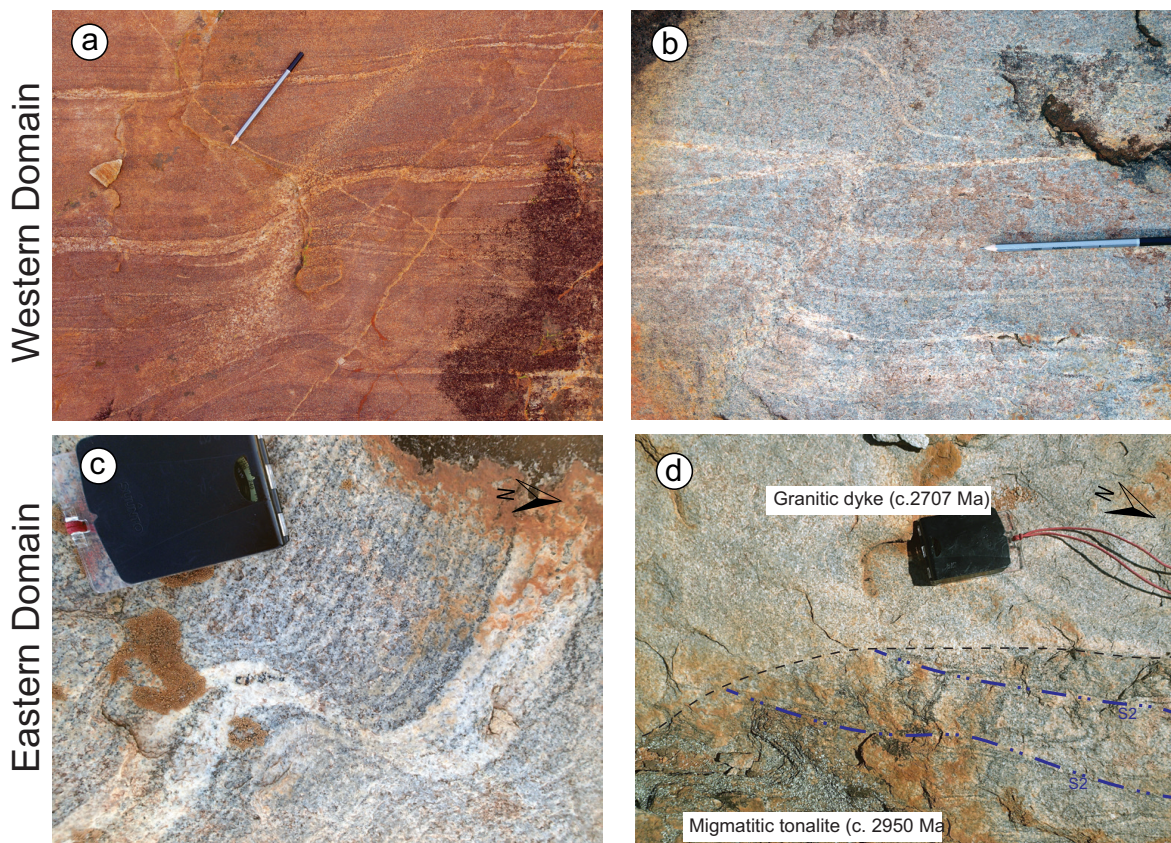


Figure 6: Representative structures in the Western Domain (Fig. 2b) where leucosome-filled shear bands display both sinistral (a) and dextral (b) shear sense on the horizontal plane. In the Eastern Domain (Fig. 2c); S_2 axial planar leucosomes invariably show dextral shear sense on the horizontal plane (c) and are cross-cut by granitic dykes (d), with faint banding reflecting homogenization of schlieren.

The Eastern Domain outcrops ~ 3 km west of the contact with the outer band of Goonetarra Granodiorite (Fig. 1) and is characterized by scattered outcrops of greenstones and migmatitic tonalite

(Fig. 2c). Deformation patterns are similar to those of the Western Domain, except for the inverted S_1 – S_2 angular relationship, suggesting the occurrence of an F_2 antiform closure to the west, towards the Central Domain (Fig. 2c). S_1 and L_1 are subvertical and more intense in the migmatitic tonalite, expressed by repetitive leucocratic-melanocratic banding parallel to narrow chains of isolated amphibolite lenses trending NNW–SSE. Vertical S_2 are commonly filled with leucosomes and show dominantly dextral displacement on horizontal exposures (Fig. 6c), offsetting S_1 fabric between 10 and 25 cm. In the western part of the domain, D_1 – D_2 fabrics are cross-cut by two granitic dykes related to the swarm described in section 3.2.3 (Figs 2c, 6d).

5 Discussion

5.1 Refolded sheath folds

Myers and Watkins (1985) interpreted the structures in the Migmatitic Domain to result from superposed folding events. If the subvertical dome-and-basin resulted from fold superposition, they would need two generations of horizontal upright folds (i.e. subhorizontal fold axes and steep axial planes). Instead, F_1 and F_2 folds have subvertical fold axes and axial planes (Fig. 2a), which gives rise to a vertical Type-3 refolded folds (Figs 4c–d–e). More significantly, the elliptical structures at outcrop and map-scales are not associated with mutually perpendicular foliations, but rather S_1 is systematically parallel to lithological contacts, and that S_2 cuts across and folds these contacts (Figs 4a–c). In the Central Domain, we found that the circumcentric S_1 planar fabric and L_1 vertical lineation formed under anatectic conditions in one progressive deformation phase (D_1) associated with sheath and isoclinal folds (Figs 4b, 7a). The sheath folds are not a result of F_1 – F_2 fold superposition because they were sheared and displaced by axial planar foliation S_2 (Figs 4a–c) and refolded by F_2 folds (Figs 4e–f, 7b).

Combining the information from the Central, Western and Eastern Domain (Fig. 2), we suggest that these domains represent a ~7 km wide, subvertical F_2 fold closure trending NNE–SSW with axial planes commonly filled with leucosomes (Figs 2a, 3a). The Central Domain is the hinge zone of this large F_2 fold, where the early domal structures are preserved and refolding patterns are well defined (Figs 7a–b), whereas the Eastern and Western Domains represent opposite fold limbs, as indicated by the angular relationships between S_1 and S_2 (Figs 7a–b). Along both limbs, rare sub-

vertical L_2 mineral lineations (Fenwick, 2014) show that the main stretching axis is subvertical and accompanied by a minor horizontal shear component along axial planar foliations (Fig. 2c). Dextral strike-slip component on the axial planar foliations is dominant in the Eastern Domain, but not in the Western Domain. Here, F_2 folds are rare and leucosome-filled shear zones occur as a conjugate set with both sinistral and dextral shear sense, striking 337° and 297° , respectively, with an acute angle facing the maximum shortening axis trending NW–SE and a NE–SW stretching axis. The combination of a NE–SW and a vertical stretching axis suggests a significant horizontal flattening pure shear component (Figs 2a–b; Fenwick, 2014).

D_2 sinistral and dextral components of shearing on vertical planes are interpreted to represent divergent axial planar foliations of F_2 folds that once filled with leucosomes facilitated shearing on limbs during folding (Fig. 7b). Anatexis weakened the migmatitic tonalite during D_2 and compaction instabilities forced the magma into axial planar foliations (Weinberg et al., 2015). Melt segregated into these planes facilitated shearing and enhanced the development of F_2 folds (Symington et al., 2014; Weinberg and Mark, 2008). Hence, D_2 shear zones nucleated on axial planar foliations with opposing shear sense on each fold limb.

The timing of the two crustal anatexis events and the significance of the ductile fabrics in the migmatitic tonalite is only partly constrained. The outer rims of zircon from the migmatitic tonalite are widely spread between 2800 and 2700 Ma (Wiedenbeck and Watkins, 1993), implying that the main melting and deformation events (D_1 and D_2) are significantly younger than the age of the protolith at 2970–2900 Ma, corresponding to the age of zircon cores.

5.2 Diapirism during anatexis: the origin of sheath folds (D_1)

The multi-scale F_1 sheath folds highlighted by the greenstone layers (Figs 2a, 7) and leucosomes (Figs 4a–c), are similar to structures developed in salt diapirs, consistent with vertical flow of buoyant material into a diapir stem (Fig. 8; Talbot and Jackson, 1987). In this study, the largest sheath folds may represent second-order structures associated with a larger diapir. The multi-scale nature of the sheath folds, varying over four orders of magnitude from 1 km to 10 cm, reflect either the characteristic scale-independence of folded rock sequences, or the contemporaneous diapiric dom-

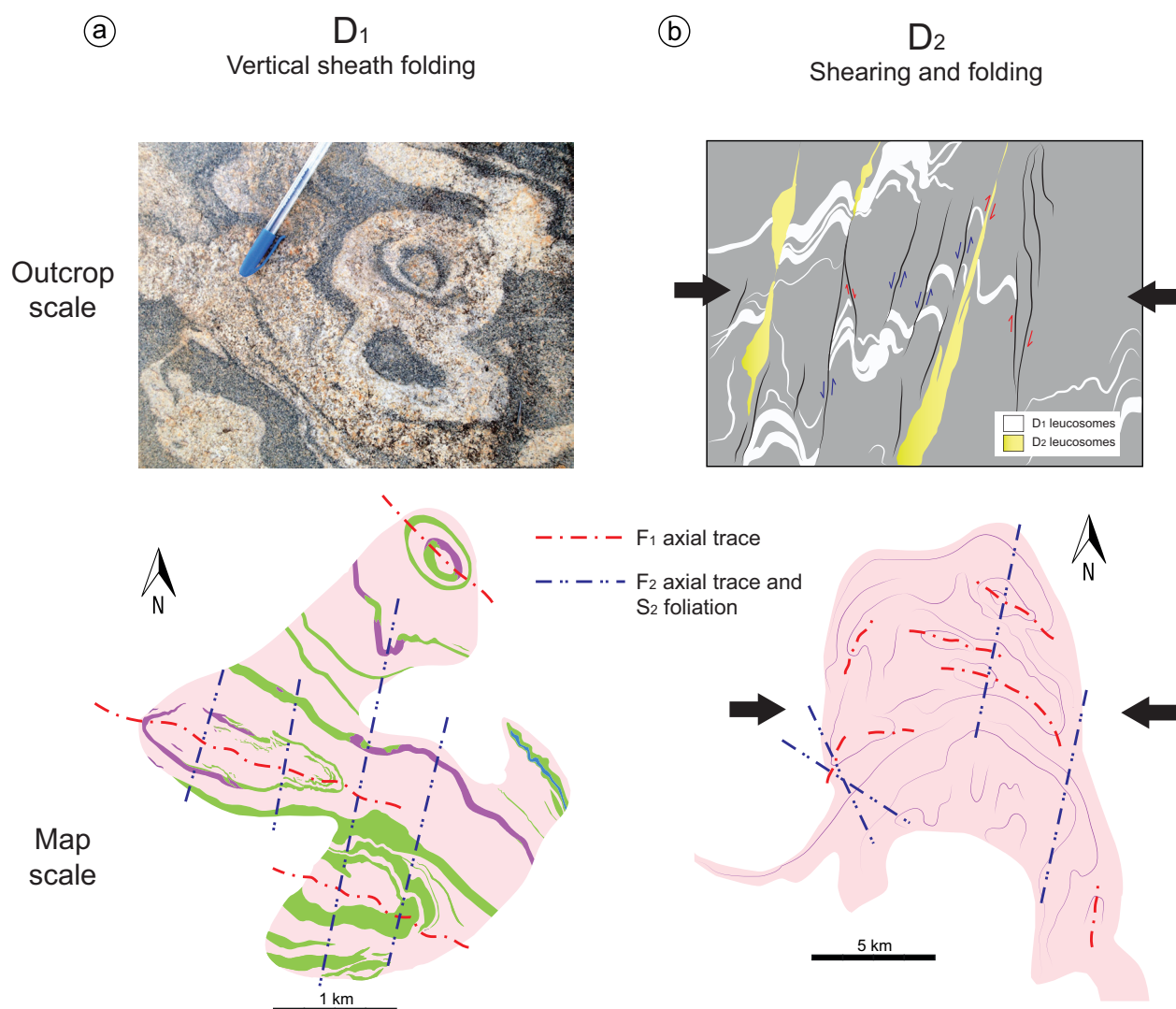


Figure 7: Summary of salient characteristics of D_1 and D_2 in the Migmatitic Domain, from outcrop to map scale. a) D_1 is dominated by syn-migmatitic pervasive foliation (S_1) and by scale-invariant F_1 sheath folds, developed during vertical flow of felsic and mafic rocks. In the Central Domain, the long axis of km-scale elliptical folds representing cross-sections of sheath folds are preferentially oriented WNW–ESE; b) D_2 is marked by ~ NNE–SSW melt-assisted shearing event (D_2) mainly localized along S_2 axial planar leucosomes, which contributed to refolding F_1 folds, resulting in the formation of vertical F_2 folds. D_2 leucosomes define a divergent axial planar foliation at the scale of the Migmatitic Domain.

ing of rocks at different wavelength (Weinberg and Schmeling, 1992). These are known as a multi-wavelength Rayleigh-Taylor instability or polydiapirism, and reflect complex density and viscosity stratigraphy of the rock sequence. Polydiapirism has been invoked to describe structural patterns in gneiss domes containing subdomes in the Proterozoic Baltic Shield (Stephansson, 1975), in the Variscan Meseta of Morocco (Bouchez and Diot, 1990) and also in salt diapirs (Schwerdtner, 1982; Talbot and Jackson, 1987). Other well-documented gneiss domes, defined by multiple domes can be found in the Greek island of Naxos (Kruckenberg et al., 2011) and in the Montagne Noire of the French Massif Central (Roger et al., 2015).

Numerical modelling by Weinberg and Schmeling (1992) shows that the optimal condition for polydiapirism occur with a three-layer stratified crust, with inverted density and marked viscosity contrast between the two bottom layers and the top layer. Analogous conditions may have occurred at c. 2760 Ma, after nearly 60 Myr of protracted mafic volcanism (development of the 2825–2805 Norie Group and 2800–2760 Ma Polelle group 2760 Ma; Van Kranendonk et al., 2013), formed an up to 8 km thick greenstone cover (Ivanic et al., 2015) on top of an interlayered felsic-mafic crust. At that stage, a first-order high density and viscosity contrast likely existed between cold, stiff and dense greenstones in the upper crust, and partially molten, buoyant rocks in the middle/lower crust. In this scenario, a second-order perturbation could have developed in zones of interlayered migmatitic tonalite and greenstones, giving rise to a multiwavelength overturn, defined by several sub-domes in the Migmatitic Domain.

5.3 EW shortening (D_2 and D_3)

Unlike D_1 , the subsequent deformation events reflect bulk EW shortening. The large-scale D_2 vertical folds mapped in the three domains described above (Fig. 2), likely result from an EW shortening event associated with renewed anatexis. Since the timing of D_2 remains poorly constrained (section

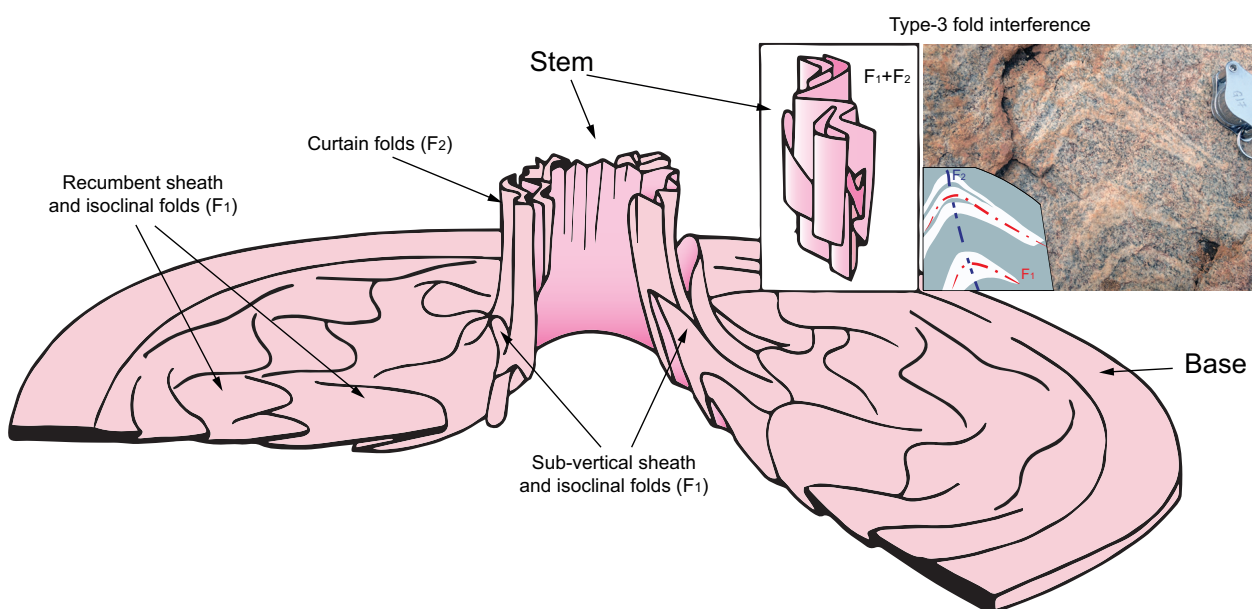


Figure 8: Cartoon comparing internal dynamics of the Migmatitic Domain to salt diapirs (modified after Talbot and Jackson, 1987) showing a base dominated by a subhorizontal flow regime that generates one or more generations of recumbent sheath and isoclinal folds. These early folds are then rotated into the diapiric stem where they are further stretched and refolded by steeply-plunging curtain folds (Talbot and Jackson, 1987). In the stem, Type-3 interference patterns are typical.

5.1), we envisage two plausible scenarios to explain the progression from early diapirism and sheath folding (D_1) to an EW compressive phase (D_2).

The first and more plausible scenario relates D_2 temporally with D_1 and diapirism, where once more, salt diapirs provide a possible analogue. The most characteristic folds recognized within salt diapirs are steeply-plunging cylindrical folds, known as curtain folds (Fig. 8). The axial planes of these folds are radial and their envelope is usually concentric on horizontal sections (Talbot and Jackson, 1987). Curtain folds are expected to form in the diapiric stem and overprint growing sheath folds that initiated at the base of the diapir (Fig. 8). Hence, the natural evolution of a salt diapir involves early recumbent folds, rotated and stretched into vertical sheath folds as they rise up the stem, that finally become compressed and refolded by steeply-plunging curtain folds giving rise to Type-3 fold superimposition patterns (Ramsay, 1962) (Fig. 8).

A difference is that F_2 axial planes are not radial in the Migmatitic Domain: they are divergent, but preferentially oriented NS (Fig. 7). In a diapiric setting, this could occur if during the rise in the diapiric stem, the migmatitic tonalites and interlayered greenstones were subjected to a minor EW compression. The finite strain ellipsoid in an EW shortened stem would have an oblate strain ellipsoid, with vertical maximum finite stretch and EW horizontal maximum shortening axis. F_2 folds with axial planes oriented ~NNW–SSE and Type-3 interference patterns (Fig. 8) are all compatible with this scenario.

The second scenario assumes that D_1 and D_2 relate to different processes and links D_2 to a regional EW shortening period, that has been documented NE of the Yalgoo Dome. Here a series of NS elongated plutons have been emplaced within an anastomosed craton-scale network of Neoproterozoic transpressive shear zones (Zibra et al., 2014a, 2014b). This regional deformation phase is part of the Neoproterozoic Orogeny, which started at c. 2730 Ma (Zibra et al., 2017). In this scenario, D_2 deformation and anatexis took place after the onset of the orogeny and before the granitic dyke swarm intruded the Migmatitic Domain at c. 2707 Ma.

The maximum age of the last deformation event (D_3), with its E-dipping shear zones and top-to-the-W vergence (Figs 4h–5), is constrained by the intrusion of granitic dykes at c. 2707 Ma. Their age corresponds to the emplacement of the voluminous Lakeside Pluton along the E-dipping Mullo

Thrust at 2710–2695 Ma (Fig. 1a; Zibra et al., 2014a). Beyond the similar age of magmatism, the Mullo Thrust has similar orientation and kinematics to the D_3 shear zones in the Migmatitic Domain, suggesting that they are part of the same tectono-magmatic event.

5.4 From vertical to horizontal tectonics

The structural evolution of the Migmatitic Domain shows a secular shift from vertical to horizontal tectonics. The dominant (D_1) structures developed in a tectonic regime involving vertical rise of partially molten crustal rocks and established the initial domal structures. These were reshaped by a local ~EW D_2 shortening generated in the diapiric stem, resulting in the large-scale vertical folds that contour the Migmatitic Domain (Fig. 7). D_1 – D_2 were subsequently overprinted by D_3 thrusting after the emplacement of c. 2707 Ma granitic dyke swarm, reflecting regional EW shortening. Elsewhere in the Youanmi Terrane, EW shortening structures developed during the Neoproterozoic Orogeny, which started at around 2730 Ma (Zibra et al., 2017). The orogeny gave rise to an anastomosing network of NS trending shear zones, continuous over hundreds of kilometers along strike (Vearncombe, 1998), reflecting long-lived, transpressional shearing coeval with 2730–2660 Ma syntectonic plutons (Zibra et al., 2014a, 2014b). This EW compressional phase was followed by the intrusion of post-tectonic granites of the 2640–2600 Ma Bald Rock Supersuite (Ivanic et al., 2012; Van Kranendonk et al., 2013). In most places, crustal reworking during the orogeny and subsequent post-orogenic intrusions almost completely obliterated felsic crustal domains older than 2730 Ma. Pre-orogenic structures in the Yalgoo dome might have survived because of the low intensity impact of the Neoproterozoic orogeny in this tract of the terrane.

6 Conclusion

The migmatitic core of the Yalgoo Dome contains 1 km to 10 cm-scale vertical sheath folds developed in one progressive deformation event (D_1). This deformation marks the diapiric rise of partially molten tonalites interlayered with minor greenstone layers, that together had been buried underneath a thick and dense greenstone sequence. Refolding of the sheath folds by large-scale D_2 folds, giving rise to the 7 km-wide vertical fold closure mapped in the Migmatitic Domain, occurred during the last phases of diapirism. The final event was the c. 2707 Ma intrusion of granitic dykes and associated thrust-to-the-west shear zones (D_3). This event, while minor in the Yalgoo Dome,

is interpreted to be part of a major deformation event to the east, where magmatic bodies hundreds of kilometers long, intruded NS trending W-verging thrust zones. In the Yalgoo Dome, the early diapiric structures were preserved only because horizontal tectonics associated with Neoproterozoic Orogeny was relatively weak. The structural evolution determined here contrasts with a previous interpretation that argued that the sheath folds resulted from fold superposition (Myers and Watkins, 1985). Instead, the evolution points towards a shift from vertical to horizontal tectonics.

Acknowledgments

This work was financially supported by ARC DP11010254. Shachar Lazar is thanked for his assistance and energy during the fieldwork.

References

- Alsop, G.I., Holdsworth, R.E., 2006. Sheath folds as discriminators of bulk strain type. *Journal of Structural Geology*, 28, pp.1588–1606.
- Bodorkos, S., Sandiford, M., 2013. Thermal and mechanical controls on the evolution of Archean crustal deformation: examples from Western Australia. *Archean Geodynamic Environment*, pp.131–147.
- Bouchez, J.L., Diot, H., 1990. Nested granites in question: contrasted emplacement kinematics of independent magmas in the Zaer pluton, Morocco. *Geology*, 18, pp. 966–969.
- Bouhallier, H., Chardon, D., Choukroune, P., 1995. Strain patterns in Archaean dome-and-basin structures: the Dharwar craton (Karnataka, South India). *Earth and Planetary Science Letters*, 135, pp. 57–75.
- Boulter, C.A., Bickle, M.J., Gibson, B., Wright, R.K., 1987. Horizontal tectonics pre-dating upper Gorge Creek group sedimentation Pilbara Block, Western Australia. *Precambrian Research*, 36, pp.241–258.
- Campbell, I.H., Hill, R.I., 1988. A two-stage model for the formation of the granite-greenstone terrains of the Kalgoorlie-Norseman area, Western Australia. *Earth and Planetary Science Letters*, 90, pp. 11–25.
- Chardon, D., Choukroune, P., Jayananda, M., 1998. Sinking of the Dharwar Basin (South India): implications for Archaean tectonics. *Precambrian Research*, 91, pp. 15–39.
- Choukroune, P., Bouhallier, H., Arndt, N.T., 1995. Soft lithosphere during periods of Archaean crustal growth or crustal reworking. *Geol. Soc. London, Spec. Publ.* 95, 67–86. Collins, W.J., 1989. Polydiapirism of the Archean Mount Edgar Batholith, Pilbara Block, Western Australia. *Precambrian Research*, 43, pp. 41–62.
- Drury, S.A., Harris, N.B.W., Holt, R.W., Reeves-Smith, G.J., Wightman, R.T., 1984. Precambrian tectonics and crustal evolution in south India. *Journal of Geology*, 92, pp. 3–20.
- Fenwick, M.J., 2014. Structural evolution of the Yalgoo Dome, Yilgarn Craton, Western Australia: a core perspective. *Geological Survey of Western Australia*, record 2015/1016.

- Foley, B.J., 1997. Reassessment of Archaean tectonics in the Yalgoo District, Murchison Province, Western Australia. Unpublished Thesis. Monash University, Melbourne, Australia.
- Fyson, W., 1984. Fold and cleavage patterns in Archean metasediments of the Yellowknife supracrustal domain, Slave Province, Canada. A. Kröner R. Greiling.-E. Schweizerbart'sche, pp. 281–293.
- Hickman, A.H., 2004. Two contrasting granite-greenstone terranes in the Pilbara Craton, Australia: evidence for vertical and horizontal tectonic regimes prior to 2900 Ma. *Precambrian Research*, 131, pp.153–172.
- Hofmann, A., Kröner, A., Xie, H., Hegner, E., Belyanin, G., Kramers, J., Bolhar, R., Slabunov, A., Reinhardt, J., Horváth, P., 2015. The Nhlngano gneiss dome in south-west Swaziland – A record of crustal destabilization of the eastern Kaapvaal craton in the Neoproterozoic. *Precambrian Research*, 258, pp.109–132.
- Ivanic, T.J., Li, J., Meng, Y., Guo, L., Yu, J., Chen, S.F., Wyche, S. and Zibra, I., 2015. Yalgoo, WA Sheet 2241: Geological Survey of Western Australia. 1:100 000 Geological Series.
- Ivanic, T.J., Van Kranendonk, M.J., Kirkland, C.L., Wyche, S., Wingate, M.T.D., Belousova, E., 2012. Zircon Lu–Hf isotopes and granite geochemistry of the Murchison Domain of the Yilgarn Craton: evidence for reworking of Eoarchean crust during Meso-Neoproterozoic plume-driven magmatism. *Lithos*, 148, pp.112–127.
- Klein, C., 2005. Some Precambrian banded iron-formations (BIFs) from around the world: their age, geologic setting, mineralogy, metamorphism, geochemistry, and origin. *American Mineralogist*, 90, pp.1473–1499.
- Kloppenburg, A., White, S., Zegers, T., 2001. Structural evolution of the Warrawoona Greenstone Belt and adjoining granitoid complexes, Pilbara Craton, Australia: implications for Archaean tectonic processes. *Precambrian Research*, 112, pp. 107–147.
- Kruckenbergh, S.C., Vanderhaeghe, O., Ferré, E.C., Teyssier, C., Whitney, D.L., 2011. Flow of partially molten crust and the internal dynamics of a migmatite dome, Naxos, Greece. *Tectonics*, 30, pp. 1–24.
- Lana, C., Kisters, A., Stevens, G., 2010. Exhumation of Mesoarchean TTG gneisses from the middle crust: insights from the Steynsdorp core complex, Barberton granitoid-greenstone terrain, South Africa. *Bulletin of the Geological Society of Maerica*, 122, pp.183–197.
- Myers, J.S., Watkins, K.P., 1985. Origin of granite-greenstone patterns, Yilgarn Block, Western Australia. *Geology*, 13, pp.778–780.
- Ramsay, J.G., 1989. Emplacement kinematics of a granite diapir: the Chindamora batholith, Zimbabwe. *Journal of Structural Geology*, 11, pp.191–209.
- Ramsay, J.G., 1962. Interference patterns produced by the superposition of folds of similar type. *Journal of Geology*, 70, pp.466–481.
- Rey, P.F., Philippot, P., Thébaud, N., 2003. Contribution of mantle plumes, crustal thickening and greenstone blanketing to the 2.75–2.65 Ga global crisis. *Precambrian Research*, 127, pp.43–60.
- Roger, F., Teyssier, C., Respaut, J.-P., Rey, P.F., Jolivet, M., Whitney, D.L., Paquette, J.-L., Brunel, M., 2015. Timing of formation and exhumation of the Montagne Noire double dome, French Massif Central. *Tectonophysics*, 640–641, pp.53–69.
- Schwerdtner, W.M., 1982. Salt stocks as natural analogues of Archaean gneiss diapirs. *Geol. Rundschau* 71, 370–379. Snowden, P., 1984. Non-diapiric batholiths in the north of the Zimbabwe Shield. *Precambrian Tectonics Illustrations*, 2, pp.189–214.
- Stephansson, O., 1975. Polydiapirism of granitic rocks in the Svecofennian of central Sweden. *Precambrian Research*, 2, pp.189–214.

- Symington, N.J., Weinberg, R.F., Hasalova, P., Wolfram, L.C., Raveggi, M., Armstrong, R. A., 2014. Multiple intrusions and remelting-remobilization events in a magmatic arc: the St. Peter Suite, South Australia. *Geological Society of the American Bulletin*, 126, pp.1200–1218.
- Talbot, C.J., Jackson, M.P.A., 1987. Internal kinematics of salt diapirs. *American Association of Petrology and Geology Bulletin*, 71, pp.1068–1093.
- Van Kranendonk, M.J., Collins, W.J., Hickman, A., Pawley, M.J., 2004. Critical tests of vertical vs. horizontal tectonic models for the Archaean East Pilbara granite-greenstone Terrane, Pilbara Craton, Western Australia. *Precambrian Research*, 131, pp.173–211.
- Van Kranendonk, M.J., Ivanic, T.J., Wingate, M.T.D., Kirkland, C.L., Wyche, S., 2013. Long-lived, autochthonous development of the Archaean Murchison domain, and implications for Yilgarn craton tectonics. *Precambrian Research*, 229, pp.49–92.
- Van Kranendonk, M.J., Smithies, R.H., Griffin, W.L., Huston, D.L., Hickman, A.H., Champion, D.C., Anhaeusser, C.R., Pirajno, F., 2014. Making it thick: a volcanic plateau origin of Palaeoarchean continental lithosphere of the Pilbara and Kaapvaal cratons. *Geological Society of London, Special Publications*, 389, pp.83–111.
- Vearncombe, J.R., 1998. Shear zones, fault networks, and Archaean gold. *Geology*, 26, pp.855–858.
- Weinberg, R.F., Mark, G., 2008. Magma migration, folding, and disaggregation of migmatites in the Karakoram Shear Zone, Ladakh, NW India. *Geological Society of the American Bulletin*, 120, pp.994–1009.
- Weinberg, R.F., Schmeling, H., 1992. Polydiapirs: multiwavelength gravity structures. *Journal of Structural Geology*, 14, pp.425–436.
- Weinberg, R.F., van der Borgh, P., 2008. Extension and gold mineralization in the Archaean Kalgoorlie Terrane, Yilgarn Craton. *Precambrian Research*, 161, pp.77–88.
- Weinberg, R.F., Veveakis, E., Regenauer-Lieb, K., 2015. Compaction-driven melt segregation in migmatites. *Geology*, 43, pp.471–474.
- Wiedenbeck, M., Watkins, K.P., 1993. A time scale for granitoid emplacement in the Archaean Murchison Province, Western Australia, by single zircon geochronology. *Precambrian Research*, 61, pp.1–26.
- Yin, A., 2004. Gneiss domes and gneiss dome systems, in: *Special Paper 380: Gneiss Domes in Orogeny*, pp. 1–14.
- Zegers, T.E., White, S.H., de Keijzer, M., Dirks, P.H., 1996. Extensional structures during deposition of the 3460 Ma Warrawoona Group in the eastern Pilbara Craton, Western Australia. *Precambrian Research*, 80, pp.89–105.
- Zibra, I., Gessner, K., Smithies, H.R., Peternell, M., 2014a. On shearing, magmatism and regional deformation in Neoproterozoic granite-greenstone systems: insights from the Yilgarn Craton. *Journal of Structural Geology*, 67, pp.253–267.
- Zibra, I., Smithies, R.H., Wingate, M.T.D., Kirkland, C.L., 2014b. Incremental pluton emplacement during inclined transpression. *Tectonophysics*, 623, pp.100–122.
- Zibra, I., Clos, F., Weinberg, R.F., Peternell, M., 2017. The c. 2730 Ma onset of the Neoproterozoic Yilgarn orogeny. *Tectonics*, 36, pp. 1787–1813.
- Zibra, I., Peternell, M., Schiller, M., Wingate, M.T.D., Lu, Y., Clos, F., 2018. Tectono-magmatic evolution of the Neoproterozoic Yalgoo Dome (Yilgarn Craton). Diapirism in a pre-orogenic setting. *Geological Survey of Western Australia, Report 176*.

CHAPTER 3

Diapirism assisted by water-present melting: insights from the migmatitic core of the Archean Yalgoo Dome, Yilgarn Craton

Frediano Clos^a, Roberto F. Weinberg^a and Ivan Zibra^{a,b} and and Martin Schwindinger^a

^a School of Earth, Atmosphere & Environment, Monash University, Clayton, 3800 VIC, Australia

^b Geological Survey of Western Australia, Perth, WA 6004, Australia



Abstract

The genesis of domes in the Archean was fundamentally different than those on modern Earth as the rate of crustal recycling was far more voluminous and triggered by extensive reheating of the crust dictated by major pulses of mantle magmatic activity. In this study, we investigate how such mantle magmatism, reflected by extrusion of mantle-derived mafic-ultramafic greenstones sequences (2825–2760 Ma) in the region of the Yalgoo Dome caused a cascade of crustal processes between 2760 and 2740 Ma. Soon after the voluminous deposition of the greenstone sequences, there was massive felsic magmatism lasting between 2760 and 2740 Ma. This melted older crustal basalts at depth and formed the Goonetarra Granodiorite exposed in the dome as a suite of transitional TTGs, enriched in LILE, Th and U. These transitional TTGs in turn, caused water-fluxed melting of older tonalites and amphibolites (2970–2900 Ma) preserved in the core of the dome as migmatitic bodies. Their anatexis occurred between 3–9 kbar and ~ 700–800 °C and 0.5–2 wt% H₂O provided by the Goonetarra Granodiorite boosted melt production 15–30 vol%. The intrusion of the Goonetarra Granodiorite, transferred not only H₂O to the older rocks but also LILE-, Th- and U- suggesting that the silicate melts, and not aqueous fluids, were the metasomatizing agent. The growth of this voluminous magmatic body and migmatization of mid-crustal levels decreased the strength of the crust, allowing for the diapiric rise of the buoyant, hot and voluminous granitoid bodies and sagduction of the thick overlying greenstones. Thus, the internal evolution and the doming process of the Yalgoo dome were spontaneous consequences of the arrival of a major thermal-magmatic mantle anomaly to the crust. This event first gave rise to a gravitationally unstable crustal stratigraphy, followed by a heat wave traveling upward through the crust. This wave first produced voluminous and hydrous transitional TTGs. Then this melt advected heat and H₂O to mid-crustal levels causing water-fluxed anatexis of older rocks and triggering diapiric doming of the entire felsic middle crust in a manner quite unlike the formation of Phanerozoic domes.

Keywords: Archean, crustal reworking, diapirism, migmatites, water-present melting

1 Introduction

Gneiss domes are salient features of the continental crust throughout Earth's history (Eskola, 1949; Teyssier and Whitney, 2002). In the Archean, large portions of the continental crust were re-worked by episodes of vertical overturn of the upper and middle crust (van Kranendonk et al., 2004) and, since then, domes have been common occurrences, with the Earth's youngest dome recorded at c. 2–8 Ma in Papua New Guinea (Little et al., 2011). Domes reflect local or regional thermo-mechanical instabilities that cause an en masse vertical re-organization of crustal rocks towards a gravitationally stable configuration (Teyssier and Whitney, 2002). As such, determining the causes and processes for dome formation from the Archean to present-day is a crucial step to understand the evolution of the continental crust through time.

Proterozoic and Phanerozoic gneiss domes occur preferentially in collisional orogens, but are also documented from a wide variety of tectonic settings (Teyssier and Whitney, 2002; Yin, 2004).

Gneiss domes can form by different processes, including crustal extension/transension (Coney, 1980; Davis, 1988; Lister and Davis, 1989; Kruckenberg et al., 2011; Roger et al., 2015; Rey et al., 2017), contraction (Burg et al., 1984; Amato et al., 1994; Yin, 2004; Gébelin et al., 2009) and diapirism/polydiapirism (Stephansson, 1975; Bateman, 1985; Collins, 1989; Bouchez and Diot, 1990; Weinberg et al., 1997). Most of these domes are cored by high-grade gneiss, with migmatites produced by dehydration of hydrous minerals, suggesting a positive feedback between high-grade metamorphism, partial melting, decompression and emplacement of granitic plutons (Teyssier and Whitney, 2002). The Canadian Thor Odin dome in British Columbia and the Leo Pargil dome in India are representative examples of migmatitic gneiss domes emplaced during rapid (<10 Myr), near-isothermal decompression, which caused partial melting by dehydration reactions (Norlander et al., 2002; Langille et al., 2012).

In the Archean, the development of gneiss domes was fundamentally different. In contrast with their Proterozoic and Phanerozoic counterparts, Archean domes were long-lived and reflected cycles of mantle-derived magmatism followed by pervasive crustal reworking (Collins, 1989; Ramsay, 1989; Chardon et al., 1998; Choukroune et al., 1995; van Kranendonk et al., 2004; Pawley et al., 2004).

The blanketing effect caused by the thick pile of greenstones and the mantle-crust heat transfer coupled with burial of radiogenic continental crust, increased the temperature and decreased the strength of the middle-to-lower crust (Rey et al., 2003; Bodorkos and Sandiford, 2006). Partial melting further enhanced thermal and mechanical softening and promoted the formation of buoyant granitoids that diapirically rose into the upper crust, together with partially molten pre-existing rocks (Campbell and Hill, 1988; van Kranendonk et al., 2015).

The Yalgoo Dome in the Yilgarn Craton of Western Australia is a large Archean dome where the initial conditions that lead to crustal reworking and diapirism can be explored. A 2825–2760 Ma voluminous mantle-derived magmatism (Ivanic et al., 2012; van Kranendonk et al., 2013) caused the development of a thick greenstone sequence on top of a 2970–2900 Ma felsic and mafic substrate. The subsequent partial melting and thermo-mechanical softening of pre-existing crustal rocks resulted in the diapiric rise of granitoids and partially molten felsic rocks (Fig. 1; Myers and Watkins, 1985; Foley, 1997; Zibra et al., 2018).

In this contribution, we present field, petrologic and geochemical data from the deepest structural level exposed in the Yalgoo Dome - the migmatitic core of the dome. This complex is characterized by 2970–2900 Ma tonalite interlayered with high-grade amphibolites (Fenwick, 2014; Zibra et al., 2018) that record 2760–2740 Ma anatexis during diapirism (Clos et al., submitted; Chapter 2). Our results, supported by phase equilibria modelling and thermobarometry, indicate that melting and reworking of the complex occurred by water-fluxed melting in the middle crust. We suggest that fluids with a magmatic origin triggered crustal recycling during the formation of the Yalgoo Dome and might represent one of the key elements to better understand dynamics and effects of the widespread intracrustal differentiation that typified the Archean eon.

2 Geological setting

2.1 Yalgoo Dome

In the western half of the Archean Yilgarn Craton, the Youanmi Terrane includes a 2970–2720 Ma greenstone sequence intruded by 2970–2600 Ma granitoids (Ivanic et al., 2012; van Kranendonk

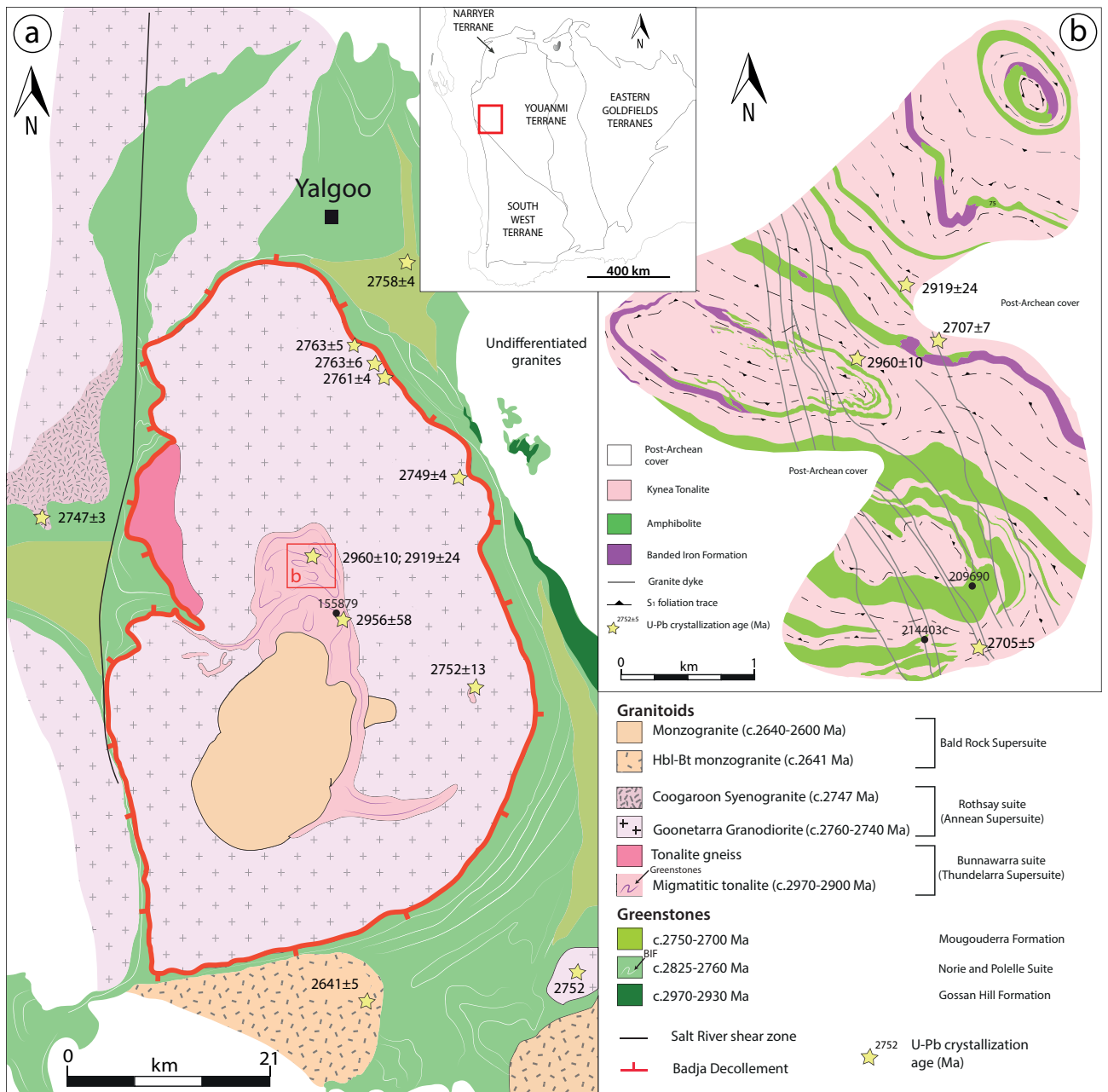


Figure 1: (a) Geological map of the Yalgoo Dome and greenstone envelope, based on field and geophysical data. Inset on upper right shows location of the studied area in the Youanmi Terrane. The Yalgoo dome comprises numerous generations of granites intruded over a time span >300 Myr: in the core, the Migmatitic Domain comprises 2970–2900 Ma migmatitic tonalite and narrow greenstone layers. This is surrounded by a wide ring of the voluminous 2760–2740 Ma Goonetarra Granodiorite that forms the remained of the dome (Zibra et al., 2018). Red rectangles indicate location of detailed map of the Migmatitic Domain in (b), an area dominated by large scale sheath folds of greenstones within migmatitic tonalites (Clos et al., submitted; Chapter 2). Location of migmatitic tonalite (sample 155879: latitude -28.75282, longitude 115.6995) and amphibolite samples (sample 214403c: -28.72008, 116.6659; sample 209690: -28.7166, 116.6690) are indicated by black dots. Yellow star indicates U-Pb zircon crystallization ages from the Geological Survey of Western Australia.

et al, 2013). A craton-scale network of transpressive shear zones that accommodated EW regional shortening during the Neoproterozoic orogeny (Zibra et al., 2017) dissects most of the terrane. In map-view these shear zones form anastomosing lenses broadly N-trending and continuous over hundreds of kilometers along strike (Zibra et al., 2014). In the westernmost part of the terrane, shear zones

have not been identified, and granite domes and greenstone keels dominate the area (Fig. 1). Here the Yalgoo Dome is exposed, a prominent elliptical granite dome surrounded by greenstones, comparable to the broad domes of the East Pilbara Craton (Collins, 1989).

The Yalgoo Dome is made of concentric core-rim distribution of granitoid intrusions, bordered by a composite greenstone belt. Greenstones include the 2963–2958 Ma Gossan Hill Formation of felsic volcanic and volcanoclastic rocks, unconformably overlain by mafic volcanic rocks, felsic volcanoclastic sandstones and banded iron formation of the 2825–2805 Ma Norie Group and the 2800–2760 Ma Polelle group, a dominantly volcanic sequence evolving from komatiitic basalts to tholeiitic basalts and andesites (van Kranendonk et al., 2013), with a minimum thickness of 8 km (Ivanic et al., 2015). Unconformably above these sequences lies the Mougooderra Formation, a siliciclastic sequence whose maximum depositional age is 2758 ± 4 Ma (Zibra et al., 2018; Fig. 1). A 1–2 km wide high-strain zone, the Badja décollement (Fig. 1; Zibra et al., 2018), juxtaposes the greenstones against the granitic dome. In the core of the dome the Migmatitic Domain is exposed, a region of $\sim 8 \times 12$ km (Figs 1, 2) defined by migmatitic tonalites-granodiorite-trondhjemite (TTG) (known as the Kynea Tonalite, Zibra et al., 2018) and interlayered high-grade greenstones (Zibra et al., 2018; Clos et al., submitted; Chapter 2). This domain is surrounded by the 2760–2740 Ma Goonetarra Granodiorite, a heterogeneous group of equigranular to porphyritic monzogranite and granodiorite, commonly containing cm-to-decametric xenoliths of migmatitic TTGs of the Migmatitic Domain (Zibra et al., 2018). Along the Badja décollement, monzogranites and granodiorites are progressively overprinted by a pervasive solid-state foliation, showing consistent dome-up kinematics (Zibra et al., 2018). The distribution of linear and planar structures in the migmatitic core of the dome, as well as in the Goonetarra Granodiorite and in the greenstones is consistent with diapiric emplacement of syn-tectonic granitic rocks and migmatitic tonalites during doming at 2760–2740 Ma (Zibra et al., 2018; Clos et al., submitted; Chapter 2).

2.1 Migmatitic Domain

The Migmatitic Domain consists of migmatitic TTGs dominated by tonalites interlayered with amphibolite and banded iron formation (Fig. 1; Zibra et al., 2018; Clos et al., submitted; Chapter

2). The TTG protolith is dated at 2960 ± 10 Ma and 2956 ± 58 Ma (Zibra et al., 2018; Fig. 3a), while Wiedenbeck and Watkins (1993) reported zircon core U-Pb ages of 2912 ± 12 Ma and rim ages of 2700–2800 Ma, interpreted as the crystallization age of the tonalitic gneiss protolith and an overgrowth linked to migmatization, respectively (Fig. 1). This domain contains multi-scale domes-and-basins which are defined in map-view by elliptical keels of greenstone cored by granitoids (Clos et al., submitted; Chapter 2). These are interpreted as vertical sheath folds developed in a single, progressive deformation event (D_1). This first deformation phase has been interpreted to result from diapiric ascent of a buoyant partially molten granitic crust. This deformation event was overprinted by a local EW contractional episode (D_2) during the last phase of doming (Clos et al., submitted; Chapter 2). D_1 and D_2 record the progressive upward flow of partially molten rocks and are interpreted to occur during diapirism and the intrusion of the voluminous Goonetarra Granodiorite, between 2760 and 2740 Ma (Zibra et al., 2018). The final event was the intrusion of granitic dykes (c. 2707 Ma) associated with a thrusting event, D_3 (Clos et al., submitted; Chapter 2). Although minor in the Yalgoo Dome, this last phase was part of a major deformation event well-recorded in the east, where magmatic bodies hundreds of kilometers long, intruded NS trending transpressional shear zones during the Neoproterozoic orogeny (Zibra et al., 2017).

In the 2970–2900 Ma core of the dome, two anatectic events accompanied D_1 and D_2 events during the exhumation of the core (Clos et al., submitted; Chapter 2). D_1 leucosomes are parallel to a pervasive S_1 gneissic foliation, associated with a steeply-plunging mineral lineation, and are overprinted by F_2 sub-vertical folds and D_2 axial planar leucosomes trending ~NS (Figs 2a-b; Fenwick, 2014; Clos et al., submitted; Chapter 2). The volume of leucosomes vary from place to place. Domains where leucosomes show diffuse boundaries with mesosomes and melanosomes are regarded as in-situ stromatic metatexites, with leucocratic fraction ranging from 10 to 30% (Figs 2a-b). Leucosomes with sharp contact with the host tonalite are interpreted to represent magma injections (Fig. 2c). These veins are coarser grained than in-situ leucosomes, and lack biotite. A mixture of injected and in-situ leucosomes occurs in nebulite diatexites, where leucosome-mesosome-melanosome layering has more than 50% leucocratic material.

Partial melting of amphibolites, which is interlayered with migmatitic tonalites, is limited to their boundaries. Here, migmatitic amphibolites have S_1 parallel leucosomes, commonly coalescing into D_2 axial planar leucosomes (Figs 2e-f). Far from the contacts, leucosomes in amphibolites are scarce. D_1 and D_2 leucosomes in both tonalite and amphibolites have the same mineral assemblage and they are distinguished only on a structural basis (Clos et al., submitted; Chapter 2).

3 Petrography and mineral chemistry

The samples selected for petrographic study are a migmatitic tonalite with D_1 leucosome (sample 155879; Figs 2b and 2d), a stromatic metaxite amphibolite with D_2 leucosome (sample 214403c; Fig. 2f) and an amphibolite (sample 209690) collected ~ 200 m from the contact with the migmatitic tonalites (Fig. 1b). Representative compositions of plagioclase, amphibole and biotite in these rocks are listed in Tables 1–2 and Appendix 3.1, 3.2 and 3.3. Electron microprobe (EMP) analyses were performed using a Cameca SX50 Electron Microprobe equipped with four Vertical Wavelength Dispersive Spectrometers (WDS) at the University of Melbourne, Australia. Carbon coated thin sections were analyzed with a beam current of 35 nA and accelerating voltage of 15 kV. All elements have detection limits below 0.05 elemental weight percent. Fe^{3+} for anhydrous minerals is calculated using the stoichiometric method of Schumacher (1991) and for amphibole, the procedure of Leake et al. (1997).

3.1 Migmatitic tonalite (sample 155879)

Stromatic metaxite tonalites (Fig. 2b) consist of biotite, plagioclase and quartz with subordinate K-feldspar and equant crystals of magnetite and accessory ilmenite. The melanosome framework is dominated by plagioclase and quartz with variable proportions of biotite (Fig. 2d). K-feldspar occurs in three interstitial forms: i) irregular patches between corroded plagioclase (Figs 3a-b), narrow films at plagioclase–plagioclase or plagioclase–quartz grain boundaries (Fig. 3c), or as small granoblastic crystals showing straight to gentle curved boundaries with plagioclase, quartz and biotite (Fig. 3d). Biotite is mostly euhedral with straight long sides and curved short sides (Figs 3b-c). Apatite, zircon and allanite are common accessories. Leucosomes have comparable mineralogy to the melanosome, but with a net modal decrease in biotite and plagioclase, balanced by an increase

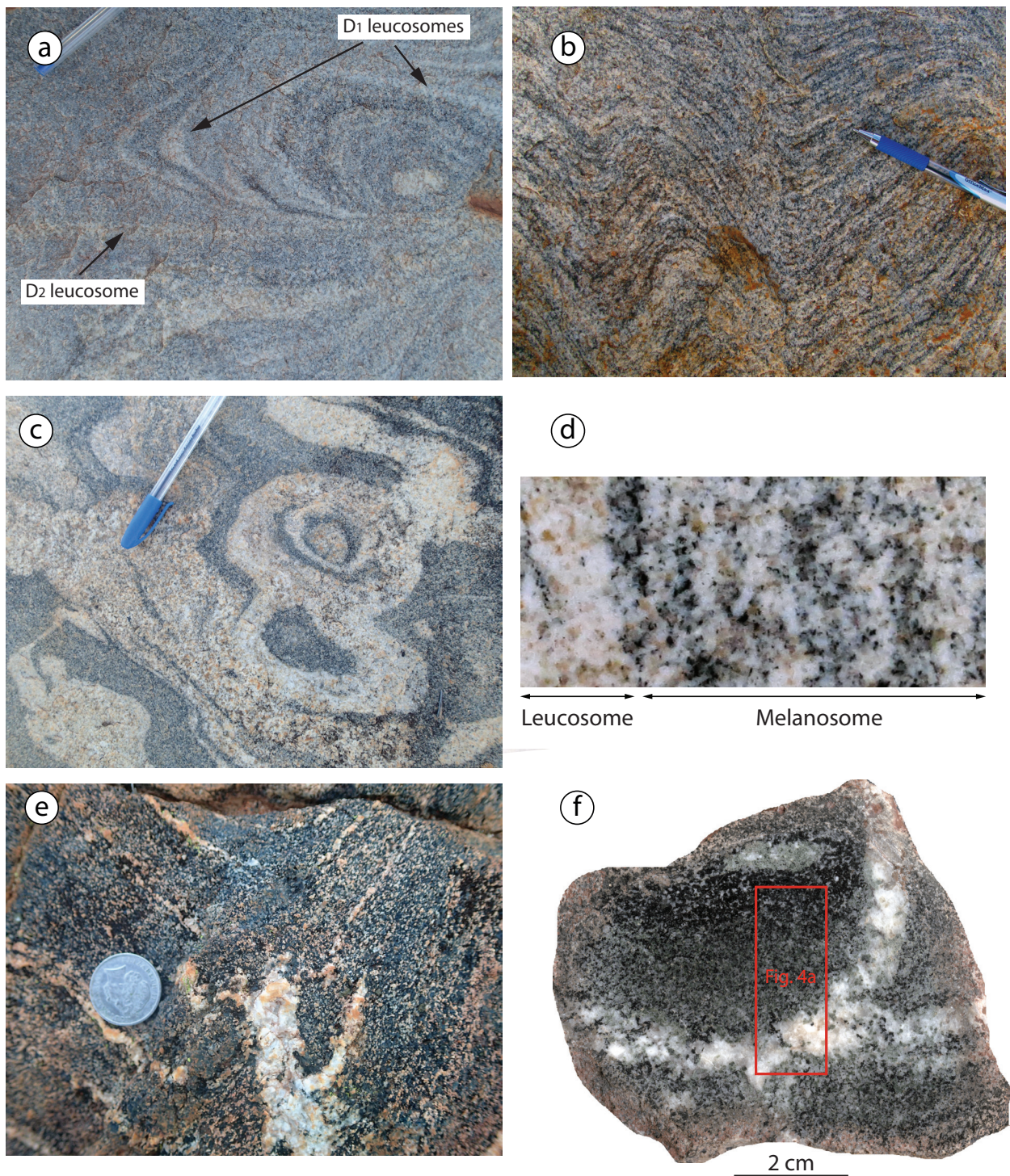


Figure 2: Field appearance of the migmatitic tonalites and amphibolites: a) tonalite showing in-situ migmatites defined by D_1 sheath fold outlined by leucosome, mesosome and melanosome layering. These are cross-cut by D_2 leucosomes. In-situ D_1 leucosomes range between 10 and 30 vol%; b) sharp boundaries between injected D_1 and D_2 leucosomes and host tonalite; c) migmatitic layering with more than 50% leucocratic material interpreted as a combination of in-situ anatexis and injected melt; d) amphibolite raft within migmatitic tonalite showing in-situ leucosomes; e) syn-anatectic deformation of amphibolite displaying D_1 leucosomes merging into an axial planar D_2 leucosomes; and f) D_1 and D_2 in-situ leucosomes showing petrographic continuity. Both leucosomes are defined by the same mineral assemblage.

in K-feldspar and quartz. The leucosomes are largely comprised of plagioclase, quartz and large K-feldspar poikilitic phenocryst (Fig. 3e). Anorthite content of plagioclase is similar in both mela-

nosome and leucosome (An_{19-21}), while the TiO_2 in biotite ranges between 2.07–3.16 wt% (Fig. 5d; Tables 1–2, Appendix 3.1).

Small subhedral crystals of epidote are associated with chlorite and biotite in retrograde assemblages (Fig. 3f). With more pronounced alteration, biotite is partially replaced by chlorite and muscovite

Migmatitic tonalite (155879)

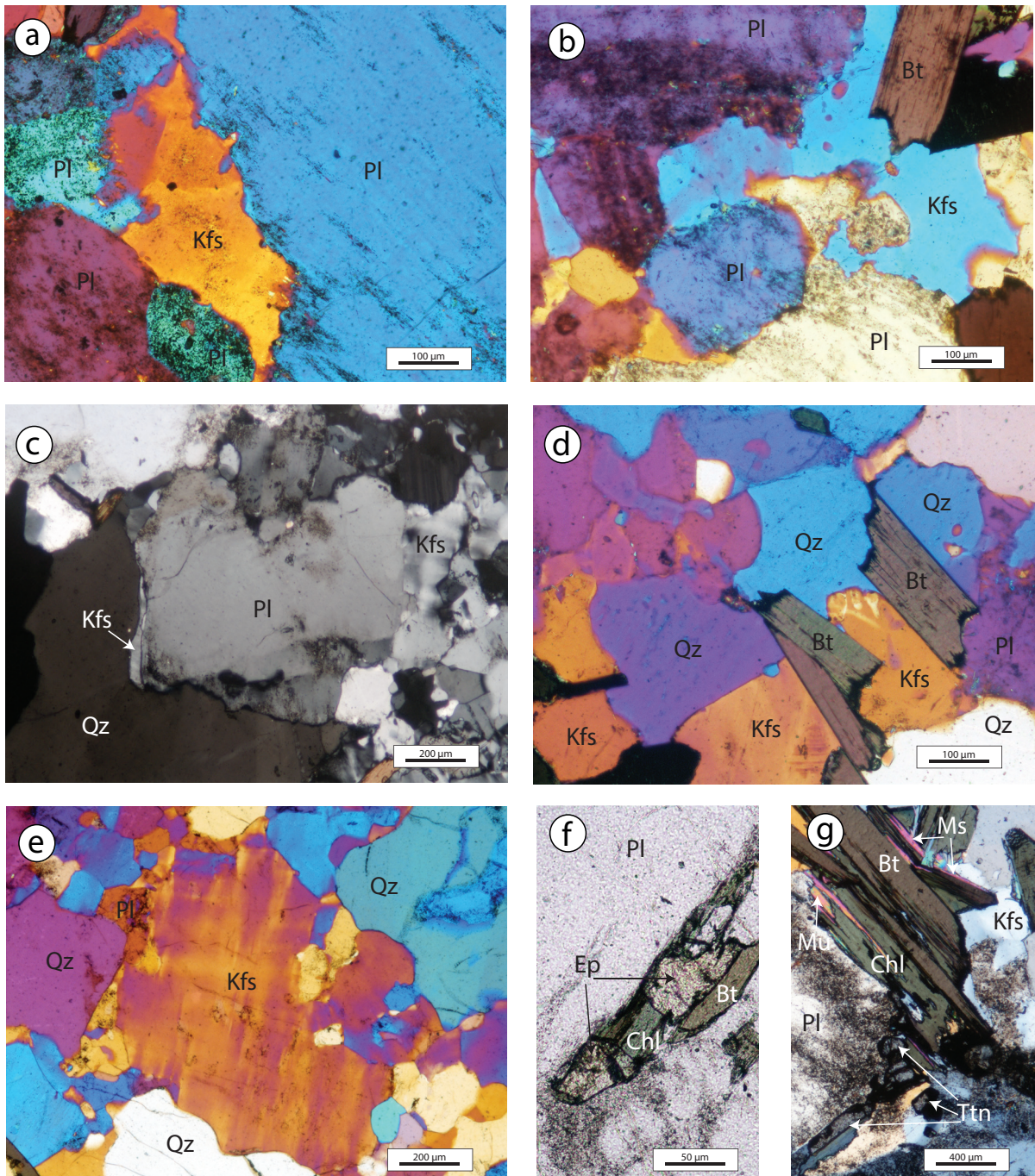


Figure 3: Minerals and microstructures in migmatite tonalite (sample 155879). a-b) Interstitial K-feldspar patches within plagioclase crystals with irregular, corroded grain boundaries while euhedral biotite shows straight margins; c) mesosome showing large deformed plagioclase and quartz with interstitial films of K-feldspar; d) area of mesosome defined by granoblastic quartz and plagioclase with interstitial K-feldspar and euhedral biotite; e-f) large K-feldspar porphyroblast in leucosome matrix. Altered plagioclase associated with epidote, chlorite and biotite (e) or biotite, chlorite, muscovite, titanite and K-feldspar patches where biotite breakdown is more accentuated (f).

(Fig. 3g). This assemblage is spatially accompanied by small K-feldspar patches and subhedral titanite crystals (Fig. 3g), likely formed by the release of K_2O and TiO_2 during chloritisation of biotite (Sawyer, 2010).

3.2 Migmatitic amphibolite (sample 214403c)

Sample 214403c (Fig. 2f) is representative of the stromatic metatexite amphibolite that develop at the contact with migmatitic tonalites (Fig. 2e). This sample has a 1.5 cm-wide leucosome separated from an amphibole-rich source by a 2.5 cm-wide melanosome (Fig. 4a). Grain size increases from the amphibole-rich source and melanosome ($< 150 \mu m$) to the leucosome (100–500 μm).

The amphibole-rich source is composed largely by subhedral amphibole and plagioclase, with subordinate titanite, and lack clinopyroxene (Fig. 4b). The melanosome comprises almost equal proportions of amphibole, clinopyroxene (diopside) and plagioclase with minor quartz and interstitial K-feldspar, titanite and accessory magnetite. Clinopyroxene and amphibole have diffuse or straight

Table 1: Representative analyses of plagioclase

Lithology	Migmatitic tonalite		Amphibolite		Migmatitic amphibolite		
	155879		209690		214403c		
Sample							
Label	P-16	P-30	P-34	P-36	P-11	P-44	P-66
			Matrix	Interstitial	Amphibole-rich source	Melanosome	Leucosome
SiO ₂	63.46	63.19	58.17	59.90	60.68	61.40	61.50
Al ₂ O ₃	22.98	22.77	25.68	24.56	25.26	24.48	24.58
FeO	0.05	0.07	0.06	0.23	0.08	0.13	0.08
MnO	0.00	0.00	0.00	b.d.l	0.00	0.03	0.00
CaO	4.02	4.17	7.43	6.12	6.65	5.65	5.72
Na ₂ O	9.00	8.74	7.08	7.88	6.96	7.92	8.05
K ₂ O	0.18	0.34	0.13	0.15	0.14	0.19	0.26
Total	99.70	99.29	98.54	98.83	99.79	99.81	100.19
Cations based on 8 oxygen							
Si	2.82	2.82	2.64	2.70	2.73	2.74	2.73
Al	1.20	1.20	1.37	1.30	1.34	1.29	1.29
Fe ²⁺	0.00	0.00	0.00	0.01	0.00	0.00	0.00
Ca	0.19	0.20	0.36	0.30	0.32	0.27	0.27
Na	0.78	0.76	0.62	0.69	0.61	0.69	0.69
K	0.01	0.02	0.01	0.01	0.01	0.01	0.01
An	19.59	20.45	36.42	29.79	34.26	27.96	27.78
Ab	79.35	77.55	62.79	69.37	64.86	70.92	70.69
Or	1.06	2.00	0.78	0.85	0.88	1.12	1.52

b.d.l. = below detection limit

Total Fe as FeO

Table 2: Representative analyses of biotite and amphibole

Mineral	Biotite		Amphibole			Migmatitic amphibolite		
	Migmatitic tonalite		Amphibolite			Migmatitic amphibolite		
Sample	155879		209690			214403c		
Label	P-57	P-37	P-L14	P-4	P-L9	P-20	P-29	P-61
			core	rim	rim	Amphibole-rich source	Melanosome	Leucosome
SiO ₂	35.62	35.42	40.59	42.10	43.01	43.86	44.24	44.80
TiO ₂	2.42	3.14	2.10	0.94	0.50	1.04	0.88	0.85
Al ₂ O ₃	15.28	14.74	11.33	9.95	9.27	10.47	9.97	8.81
Cr ₂ O ₃	0.00	b.d.l.	0.00	0.00	0.00	0.08	0.13	0.15
FeO _T	23.10	21.87	21.20	21.42	20.59	16.73	18.20	18.53
MnO	0.31	0.29	0.34	0.30	0.32	0.32	0.29	0.33
MgO	8.96	9.88	7.19	7.87	8.91	10.97	10.40	10.41
CaO	b.d.l.	0.00	11.70	11.82	11.90	12.05	12.35	12.20
Na ₂ O	b.d.l.	0.06	1.42	1.15	1.01	1.21	1.06	0.98
K ₂ O	9.93	9.93	1.34	1.07	0.88	1.24	1.16	0.98
Total	95.63	95.32	97.22	96.62	96.38	97.97	98.69	98.04
Si			6.26	6.48	6.57	6.51	6.56	6.69
Ti			0.24	0.11	0.06	0.12	0.10	0.10
Al			2.06	1.81	1.67	1.83	1.74	1.55
Fe ³⁺			0.37	0.56	0.71	0.50	0.48	0.52
Fe ²⁺			2.36	2.20	1.92	1.57	1.78	1.80
Mn			0.04	0.04	0.04	0.04	0.04	0.04
Mg			1.65	1.81	2.03	2.43	2.30	2.31
Ca			1.93	1.95	1.95	1.92	1.96	1.95
Na			0.42	0.34	0.30	0.35	0.31	0.28
K			0.26	0.21	0.17	0.23	0.22	0.19
H			2.00	2.00	2.00	2.00	2.00	2.00

b.d.l. = below detection limit

Amphibole cations calculated for 23 oxygens with Fe²⁺ and Fe³⁺ calculated on the basis of 13 cations excluding Ca, Na, and K (Leake et al., 1997)

Migmatitic amphibolite (214403c)

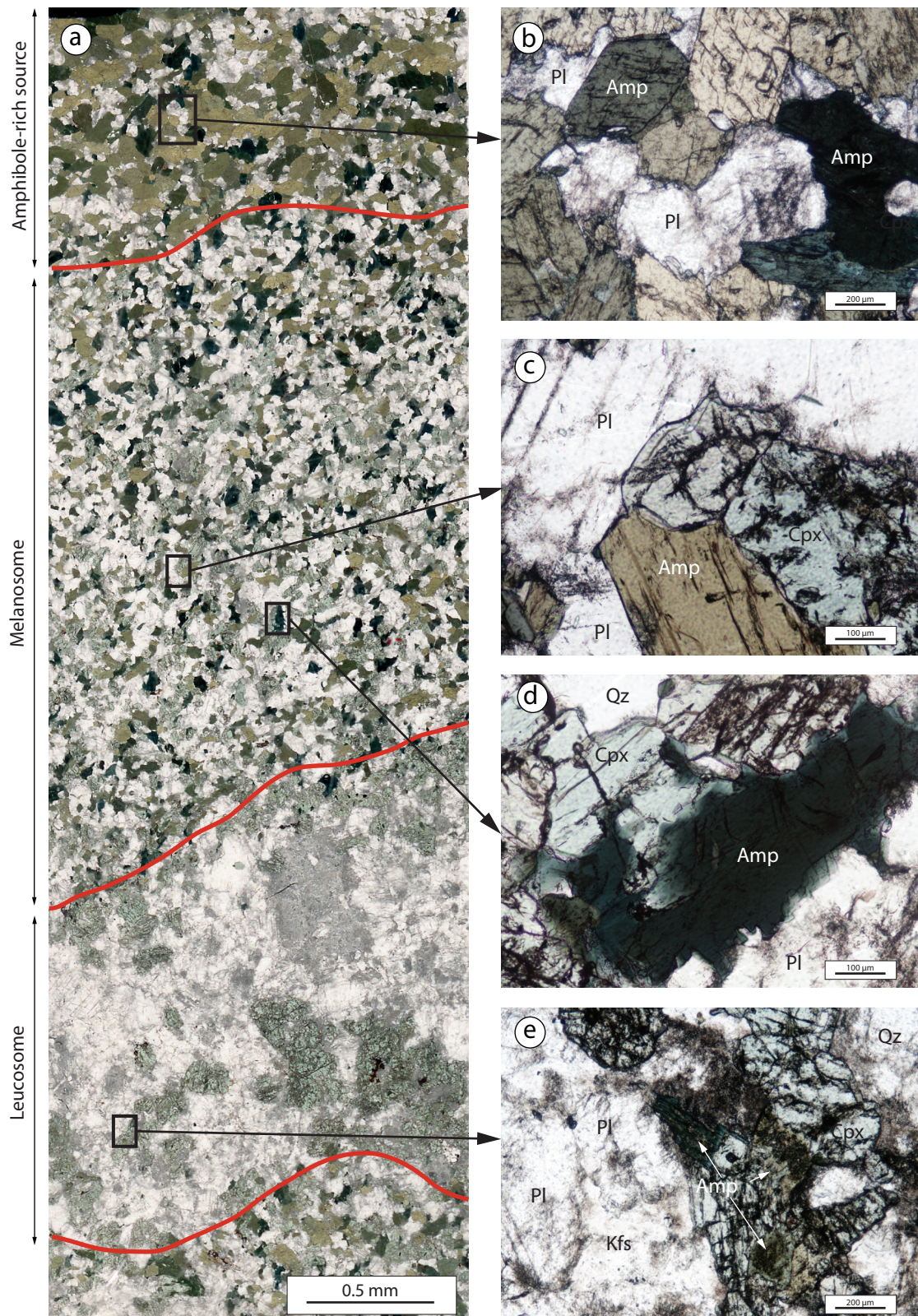


Figure 4: Representative minerals and textures in the migmatitic amphibolite (214403c): a) thin section scan showing the transition from amphibole-rich source to melanosome and leucosome; b) amphibole-rich source with large amphibole and plagioclase; c) texturally equilibrated clinopyroxene and amphibole with straight grain boundaries; d) clinopyroxene predated by anhedral amphibole in the melanosome; and e) in the leucosome, clinopyroxene is commonly/generally surrounded by amphibole.

margins (Figs 4c-d). Leucosomes are mainly composed of plagioclase, quartz, K-feldspar and large anhedral crystals of clinopyroxene clustered at the contact with the melanosome. Amphiboles can be found either as medium-grained subhedral crystals or replacing clinopyroxene (Fig. 4e). Modal proportions of clinopyroxene, plagioclase, quartz and K-feldspar increase from melanosome to leucosomes, while amphibole decreases (Fig. 4a).

Amphiboles have compositions that spread over the pargasite-edenite boundary (Fig. 5a). The Mg# decreases slightly from amphibole-rich source to leucosome, while the Si content increases from 6.40 to 6.50 a.p.f.u (Fig. 5a). K and Na show a decrease, from 0.25 to 0.18 and 0.33 to 0.28 a.p.f.u.,

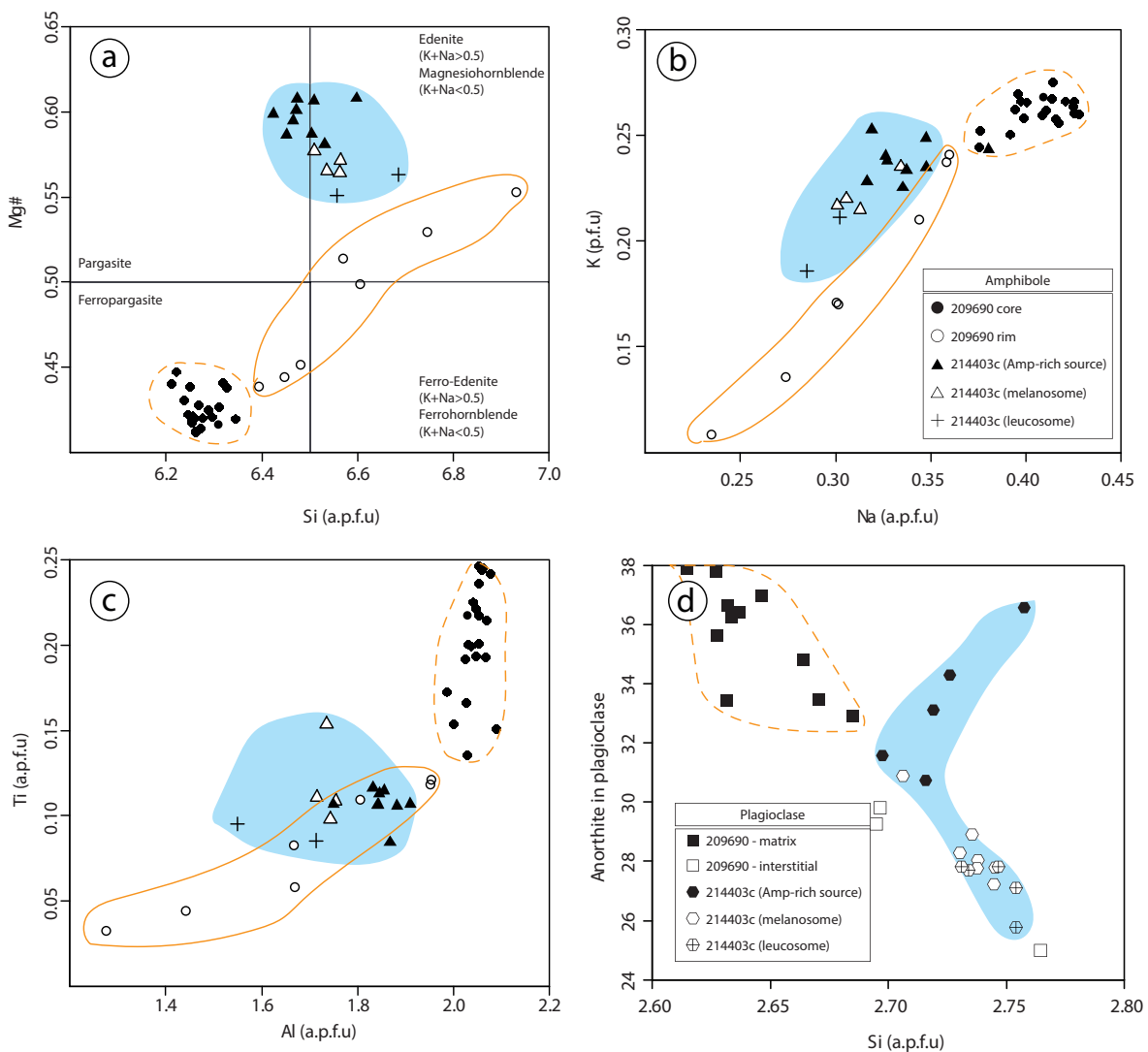


Figure 5: Migmatitic amphibolite (214403c) and amphibolite (209690) mineral composition. Amphibole composition is shown in a Mg# vs Si (a), K vs Na (b) and Ti vs Al diagrams (c). Plagioclase composition is shown by the anorthite content vs Si diagram in (d). $Mg\# = Mg^{2+} / (Mg^{2+} + Fe^{2+})$; a.p.f.u. = anion per formula unit. Plotted with GCDkit (Janousek et al., 2006).

Amphibolite (209690)

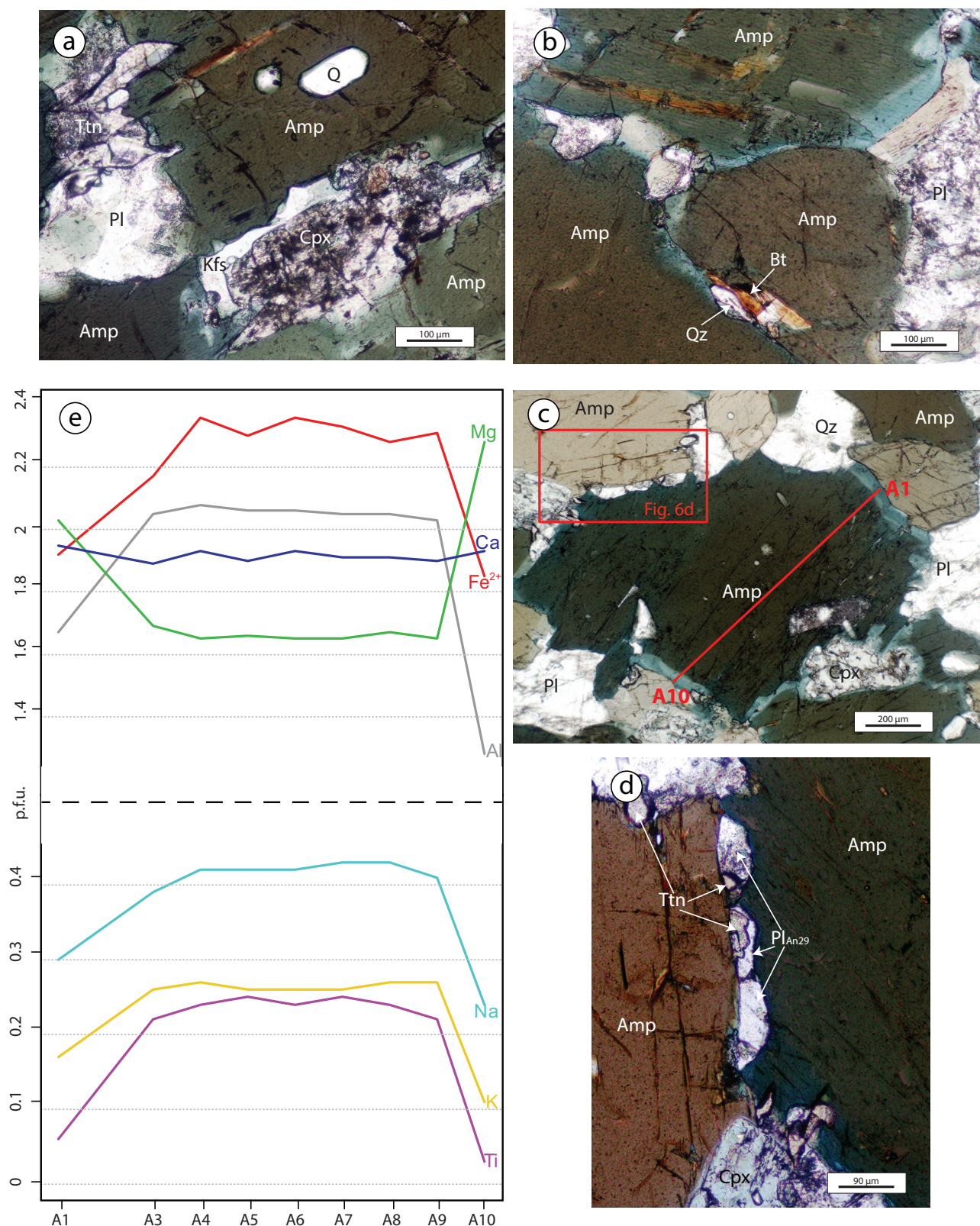


Figure 6: Representative minerals and textures in amphibolite sample 209690. Amphibole, plagioclase and clinopyroxene are commonly associated with large anhedral titanite, interstitial films of K-feldspar (a) and rare biotite (b). Large amphibole grains display pale green rims (c) and are bounded along their edges by smaller titanite grains embedded in more sodic plagioclase crystals (d). Major element line scans for amphibole in Fig. 6c illustrate the marked depletion in Fe, Al, Na, K and Ti in amphibole rims (e).

respectively (Fig. 5b). Ti remains constant at ~ 0.10 a.p.f.u ($\text{TiO}_2 = 0.85\text{--}1.05$ wt% in Table 2 and Appendix 3.2), but the Al content decreases from 1.90 a.p.f.u in the amphibole-rich source to 1.60 a.p.f.u in the leucosome (Fig. 5c). In line with the change in composition of the amphiboles, anorthite content of plagioclase is higher in the amphibole-rich source ($\text{An}_{36\text{--}31}$), reflecting the lack of clinopyroxene, and decreases in both the melanosome ($\text{An}_{31\text{--}27}$) and leucosome ($\text{An}_{28\text{--}25}$) (Fig. 5d, Table 1).

3.3 Amphibolite (sample 209690)

Sample 209060 is a representative amphibolite away from the contacts with the migmatitic tonalites. The rock comprises bottle-green amphibole, plagioclase, diopside clinopyroxene ($\sim 20\%$), minor quartz and rare biotite shielded by amphiboles (Figs 6a-b). The amphiboles are typically zoned, showing narrow pale green rims (Figs 6b-c). Rare biotite is associated with quartz (Fig. 6b). Titanite forms large anhedral crystals (Fig. 6a) or small sub-euhedral crystals along amphibole grain boundaries (Fig. 6d). Narrow films of K-feldspar occur between amphibole and clinopyroxene grains (Fig. 6a).

The amphibole cores are ferropargasites, while the rims show a linear trend toward the magnesiohornblende boundary (Fig. 5a). The cores are particularly enriched in K, with ~ 0.25 a.p.f.u (Fig. 5b), and display little compositional variation for major elements (except for Ti, which varies from 0.10 to 0.25, Fig. 5c). Amphibole rims show a pronounced decline in K, Na, Ti, Al and Fe (Figs 5b-c and 6e) that can be related to the crystallization of K-feldspar (Fig. 6a), titanite and more sodic plagioclase ($\text{An}_{29\text{--}26}$), which crystallized interstitially along the amphibole–amphibole or amphibole–clinopyroxene boundaries (Figs 6a-c-d). Plagioclase in the matrix shows fairly constant compositions, with anorthite content varying from 38 to 33 (Fig. 5d, Table 1; Appendix 3. 3).

4 Melting conditions

4.1 Migmatitic tonalite

4.1.1 Melting reactions

The distribution of minerals and their microstructures in anatectic granitoids can be used to determine the melting reactions (Sawyer, 2010; Carvalho et al., 2016). In the migmatitic tonalites, the mode of quartz and K-feldspar increases from melanosome to leucosome, while biotite and plagioclase decreases. Second, the euhedral biotite with straight grain boundaries (Figs 4b-d) and absence of prograde ferromagnesian peritectic minerals in the migmatitic tonalite suggest that biotite remained stable during anatexis (Busch, 1974; Sawyer, 2010). Third, the matrix of the melanosome is mainly comprised of corroded plagioclase and minor quartz, with grain boundaries filled by irregular patches and films of K-feldspar (Figs 4a-c), interpreted to represent crystallization of former melt (Sawyer, 2001; Holness and Sawyer, 2008; Sawyer, 2010). Similar microstructures have been reported in water-fluxed melting of Archean leucogranodiorites in the Opatica Subprovince of the Canadian Shield (Sawyer, 2010) and São Francisco Craton (Carvalho et al., 2016), where they were interpreted as residual rocks after melt extraction. We infer that primary K-feldspar crystals were completely consumed during partial melting, because they are absent in the melanosome. These observations suggest that partial melting of tonalite occurred initially via the reaction plagioclase + quartz + K-feldspar + H₂O = melt (reaction 1) until K-feldspar exhaustion, and probably proceeded by plagioclase + quartz + H₂O = melt (reaction 2) at higher temperature.

4.1.2 Pseudosection modelling

Phase equilibria modelling was undertaken in the Na₂O–CaO–K₂O–FeO–MgO–Al₂O₃–SiO₂–H₂O–TiO₂–O₂ (NCKFMASHTO) chemical system with *Perple_X* version 6.7.9 (Connolly, 2009) for a representative tonalite (sample 155879 in figures 2b and 2d). Bulk rock analysis of this tonalite was performed at the Geological Survey of Western Australia (GSWA) in Perth and is given in the caption of figure 7. The results of the modelling are presented for: i) a dry model (Fig. 7a) with a H₂O content (0.27 wt%) necessary to saturate the solidus at 8 kbar, and model dehydration melting conditions, ii) a wet model with 1.27 wt% H₂O in order to simulate 1 wt% water-excess conditions during melting (Fig. 7b), and iii) variable water content between 0.27–3.27 wt% H₂O at pressure fixed at 5 kbar as it represents mid-crustal conditions (Figs 8a-b). Here, water excess refers to the H₂O content above that necessary to saturate the solidus at 8 kbar. The a–x relations used are melt(G), Augite(G) and cAmph(G) from Green et al., 2016; Gt(W), Opx(W), Bi(W) from White et

al. (2014a); Mica(W) and Chl(W) from White et al. (2014b); Ep(HP11) from Holland and Powell (2011); Ilm(WPH) from White et al. (2000) with exclusion of the “geik” endmember as proposed by Green et al. (2016); Sp(WPC) from White et al. (2002) and feldspar_B from Benisek et al. (2010). Quartz (Q), rutile (Ru), titanite (Ttn), and aqueous fluid (H₂O) were treated as pure phases. Mineral abbreviations (Whitney and Evans, 2010): melt (L), garnet (Grt), clinopyroxene (Cpx), orthopyroxene (Opx), amphibole (Amp), biotite (Bt), magnetite (Mag), ilmenite (Ilm), plagioclase (Pl), K-feldspar (Kfs), muscovite (Ms), chlorite (Chl), quartz (Qz), rutile (Rt), titanite (Ttn), albite (Ab), andalusite (And), sillimanite (Sil) and aqueous fluid (H₂O).

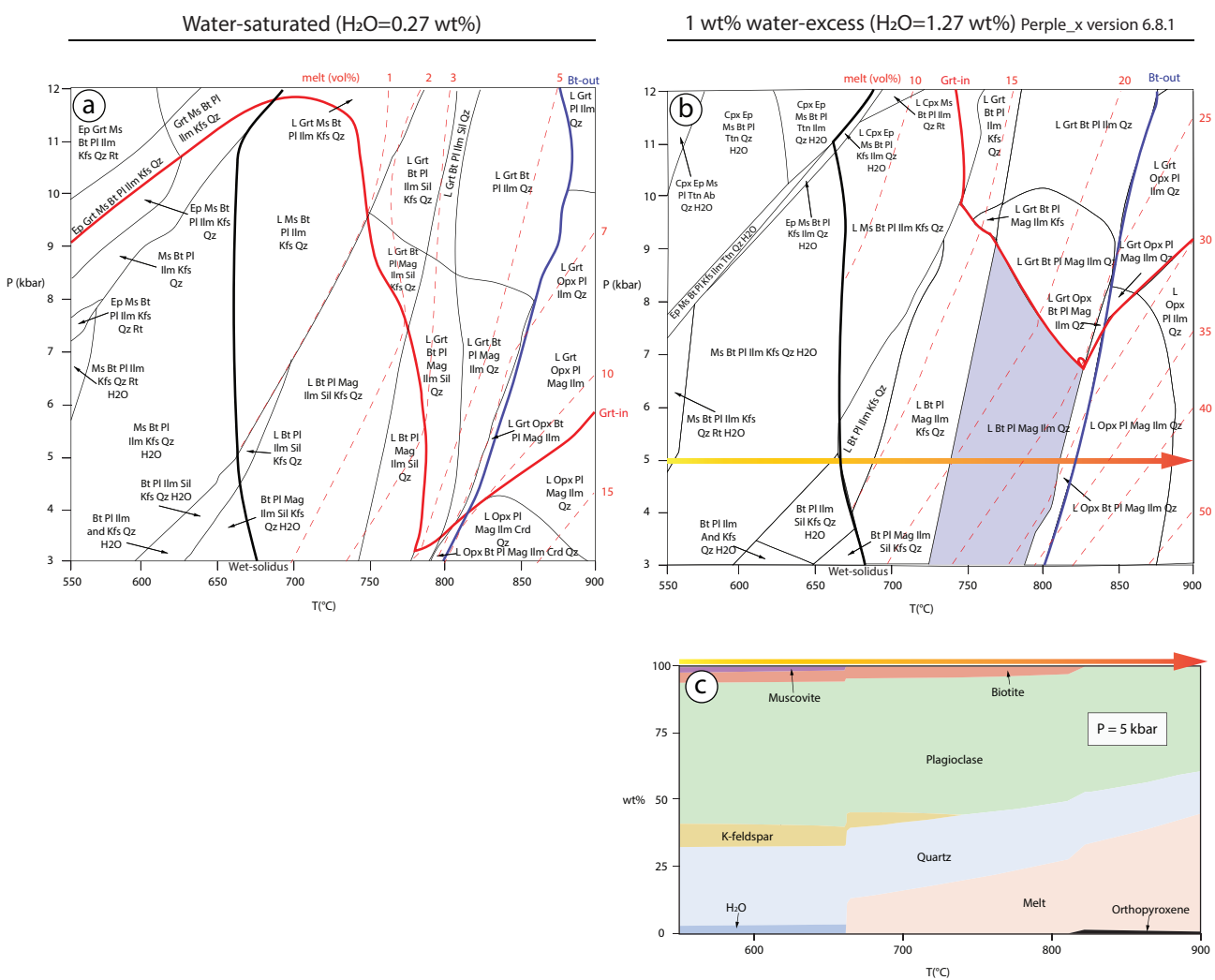
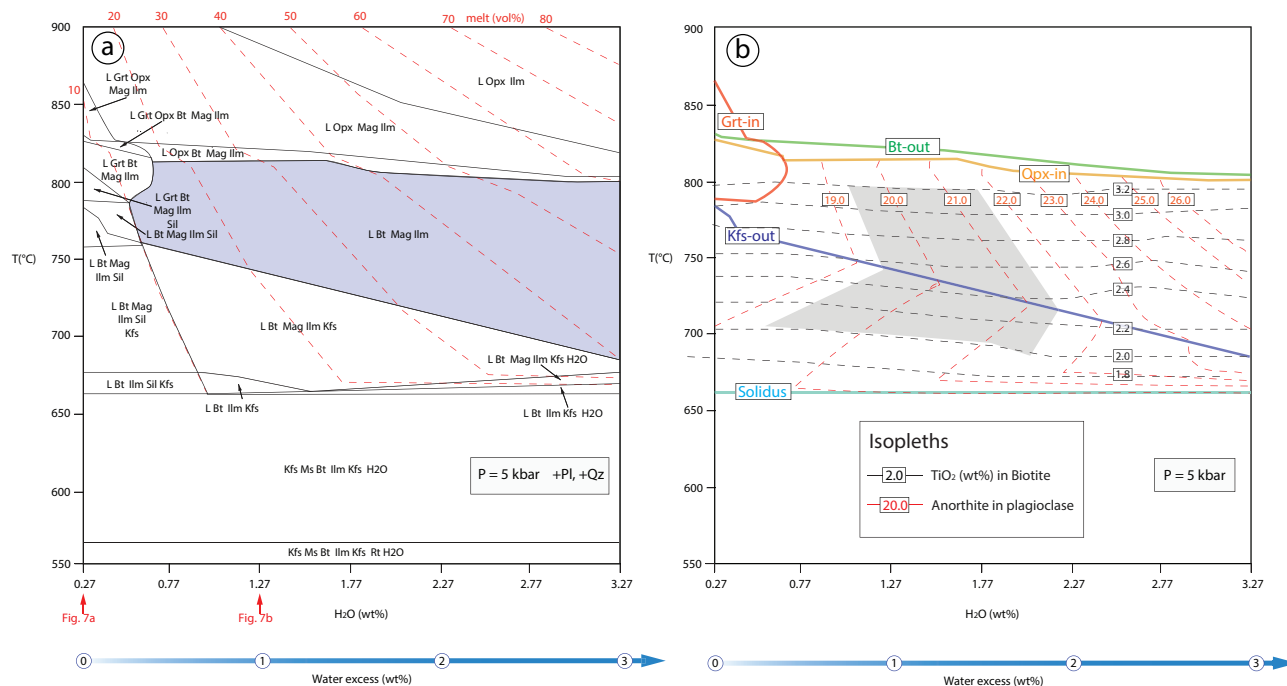


Figure 7: Perple_X phase diagram modelling for the representative migmatite tonalite sample (155879). a) P–T pseudosection for $H_2O = 0.27$ wt%, which saturates the solidus at 8 kbar (composition in moles: 1.198 SiO₂, 0.003 TiO₂, 0.151 Al₂O₃, 0.021 FeO, 0.013 MgO, 0.041 CaO, 0.079 Na₂O, 0.024 K₂O, 0.015 H₂O and 0.002 O₂). b) P–T pseudosection with $H_2O = 1.27$ wt% representing 1 wt% water excess at 8 kbar. Wet solidus is the thick black line; red line is garnet-in reaction; blue line is biotite-out reaction. Red dashed line is vol% of melt. Shaded field in (b) marks the stability field of the stable mineral assemblage (composition in moles: 1.198 SiO₂, 0.003 TiO₂, 0.151 Al₂O₃, 0.021 FeO, 0.013 MgO, 0.041 CaO, 0.079 Na₂O, 0.024 K₂O, 0.071 H₂O, and 0.002 O₂). c) Mineral phase (wt%) between 550–900 °C at the fixed pressure of 5 kbar for 1 wt% excess water phase diagram marked by the horizontal arrow in (b).

In Fig. 7a for the dry system, the volume of melt generated before biotite is exhausted at $T > 800$ °C is less than 5% (Fig. 7a). These small volumes of melt are expected from the low H_2O content in the rock (0.27 wt%). These estimates are in line with results from vapor absent experimental melting of tonalites (Patiño Douce and Beard, 1995; Watkins et al., 2007), but are in stark contrast with the presence of 10–30 vol% of in-situ leucosomes (Figs 2a-b). In addition, the phase diagram predicts sillimanite at $T < 770$ °C and sillimanite+garnet at higher temperatures (Fig. 7a), which are not part of the paragenesis of the migmatitic tonalites.

Peak conditions and melt volume are better approximated by calculations including water-excess partial melting. The addition of 1 wt% excess H_2O reduces the stability field of garnet to pressures above 7 kbar and suppresses sillimanite (Fig. 7b) while also generating more voluminous melt fractions. Thus, the observed peak mineral assemblage in the migmatitic tonalites is stable in the 3–9 kbar and 730–780 °C interval (Figs 7b), further supporting the inference that melting occurred in the presence of excess H_2O (reaction 1 above). Figure 7c shows that this reaction takes place between 660–740 °C at 5 kbar, until complete breakdown of K-feldspar. At temperatures between 740 and 810 °C, melting continues via congruent melting of plagioclase and quartz (reaction 2 above).



The upper temperature limit for anatexis in the migmatitic tonalite is ~ 810–820 °C, after which biotite is rapidly consumed to form peritectic orthopyroxene via the incongruent melting reaction $\text{plagioclase} + \text{quartz} + \text{biotite} = \text{orthopyroxene} + \text{melt}$ (reaction 3) (Figs 7b-c).

With 1 wt% excess H₂O, the volume of melt range between 20 and 30% at 730–780 °C (Fig. 7a), in agreement with field estimates (Figs 2a-b). It is notoriously difficult to estimate the volume of melt flow in anatectic terranes because of melt flow and crystallization, but given the volume of leucosomes present and the degree of disaggregation of the protolith we assume that melt fraction reached 20-30 % as a reasonable working hypothesis. Increasing the H₂O content up to 3 wt% at the fixed pressure of 5 kbar (Fig. 8a) further increases the amount of melt produced, up to 60% in volume. The intersection of anorthite content in plagioclase (An₁₉₋₂₁) and TiO₂ in biotite (TiO₂=2.07–3.16 wt%) isopleths indicates temperature of 700–800 °C and 0.5–2 wt% excess of water (Fig. 8b). Within this interval, the melt volume ranges between 15 and 35%. Our results are corroborated by the melting experiments of van der Molen and Paterson (1979) who found that the amount of melt in a granitic rock at 800 °C and 3 kbar is controlled by the amount of water and can reach up to 25 vol% of melt with the addition of 1 wt% of H₂O. Biotite dehydration melting does not occur at these conditions (Fig. 9a), indicating the need of water-influx for a substantial melting of the tonalites.

In summary, the pseudosection calculations define a relatively broad range of water excess conditions (between 0.5 and 2 wt%) and P–T conditions varying between 3–9 kbar and c. 700–800 °C where both the mineral paragenesis and the volumes of leucosomes can be explained.

4.2 Amphibolite

4.2.1 Melting reactions

The experimental studies of Beard and Logfren (1991) demonstrated that, during partial melting of mafic rocks at less than 7 kbar, melting reaction and composition of the restite are strongly influenced by water content. In dehydration melting experiments, melts coexist with a plagioclase-rich residue (>50%) and both orthopyroxene and clinopyroxene as peritectic minerals. In water-saturated experiments, the residue is amphibole-rich and plagioclase-poor, with peritectic amphibole and clinopyroxene as the only ferromagnesian phases. Thus, the amphibole-rich residue and the absence

of orthopyroxene suggests that the migmatitic amphibolite (Fig. 4) underwent water-fluxed melting via the reaction amphibole + plagioclase + H₂O = melt + clinopyroxene ± amphibole.

In the amphibolite away from the contacts with migmatitic tonalites, macroscopic evidence of partial melting is absent, but the presence of films of K-feldspar (Fig. 6a) and pockets of Na-rich plagioclase (An₂₉) associated with titanites (Fig. 6d) along the grain boundaries of larger amphiboles, is interpreted to indicate the presence of former melt pockets. The elements required to form these minerals were supplied from the loss of K, Na, Al and Ti recorded by amphibole rims (Fig. 6e). The K, Na, Ti and Al content of these rims is similar to the amphiboles in the migmatitic amphibolite (Figs 5b-c) and, as such, they might have equilibrated at equivalent P–T conditions.

4.2.2 P–T estimates

We assessed the P–T conditions during amphibolite metamorphism by employing hornblende–plagioclase using the thermobarometers of Schmidt (1992), Holland and Blundy (1994), Anderson (1995), Bhadra and Bhattacharya (2007) and Molina et al. (2015) and the semi-quantitative estimation of Ernst and Liu (1998). The results are shown in Table 3 and plotted in figure 9b. The P–T conditions reached in the migmatitic amphibolite were ~ 700–750 °C and 4–6 kbar (Table 3). These P–T estimates confirm that melting is caused by addition of fluids rather than amphibole dehydration reactions, because amphibole breakdown takes place at temperature higher than 850 °C, with the more magnesian end-members surviving up to 1000 °C (Fig. 9b; Vielzeuf and Schmidt, 2001; Wyllie and Wolf, 1993; Springer and Seck, 1997; Patino-Douce and Beard, 1995; Rushmer, 1991).

The core of amphibole and plagioclase (An_{33–38}) pair in the amphibolite away from the contact with the migmatites tonalites recorded higher temperatures of almost 800 °C and 5–7 kbar (Table 3).

This peak temperature might have recorded an earlier metamorphic event and might have caused dehydration melting of biotite, explaining the preservation of biotite only as inclusions in amphiboles (Fig. 6a-b). Alternatively, the higher temperature recorded in the core of amphiboles might represent the initial crystallization of magmatic amphiboles in basalts and were preserved during metamorphism. Hornblende–plagioclase thermobarometers were also applied on the amphibole rim and interstitial plagioclase (An_{26–29}) pair but they yielded discordant results and were not considered

Table 3: Hbl-Pl thermobarometry

Lithology	Amphibolite		Migmatitic amphibolite		
	209690		214403C		
Sample	core		Amphibole-rich source	Melanosome	Leucosome
HB ₉₄	790 ± 20 °C (at 6.3 kbar)		731 ± 31 °C (at 6.18 kbar)	720 ± 16 °C (at 5 kbar)	726 ± 15 °C (at 4.7 kbar)
BB ₀₇ P1	6.0 ± 1.9 kbar		6.0 ± 0.8 kbar		
BB ₀₇ P2	6.6 ± 1.7 kbar		6.38 ± 0.8 kbar		
BB ₀₇ average	6.3 ± 1.8 kbar		6.1 ± 0.8 kbar		
S ₉₂			4.7 ± 0.8 kbar		
AS ₉₅			685 ± 20 °C, 5.1 ± 0.2 kbar	678 ± 10 °C, 4.7 ± 0.7 kbar	
MO ₁₅	5.6 ± 0.7 kbar (at 790 °C)	6.2 ± 1.3 kbar (at 730 °C)	5.0 ± 0.7 kbar (at 730 °C)	4.5 ± 1.1 kbar (at 730 °C)	
EL ₉₈	850 °C, 5.5 kbar		710 °C, 6 kbar	740 °C, 5 kbar	680 °C, 6 kbar
Calibration precision					
HB ₉₄ = Holland and Blundy, 1994	± 40 °C				
BB ₀₇ = Badhra and Battacharya, 2007	± 2 kbar				
S ₉₂ = Schmidt 1992					
AS ₉₅ = Anderson 1995	± 0.6 kbar				
MO ₁₅ = Molina et al., 2015	± 1.5 to ± 2.3 kbar				
EL ₉₈ = Ernst and Liu 1998	± 2 kbar, ± 50 °C				

Amphibole and plagioclase analyses used for thermobarometry are presented in Appendix 2 and 3.

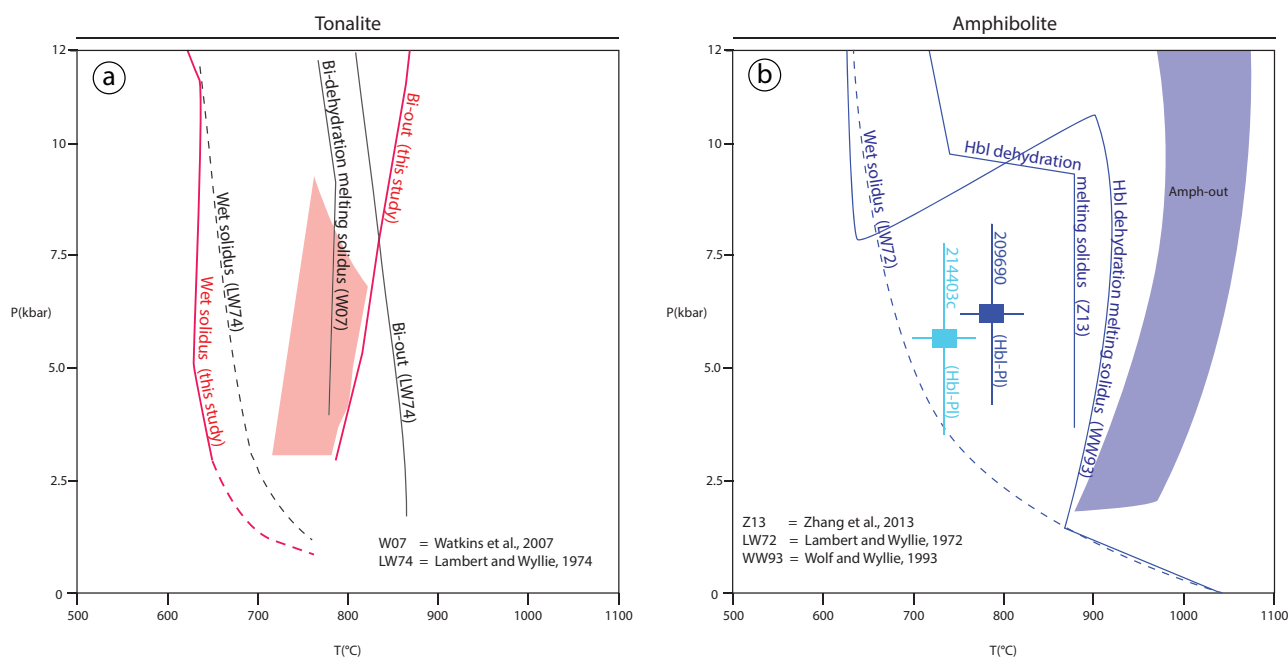


Figure 9: P–T diagrams comparing results obtained in this study and the literature for tonalite and amphibolite. (a) Red shaded area represents the field of peak mineral assemblage in Fig. 6b plotted alongside biotite-out and wet solidus lines found in this study (Fig. 7b) and from Lambert and Wyllie (1974) and Watkins et al. (2007). (b) Blue and light blue squares show the Hbl-Pl thermobarometry results for sample 214403c and 209690; calibration uncertainty bars are $T = \pm 40$ °C and $P = \pm 2$ kbar (Table 3). Amphibole (Hbl) dehydration melting solidus lines are from Wyllie and Wolf (1993) and Zhang et al. (2013) while wet solidus is from Lambert and Wyllie (1972). Blue shaded area indicates the amphibole-out area obtained by Vielzeuf and Schmidt (2001), Wolf and Wyllie (1993), Springer and Seck (1997), Patino-Douce and Beard (1995) and Rushmer (1991) (diagram modified after Qian and Herman, 2013).

for further interpretations as subsolidus re-equilibration during cooling might have altered the composition of the amphibole rims.

5 Discussion

5.1 Reworking of middle crust

Gneiss and migmatitic domes are common occurrences in the crustal record since the Archean, but the causes of their formation are fundamentally different. Phanerozoic domes are smaller, and they are mostly confined to localities in which thrust stacking was important for crustal thickening (Choukroune et al., 1995; Teyssier and Whitney, 2002; Yin, 2004) or in extensional settings (Kruckenberg et al., 2011; Rey et al., 2017). Instead the formation of gneiss domes was related to large-scale crustal reworking caused by vast volumes of juvenile material added to the growing continents. For instance, in the Pilbara Craton, plume-derived basalts and komatiite greenstones up to 12–20 km in thickness (Van Kranendonk et al., 2004, 2015) were deposited above older continental crust, generating a gravitational instability. Burial of radiogenic continental crust in association with the blanketing effect from the greenstone cover and crust-mantle heat exchange, promoted partial melting weakening the entire sequence and activated doming processes (Collins, 1989; Choukroune et al. 1995; Chardon et al., 1998; Van Kranendonk et al., 2004; Van Kranendonk et al., 2015).

Similarly, doming of the Yalgoo Dome was preceded by the emplacement of the voluminous greenstones of the Norie Group of unknown thickness and the >8 km thick Polelle Group between 2825 and 2760 Ma (Ivanic et al., 2015), on top of the 2970–2900 Ma tonalite and coeval greenstones of the Gossan Hill Formation (2963–2958 Ma; Ivanic et al., 2015; Zibra et al., 2018). The time lag between greenstone development ending at 2760 Ma and the 2760–2740 Ma emplacement of the voluminous Goonetarra Granodiorite and migmatization of the 2970–2900 Ma tonalites (Zibra et al., 2018) may simply reflect the time necessary to heat up the crust (Campbell and Hill, 1988; Van Kranendonk et al., 2013, 2015). In this study, we have shown that partial melting of the 2970–2900 Ma tonalites and interlayered amphibolites was prompted not only by an increase in temperature, but also by the influx of H₂O (water-excess conditions). Phase diagrams constrain the field of anatexis of the tonalite to mid-crustal conditions, between 3 and 9 kbar and 700 and 800 °C (Fig. 7b), with

excess water ranging between 0.5 and 2 wt% (Fig. 8b). Migmatitic amphibolites record comparable but more narrowly constrained P–T conditions, with water-present anatexis between 4 and 6 kbar and 700–750 °C. Amphibolites further away from the contact preserve a mineral assemblage equilibrated at 800 °C (Table 3) with only minimal traces of melting (Fig. 6a). We interpret this as indicative of an earlier metamorphism that was insufficient to trigger amphibole-dehydration melting reactions, and preserved because water-fluxed melting was minimal and incapable of retrogressing peak assemblages to the anatectic conditions recorded by the contact migmatitic amphibolite. Thus, the key component controlling melting of amphibolites was the availability of fluids. The location of migmatitic amphibolites along the lithological boundary with tonalites suggest that amphibolites had low permeability and H₂O only accessed its margins.

These P–T–X_{H₂O} conditions are consistent with experiments of water-present melting of both tonalites (Fig. 9a; Lambert and Wyllie, 1974; Watkins et al., 2007) and amphibolitic/basaltic protoliths (Fig. 9b; Lambert and Wyllie, 1972; Beard and Logfren, 1991; Wyllie and Wolf, 1993; Zhang et al., 2013). Water-present melting has been identified in other Archean terranes such as the Lisalmi block in central Finland (Nehring et al., 2009), the Opatica Subprovince of the Canadian Shield (Sawyer, 2010), the Gyeonggi Massif in the Korean Peninsula (Lee and Choo, 2013), the North Dabie in the North China Craton (Hu et al., 2016) and the São Francisco Craton (Carvalho et al., 2016). These studies corroborate our conclusions that water-present melting was an effective mechanism for local reworking of Archean intermediate crustal levels.

5.2 Origin of the Goonetarra Granodiorite

The 2760–2740 Ma Goonetarra Granodiorite is a calc-alkalic and mildly peraluminous (Chapter 4) rock with a normalized REE pattern as those of the TTGs, marked by depletion in HREE (Fig. 10a). These granitoids have a narrow silica range (70–76 wt% SiO₂) and large LILE variations (Figs 10b-c-d). They are more potassic than the 2970–2900 Ma migmatitic TTGs (K₂O/Na₂O < 0.6 compared to K₂O/Na₂O = 0.6–1 of Goonetarra Granodiorite) and silica correlates positively with K₂O/Na₂O, which increases from 0.6 at 70 wt% SiO₂, up to 1.5 at 75 wt% SiO₂ (Fig. 10b). These granitoids have a geochemical signature more akin to the transitional TTGs, a group of granites identified

in the Yilgarn and Pilbara Cratons and characterized by broadly TTG-like compositions, but marked by LILE, Th and U enrichment (Fig. 10c-d) (Champion and Smithies, 2001, 2007). Transitional TTGs were initially interpreted as high fraction melting of pre-existing TTGs. Collins et al. (1993) proposed that high fraction water-fluxed melting of dacitic/tonalitic protoliths, involving complete dissolution of plagioclase, could explain the composition of c. 3300 Ma transitional trondhjemites and tonalites in Mt Edgar Dome of the Pilbara Craton. Water-fluxed melting would occur close to the eutectic and would generate melts more sodic than the source (Collins et al., 1993). However, this process cannot explain the origin of the transitional TTGs in the Yalgoo dome, because these rocks are consistently more potassic than TTGs at equivalent silica contents (Fig. 10b). For this reason, Champion and Smithies (2007) proposed a new model, where transitional TTG magmas form by partial melting of a basaltic source in the deep crust that is more enriched in LILE, Th and U than the average basaltic TTGs protolith. Alternatively, felsic volcanic and sedimentary rocks interbedded with basalts could potentially generate enriched TTGs melts (Champion and Smithies, 2007).

5.3 Source of fluids

One of the difficulties with water-fluxed melting is that the wet-solidus traps any fluid migrating up-temperature. Such fluid would be consumed to produce melt by reactions with negative volume change, ΔV , which reduces the mean pressure, thus attracting nearby fluids and magmas (Weinberg and Hasalová, 2015). However this is not the case in the Yalgoo Dome where melting occurred above the water saturated solidus. Therefore there must have been a mechanism for aqueous fluids to bypass this water saturated fluid trap. One possibility involves shear zones which attract regional fluids in channels and fracture networks and provides a fluid pathway (Sawyer, 2010). One example of water-fluxed melting in an Archean shear zone is melting of suprasolidus mid-crustal rocks in the São Francisco Craton in Brazil. Here, a regional-scale shear zone provided fluids to rework and extensively melt TTGs at ~ 730 °C and 5–6 kbar (Carvalho et al., 2016). A second possibility is that silicate melts transport dissolved H₂O and bypass the water-saturated fluid trap during decompression (Weinberg and Hasalová, 2015). The crystallization of these silicate magmas advect heat and release fluids that might cause melting if the conditions of adjoining rocks are above the wet-solidus

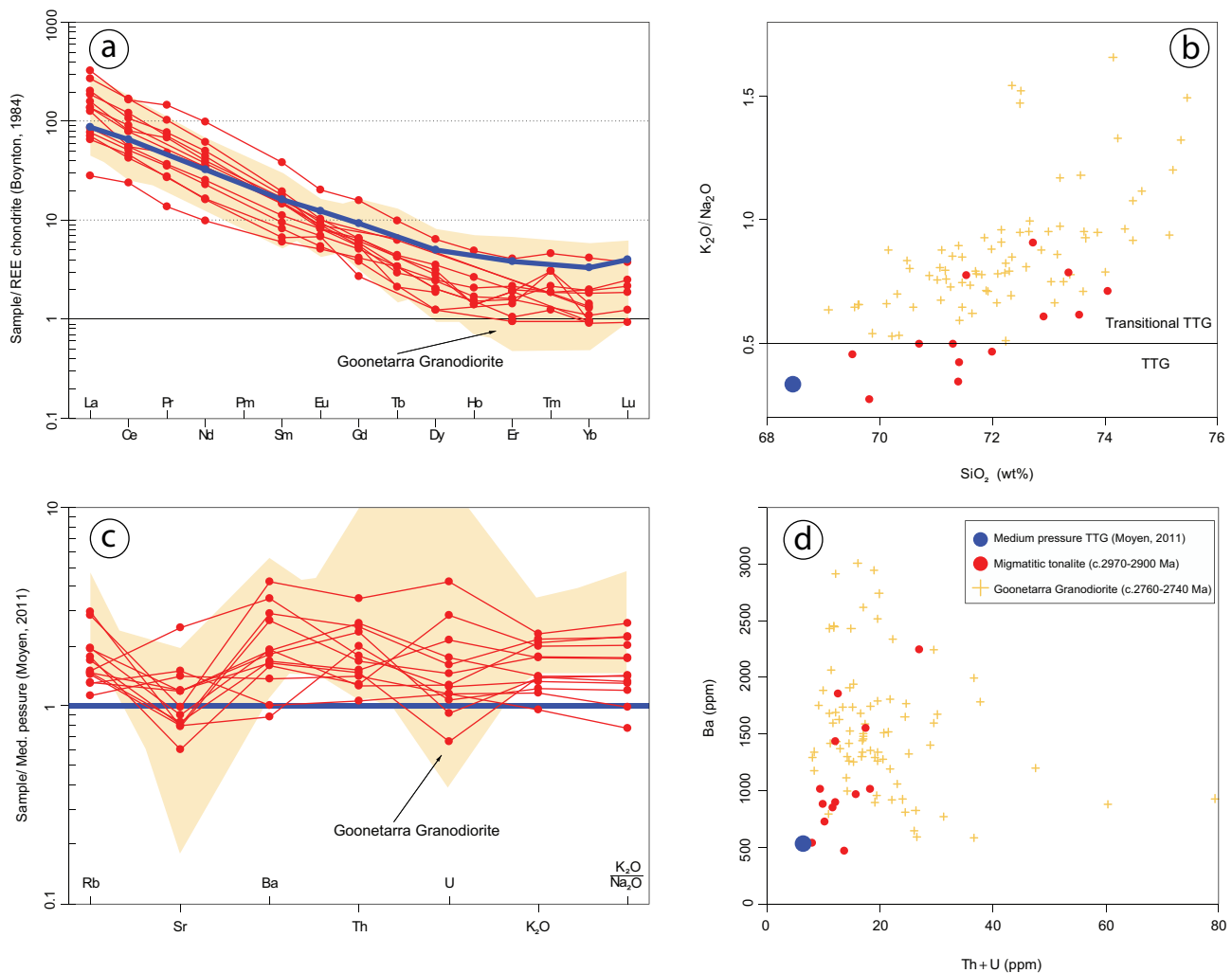


Figure 10: Diagrams comparing the chemical composition of the 2970–2900 Ma migmatitic tonalites and 2760–2740 Ma Goonetarra Granodiorite with the average composition of the medium pressure TTGs of Moyén (2011). a) Chondrite normalized REE spider plots (Boynton, 1984) showing that the Goonetarra Granodiorite and the migmatitic tonalites have similar REE patterns and define a steeper slope compared to the medium-PTTG of Moyén (2011); b) K_2O/Na_2O vs SiO_2 (wt%) separates the sodic TTGs from the more potassic transitional TTGs (Chapter 4); c) Spider plot showing Rb, Sr, Ba, Th, U, K_2O and K_2O/Na_2O distribution normalized by the medium-P TTG of Moyén (2011); d) Ba vs Th+U. Orange shaded area represent the field occupied by transitional TTGs of the Goonetarra Granodiorite. The analyses are from the Geological Survey of Western Australia (GSWA) and Geoscience Australia (GA) database and can be viewed in Appendix 3.4.

(Holk and Taylor, 2000; Schwindinger and Weinberg, 2017).

Given that magmas are generally hydrous and that the migmatization of the 2970–2900 Ma tonalite-amphibolite sequence was coeval with intrusion of the voluminous Goonetarra Granodiorite (Zibra et al., 2018; Clos et al., submitted; Chapter 2), we argue that this magma was the likely H_2O transport agent that triggered anatexis. We note that the transfer of H_2O from the Goonetarra Granodiorite to the surroundings did not need to be through an intermediate, separate aqueous phase. If a chemical potential gradient existed between H_2O -rich granodiorite and the drier surroundings, then H_2O would have diffused out of the granodiorite (White and Powell, 2010; Weinberg and Hasalová, 2015; Schwindinger and Weinberg, 2017), causing partial melting of the 2970–2900 Ma to-

nalite-amphibolite sequence. This influx of magmatic fluids into mid-crustal rocks affected not only melt volume and reactions (Fig. 7), but also chemistry of the host rocks. Indeed, the 2970–2900 Ma migmatitic TTGs are compositionally similar to the average medium pressure TTGs of Moyen (2011) (Fig. 10a), except for a heterogeneous enrichment in LILE, Th and U matching the pattern in the transitional TTGs of the Goonetarra Granodiorite (Figs 10b-c-d). We therefore propose that the Goonetarra Granodiorite could be a source of metasomatic LILE-rich fluids and melts (Figs 10c-d) and we note that some of the most enriched samples from the migmatitic TTGs match samples of the Goonetarra Granodiorite (Figs 10c-d). While LILE are enriched in hydrothermal fluids released by magmas, Th and U are generally transported by melts. We therefore suggest that Goonetarra granodiorite magmas interacted with TTGs and triggered anatexis transferring LILE, Th and U.

5.4 Role of fluids during diapirism

Many experiments over the past 30 years showed that incipient melting dramatically reduces the strength of granitic rocks (Murrel and Chakravarty, 1973; Murrel and Ismail, 1976; Arzi, 1978; van der Molen and Paterson, 1979; Dell'Angelo and Tullis, 1998). These investigations documented the presence of a “rheological critical melt percentage” (Arzi, 1978), a restricted melt fraction between 10 and 30 vol% in which the viscosity of the rock decreases from solid to almost liquid. The more recent work of Rosenberg and Handy (2005) refined this concept, and demonstrated that when granular interconnectivity is reached at the critical melt volume of ~7%, which they called the melt connectivity transition, the strength drops two to three orders of magnitude. A second geometric threshold occurs at >50 vol% of melt (solid-to-liquid transition) when the continuity of the solid framework is lost and rock strength decreases another ten orders of magnitude. The drop of strength at the melt connectivity transition is considered the most significant for the rheology of the continental crust (Rosenberg and Handy, 2005; Vanderhaeghe, 2009). Indeed, the strength of partially molten rocks with >7 vol% of melt is small when compared with unmelted rocks and a further decrease at the solid-to-liquid transition is considered irrelevant for crustal scale processes.

These findings have profound implications for our understanding of the rheology of the tonalites exposed in the Migmatitic Domain. At 700–800 °C and in absence of external fluids, the tonalites

would have had high viscosity, because small melt fractions (< 5 vol%) would only have a marginal impact on rock strength (Fig. 7a). Increased melt fertility caused by small additions of H₂O raises melt fraction to 15–30 vol% (Fig. 7b), well above the melt connectivity transition, reducing the strength of the tonalites by a few orders of magnitude. Van der Molen and Paterson (1979) showed that the strength of deformed partially molten tonalitic rocks (at a fixed strain rate of 10⁻⁵ s⁻¹) decreases from 250 MPa at 5 vol %, to 60 MPa at 15 vol % and to <1 MPa at 24 vol %. The set-up of the experiment at 24 vol % required the addition of 1 wt% H₂O, closely simulating the conditions in the phase diagram in Fig. 7b. We conclude that the addition of H₂O not only enhanced melt production, but weakened the rock causing a decrease in viscosity and density, increasing the buoyancy of these granites compared with the thick denser greenstone overburden. To restore equilibrium in the crust, the greenstones sagducted into middle crustal levels causing the diapiric rise of magmatic and migmatitic bodies to form the dome-and-keel structure defined by the Yalgoo Dome and surroundings (Fig. 11). The key factor controlling the speed of the instability was the viscosity of the overburden, likely to have been more viscous than the partially molten granitic lower crust. As the greenstones sank, the increase in temperature may have weakened these rocks, reducing their viscosity and accelerating the instability in a positive feedback loop.

In summary, the formation of the dome-and-keel architecture in the Yalgoo Dome was initiated by an enhanced period of mantle activity between 2825–2760 Ma, which gave rise to a crustal-scale gravitational instability with the deposition of thick packages of greenstones in the upper crust, as well as causing a major thermal perturbation. This triggered cascading reactions in the crust starting with the partial melting of the mafic lower crust, by heat and water influx, producing the 2760–2740 Ma Goonetarra Granodiorite, a suite of transitional TTGs. These magmas rose and intruded an older mid-crustal sequence, comprising the 2970–2900 Ma tonalites (a TTG suite) and amphibolites. The Goonetarra Granodiorite was thus the transport agent of heat and fluids that for over ~20 Myr caused the partial melting of the tonalite-amphibolite surroundings (Fig. 11). As this process progressed, it gradually weakened the strong mid-crustal levels, which in turn allowed doming of the gravitationally unstable low-density granitoids and sagduction of the dense, overlying greenstone packages. We conclude that the magmatic history of the Yalgoo Dome records the upward migration

of a wave of heat and fluids mediated by crustal anatexis and magma migration. This process lasted more than 20 Myr and is responsible for the plutonic and diapiric history of the dome.

6 Conclusion

The high-grade rocks in the migmatitic core of the Yalgoo Dome record anatexis during diapirism.

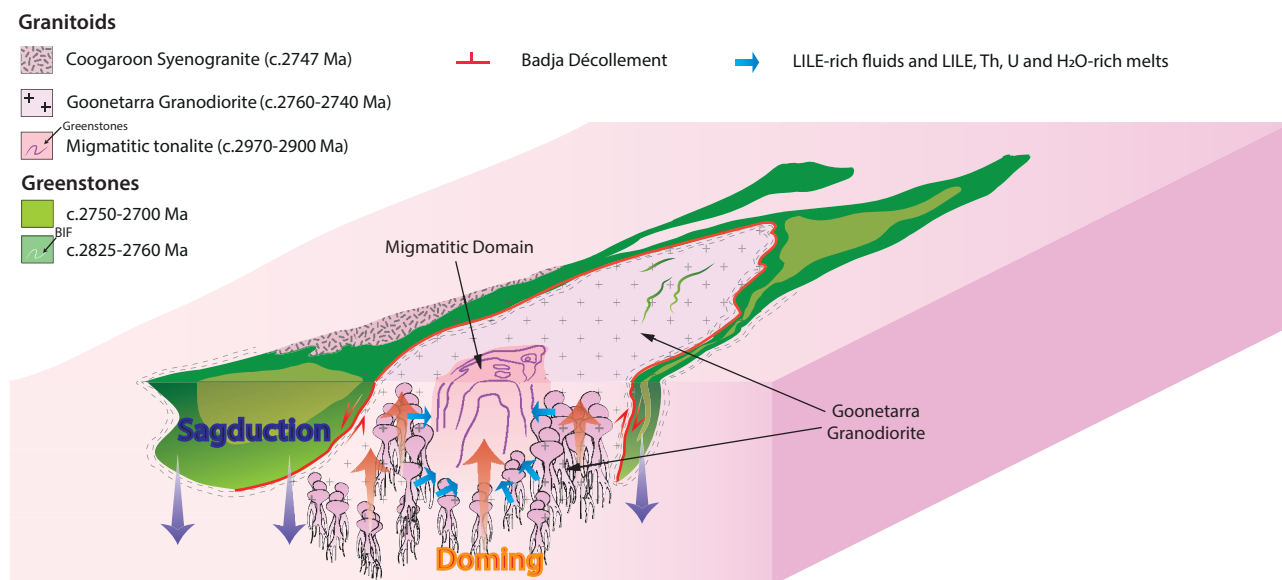


Figure 11: Cartoon illustrating the dome-forming episode at 2760–2740 Ma, when the primary intrusion of the Goonetarra Granodiorite released fluids that triggered partial melting of the 2970–2900 Ma tonalite. Presence of magmatic and migmatitic bodies in the middle crust caused a density and viscosity contrast with supracrustal rocks, triggering the sinking of the dense greenstones, and the rise of buoyant granitic rocks.

The migmatitic tonalites and amphibolites recorded water-excess partial melting at middle crustal conditions. Phase equilibria modelling and thermobarometry indicate that melting and reworking of the migmatitic core occurred at 3–9 kbar and c. 700–800 °C. Widespread melting and remobilization of mid-crustal rocks occurred with an external influx of c. 0.5–2 wt% of H₂O, most likely derived from the crystallization of the voluminous Goonetarra Granodiorite between 2760 and 2740 Ma. These LILE-rich magmas formed in the lower crust and were the transport agent of fluids and heat to upper crustal levels where they triggered partial melting and LILE-metasomatism of the migmatitic tonalites. In this large-scale re-organization of the crust, H₂O transfer through the crust assisted remobilization of mid-crustal rocks by enhancing melt production of tonalites from <5 vol% to up to 15–30 vol%. The accumulation of the voluminous Goonetarra Granodiorite and the anatexis of pre-existing mid-crustal rocks decreased both the density and viscosity of mid-crustal levels below a mafic-ultramafic upper crust. This eventually triggered diapirism in response to this

crustal scale gravitational instability. The history of crustal magmatism and diapiric rise of the Yal-goo dome is a record of the passage of a heat and H₂O wave through the crust that lasted between 2760–2740 Ma, following the voluminous mantle magmatism that ended at 2760 Ma associated with the deposition of the thick overburden of mafic-ultramafic volcanic rocks.

Acknowledgments

This work is part of the first author's Ph.D. thesis, and was financially supported by ARC DP11010254. Shachar Lazar is thanked for his assistance and energy during the fieldwork and the staff of the Geological Survey of Western Australia at the Carlisle laboratories for their sample handling.

References

- Amato, J.M., Wright, J.E., Gans, P.B. and Miller, E.L., 1994. Magmatically induced metamorphism and deformation in the Kigluaik gneiss dome, Seward Peninsula, Alaska. *Tectonics*, 13(3), pp.515–527.
- Anderson, J.L. and Smith, D.R., 1995. The effects of temperature and fO₂ on the Al-in-hornblende barometer. *American Mineralogist*, 80(5–6), pp.549–559.
- Arzi, A.A., 1978. Critical phenomena in the rheology of partially melted rocks. *Tectonophysics*, 44(1–4), pp.173–184.
- Bateman, R., 1985. Aureole deformation by flattening around a diapir during in situ ballooning: the Cannibal Creek granite. *The Journal of Geology*, 93(3), pp.293–310.
- Beard, J.S. and Logfren, G.E., 1991. Dehydration melting and water-saturated melting of basaltic and andesitic greenstones and amphibolites at 1, 3, and 6.9 kb. *Journal of Petrology*, 32(2), pp.365–401.
- Benisek, A., Dachs, E. and Kroll, H., 2010. A ternary feldspar-mixing model based on calorimetric data: development and application. *Contributions to Mineralogy and Petrology*, 160(3), pp.327–337.
- Bhadra, S. and Bhattacharya, A., 2007. The barometer tremolite+ tschermakite+ 2 albite= 2 pargasite+ 8 quartz: constraints from experimental data at unit silica activity, with application to garnet-free natural assemblages. *American Mineralogist*, 92(4), pp.491–502.
- Bodorkos, S. and Sandiford, M., 2006. Thermal and mechanical controls on the evolution of Archean crustal deformation: examples from Western Australia. *Archean Geodynamics and Environments*, pp.131–147.
- Bouchez, J.L. and Diot, H., 1990. Nested granites in question: Contrasted emplacement kinematics of independent magmas in the Zaër pluton, Morocco. *Geology*, 18(10), pp.966–969.
- Boynton, W.V., 1984. Cosmochemistry of the rare earth elements: meteorite studies. In: Henderson, P. (Ed.), *Rare Earth Element Geochemistry*. Elsevier, Amsterdam, pp. 63–114.
- Burg, J.P., Brunel, M., Gapais, D., Chen, G.M. and Liu, G.H., 1984. Deformation of leucogranites of the crystalline Main Central Sheet in southern Tibet (China). *Journal of Structural Geology*, 6(5), pp.535–542.

- Büsch, W., Schneider, G. and Mehnert, K.R., 1974. Initial melting at grain boundaries. Part II: melting in rocks of granodioritic, quartzdioritic and tonalitic composition. *Neues Jahrbuch für Mineralogie, Monatshefte*, 8, pp.345–370.
- Campbell, I.H. and Hill, R.I., 1988. A two-stage model for the formation of the granite-greenstone terrains of the Kalgoorlie-Norseman area, Western Australia. *Earth and Planetary Science Letters*, 90(1), pp.11–25.
- Carvalho, B.B., Sawyer, E.W. and Janasi, V.A., 2016. Crustal reworking in a shear zone: transformation of metagranite to migmatite. *Journal of Metamorphic Geology*, 34(3), pp.237–264.
- Champion, D.C. and Smithies, R.H., 2001. Archaean granites of the Yilgarn and Pilbara cratons, Western Australia. K.F. Cassidy, J.M. Dunphy and M.J. Van Kranendonk (Eds.), 4, pp.134–136.
- Champion, D.C. and Smithies, R.H., 2007. Geochemistry of Paleoproterozoic Granites of the East Pilbara Terrane, Pilbara Craton, Western Australia: implications for Early Archaean Crustal Growth. *Developments in Precambrian Geology*, 15, pp.369–409.
- Chardon, D., Choukroune, P. and Jayananda, M., 1998. Sinking of the Dharwar basin (South India): implications for Archaean tectonics. *Precambrian Research*, 91(1–2), pp.15–39.
- Choukroune, P., Bouhallier, H. and Arndt, N.T., 1995. Soft lithosphere during periods of Archaean crustal growth or crustal reworking. *Geological Society, London, Special Publications*, 95(1), pp.67–86.
- Clos, F., Weinberg, R.F., Zibra, I. and Fenwick, M.J. (submitted). Archean diapirism recorded by vertical sheath folds in the core of the Yalgoo Dome, Yilgarn Craton. *Precambrian Research*.
- Collins, W.J., 1989. Polydiapirism of the Archean Mount Edgar Batholith, Pilbara Block, Western Australia. *Precambrian Research*, 43(1–2), pp.41–62.
- Collins, W.J., 1993. Melting of Archaean sialic crust under high aH₂O conditions: genesis of 3300 Ma Na-rich granitoids in the Mount Edgar Batholith, Pilbara Block, Western Australia. *Precambrian research*, 60(1–4), pp.151–174.
- Coney, P.J., 1980. Cordilleran metamorphic core complexes: an overview. *Geological Society of America Memoirs*, 153, pp.7–31.
- Connolly, J.A.D., 2009. The geodynamic equation of state: what and how. *Geochemistry, Geophysics, Geosystems*, 10.
- Dell'Angelo, L.N. and Tullis, J., 1988. Experimental deformation of partially melted granitic aggregates. *Journal of Metamorphic Geology*, 6(4), pp.495–515.
- Ernst, W.G. and Liu, J., 1998. Experimental phase-equilibrium study of Al- and Ti-contents of calcic amphibole in MORB—a semi-quantitative thermobarometer. *American mineralogist*, 83(9–10), pp.952–969.
- Eskola, P.E., 1948. The problem of mantled gneiss domes. *Quarterly Journal of the Geological Society*, 104(1–4), pp.461–476.
- Fenwick, M.J., 2014. Structural evolution of the Yalgoo Dome, Yilgarn Craton, Western Australia: a core perspective. *Geological Survey of Western Australia, record 2015/1016*.
- Foley, B.J., 1997. Reassessment of Archaean tectonics in the Yalgoo District, Murchison Province, Western Australia. Unpublished Thesis. Monash University, Melbourne, Australia.
- Gébelin, A., Roger, F. and Brunel, M., 2009. Syntectonic crustal melting and high-grade metamorphism in a transpressional regime, Variscan Massif Central, France. *Tectonophysics*, 477(3), pp.229–243.
- Green, E.C.R., White, R.W., Diener, J.F.A., Powell, R., Holland, T.J.B. and Palin, R.M., 2016. Activity–composition relations for the

- calculation of partial melting equilibria in metabasic rocks. *Journal of Metamorphic Geology*, 34(9), pp.845–869.
- Holk, G.J. and Taylor Jr, H.P., 2000. Water as a petrologic catalyst driving 18O/16O homogenization and anatexis of the middle crust in the metamorphic core complexes of British Columbia. *International Geology Review*, 42(2), pp.97–130.
- Holland, T. and Blundy, J., 1994. Non-ideal interactions in calcic amphiboles and their bearing on amphibole-plagioclase thermometry. *Contributions to Mineralogy and Petrology*, 116(4), pp.433–447.
- Holland, T.J.B. and Powell, R., 2011. An improved and extended internally consistent thermodynamic dataset for phases of petrological interest, involving a new equation of state for solids. *Journal of Metamorphic Geology*, 29(3), pp.333–383.
- Holness, M.B. and Sawyer, E.W., 2008. On the pseudomorphing of melt-filled pores during the crystallization of migmatites. *Journal of Petrology*, 49(7), pp.1343–1363.
- Hu, Z.P., Zhang, Y.S., Hu, R., Wang, J., Siebel, W. and Chen, F., 2016. Amphibole-bearing migmatite in North Dabie, eastern China: water-fluxed melting of the orogenic crust. *Journal of Asian Earth Sciences*, 125, pp.100–116.
- Ivanic, T.J., Van Kranendonk, M.J., Kirkland, C.L., Wyche, S., Wingate, M.T. and Belousova, E.A., 2012. Zircon Lu–Hf isotopes and granite geochemistry of the Murchison Domain of the Yilgarn Craton: evidence for reworking of Eoarchean crust during Meso-Neoproterozoic plume-driven magmatism. *Lithos*, 148, pp.112–127.
- Ivanic, T.J., Li, J., Meng, Y., Guo, L., Yu, J., Chen, S.F., Wyche, S. and Zibra, I., 2015. Yalgoo, WA Sheet 2241: Geological Survey of Western Australia. 1:100 000 Geological Series.
- Janoušek, V., Farrow, C.M. and Erban, V., 2006. Interpretation of whole-rock geochemical data in igneous geochemistry: introducing Geochemical Data Toolkit (GCDkit). *Journal of Petrology*, 47(6), pp.1255–1259.
- Kruckenberger, S.C., Vanderhaeghe, O., Ferré, E.C., Teyssier, C. and Whitney, D.L., 2011. Flow of partially molten crust and the internal dynamics of a migmatite dome, Naxos, Greece. *Tectonics*, 30(3), pp.1–24.
- Lambert, I.B. and Wyllie, P.J., 1972. Melting of gabbro (quartz eclogite) with excess water to 35 kilobars, with geological applications. *The Journal of Geology*, 80(6), pp.693–708.
- Lambert, I.B. and Wyllie, P.J., 1974. Melting of tonalite and crystallization of andesite liquid with excess water to 30 kilobars. *The Journal of Geology*, 82(1), pp.88–97.
- Langille, J.M., Jessup, M.J., Cottle, J.M., Lederer, G. and Ahmad, T., 2012. Timing of metamorphism, melting and exhumation of the Leo Pargil dome, northwest India. *Journal of Metamorphic Geology*, 30(8), pp.769–791.
- Leake, B.E., Woolley, A.R., Arps, C.E., Birch, W.D., Gilbert, M.C., Grice, J.D., Hawthorne, F.C., Kato, A., Kisch, H.J., Krivovichev, V.G. and Linthout, K., 1997. Report. Nomenclature of amphiboles: report of the subcommittee on amphiboles of the international mineralogical association commission on new minerals and mineral names. *Mineralogical Magazine*, 61(2), pp.295–321.
- Lee, Y. and Cho, M., 2013. Fluid-present disequilibrium melting in Neoproterozoic arc-related migmatites of Daeijak Island, western Gyeonggi Massif, Korea. *Lithos*, 179, pp.249–262.
- Lister, G.S. and Davis, G.A., 1989. The origin of metamorphic core complexes and detachment faults formed during Tertiary continental extension in the northern Colorado River region, USA. *Journal of Structural Geology*, 11(1–2), pp.65–94.
- Little, T.A., Hacker, B.R., Gordon, S.M., Baldwin, S.L., Fitzgerald, P.G., Ellis, S. and Korchinski, M., 2011. Diapiric exhumation of Earth's youngest (UHP) eclogites in the gneiss domes of the D'Entrecasteaux Islands, Papua New Guinea. *Tectonophysics*, 510(1), pp.39–68.

- Molina, J.F., Moreno, J.A., Castro, A., Rodríguez, C. and Fershtater, G.B., 2015. Calcic amphibole thermobarometry in metamorphic and igneous rocks: new calibrations based on plagioclase/amphibole Al-Si partitioning and amphibole/liquid Mg partitioning. *Lithos*, 232, pp.286–305.
- Moyen, J.F., 2011. The composite Archaean grey gneisses: petrological significance, and evidence for a non-unique tectonic setting for Archaean crustal growth. *Lithos*, 123(1), pp.21–36.
- Moyen, J.F. and Martin, H., 2012. Forty years of TTG research. *Lithos*, 148, pp.312–336.
- Murrell, S.A.F. and Chakravarty, S., 1973. Some new rheological experiments on igneous rocks at temperatures up to 1120 °C. *Geophysical Journal International*, 34(2), pp.211–250.
- Murrell, S.A.F. and Ismail, I.A.H., 1976. The effect of decomposition of hydrous minerals on the mechanical properties of rocks at high pressures and temperatures. *Tectonophysics*, 31(3–4), pp.207–258.
- Myers, J.S. and Watkins, K.P., 1985. Origin of granite-greenstone patterns, Yilgarn block, Western Australia. *Geology*, 13(11), pp.778–780.
- Nehring, F., Foley, S.F., Hölttä, P. and Van Den Kerkhof, A.M., 2009. Internal differentiation of the Archean continental crust: fluid-controlled partial melting of granulites and TTG–amphibolite associations in central Finland. *Journal of Petrology*, 50(1), pp.3–35.
- Norlander, B.H., Whitney, D.L., Teyssier, C. and Vanderhaeghe, O., 2002. Partial melting and decompression of the Thor-Odin dome, Shuswap metamorphic core complex, Canadian Cordillera. *Lithos*, 61(3), pp.103–125.
- Patiño Douce, A.E and Beard, J.S., 1995. Dehydration-melting of biotite gneiss and quartz amphibolite from 3 to 15 kbar. *Journal of Petrology*, 36(3), pp.707–738.
- Pawley, M.J., Van Kranendonk, M.J. and Collins, W.J., 2004. Interplay between deformation and magmatism during doming of the Archaean Shaw granitoid complex, Pilbara Craton, Western Australia. *Precambrian Research*, 131(3), pp.213–230.
- Qian, Q. and Hermann, J., 2013. Partial melting of lower crust at 10–15 kbar: constraints on adakite and TTG formation. *Contributions to Mineralogy and Petrology*, 165(6), pp.1195–1224.
- Ramsay, J.G., 1989. Emplacement kinematics of a granite diapir: the Chindamora batholith, Zimbabwe. *Journal of Structural Geology*, 11(1–2), pp.191–209.
- Rey, P.F., Philippot, P. and Thébaud, N., 2003. Contribution of mantle plumes, crustal thickening and greenstone blanketing to the 2.75–2.65 Ga global crisis. *Precambrian Research*, 127(1), pp.43–60.
- Rey, P.F., Mondy, L., Duclaux, G., Teyssier, C., Whitney, D.L., Bocher, M. and Prigent, C., 2017. The origin of contractional structures in extensional gneiss domes. *Geology*, 45(3), pp.263–266.
- Roger, F., Teyssier, C., Respaut, J.P., Rey, P.F., Jolivet, M., Whitney, D.L., Paquette, J.L. and Brunel, M., 2015. Timing of formation and exhumation of the Montagne Noire double dome, French Massif Central. *Tectonophysics*, 640, pp.53–69.
- Rosenberg, C.L. and Handy, M.R., 2005. Experimental deformation of partially melted granite revisited: implications for the continental crust. *Journal of Metamorphic Geology*, 23(1), pp.19–28.
- Rushmer, T., 1991. Partial melting of two amphibolites: contrasting experimental results under fluid-absent conditions. *Contributions to Mineralogy and Petrology*, 107(1), pp.41–59.
- Sawyer, E.W., 2001. Melt segregation in the continental crust: distribution and movement of melt in anatectic rocks. *Journal of Meta-*

- morphic Geology, 19(3), pp.291–309.
- Sawyer, E.W., 2010. Migmatites formed by water-fluxed partial melting of a leucogranodiorite protolith: microstructures in the residual rocks and source of the fluid. *Lithos*, 116(3), pp.273–286.
- Schmidt, M.W., 1992. Amphibole composition in tonalite as a function of pressure: an experimental calibration of the Al-in-hornblende barometer. *Contributions to Mineralogy and Petrology*, 110(2–3), pp.304–310.
- Schumacher, J.C., 1991. Empirical ferric iron corrections: necessity, assumptions, and effects on selected geothermobarometers. *Mineralogical Magazine*, 55(378), pp.3–18.
- Schwindinger, M. and Weinberg, R.F., 2017. A felsic MASH zone of crustal magmas—Feedback between granite magma intrusion and in situ crustal anatexis. *Lithos*, 284, pp.109–121.
- Springer, W. and Seck, H.A., 1997. Partial fusion of basic granulites at 5 to 15 kbar: implications for the origin of TTG magmas. *Contributions to Mineralogy and Petrology*, 127(1), pp.30–45.
- Stephansson, O., 1975. Polydiapirism of granitic rocks in the Svecofennian of central Sweden. *Precambrian Research*, 2(2), pp.189–214.
- Teyssier, C. and Whitney, D.L., 2002. Gneiss domes and orogeny. *Geology*, 30(12), pp.1139–1142.
- Van der Molen, I. and Paterson, M.S., 1979. Experimental deformation of partially-melted granite. *Contributions to Mineralogy and Petrology*, 70(3), pp.299–318.
- Van Kranendonk, M.J., Collins, W.J., Hickman, A. and Pawley, M.J., 2004. Critical tests of vertical vs. horizontal tectonic models for the Archaean East Pilbara granite–greenstone terrane, Pilbara craton, Western Australia. *Precambrian Research*, 131(3), pp.173–211.
- Van Kranendonk, M.J., Ivanic, T.J., Wingate, M.T., Kirkland, C.L. and Wyche, S., 2013. Long-lived, autochthonous development of the Archaean Murchison Domain, and implications for Yilgarn Craton tectonics. *Precambrian Research*, 229, pp.49–92.
- Van Kranendonk, M.J., Smithies, R.H., Griffin, W.L., Huston, D.L., Hickman, A.H., Champion, D.C., Anhaeusser, C.R. and Pirajno, F., 2015. Making it thick: a volcanic plateau origin of Palaeoarchean continental lithosphere of the Pilbara and Kaapvaal cratons. *Geological Society, London, Special Publications*, 389(1), pp.83–111.
- Vanderhaeghe, O., 2009. Migmatites, granites and orogeny: Flow modes of partially-molten rocks and magmas associated with melt/solid segregation in orogenic belts. *Tectonophysics*, 477(3), pp.119–134.
- Vielzeuf, D. and Schmidt, M.W., 2001. Melting relations in hydrous systems revisited: application to metapelites, metagreywackes and metabasalts. *Contributions to Mineralogy and Petrology*, 141(3), p.251.
- Watkins, J.M., Clemens, J.D. and Treloar, P.J., 2007. Archaean TTGs as sources of younger granitic magmas: melting of sodic metatonalites at 0.6–1.2 GPa. *Contributions to Mineralogy and Petrology*, 154(1), pp.91–110.
- Weinberg, R.F., 1997. Diapir-driven crustal convection: decompression melting, renewal of the magma source and the origin of nested plutons. *Tectonophysics*, 271(3), pp.217–229.
- Weinberg, R.F. and Hasalová, P., 2015. Water-fluxed melting of the continental crust: a review. *Lithos*, 212, pp.158–188.
- White, R.W., Powell, R., Holland, T.J.B. and Worley, B.A., 2000. The effect of TiO₂ and Fe₂O₃ on metapelitic assemblages at

greenschist and amphibolite facies conditions: mineral equilibria calculations in the system $K_2O-FeO-MgO-Al_2O_3-SiO_2-H_2O-TiO_2-Fe_2O_3$. *Journal of Metamorphic Geology*, 18(5), pp.497–512.

- White, R.W., Powell, R. and Clarke, G.L., 2002. The interpretation of reaction textures in Fe-rich metapelitic granulites of the Musgrave Block, central Australia: constraints from mineral equilibria calculations in the system $K_2O-FeO-MgO-Al_2O_3-SiO_2-H_2O-TiO_2-Fe_2O_3$. *Journal of metamorphic Geology*, 20(1), pp.41–55.
- White, R.W. and Powell, R., 2010. Retrograde melt-residue interaction and the formation of near-anhydrous leucosomes in migmatites. *Journal of Metamorphic Geology*, 28, pp. 579–597.
- White, R.W., Powell, R., Holland, T.J.B., Johnson, T.E. and Green, E.C.R., 2014. New mineral activity–composition relations for thermodynamic calculations in metapelitic systems. *Journal of Metamorphic Geology*, 32(3), pp.261–286.
- White, R.W., Powell, R. and Johnson, T.E., 2014. The effect of Mn on mineral stability in metapelites revisited: new a–x relations for manganese-bearing minerals. *Journal of Metamorphic Geology*, 32(8), pp.809–828.
- Whitney, D.L. and Evans, B.W., 2010. Abbreviations for names of rock-forming minerals. *American Mineralogist*, 95(1), pp.185–187.
- Wiedenbeck, M. and Watkins, K.P., 1993. A time scale for granitoid emplacement in the Archean Murchison Province, Western Australia, by single zircon geochronology. *Precambrian Research*, 61(1–2), pp.1–26.
- Wyllie, P.J. and Wolf, M.B., 1993. Amphibolite dehydration-melting: sorting out the solidus. Geological Society, London, Special Publications, 76(1), pp.405–416.
- Yin, A., 2004. Gneiss domes and gneiss dome systems. Geological Society of America Special Papers, 380, pp.1–14.
- Zhang, C., Holtz, F., Koepke, J., Wolff, P.E., Ma, C. and Bédard, J.H., 2013. Constraints from experimental melting of amphibolite on the depth of formation of garnet-rich restites, and implications for models of Early Archean crustal growth. *Precambrian Research*, 231, pp.206–217.
- Zibra, I., Gessner, K., Smithies, H.R., Peternell, M., 2014a. On shearing, magmatism and regional deformation in Neoproterozoic granite-greenstone systems: insights from the Yilgarn Craton. *Journal of Structural Geology*, 67, pp.253–267.
- Zibra, I., Clos, F., Weinberg, R.F., Peternell, M., 2017. The c. 2730 Ma onset of the Neoproterozoic Yilgarn orogeny. *Tectonics*, 623, pp.100–122.
- Zibra, I., Peternell, M., Schiller, M., Wingate, M.T.D., Lu, Y., Clos, F., 2018. Tectono-magmatic evolution of the Neoproterozoic Yalgoo Dome (Yilgarn Craton). Diapirism in a pre-orogenic setting. Geological Survey of Western Australia, Report 176.

Supplementary material

Supplementary material 1: Representative analyses of biotite and plagioclase_sample 155879

Refer to electronic data file" Appendix 3.1.xls"

Supplementary material 2: Representative analyses of amphibole and plagioclase_sample214403c

Refer to electronic data file" Appendix 3.2.xls"

Supplementary material 3: Representative analyses of amphibole_sample209690

Refer to electronic data file" Appendix 3.3.xls"

Supplementary material 4: Major and trace elements chemistry of the Goonetarra Granodiorite and the Kynea Tonalite.

Refer to electronic data file" Appendix 3.4.xls"

CHAPTER 4

Building the Archean continental crust: 300 Myr of felsic magmatism in the Yalgoo dome (Yilgarn Craton)

Frediano Clos^a, Roberto F. Weinberg^a and Ivan Zibra^{a,b}

^a School of Earth, Atmosphere & Environment, Monash University, Clayton, 3800 VIC, Australia

^b Geological Survey of Western Australia, Perth, WA 6004, Australia



Abstract

The evolution of granitic magmatism in the Yalgoo dome of the Yilgarn Craton offers a singular perspective on processes needed to build a felsic continental crust as the dome exposes all five granitoid groups that typify late Archean terranes. These five groups can be correlated with three major phases of juvenile magmatism and greenstone formation, culminating in four stages of granitic activity. The first phase includes 2970–2900 Ma old rocks of the tonalite-trondhjemite-granodiorite series (TTG) and coeval greenstones (Stage 1). Following a lapse of c. 100 Myr, the outset of the second phase was marked by the eruption of the voluminous greenstones of the Norie and Polelle Group at 2825–2760 Ma. Thermal incubation of the crust caused a complete reheating and softening of the crust and its underlying metasomatized mantle, resulting in a short crustal reworking episode (< 20 Ma) recorded by the diapiric intrusion of 2760–2740 Ma transitional TTGs and high-Mg granitic rocks (Stage 2). The third phase of crustal reworking is associated with the onset of the orogeny in the Murchison Domain and resulted in the intrusion of a swarm of transitional TTG dykes at c. 2707 Ma during regional EW shortening (Stage 3). This phase was then followed by the post-orogenic and post-volcanic A-type and the voluminous low-Ca granites (Stage 4). The secular change in major and trace element chemistry of granitic rocks records a 300 Myr period of crustal evolution (from TTGs to low-Ca granites) and reflects the progressive modification of the melting source, from basaltic to granitic, and from deep to shallow. The evolution of the Yalgoo dome culminated by ~2600 Ma and reflects the process of stabilization of continental crust through intermittent episodes of enhanced mantle activity and extensive crustal reworking.

Keywords: Archean, continents, crustal evolution, Yilgarn Craton, Yalgoo Dome, granites

1 Introduction

The Archean geological record represents one third of Earth's history, during which ~70% of the present-day volume of continental crust formed (Taylor and McLennan, 1995; Dhuime et al., 2011; Guitreau, 2012). Despite post-Archean reworking of most of the Archean terranes, 35 large crustal blocks and minor slivers preserve information on crustal processes on early Earth (Bleeker, 2003). The crust evolved from a more mafic bulk composition before 3000 Ma, to an intermediate bulk composition by 2500 Ma (Dhuime et al., 2012; 2015; Keller and Schoene, 2012; Tang et al., 2016). This time interval corresponds with the global transition from a dominant TTG to a more K-rich magmatism (Moyen, 2011; Laurent et al., 2014) and was associated with a five-fold increase in the mass of the upper continental crust due to addition of granitic rocks (Tang et al., 2016). Bulk rock chemistry (Laurent et al., 2014; Moyen, 2011) together with Hf isotope studies (Amelin et al., 2000; Griffin et al., 2004; Davis et al., 2005; Zhang et al., 2006; Ivanic et al., 2012) and U-Pb geochronology on granitic rocks document this transition and arguably demonstrate that Archean continental crust has evolved through phases of mafic-ultramafic juvenile magmatism (i.e. greenstones) followed by episodes of crustal reworking (Campbell and Hill, 1988).

The Yalgoo dome offers a unique view on the fundamental processes necessary to generate felsic continental crust because all five granitoid groups that typify late Archean terranes outcrop in the dome and in its most immediate surroundings. Our new data collection of bulk rock chemistry identify five granitic groups, ranging (with decreasing age) from (1) TTGs (2) to transitional TTGs and (3) high-Mg granitic rocks, post-dated by (4) A-type and (5) low-Ca granites. These granitic rocks are normally distributed throughout cratons and are rarely found in the same crustal section. Thus, the Yalgoo dome records the magmatic evolution of the same lithospheric column through a time span of more than 300 Myr, which enables identification of the main processes needed to build felsic continental crust by the end of the Archean Eon.

In this contribution, we investigate the geochemical evolution recorded in these five groups to propose a four stage tectono-magmatic evolution model linking their petrogenesis with three main pulses of mafic-ultramafic juvenile mantle inputs that may account for the diversity of late Archean

granitic rocks in the Yalgoo dome. Over 300 Ma of felsic magmatism in the Yalgoo dome reflects, within a single domal structure, the crustal processes that are crucial to build Archean crust.

2 Geological setting

The Murchison Domain is part of the Youanmi Terrane in the Archean Yilgarn Craton (Cassidy et al., 2006; Fig. 1) and includes 2960–2720 Ma greenstone successions intruded by 2970–2600 Ma granitic rocks (Van Kranendonk et al., 2013). Most of the terrane is dissected by a craton-scale network of transpressive shear zones and syn-tectonic plutons that accommodate regional EW shortening (Zibra et al., 2014a). The three main syntectonic plutons are the 2730–2710 Ma Yarraquin pluton (Zibra et al., 2017), the 2710–2695 Ma Lakeside pluton (Zibra et al., 2014a) and the 2680–2660 Ma Cundimurra pluton (Zibra et al., 2014b). Together, they show a nearly continuous 70 Ma of magmatic activity, during which a north-trending magmatic to high temperature solid state fabric developed during crystallisation. Elongated granite-greenstone patterns are truncated by a series of undeformed, post-tectonic, subcircular granites emplaced between 2640–2600 Ma and known as the Bald Rock Supersuite (Ivanic et al., 2012; Van Kranendonk et al., 2013).

Significantly, the shear zones that dominate the main regional grain in the east section of the Murchison Domain are absent in the westernmost part of the domain, where the Yalgoo dome is exposed. Unlike the elongated plutons in the east, this dome is a prominent 100 km long and 50 km wide elliptical granite dome enveloped by greenstone belts, comparable to the broad domes of the Paleoproterozoic East Pilbara Craton (e.g. Collins, 1989). Greenstone belts wrapping around the Yalgoo dome include the 2963–2958 Ma Gossan Hill Formation comprising felsic volcanic and volcanoclastic rocks, unconformably overlain by mafic volcanic rocks, felsic volcanoclastic sandstones and banded iron formation of the 2825–2805 Ma Norie Group (Van Kranendonk et al., 2013). On top of the Norie Group lies the voluminous 2800–2760 Ma Polelle Group, a continuous volcanic succession evolving from komatiitic basalts to tholeiitic basalts and minor andesites up to 8 km thick (Ivanic et al., 2015). These rocks are unconformably overlain by the Mougooderra Formation, a siliciclastic succession containing felsic volcanics dated at 2758±4 Ma (GSWA ID 211101) and present only in the Yalgoo dome area (Ivanic et al., 2015). The dome itself is composed of several granitic

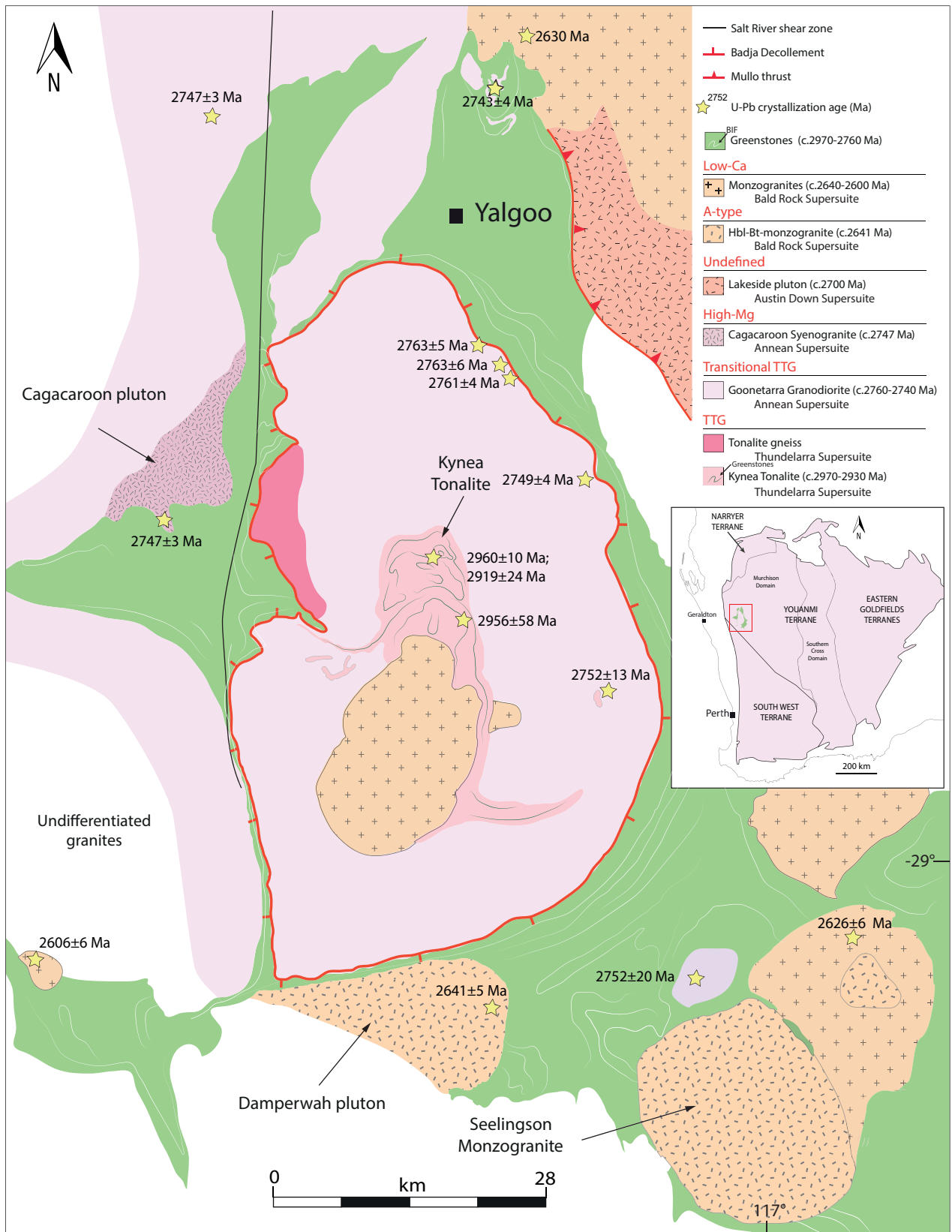


Figure 1: Geological map of the Yalgoo dome and greenstone envelope. Inset in the upper right shows location of the studied area in the Murchison Domain, Yilgarn Craton. The batholith comprises multiple generations of granites intruded over a time span >300 Myr. Yellow star indicates U-Pb zircon crystallization ages Geological Survey of Western Australia (Zibra et al., 2018).

intrusions (2760–2600 Ma) that are progressively younger and compositionally more evolved toward the center of the dome (Goonetarra Granodiorite in Fig. 1; Zibra et al., 2018). Breaking this

general younging trend, the oldest rocks outcrop in the core of the dome forming a well exposed region, $\sim 8 \times 12$ km in dimension (Fig. 1). This unit comprises 2970-2900 Ma migmatitic tonalite (Kynea Tonalite) interlayered with remnants of amphibolite and banded iron formation (Myers and Watkins, 1985), intruded by a north-trending, subvertical swarm of granitic dykes dated at c. 2707 Ma (Zibra et al., 2018).

3 Late Archean granitic rocks

Archean terranes are dominated by voluminous TTGs ($\sim 50\%$), greenstones ($\sim 30\%$) and K-rich granite ($< 20\%$; Condie, 1993). While K-rich granitic rocks are a minor constituent of Paleo- to Mesoproterozoic terranes, they become more widespread toward the end of the Archean Eon, representing the last magmatic episode in every Archean craton (Condie, 1993). The classification scheme proposed in this work is based on the original granitic groups identified in the Yilgarn Craton by Champion and Sheraton (1997), but with a revised nomenclature. Following Champion and Smithies (2001), we subdivided the High-Ca group of Champion and Sheraton (1997) into a TTG ($K_2O/Na_2O < 0.6$) and a transitional TTG group ($K_2O/Na_2O > 0.6$ and high LILE, U, Th content), both distinguished by a strong HREE depletion. The mafic and the high-HFSE groups of Champion and Sheraton (1997) are renamed “high-Mg” and “A-type”, respectively. In the following section is presented a brief literature review of Archean TTGs and K-rich granitoids (transitional TTGs, high-Mg,

Yilgarn Craton	Murchison Domain	Other terranes	This work
High-Ca	-	TTG	TTG
High-Ca	Cullculli, Big Bell	Medium-K, Hybrid	Transitional TTG
Mafic	Cullculli	Sanukitoid high-Mg diorites	high-Mg
High-HFSE	Eelya	A-type	A-type
Low-Ca	Walganna and Wogala	High-K, Potassic, Biotite/2 micas granite	Low-Ca

Table 1: Nomenclature comparison between Yilgarn Craton (Champion and Sheraton, 1997), Murchison Domain (Ivanic et al., 2012), other Archean terranes (Heilimo et al., 2010; Moyen, 2011; Farina et al., 2015; Laurent et al., 2014) and the nomenclature used in this work.

A-type and low-Ca).

3.1 TTG

The term TTG as used here refers to high-Al TTG classification of Barker and Arth (1976). In all preserved Archean cratons, these represent the first preserved evidence of felsic continental crust (Champion and Smithies, 2007; Laurent et al., 2014). These rocks show internal variations, but invariably comprise Al- and Na-rich granitic rocks with marked HREE, Nb-Ta-Ti depletions and variable Sr enrichments (Barker and Arth, 1976). After more than 40 years of research (see review of Moyen and Martin, 2012), there is a consensus that the diagnostic trace element geochemistry of TTGs is produced by partial melting of a hydrous mafic parent with variable proportions of garnet, amphibole, plagioclase and rutile left behind in the restite (Martin, 1987).

3.2 Transitional TTG

This term was introduced by Champion and Smithies (2001) to describe a group of granites identified in the Yilgarn and Pilbara Cratons and characterized by broadly TTG-like compositions, but marked by further LILE, Th and U enrichment. These rocks are found in many other Archean terranes worldwide, including the Yilgarn Craton (Champion and Sheraton, 1997), Tanzania Craton (Opiyo-Akech et al., 1999), western Dharwar Craton (Prabhakar et al., 2009), Pilbara Craton (Champion and Smithies, 2007), Karelian Province (Mikkola et al., 2011), Amazonian Craton (Almeida et al., 2010), Kaapvaal Craton (Laurent et al., 2014) and São Francisco Craton (Farina et al., 2015), and commonly post-date the main TTG phase except in the Wyoming Province where they are apparently coeval with TTG (Frost et al., 2006). In most provinces, transitional TTGs make up 10–15% of the granitic rocks, but in the Yilgarn Craton (Champion and Sheraton, 1997) and the Wyoming Province they make up >60% of the total. Transitional TTGs might be compared to hybrid granites (Laurent et al., 2014), high-Ca granites (Champion and Sheraton, 1997), medium-K granites (Farina et al., 2015), TTG *sensu lato* (Mikkola et al., 2011) and high Ba-Sr granites (Peng et al., 2013), but rocks from these terranes should be compared with care as they might have geodynamic significance.

3.3 High-Mg granitic rocks

This group is defined by an enigmatic geochemical signature with high contents of compatible elements (MgO, Ni, Cr and V) and a noticeable enrichment in LILEs (Defant and Drummond, 1990; Rapp et al., 1999; Smithies and Champion, 2000). In late Archean terranes, granitic rocks with similar composition were collectively grouped as high-Mg diorites (Smithies and Champion, 2000) or Archean sanukitoids (Shirey and Hanson, 1984; Smithies and Champion, 2000; Heilimo et al., 2010; Laurent et al., 2014) based on geochemical similarities with Miocene high-Mg andesites from the Setouchi volcanic belt in Japan (sanukites of Tatsumi and Ishizaka, 1981).

3.4 A-type granites

A-type granites are felsic rocks rich in FeO_T , K_2O , P_2O_5 , TiO_2 and HFSE with moderately fractionated REE patterns and marked negative Eu-Sr anomalies (Whalen et al., 1987; Frost and Frost, 2011). Compositionally similar granites are considered to be post-collisional in most Proterozoic (Duchesne et al., 2010) and Neoproterozoic terranes, including the Yilgarn Craton where they are known as high-HFSE granitic rocks (Champion and Sheraton, 1997).

3.5 Low-Ca granites

The granites of the low-Ca group form post-tectonic intrusions (biotite-bearing monzogranites and syenogranites) that truncate older granite and greenstones (Champion and Sheraton, 1997) between 2640 and 2600 Ma (Van Kranendonk et al., 2013). These intrusions are defined by high $\text{K}_2\text{O}/\text{Na}_2\text{O}$ ratio, low Al_2O_3 and Sr content along with moderately fractionated REE patterns, with large negative Eu anomalies (Champion and Sheraton, 1997; Laurent et al., 2014). In other cratons they are referred as high-K granites (Whalen, 2004; Almeida et al., 2010; Farina et al., 2015) or biotite-two mica granites (Laurent et al., 2014).

4 Granitic groups in the Yalgoo dome

In this section we describe the geology, petrography and geochemistry of the five granitic rock groups cropping out within the Yalgoo dome and two plutons in the immediate surrounding area

(Fig. 2). This study is based on 149 whole rock analysis: 92 analyses are from the Geological Survey of Western Australia (GSWA) database and 57 from Geoscience Australia (GA). All analyses can be found in Appendix 4.1 and the average compositions of each granite group is presented in Table 2. All ages reported here reflect the age of the protolith and were obtained by U-Pb SHRIMP on zircons according to the GSWA standard. The geochronology data for each individual data can

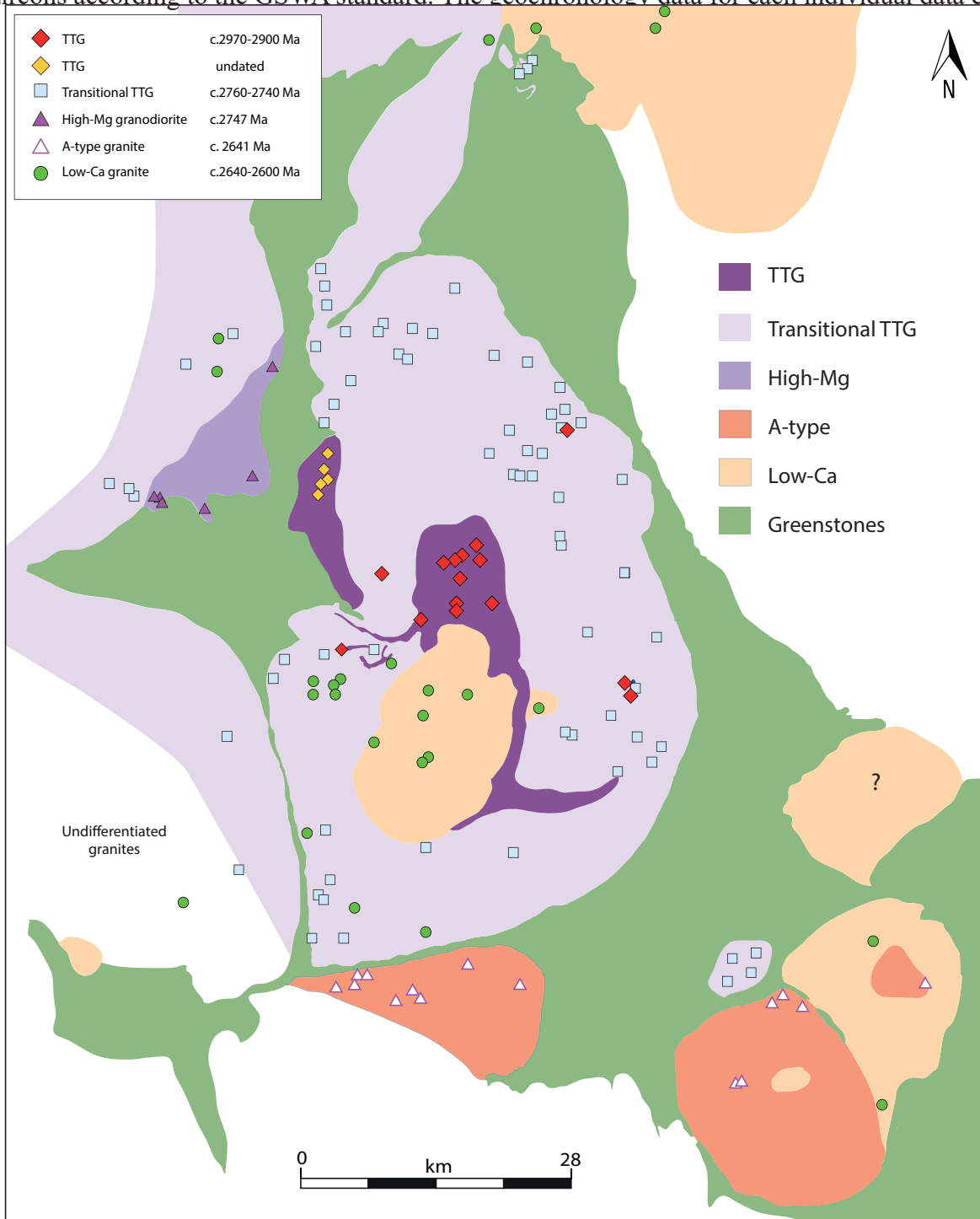


Figure 2: Yalgoo dome map showing the location of the individual bulk rock analyses (Appendix 4.1) and the distribution of the five granitic groups.

be found in the compilation of geochronology information of the GSWA (Geological Survey of Western Australia, 2016).

4.1 TTG

4.1.1 Field relationships, age and petrography

TTGs belong to the Thundelarra Supersuite (Zibra et al., 2018) and are found in two distinct structural domains: in the migmatitic core of the Yalgoo dome and along the NW flank of the dome (Fig. 3). The rocks in the core include migmatitic tonalites, intruded into an older metamorphosed greenstone succession comprising amphibolite and banded iron formation that now form remnants inside the complex (Myers and Watkins, 1985; Fenwick, 2014). Wiedenbeck and Watkins (1993) report U-Pb ages of 2912 ± 12 Ma from zircon cores (sample GSWA ID 833339) and 2700–2800 Ma from rims, interpreted as the crystallisation age of the protolith and an overgrowth linked to migmatization, respectively (Fig. 3a). More recent investigations of rocks of the Yalgoo dome further constrain the age range of the protolith to 2960 ± 10 Ma (GSWA ID 209689) and 2956 ± 58 Ma (GSWA ID 155879) (Zibra et al., 2018).

The TTGs in the core of the dome are a biotite-rich, grey tonalite gneiss with a pervasive solid-state foliation delineated by preferential alignment of biotite. These gneisses have a well-developed migmatitic layering (Fig. 3a) and the fraction of leucocratic material is variable, resulting in heterogeneous appearance. Layering is defined by alternations of melanosome, mesosome and melanosome. The mesosome comprises abundant plagioclase, quartz and interstitial K-feldspar and accessory titanite, epidote. Biotite is the dominant ferromagnesian mineral and is commonly partially replaced by chlorite. Leucosomes exhibit the same mineralogy, but with a net decrease in biotite and an increase in K-feldspar content.

The TTGs on the NW side of the dome comprise an undated tonalite gneiss (Fig. 1), consisting of plagioclase, quartz, K-feldspar and biotite with accessory titanite and epidote. Primary magmatic fabrics are partially overprinted by a solid state foliation, which varies in intensity, yet increases toward the greenstone contact in the west.

4.1.2 Geochemistry

TTGs in the Yalgoo dome are typical calc-alkalic to calcic, mildly peraluminous ($1 < A/CNK < 1.1$; Figs 4b–c) and sodic granitic rocks with $K_2O/Na_2O < 0.6$ (Fig. 5; Moyen and Martin, 2012; Laurent et al., 2014). High silica ($SiO_2 > 69.0$ wt%) and Al_2O_3 (14.3–16.3 wt%) contents are associated with low ferro-magnesian oxides (Table 2) and variable CaO (1.5 to 4.0 wt%) (Fig. 5). REE are strongly fractionated with a characteristic depletion in HREE on normalised trace element diagrams (Fig. 6) and $La/Yb > 50$ for most of the samples (Fig. 4f). The undated TTGs on the NW margin of the dome show LILE contents comparable to average Archean TTGs (Moyen, 2011; Moyen and Martin, 2012) with Sr = 236–439 ppm, Ba = 234–845 ppm, Rb = 54.9–92.3 ppm and low K_2O content (1.19–2.07 wt%) (Fig. 5). In contrast, the 2950 Ma TTGs in the core of the dome (Fig. 1), are characterized by a heterogeneous LILE enrichment, with higher K_2O (1.57–3.77 wt%), Ba (465–2242 ppm), Sr (290–1201 ppm) and Rb (71–321 ppm).

4.2 Transitional TTG

4.2.1 Field relationships, age and petrography

Transitional TTGs comprise large intrusions of granodiorite and monzogranite, belonging to the Goonetarra Granodiorite (Annean Supersuite; Van Kranendonk et al., 2013). Transitional TTGs cover most of the dome (Fig. 1), with multiple intrusions of porphyritic to equigranular granitic rocks containing centimetre- to metre-sized xenoliths of 2970–2900 Ma migmatitic tonalites (Fig. 3c). The oldest intrusions outcrop along the NE margin and are dated at 2760 Ma (2763 ± 5 Ma, GSWA ID 214138; 2761 ± 4 Ma, GSWA ID 214139; 2763 ± 6 Ma, GSWA ID 214101; Zibra et al., 2018). In other parts of the dome, these granitic rocks are possibly younger and vary in age down to 2740 Ma (2752 ± 13 Ma, GA ID 155858; 2752 ± 20 Ma, GSWA ID 999564016c; 2749 ± 4 Ma, GA ID 155822; 2743 ± 4 Ma, GA ID 999564100; 2747 ± 3 Ma, GA ID 999569164a) suggesting that most of the dome developed in ~20 Ma between 2760 and 2740 Ma.

Distant from the margins, these granitic rocks show a magmatic fabric marked by the preferred orientation of plagioclase and K-feldspar phenocrysts in a matrix of quartz and biotite with minor

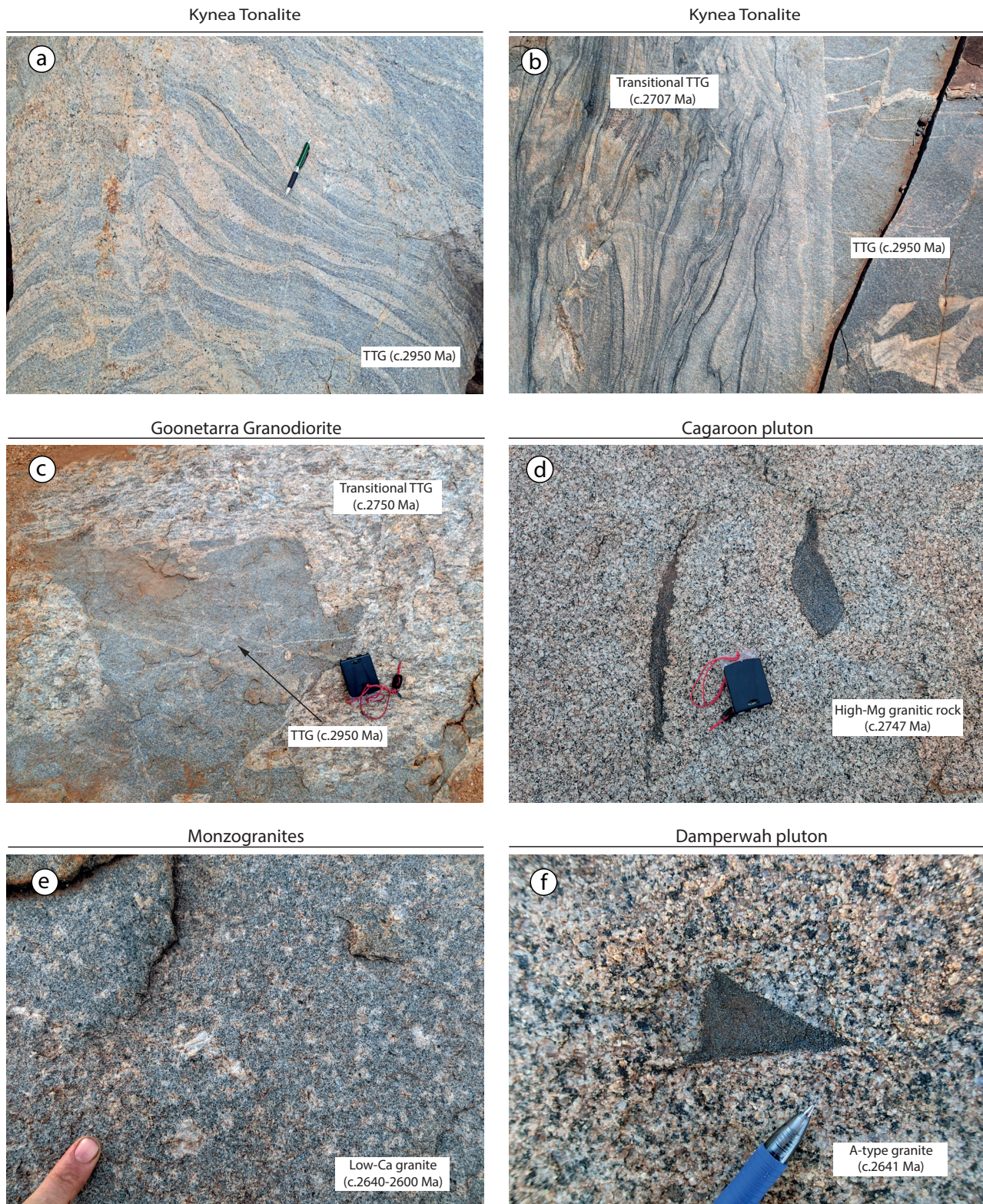


Figure 3: Field photographs of representative examples of the diverse late Archean granitic rocks from the Yalgoo dome: (a) 2970–2900 Ma tonalites (Kynea Tonalite) shows migmatitic structures; (b) polyphase 2970–2900 Ma migmatitic tonalite (right side) is cut by c. 2707 Ma biotite-rich schlieren granitic dykes (left side) with transitional TTG composition. Long side is 85 cm; (c) K-feldspar porphyritic Goonetarra Granodiorite (2760–2740 Ma) with transitional TTG composition containing angular xenolith of 2970–2900 Ma migmatitic tonalite; (d) Coarse-grained hornblende-bearing granite (Cagacaron Syenogranite) is a high-Mg intrusion containing phenocrysts of K-feldspar and mafic enclaves rich in pyroxene and hornblende; (e) low-Ca coarse-grained monzogranite with preferred orientation of large K-feldspar porphyroclasts; (f) The Damperwah pluton is an A-type granite characterized by mesocratic, equigranular magmatic textures with angular enclaves of banded iron formation such as the one shown. Mafic phase is composed by intergrowth of Fe-rich hornblende and biotite.

epidote, titanite and magnetite. At the granite–greenstones boundaries, magmatic textures are overprinted by a high-grade solid state foliation with steeply plunging mineral lineations and dome-up, greenstone-down sense of motion (Foley, 1997; Zibra et al., 2018). This foliation is concordant with the elliptical shape of the dome and the contact with the greenstones.

Younger transitional TTGs form a dyke swarm that intrudes the Kynea Tonalite in the core of the dome at 2700 Ma (2700±7 Ma, GSWA ID 214315; 2706±5 Ma, GSWA ID 214324; Zibra et al., 2018) and are temporally and compositionally similar to the Big Bell Suite (Ivanic et al., 2012). Most of these dykes have a granitic composition and an equigranular magmatic texture with plagioclase, K-feldspar quartz and biotite, and accessory titanite, magnetite, apatite and epidote.

4.2.2 Geochemistry

Transitional TTGs (c. 2760–2740 Ma) are calc-alkalic (Fig. 4b) and mildly peraluminous ($1 < A/CNK < 1.1$; Fig. 4c) granitic rocks with a narrow silica range (70.0–76.0 wt% SiO₂) and large LILE variations (Fig. 5; Table 2). They are more K-rich than TTGs (Fig. 4a) and silica correlates negatively with major oxides except K₂O, which increases from 3.0 wt% (at 70.0 wt% SiO₂) up to 5.0 wt% (at 75.0 wt% SiO₂; Fig. 5). Normalised trace elements patterns are like those of the TTGs, marked by depletion in HREE (Fig. 6), a negative to positive Eu anomaly (Eu*/Eu = 0.5–2; Fig. 4d) and a range of La/Yb ratios (17–213; Fig. 4f). At any silica content, LILE, Th and U content is significantly higher in transitional TTGs than in TTGs (Fig. 5).

The c. 2707 Ma transitional TTGs in dykes are chemically similar to their older counterparts except for a slightly larger range in K₂O (2.4–6.6 wt%), Al₂O₃ (13.7–16.8 wt%) and Ba (1376–4303 ppm), accompanied by an exclusively positive Eu anomaly (Eu*/Eu > 1.5; Fig. 4d).

4.3 High-Mg group: Cagacaroon pluton

4.3.1 Field relationships, age and petrography

This group of high-Mg magmatic rocks forms an intrusion known as the Cagacaroon Syenogranite (Fig. 1), comprising a mesocratic K-feldspar porphyritic granite with amphibole as the major mafic

Table 2

Major and trace element average and standard deviation for major granitic suites in the Valgeoo Dome (S.D. = Standard deviation).

Name	S.D.	Goonetarra Granodiorite	S.D.	Dykes	S.D.	Carcarron Syenogranite	S.D.	Damperwah and Seelingsoon	S.D.	Post-tectonic granites	S.D.	
Suite	TTG	Transitional TTG	Transitional TTG	High-Mg	A-type	Low-Ca	Low-Ca	Low-Ca	Low-Ca	Low-Ca	Low-Ca	
Age (Ma)	2970-2900	2760-2740	2707-2700	2747	2641	2640-2600	2640-2600	2640-2600	2640-2600	2640-2600	2640-2600	
SiO ₂	71.93	1.33	72.20	1.48	72.56	2.05	63.28	2.42	70.89	1.25	73.48	1.84
TiO ₂	0.23	0.09	0.20	0.07	0.12	0.03	0.66	0.13	0.48	0.14	0.20	0.11
Al ₂ O ₃	15.13	0.52	14.81	0.57	15.31	1.13	14.35	0.79	13.27	0.36	13.58	0.53
FeO ^T	1.87	0.43	1.59	0.51	1.11	0.26	4.91	0.86	3.79	0.78	1.61	0.64
MgO	0.51	0.20	0.40	0.15	0.17	0.02	2.91	0.28	0.37	0.07	0.28	0.16
CaO	2.06	0.33	1.72	0.41	1.60	0.37	3.70	0.68	2.26	0.60	1.07	0.37
Na ₂ O	4.81	0.42	4.29	0.40	4.44	0.41	3.51	0.11	3.10	0.19	3.42	0.36
K ₂ O	2.57	0.67	3.64	0.65	4.10	1.46	4.45	0.58	4.06	0.36	4.91	0.54
P ₂ O ₅	0.08	0.03	0.07	0.03	0.04	0.01	0.40	0.07	0.14	0.06	0.07	0.05
MnO	0.03	0.02	0.05	0.03	0.01	0.00	0.11	0.04	0.09	0.04	0.06	0.04
LOI	0.38	0.14	0.71	0.46	0.31	0.05	0.81	0.40	0.85	0.68	0.99	0.77
Total	99.61		99.68		99.76		99.09		99.24		99.63	
Ba	1133.28	488.16	1557.52	563.77	2244.43	1150.68	2353.87	283.36	1604.22	264.20	717.37	313.33
Ce	63.27	36.63	64.16	25.33	51.23	19.67	119.20	17.19	233.28	144.48	117.20	62.24
Cr	76.57	73.20	11.79	34.17	102.00	23.45	102.67	54.81	62.70	86.57	12.56	46.55
Cs	8.43	12.87	3.29	2.76	3.57	3.01	7.08	5.24	3.60	1.35	5.77	3.12
Dy	0.87	0.43	0.91	0.39	0.59	0.11	3.48	0.59	9.27	1.44	4.39	2.25
Er	0.39	0.17	0.43	0.22	0.30	0.08	1.61	0.19	5.24	1.10	2.54	1.33
Fu	0.64	0.26	0.65	0.18	0.50	0.11	1.95	0.29	2.77	0.54	0.55	0.25
Ga	20.70	2.04	18.70	2.13	18.08	1.15	17.76	1.17	19.10	2.03	18.61	1.21
Gd	1.53	0.84	1.66	0.58	0.97	0.16	5.72	0.92	10.93	1.37	1.37	5.05
Ge	0.63	0.11	0.82	0.18	0.53	0.05	1.16	0.27	1.46	0.16	1.24	0.15
Hf	3.87	0.85	3.62	0.79	3.22	0.80	5.51	1.03	12.10	1.11	5.42	1.86
Ho	0.16	0.08	0.17	0.09	0.10	0.03	0.58	0.08	1.84	0.33	0.87	0.47
In	0.02	0.01	0.01	0.00	0.01	0.00	0.03	0.00	0.09	0.01	0.03	0.01
La	41.63	26.09	38.65	15.31	24.77	6.12	71.57	11.98	118.40	69.50	62.03	32.31
Li	65.19	61.45	21.39	13.92	11.50	6.31	20.53	10.99	27.99	11.89	35.89	18.35
Lu	0.07	0.03	0.08	0.05	0.03	0.01	0.23	0.04	0.72	0.21	0.36	0.16
Mo	1.28	2.32	0.28	2.62	1.10	0.83	1.67	1.17	1.75	1.44	2.92	0.54
Nb	4.66	2.27	4.73	2.62	1.92	0.53	8.38	1.59	19.78	2.92	17.44	7.80
Nd	21.07	13.91	19.54	7.48	12.30	2.13	47.28	11.01	72.04	17.21	37.06	19.57
Ni	7.73	8.60	4.55	1.66	2.92	1.20	59.43	31.10	7.49	8.52	3.81	2.07
Pb	25.79	7.94	39.03	14.14	38.30	9.54	44.15	9.34	39.43	8.08	56.54	17.37
Pr	6.62	4.63	6.14	2.37	3.97	0.87	13.32	2.94	19.16	5.68	11.47	6.12
Rb	111.54	64.97	136.67	45.19	107.95	38.59	203.30	40.91	152.71	37.51	328.25	70.54
Sm	2.75	1.59	2.64	0.93	1.67	0.26	7.27	1.20	12.55	1.64	6.14	2.92
Sr	523.02	224.99	411.61	192.98	405.33	55.89	609.92	83.46	188.79	34.00	91.95	36.77
Ta	0.54	0.38	0.60	0.37	0.24	0.05	0.87	0.15	1.37	0.38	1.98	0.94
Th	11.29	4.25	16.48	8.59	10.27	1.29	25.57	7.09	36.12	37.32	37.93	13.45
Tm	0.08	0.04	0.09	0.04	0.09	0.01	0.25	0.06	0.85	0.14	0.44	0.19
U	2.16	1.22	3.70	3.26	1.34	0.66	4.78	0.78	3.91	1.58	19.20	21.79
V	24.21	7.91	18.08	7.89	17.50	9.19	90.67	19.02	12.70	4.79	10.05	12.22
Y	4.86	2.77	5.45	4.22	3.32	0.92	17.57	2.83	53.25	10.42	30.04	19.12
Yb	0.32	0.17	0.39	0.22	0.27	0.08	1.41	0.18	4.77	1.16	2.42	1.21
Zr	147.73	39.12	128.00	34.75	121.50	28.76	177.17	37.41	406.93	86.25	179.13	97.76

phase (Fig. 3d). The pluton is a wedge-shaped intrusion, $\sim 125 \text{ km}^2$ in size, and dated at $2747 \pm 3 \text{ Ma}$. It belongs to the Annean Supersuite of Van Kranendonk et al. (2013) (GA geochron ID 99969142), and is broadly contemporaneous with the transitional TTGs of the adjacent Yalgoo dome. It contains ubiquitous, elongated microgranular mafic enclaves rich in amphibole (Fig. 3d) and its field appearance is similar to plutons of the Cullculli Suite described by Ivanic et al. (2012). Primary magmatic textures are overprinted by a solid-state foliation, parallel to the contact with the greenstones. Large, euhedral K-feldspar and rare plagioclase porphyroclasts are deformed and surrounded by oriented mineral aggregates of large hornblende and smaller biotite, epidote, titanite and magnetite. Occasionally, large amphibole grains preserve relict cores of recrystallized clinopyroxenes.

4.3.2 Geochemistry

Rocks of the Cagacaroon pluton differ from other groups because of their magnesian (Fig. 4a), calc-alkalic to alkali-calcic (Fig. 4b) and metaluminous nature (Fig. 4c). The granodiorite displays high Mg# (46-60) and MgO (2.2–4.2 wt%), K_2O (3.7–5.4 wt%) and CaO (3.2–5.0 wt%) contents at low silica content (58.9–66.4 wt%) (Fig. 5). The most distinctive geochemical feature of these rocks are trace element signatures comparable to those of Archean sanukitoids (Martin et al., 2005, 2009; Heilimo et al., 2010; Laurent et al., 2014) and the geochemistry of the Cullculli Suite of the northern Murchison Domain (Ivanic et al., 2012), including strong LILE enrichments with Ba >2000 ppm, Sr=565–768 ppm and Rb=176–269 ppm (Fig. 5; Table 2) accompanied by moderate enrichment in mantle compatible elements, such as Cr (42–176 ppm), Ni (33–120 ppm) and V (67–127 ppm) (Appendix 4.1; Table 2). REE patterns are fractionated with La/Yb ~ 50 (Fig. 4f) and moderate depletion in HREE (Fig. 6) ('spoon-shaped patterns' are comparable to Cullculli Suite rocks in the northern Murchison Domain, Fig. 4b, Ivanic et al., 2012). HFSE contents are similar to TTGs and transitional TTGs, with low Zr (142–244 ppm) and Nb (6–11 ppm) concentrations, but La (62–93 ppm) and TiO_2 concentrations (0.5–0.9 wt%) are higher (Table 2).

4.4 A-type group: Damperwah and Seelingson monzogranite

4.4.1 Field relationships, age and petrography

The Damperwah pluton and part of the Seelingson pluton (Fig. 1) comprise a hornblende-bio-

tite-bearing monzogranite which intruded an area of more than 220 km² and 270 km², respectively, south of the Yalgoo dome. The Damperwah pluton has been dated at 2641±5 Ma (GSWA ID 83407). Like the slightly younger low-Ca granites (described below), they shows sub-circular, discordant outcrop patterns which cut stratigraphic units and tectonic features associated with folding in the greenstones. Igneous textures lacking solid-state overprint suggest that intrusion post-dated the peak of regional deformation and genesis of the Yalgoo dome. This monzogranite pluton is rich in hornblende- or pyroxene-diorite and banded iron formation enclaves (Fig. 3f), ranging in size from a few cm up to several metres. Mineral paragenesis is defined by aggregates of Fe-rich hornblende, biotite, quartz and ilmenite surrounded by plagioclase, quartz and rare K-feldspar porphyroclasts. Minor amounts of fayalitic olivine, clinopyroxene, apatite and zircon are common, but do not occur in all samples (Wiedenbeck and Watkins, 1993).

4.4.2 Geochemistry

This pluton is a felsic (SiO₂=68.9–72.3 wt%), calc-alkalic, ferroan and metaluminous to peraluminous monzogranite (Figs 4a-c), comparable to worldwide A-type granitic rocks (Eby, 1992; Frost and Frost, 2011). Like the low-Ca granites, it shows low Al₂O₃ (12–9–13.8 wt%) and Na₂O (2.9–3.2 wt%), but K₂O (3.8–4.6 wt%) and CaO (1.3–2.8 wt%) contents are similar to those of Transitional TTGs (Fig. 4), resulting in K₂O/Na₂O>1 (Fig. 4c). For a given silica content, it is significantly enriched in HFSE with the highest Zr (265–521 ppm), Hf (12–13 ppm), Y (36–68 ppm) and TiO₂ (0.3–0.6 wt%) concentration amongst all granite groups studied here. HREE contents are very high (Fig. 6) and define a seagull-like REE pattern with La/Yb~10 (Fig. 4f) and a moderate negative Eu anomaly (Eu*/Eu ~0.8–1.0; Fig. 4d). The relative behavior of the LILE differs from that in the other granite types in that Ba, Rb and Pb are enriched, as in the other granite groups, but Sr is strongly depleted and shows values comparable only to those of the low-Ca granites (Fig. 5; Table 2). Many of the chemical features of the Damperwah and Seelingson pluton are also shared with the contemporaneous low-Ca group. The Damperwah A-type pluton is more enriched in CaO and depleted in K₂O than the low-Ca group, but share a similar Sr-Al₂O₃ depletion (Fig. 4) and high HREEs content (Fig. 6), which indicate generation at medium crustal pressures <10 kbar, outside the stability field of garnet.

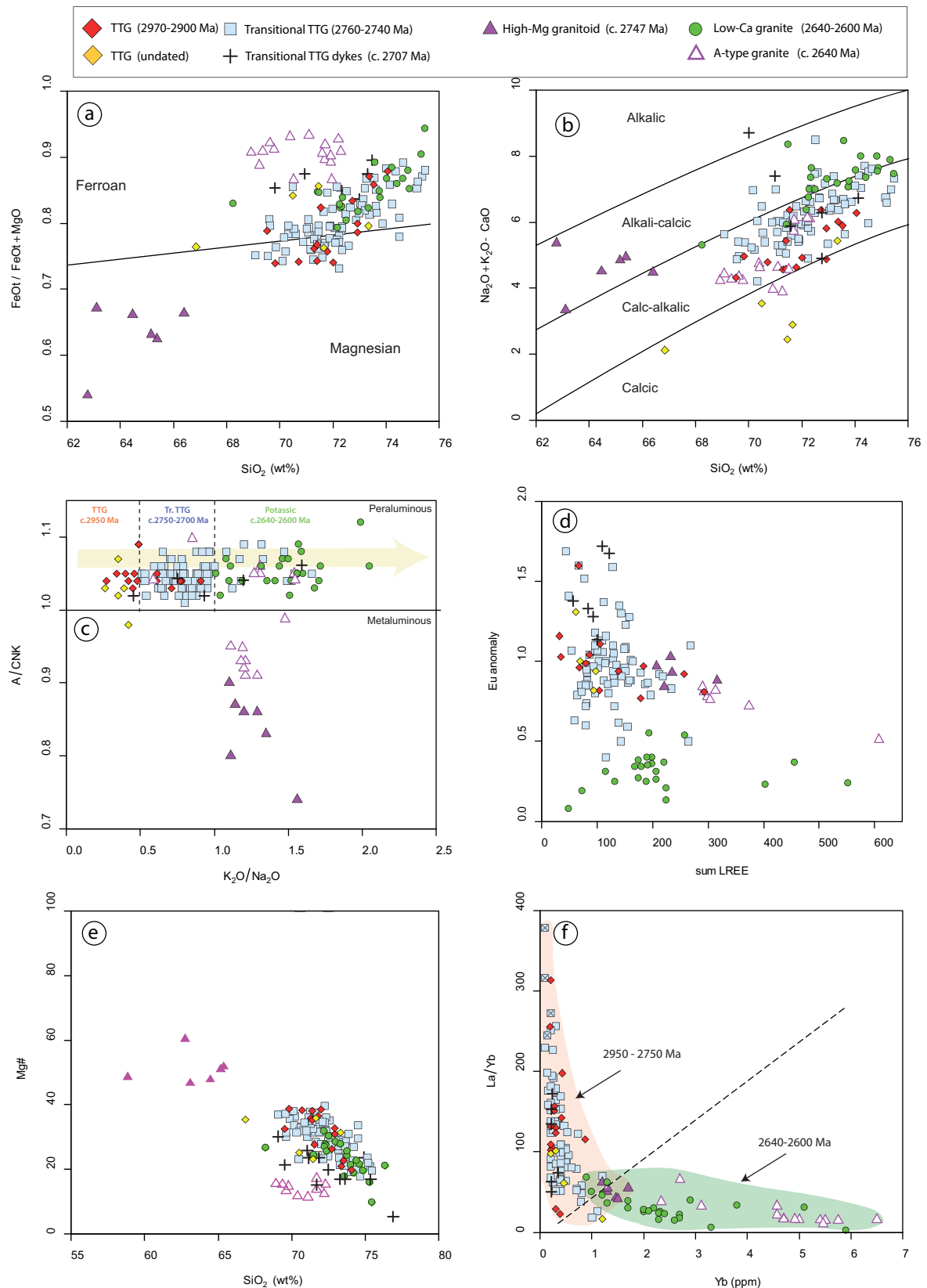


Figure 4: (a) Plot of SiO_2 versus $\text{FeO}_1/(\text{FeO}_1 + \text{MgO})$ content of all major suites bringing out the difference between the A-type samples of the Damperwah Pluton and the high-Mg nature of the Cagacaroon pluton; (b) $(\text{Na}_2\text{O} + \text{K}_2\text{O}) - \text{CaO}$ versus SiO_2 . Most samples are calc-alkaline with the exception of the alkali-calcic samples from the Cagacaroon pluton; (c) $\text{K}_2\text{O}/\text{Na}_2\text{O}$ versus aluminium saturation index (A/CNK), showing that TTG, transitional TTG and low-Ca are slightly peraluminous and become increasingly rich in K_2O with time, while high-Mg and A-type are metaluminous with $\text{K}_2\text{O}/\text{Na}_2\text{O} > 1$; (d) sum of light rare earth elements ($\Sigma_{\text{LREE}} = \text{La} + \text{Ce} + \text{Nd}$) versus Eu anomaly (Eu_n/Eu^* where $\text{Eu}^* = \sqrt{\text{Sm}_n \cdot \text{Gd}_n}$ and concentrations normalized to C_1 chondrites of McDonough and Sun, (1995)); (e) $\text{Mg}\#$ ($\text{Mg}^{2+}/\text{Mg}^{2+} + \text{Fe}^{2+}$, with Fe total as Fe^{2+}) versus SiO_2 ; (f) Yb versus La/Yb .

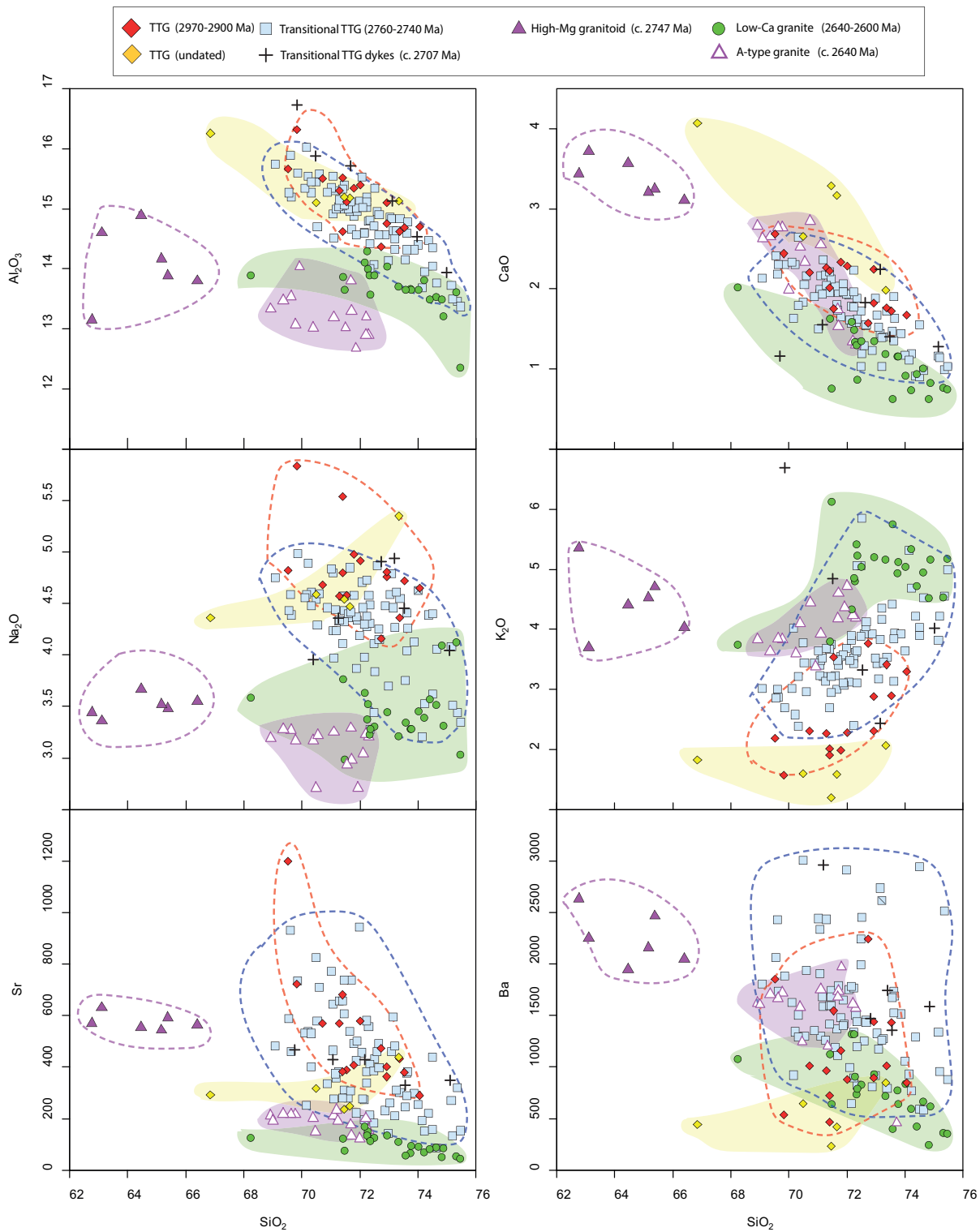


Figure 5: Representative major (wt%) and trace elements (ppm) geochemistry of the five granitic rock groups in the Yalgoo dome: Al_2O_3 (a), CaO (b), Na_2O (c), K_2O (d), Sr (e), and Ba (f) versus SiO_2 .

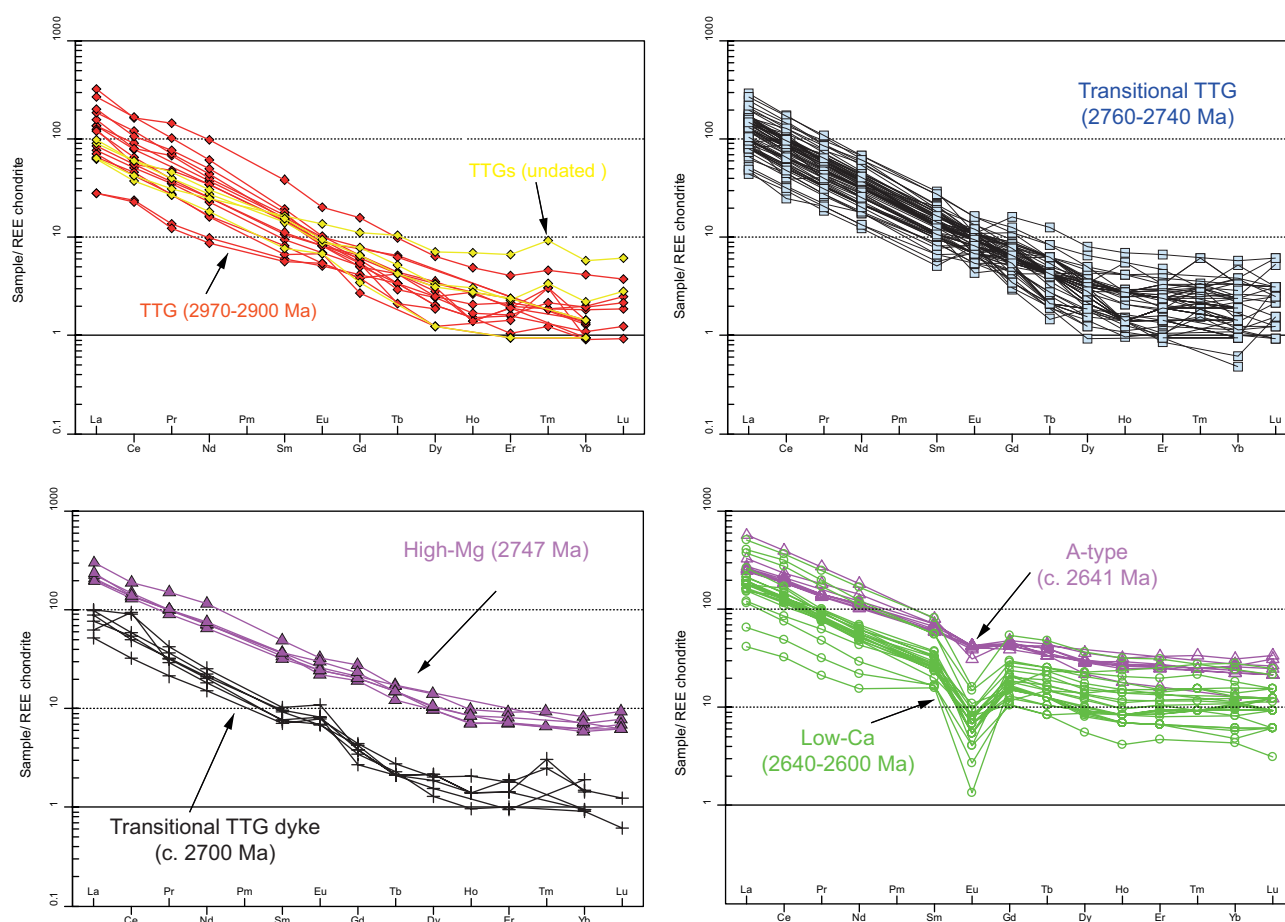


Figure 6: Chondrite normalized REE spider plots (Boynton, 1984) of the main granitic rock group.

4.5 Low-Ca granites

4.5.1 Field relationships, age and petrography

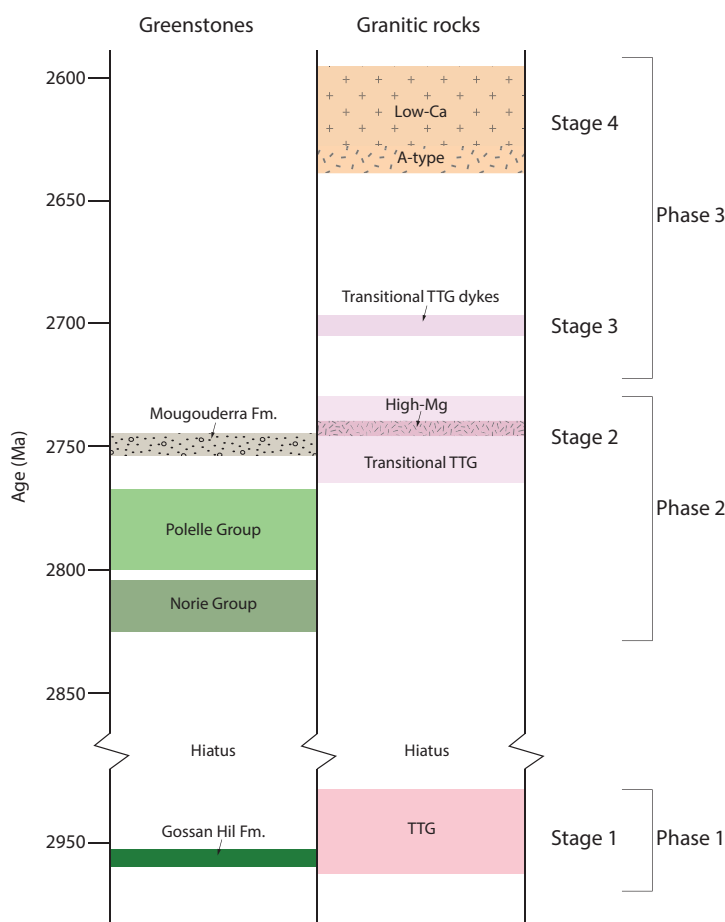
Low-Ca granites form post-tectonic intrusions with sub-circular map patterns, which truncate older rocks in the Yalgoo dome and surrounding greenstones (Fig. 1). Contacts with country rocks are sharp and weakly deformed. They are coarse-grained (Fig. 3e), equigranular leucogranites with K-feldspar-rich domains surrounded by quartz, plagioclase, biotite with minor chlorite, and muscovite. They are dated at 2626 ± 6 (GSWA ID 207630) Ma and 2606 ± 6 Ma (GSWA ID 83551) and are compositionally related to the contemporaneous post-tectonic granites of the 2640–2600 Ma Bald Rock Supersuite (Van Kranendonk et al., 2013) reported throughout the Yilgarn Craton (Champion and Sheraton, 1997). Because of this similarity, we take the age range of these granitic rocks to be that of the Bald Rock Supersuite (2640-2600 Ma).

4.5.2 Geochemistry

Low-Ca granites are calc-alkaline and peraluminous (Figs 4b–c) and are the most potassic of the five groups described here ($K_2O/Na_2O > 1$; Fig. 4c). For a given SiO_2 content (71.0–75.0 wt%) they show lower Al_2O_3 (11.08–14.28 wt%), CaO (< 2.0 wt%), Na_2O (< 4.1 wt%), and higher K_2O (3.7–6.1 wt%) contents than the TTGs and Transitional TTGs (Fig. 5). Compared to Transitional TTGs, HFSE concentrations are high (Nb=5–42 ppm, La= 37–156 ppm; Th=14–84 ppm; U=4–93 ppm, Y=10–81.0 ppm) despite highly variable Zr (81–524 ppm) and Hf (3.3–9.5) concentrations. Concentrations of Ba (110–1300 ppm) and Sr (22–166 ppm) are lower, but those of Rb (172–453 ppm), Pb (22–107 ppm) and Li (6–57 ppm) are higher (Table 2). Chondrite normalised REE in figure 6 shows a seagull-like pattern (Fig. 4e-f, Walganna and Wogala Suites, Ivanic et al., 2012), defined by relatively high HREE content ($Yb= 1–6$ ppm; Table 2), $La/Yb < 25$ (Fig. 4f) and a marked negative Eu anomaly ($Eu^*/Eu < 0.5$; Fig. 4d).

5 Discussion

In the Yalgoo dome and its most immediate surroundings, we identified five granitic groups sug-



gesting a >300 Myr long evolution of protracted, but pulsed magmatic stages. This evolution can be divided into four stages based on a distinctive age, geochemical signature and structural location within the dome (Fig. 2)

Figure 7: Comparative time-space diagram of the Yalgoo dome showing the temporal relationship between greenstones and granitic rocks and their subdivision in 4 stages of felsic magmatism occurring in three phases of mantle-derived magmatism (i.e. greenstones) followed by crustal reworking (i.e. granitic rocks). Phase 3 greenstones are absent in the Yalgoo dome area, but have been reported in the NE part of the Murchison Domain (Ivanic et al., 2012; Van Kranendonk et al., 2013).

so that TTGs define Stage 1 (2970–2900 Ma), high-Mg granitic rocks and transitional TTGs come together under Stage 2 (2760–2740 Ma), transitional TTG dyke in Stage 3 (c. 2707 Ma) and A-type and low-Ca are grouped in Stage 4 (2760–2740 Ma) (Fig. 7). We first describe each of the four stages before dividing them into three major phases based on correlation with major episodes of mantle-derived magmatism forming the greenstones (Fig. 7).

5.1 STAGE 1: TTG magmatism (2970–2900 Ma)

Geochemical modelling by Moyen (2011) showed that TTGs can be subdivided in three subgroups, indicating different melting pressures in the source. At low pressure (12–15 kbar), meta-basic rocks exhibit a garnet-poor, plagioclase-rich mineral paragenesis (Moyen and Martin, 2012), and melts derived from this assemblage are enriched in HREE, but depleted in elements compatible in plagioclase such as Sr, Na₂O and Al₂O₃. These felsic melts produce rocks equivalent to the low-Al TTG of Barker and Arth (1976). By contrast, at high pressures ($P > 20$ kbar), melting of mafic rocks produces felsic melts with high Na₂O, Al₂O₃ and Sr, but low HREE, suggesting a garnet-rich, but plagioclase-free (i.e. eclogitic) residue. In between these two end-members, there is a third group that forms between 15 and 20 kbar and displays an intermediate geochemical signature, reflecting a source with abundant garnet and amphibole, but minor plagioclase.

Phase equilibrium modelling of an enriched Archean tholeiite by Palin et al. (2016) indicates that TTG magmas could have developed at 800–950 °C and 10–18 kbar. Moreover, these authors contend that the protolith is most fertile (15–35% melting) when crossing the wet-solidus at $P = 11–12$ kbar and that the three groups introduced by Moyen (2011) could form from the same source, at various depth and temperature during the same tectono-metamorphic episode. Similarly, the melting experiments of Qian and Hermann (2013) and Zhang et al. (2013) demonstrate that low-to-intermediate pressure TTGs can be generated by anatexis of hydrous mafic rocks at 800–950°C and 10–12 kbar. In addition, Johnson et al. (2017) showed that low-Mg basalts such as the Coucal formation in the Pilbara Craton, have the potential to generate TTG melts at pressures as low as 7 kbar.

The difficulty with interpreting TTGs is that melting within this range of conditions might occur in more than one geodynamic setting (Arth and Hanson, 1975; Condie, 1981; Martin, 1986). Indeed,

in the last three decades, the ideal geodynamic setting for the origin of TTGs has been intensely debated between proponents of subduction zones (Defant and Drummond, 1990; Martin and Moyen, 2012) and those who favor melting at the base of oceanic plateaux or tectonically overthickened crust (Collins et al., 1998; Smithies et al., 2009; Van Kranendonk et al., 2015). These are just some of the numerous models proposed in the attempt to reconcile the formation of Archean TTG to a tectonic setting. This remains elusive because several mechanisms and settings have the potential to generate TTG-like magmas (e.g. Sizova et al., 2015; Moyen and Laurent, 2018). These reasons, altogether with the pervasive migmatization and heterogenous metasomatization of the TTGs in the Yalgoo Dome (Chapter 3), prevent the determination of the depth of melting as shown in the work of Moyen (2011). Any inference about the depth of melting might be biased and might lead to incorrect formulation of geodynamic models. TTGs in the Yalgoo might have formed by slab melting or by intracrustal melting, but either way these granitoids represent the first formation of felsic crust in the area.

5.2 STAGE 2: high-Mg granitic rocks and transitional TTGs (2760–2740 Ma)

After Stage 1, felsic magmatism resumed in the Yalgoo dome at c. 2760 Ma. Granitic rocks are dominated by the 2760–2740 Ma transitional TTGs that were accompanied in time by the intrusion of the high-Mg Cagacaroon pluton at c. 2747 Ma in the greenstone cover (Fig. 1). They are grouped together not only because they occurred in the same time slice but also because their origin could be related. In this section we briefly outline the mainstream genetic model for the genesis of high-Mg granitic rocks and transitional TTGs, then we propose an integrated model to explain their coeval occurrence in the Yalgoo dome.

5.2.1 Origin of the high-Mg granitic rocks: Cagacaroon Syenogranite

High-Mg granitic rocks enriched in Cr, Ni and LILE are viewed by some authors as sanukitoids, hence they are often related to a source component derived from subduction-metasomatized lithosphere (Shirey and Hanson, 1984; Martin et al., 2005, 2009; Heilimo et al., 2010). In a convergent setting, sanukitoids can form by two distinct processes, depending on the degree of interaction between slab-derived melts and mantle wedge peridotite. The first is a one-step process, where

slab-derived melts incorporate or digest variable amounts of peridotite before crustal emplacement (Rapp et al., 1999, 2010). The second is a two-step process: slab-derived melts react completely with mantle peridotite during ascent, and crystallize in the mantle wedge to create an enriched mantle, including variable proportions of phlogopite and pargasite (Martin et al., 2005, 2009). A subsequent thermal anomaly can destabilise this metasomatized mantle and generate sanukitoids up to several hundred million years after the emplacement of the TTG melt (Stern and Hanson, 1991; Rapp et al., 1999, 2010; Laurent et al., 2014).

Given that the only modern geodynamic environment capable of supplying sufficient volumes of hydrous and LILE-enriched metasomatic agents to the upper mantle is a subduction zone, many authors contend that similar processes would have characterized the Archean (Heilimo et al., 2010; Farina et al., 2015). However, granitic rocks with a sanukitoid-like signature are also reported in other geological contexts. For example, intracontinental high-Mg granitic rocks in the North China Block are viewed as partial melting of mafic rocks during regional lower crust delamination in the Cretaceous (Gao et al., 2009). In this case, delaminating mafic lower crust has the potential to produce melts with TTG-like composition that might interact with peridotites before intruding the crust, forming high-Mg (i.e. sanukitoids) intrusions. Another example is the occurrence of K-rich granitic rocks enriched in Mg, Cr and Ni along the Red River-Ailao and Shan-Batang-Lijiang faults in eastern Tibet (Campbell et al., 2014). At various points along this 1500 km long transpressional lineament, continental crust was down-thrusted into the upper mantle, melted and interacted with the overlying mantle rocks (see Fig. 7 in Campbell et al., 2014). In essence, high-Mg granitic rocks formed along crustal-scale structures that tapped a previously enriched mantle which not necessarily formed in an active subduction system, but may also include delamination, subcretion or dripduction (Moyen and Laurent, 2018).

5.2.2 Origin of the transitional TTGs

In many Archean terranes, granitic rocks with transitional TTG composition are viewed as hybrid, formed by mixing and mingling of different magmas. For instance, the hybrid granitic rocks in the Limpopo Belt (Laurent et al., 2014) display multiple evidence for a mixing origin, such as

rapakivi-textured feldspars, quartz ocelli, magma mingling and a bulk chemistry inconsistent with melting of a single protolith. Likewise, the geochemical modelling of Almeida et al. (2010) shows that mixing between fractionated high-Mg granitic rocks (i.e. sanukitoids) and trondhjemitic melts derived from partial melting of mafic metavolcanic rocks can account for the chemical signature of transitional TTGs in the Amazonian Craton.

The mixing hypothesis to explain the contemporaneous appearance of high-Mg (i.e. sanukitoids)

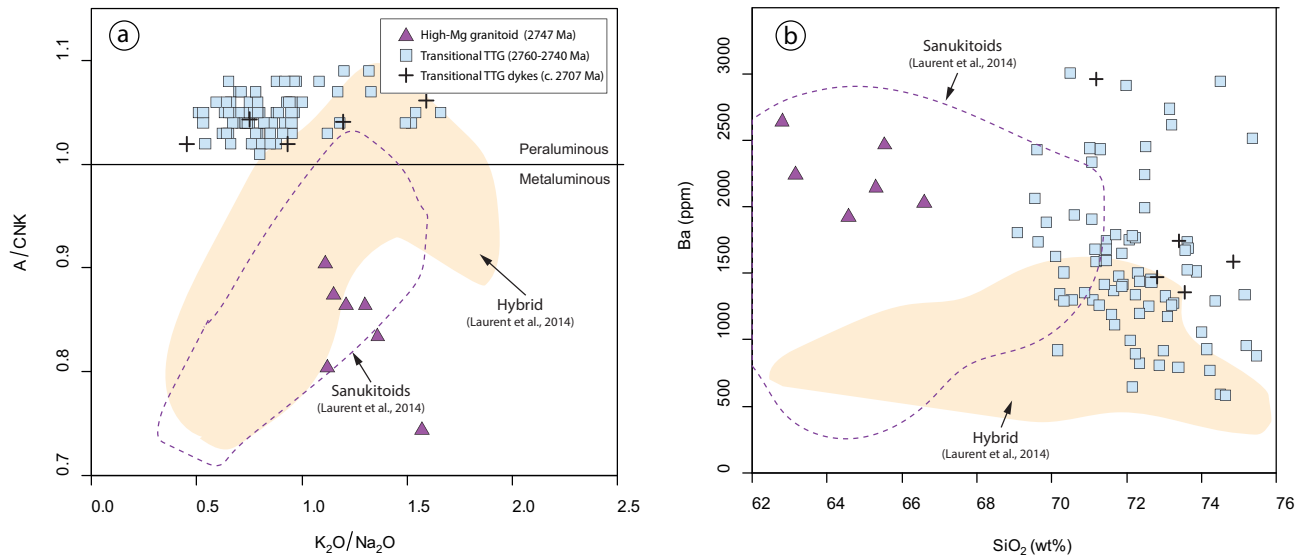


Figure 8: K₂O/Na₂O versus aluminium saturation index and b) SiO₂ (wt%) versus Ba (ppm) diagrams comparing the composition of sanukitoids and hybrid granites (i.e. granites derived from mixing of sanukitoids and crustal melts) from Laurent et al. (2014) with high-Mg granitic rock and transitional TTGs from the Yalgoo dome.

and transitional TTGs has been successfully applied in the Limpopo Belt in South Africa by Laurent et al. (2014), but it may not be pertinent for the Yalgoo dome. In contrast to the Limpopo Belt, transitional TTGs in the Yalgoo dome lack textural evidence for magma mixing and mingling. Also, their chemistries are different: transitional TTGs in the Yalgoo dome are less potassic, lack silica-poor members (SiO₂ < 70.0 wt%) and are consistently more enriched in Ba (Fig. 8). If mixing between TTG melts and high-Mg magmas occurred in the Yalgoo dome, the hybrids have been homogenized and fully equilibrated. Alternatively, they might have formed by entirely different processes.

We suggest, following Champion and Smithies (2007), that the geochemical signature of transitional TTGs in the Yalgoo dome reflects its source. High LILE, Th and U concentrations are characteristics of Archean granites comprising material from older felsic crust (Moyen, 2011). However, the

older, 2970–2920 Ma TTGs outcropping at the present erosion surface are not suitable protoliths as they have similar bulk composition (70.0–75.0 wt% SiO_2), but lower K_2O content than transitional TTGs. Given that the 2760–2740 Ma transitional TTGs have the same bulk composition and REE depletion as most Archean TTGs, but are more enriched in LILE and radiogenic elements, we contend they formed from an unexposed basaltic source in the deep crust, a source more enriched and evolved than the average basaltic protolith for TTGs. Alternatively, felsic volcanic and sedimentary rocks interbedded with basalts could generate enriched TTGs melts (Champion and Smithies, 2007).

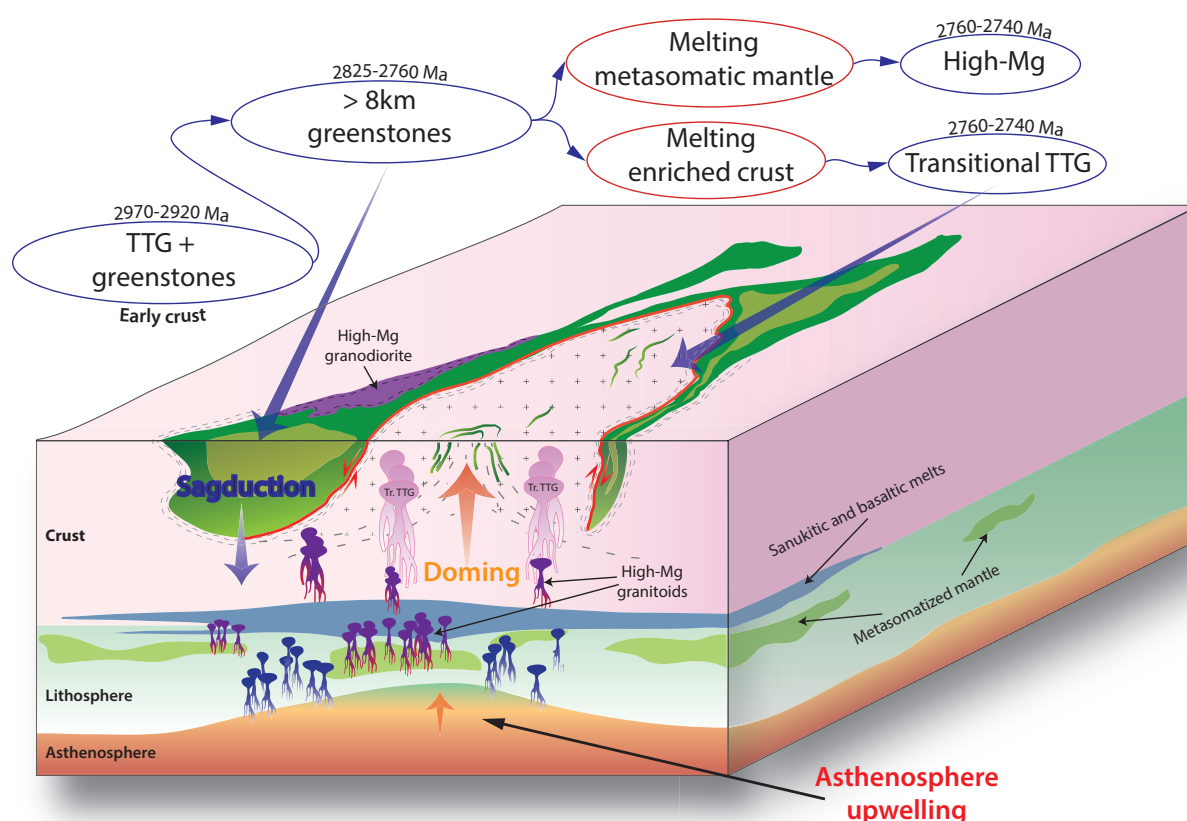


Figure 9: Cartoon illustrating the scenario at 2760–2740 Ma (Stage 2) where the coeval occurrence of transitional TTGs and high-Mg granitic rocks is related to the main dome-forming event.

5.2.3 Lithospheric reworking

The contemporaneity of high-Mg felsic magmas and transitional TTGs in the Yalgoo dome can be interpreted as in-situ melting of a lithospheric column comprising a metasomatized mantle and an overlying felsic and basic crust. A three-step model is suggested: a) metasomatization of the

sub-continental lithospheric mantle (SCLM) by some form of crustal recycling in the mantle (subduction, subcretion, delamination or dripduction), b) mantle-derived magmatism culminating in the eruption of the Norie Group (2825–2805 Ma) and the ~8 km thick Polelle Group (2800–2760 Ma; Ivanic et al., 2012; Van Kranendonk et al., 2013; Ivanic et al., 2015). The rise in temperature from mafic underplating, thermal blanketing from the erupted greenstones (Rey et al., 2003) and radiogenic decay in buried felsic rocks caused partial melting of both crust and metasomatized SCLM generating high-Mg melts and transitional TTGs (Fig. 9). c) High-Mg magmas rise to the base of the crust, some pond and trigger further melting of enriched basalts in the lower crust to develop more transitional TTGs, others, perhaps more fractionated and buoyant magmas, rise with little interaction with the lower crust to form the high-Mg intrusions (Fig. 9). A variant of this model

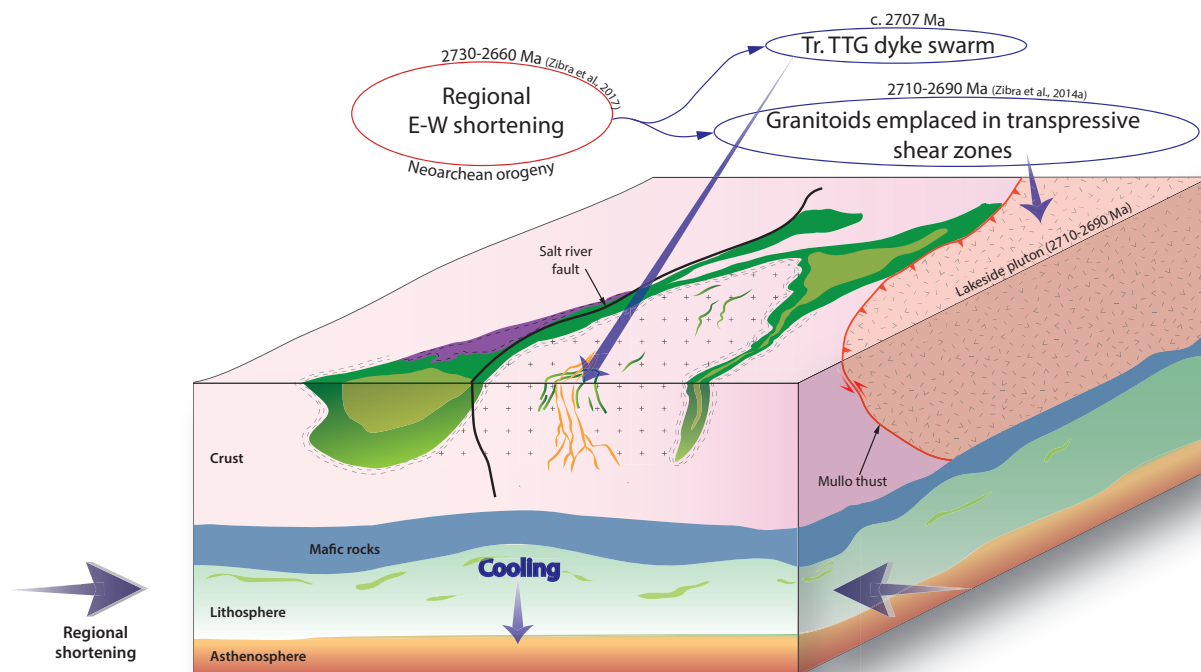


Figure 10: Cartoon showing the effect of the Neoproterozoic orogeny (2730–2660 Ma) in the Yalgoo dome (Stage 3). East–west regional shortening caused the emplacement of the voluminous Lakeside Pluton (2710–2690 Ma) and the emplacement of transitional TTGs dykes in the Kynea Tonalite, in the core of the dome.

has been proposed by Ivanic et al. (2012), which interpreted high-Mg granitic rocks as mafic-felsic magma mixing rather than partial melting of a metasomatized mantle.

5.3 STAGE 3: transitional TTGs dykes (c. 2700 Ma)

In the Murchison Domain, the second phase of crustal formation was initiated by a new stage of mantle-derived melts, including komatitic basalts of the 2735–2710 Ma Yalgowra Suite and 2720 Ma Glen Group (Ivanic et al., 2012). This renewed mantle-derived magmatism induced a second and more pronounced phase of crustal reworking with emplacement of voluminous felsic plutons with mainly TTG composition during the 2730–2660 Ma interval. These TTGs are contemporaneous with an anastomosed craton-scale network of Neoproterozoic transpressive shear zones that accommodated regional EW shortening during the Neoproterozoic Yilgarn Orogeny (<2730 Ma; Zibra et al., 2017).

Stage 3 is recorded by north-trending shear zones and the emplacement of granitic dykes (c. 2707 Ma; Fig. 3b). Their ages are identical to the time of emplacement of the Lakeside pluton at 2710–2695 Ma, a voluminous intrusion adjacent to the Yalgoo dome (Fig. 1; Zibra et al., 2014a). We conclude that the same tectono-magmatic episode caused the intrusion of a swarm of granitic dykes in the Yalgoo dome and the Lakeside pluton. However, granitic rocks in the Lakeside pluton are mainly TTGs (Zibra et al., 2014a), while the granitic dykes are transitional TTGs comparable to the more abundant 2760–2740 Ma transitional TTGs (Figs 4, 6; Stage 2). This suggests that they might derive from the reactivation of the same enriched source that generated the 2760–2740 Ma transitional TTGs (Fig. 10).

5.4 STAGE 4: Post-tectonic granites (2640–2600 Ma): A-type and low-Ca granites

The transitional TTG dykes emplaced during the Neoproterozoic Yilgarn Orogeny (Stage 3) were followed by the emplacement of two groups of post-tectonic, undeformed K-rich granites between 2640 and 2600 Ma: the A-type intrusions in the Damperwah and Seelingson pluton (Fig. 1) and numerous low-Ca plutons of the Bald Rock Supersuite (Van Kranendonk et al., 2013).

5.4.1 Origin of the A-type granites

There are many controversies regarding the origin of A-type granitic rocks as they appear to be attributable to fractionation of mantle-derived mafic magmas, high temperature dry partial melting of quartzofeldspathic rocks in the crust or by mixing processes (Eby, 1992; Skjerlie and Johnston,

1992). Under some conditions, fractionation of mantle-derived mafic magma generates melts with alkaline compositions (King et al., 1997; Frost and Frost, 2011). The metaluminous to weakly peraluminous nature of the calc-alkaline Damperwah pluton (Fig. 4c) argues against this origin. The high SiO_2 (>69.0 wt%; Fig. 5) content combined with high Ba concentrations (Table 2; Fig. 4) suggest that their origin from fractional crystallization of mantle-derived magmas is unlikely, and suggest instead that they might form from low pressure-high temperature melting of residual rocks in the crust or by mixing of basaltic and granitic magmas (Whalen et al., 1987; Frost and Frost, 2011).

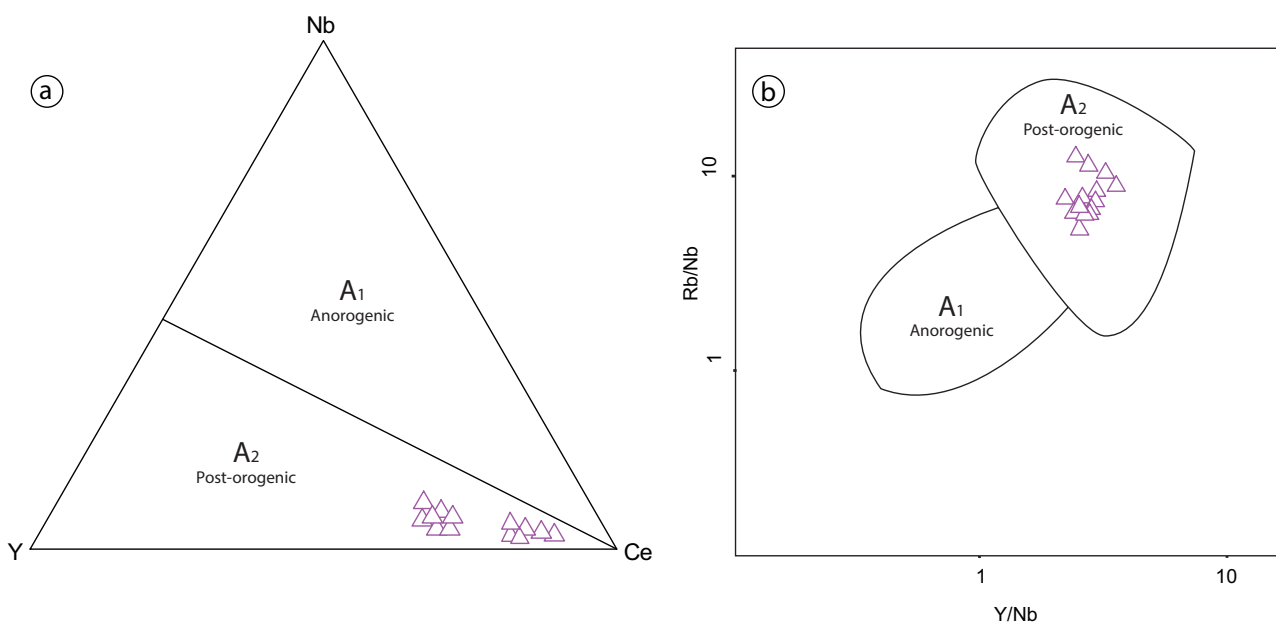


Figure 11: The A_1 and A_2 subgroup discriminations for the A-type granite of the Damperwah pluton (after Eby, 1992). a) A_1 corresponds to the field of alkaline A-type granitic rocks formed in an anorogenic setting by fractional crystallization of basalts while b) A_2 field correspond to calc-alkaline A-type granitic rocks typical in a post-orogenic environment.

The chemical composition of the Damperwah and Seelingson plutons is analogous to the Paleoproterozoic A-type granites exposed along the margin of the Archean North China Craton (Deng et al., 2016) and in Carajás, Brazil (Dall'Agnol and Oliveira, 2007). The main petrogenetic models proposed for these terranes advocate for a low pressure-high temperature partial melting of Neoproterozoic calc-alkaline rocks at low (Deng et al., 2016) or high oxygen fugacity (Dall'Agnol and Oliveira, 2007). We contend that the A-type intrusions in the Yalgoo dome formed in a similar way. The

pervasive presence of ilmenite and Fe-rich amphibole in the Damperwah pluton, as observed also in the Paleoproterozoic A-type granitic rocks in China (Deng et al., 2016) indicates low fO_2 (Anderson and Smith, 1995).

Notwithstanding questions about the petrogenesis of the A-type granitic rocks, it is widely accepted that they form in an extensional regime, either post-orogenic or anorogenic (Whalen et al., 1987; Frost and Frost, 2011). These two settings can be differentiated chemically according to the diagrams of Eby (1992) (Fig. 11). Eby's A_1 group represents alkaline granitic rocks formed by fractional crystallization of basalts in an anorogenic setting. His A_2 group comprises post-orogenic, calc-alkaline granitic rocks, such as the post-tectonic A-type granite typical of most Proterozoic terranes (Frost et al., 1999; Dall'Agnol and Oliveira, 2007; Duchesne et al., 2010; Deng et al., 2016). The Damperwah pluton presented here corresponds to the A_2 group because of its elevated Rb/Nb and Y/Nb (Fig. 11) and as suggested Eby (1992), it could be generated from melting of quartzo-feldspathic crust or, less likely by fractionation of underplated mafic magmas that has been through a phase of continent-continent collision or island-arc magmatism.

5.4.2 Origin of the low-Ca granites

The large majority of authors consider low-Ca granites to be derived from low degree partial melting of felsic rocks (TTGs, felsic volcanic rocks) at shallow crustal depths (Whalen et al., 2004; Frost et al., 2006; Almeida et al., 2013; Farina et al., 2015). Their geochemistry suggests that plagioclase fractionation or retention in the source played a key role, resulting in melts depleted in Sr, Al, Na and Ca with marked negative Eu anomalies (Dey et al., 2012; Farina et al., 2015).

5.4.3 Lower crust delamination

The sudden change in the nature of magmatism to A-type and low-Ca across the Yilgarn craton needs to be explained by wide regional changes. Ivanic et al. (2012) proposed a delamination model to link the change in chemical composition of 2640–2600 granites and the post-tectonic environment. After the end of the Neoproterozoic Orogeny, removal of lower crust by post-orogenic delamination would result in asthenospheric upwelling that could have heated up the crust sufficiently. In these models, the A-type and low-Ca would form by high temperature, dehydration melting of

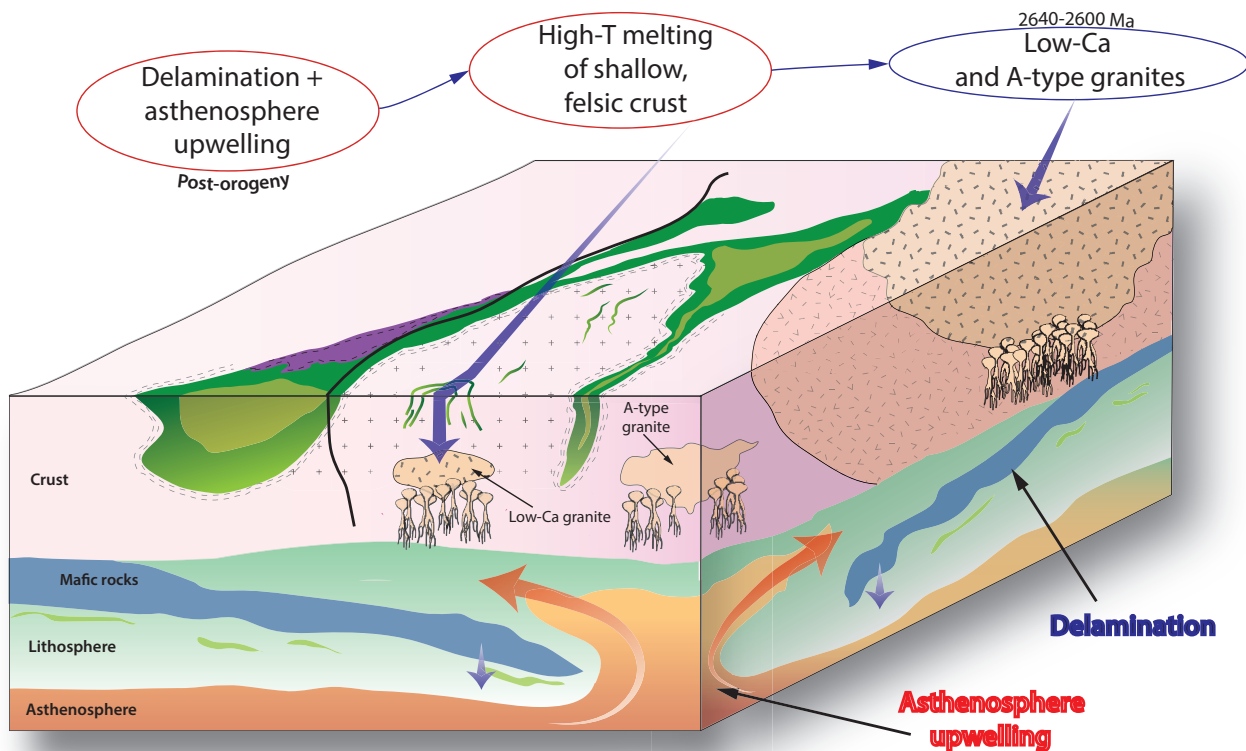


Figure 12: Cartoon showing the post-orogeny phase in the Yalgoo dome between 2640–2600 Ma (Stage 4). Regional delamination. After the end of the Neoproterozoic Orogeny (Stage 3), regional delamination could result in asthenospheric return flow that could have heated up the crust and allowed high temperature, dehydration melting of more evolved rocks in upper levels of the crust forming both A-type and low-Ca granites.

quartzo-feldspathic rocks in upper levels of the crust (Fig. 12) (Ivanic et al., 2012).

In the Yalgoo region, the geochemistry of the A-type Damperwah and Seelingson pluton is consistent with an emplacement in a post-orogenic extensional environment as suggested by Champion and Cassidy (1997) and Cassidy et al. (2002) for identical granitic rocks (their high-HFSE granites) in the Eastern Goldfields Terranes (Fig. 1). In addition, since A-type and low-Ca plutons shows comparable Sr- Al_2O_3 depletion (Fig. 4) and high HREEs content (Fig. 5), it is probable that they formed in a similar tectono-magmatic environment, but from slightly different sources at different crustal levels.

5.5 Implications for incremental formation of Archean continental crust

The four stages of granitic activity at 2970–2900 Ma, 2760–2740 Ma, c. 2707 Ma and 2640–2600 Ma were linked three distinct phases of enhanced mantle activity (Figs 7, 13). These episodes of mantle-derived mafic-ultramafic magmatism resulted in repeated crustal reworking, resulting in the intrusion of granitic rocks. The first phase is marked by the coeval formation of Stage 1 TTGs and

the greenstones of the Gossan Hill Formation (c. 2963–2958 Ma) (Phase 1; Fig. 7). This earliest crustal reworking episode involved an older mafic crust, whose partial melting generated the TTG magmas at 2970–2900 Ma. After a magmatic hiatus of more than 100 Myr, a second phase began with the eruption of the 2825–2805 Ma Norie Group and the voluminous 2800–2760 Ma Polelle Group (Ivanic et al., 2012; Van Kranendonk et al., 2013; Ivanic et al., 2015) and culminated with the diapiric emplacement of Stage 2 granitic rocks (Phase 2; Fig. 7). Time lag between greenstones and granitic intrusions simply reflect the time necessary to heat up the lithosphere. This thermal incubation resulted in a complete reheating and remobilization of a mafic-felsic crust, resulting in the intrusion of transitional TTGs, and its underlying metasomatized mantle resulting in the intrusion of high-Mg granitic rocks. This short-lived episode (c. 20 M.yr) of crustal reworking was dominated by buoyant forces of plutonic and migmatitic bodies resulting in the vertical re-arrangement of the crust in a negligible regional stress field.

The onset of this third phase (Phase 3; Fig. 7) is associated with a new stage of mantle-derived melts, with komatitic basalts such as those of the 2735–2710 Ma Yalgowra Suite and 2720 Ma Glen Group, outcropping only in the northern part of the Murchison Domain (Ivanic et al., 2012). Although crustal reworking was dominant in the NW part of the Murchison Domain and in the Southern Cross Domain, in the Yalgoo dome, Phase 3 initiated in an orogenic setting subject to EW shortening resulting in the emplacement of Stage 3 transitional TTG dykes during the Neoproterozoic Yilgarn Orogeny (2730–2640 Ma; Zibra et al., 2017). This phase was then followed by the post-orogenic A-type and the voluminous Low-Ca granites of Stage 4 (Figs 7, 13). These crustal reworking events involved an increasingly larger amount of previously formed felsic rocks and give rise to K-rich granitic intrusions. In particular, the final development of the crust in the Yalgoo dome occurred during the intrusion A-type and low-Ca granites, granitic rocks generated by high-temperature low-pressure partial melting of quartzo-feldspathic sources (stage 4).

These peak ages are corroborated by recent Lu-Hf isotopes data on zircons from mainly granitic rocks in the NW part of the Murchison Domain (Ivanic et al., 2012). Early 2970–2920 Ma granitoids display ϵ_{Hf} varying between -4 and +2 and were explained as a juvenile input into a Meso- to Paleoproterozoic crust (Ivanic et al., 2012). The second phase of juvenile magmatism at 2825–2760

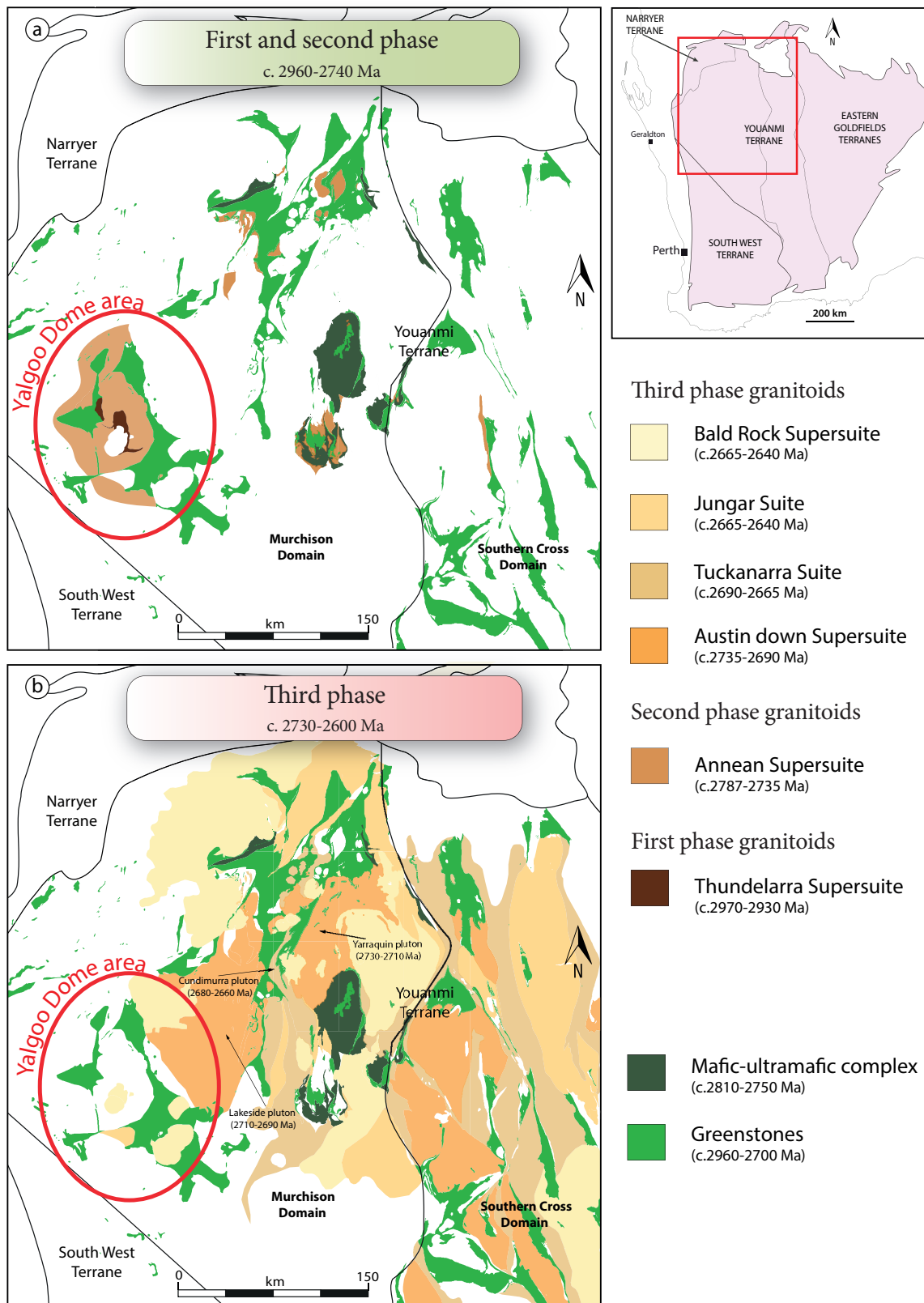


Figure 13: Map of the distribution showing the distribution of the three phases of crustal reworking in Youanmi Terrane (Ivanic et al., 2012; Van Kranendonk et al., 2013): (a) the first and second phase granitoids comprise, respectively the Thundelarra (2970–2930 Ma) and Annean Supergroup (2787–2735 Ma). These units are well-preserved only in the westernmost part of the terrane, where the Yalgoo dome is exposed. The large majority of the terrane is defined by granitoids of the third phase, mostly intruded in an anastomosed network of shear zones coeval with the emplacement of syn-tectonic granitic rocks of the Austin Down Supersuite (2735–2690 Ma) and Tuckanarra Suite (2690–2665 Ma). Note the location of the Yarraquin pluton (2730–2710 Ma; Zibra et al., 2017), Lakeside pluton (2719–2695 Ma; Zibra et al., 2014a) and Cundimurra pluton (2680–2660 Ma; Zibra et al., 2014b). This phase is dominated by east–west compression followed by the emplacement of numerous post-tectonic plutons belonging to the Bald Rock Supersuite (2640–2600 Ma).

Ma shows ϵ_{Hf} from 0 to +3 and matured from a 3040 Ma source. A sudden change in the melting source occurred at 2760–2730 Ma, as the felsic volcanics of the Greensleeves and Annean Supersuite granitoids (Fig. 13) show a wide vertical array of ϵ_{Hf} , varying from 0 to -10 and were interpreted as incorporation of a 3000–3700 Ma component in the source. The ϵ_{Hf} on c. 2720 and 2640 Ma granitoids indicates reactivation of a c. 3040 Ma source. The 2640–2600 Ma Bald Rock Suite (Fig. 13) is characterized by ϵ_{Hf} between -4 and -12 and was explained as melting of a source old up to 3800 Ma or by mixing of with a more juvenile component between 3000 and 2700 Ma.

The >300 Myr magmatic evolution of the Yalgoo dome has several ramifications for the formation and evolution of the crust at the end of the Archean eon. Three processes must take place to develop a felsic continental crust: i) sequential phases of mantle-derived mafic-ultramafic magmatism accompanied by crustal reworking, culminating in the intrusion of granitic rocks, ii) the source of granitoids evolves through time from basaltic to felsic and iii) the anatectic, recycling zone giving rise to granitic rocks become shallower in time (post-2750 Ma rocks in Ivanic et al., 2012). Our data supports the in-situ incremental growth of continental crust, but in a stepwise manner linked to major stages of crustal reworking at 2970–2900 Ma, 2760–2740 Ma, c. 2707 Ma and 2640–2600 Ma. Intermittent episodes of enhanced mantle activity added juvenile material and reheated the entire crust, causing reworking on a scale and style exclusive of the Archean eon.

6 Conclusion

The different granitic rock throughout all late Archean cratons groups are remarkably comparable both in terms of their chemistry and relative timing and can be separated into a five granitic rock group: TTG, transitional TTG, high-Mg, A-type and low-Ca. All these groups are well-exposed in the Yalgoo region and their field, geochemical and geochronological characteristics indicate a four stage magmatic evolution linked with three major phases of juvenile magmatism and greenstone formation. The rocks of the first phase are sparingly preserved and include coeval greenstones and TTGs (Stage 1) at 2970–2900 Ma. The second phase started with the deposition of the Norie and Polelle Group at 2825–2760 Ma, voluminous sequences of mafic-to-ultramafic rocks that led to a thermal incubation of the crust and vertical crustal reworking with diapiric intrusion of 2760–2740

Ma transitional TTGs and high-Mg granitic rocks (Stage 2). The third phase of crustal reworking is associated with the onset of the Neoproterozoic Yilgarn Orogeny in the Murchison Domain and culminated in the intrusion of a swarm of transitional TTG dykes at c. 2707 Ma during regional EW shortening (Stage 3). The secular change from TTGs to low-Ca granites reflects the progressive modification of the melting source, from basaltic to granitic, and from deep to shallow melting depths. In essence, the crustal evolution of the Yalgoo dome at the end of the Archean eon shows a case example of in-situ formation of felsic continental crust through three phases of juvenile magmatism followed by several melting events that progressively stabilized the continental crust. Although the incremental development of granitic masses is crucial to add buoyancy to the continental crust, the long-term resiliency of Archean cratons was greatly enhanced by their depleted and buoyant mantle keels. These roots protected Archean crust during collisional events and deviated mantle-upwelling to the edges of cratons. The development of these lithospheric roots is broadly coeval with crustal growth of Archean cratons, but the minimal exposure of this mantle rocks impedes more accurate correlations and deeper insights of the elusive Archean processes of crustal formation and reworking.

Acknowledgments

This work was financially supported by ARC DP11010254. Shachar Lazar is thanked for his assistance and energy during the fieldwork and the Staff at the Carlisle labs for their sample handling. Tim J. Ivanic and Hugh Smithies are thanked for their feedback, which helped to improve the quality of the submitted manuscript.

References

- Alsop, G.I., Holdsworth, R.E., 2006. Sheath folds as discriminators of bulk strain type. *Journal of Structural Geology*, 28, pp.1588–1606.
- Bodorkos, S., Sandiford, M., 2013. Thermal and mechanical controls on the evolution of Archean crustal deformation: examples from Western Australia. *Archean Geodynamic Environment*, pp.131–147.
- Bouchez, J.L., Diot, H., 1990. Nested granites in question: contrasted emplacement kinematics of independent magmas in the Zaer pluton, Morocco. *Geology*, 18, pp. 966–969.
- Bouhallier, H., Chardon, D., Choukroune, P., 1995. Strain patterns in Archean dome-and-basin structures: the Dharwar craton (Karnataka, South India). *Earth and Planetary Science Letters*, 135, pp. 57–75.
- Boulter, C.A., Bickle, M.J., Gibson, B., Wright, R.K., 1987. Horizontal tectonics pre-dating upper Gorge Creek group sedimentation Pilbara Block, Western Australia. *Precambrian Research*, 36, pp.241–258.

- Campbell, I.H., Hill, R.I., 1988. A two-stage model for the formation of the granite-greenstone terrains of the Kalgoorlie-Norseman area, Western Australia. *Earth and Planetary Science Letters*, 90, pp. 11–25.
- Chardon, D., Choukroune, P., Jayananda, M., 1998. Sinking of the Dharwar Basin (South India): implications for Archaean tectonics. *Precambrian Research*, 91, pp. 15–39.
- Choukroune, P., Bouhallier, H., Arndt, N.T., 1995. Soft lithosphere during periods of Archaean crustal growth or crustal reworking. *Geol. Soc. London, Spec. Publ.* 95, 67–86. Collins, W.J., 1989. Polydiapirism of the Archean Mount Edgar Batholith, Pilbara Block, Western Australia. *Precambrian Research*, 43, pp. 41–62.
- Drury, S.A., Harris, N.B.W., Holt, R.W., Reeves-Smith, G.J., Wightman, R.T., 1984. Precambrian tectonics and crustal evolution in south India. *Journal of Geology*, 92, pp. 3–20.
- Fenwick, M.J., 2014. Structural evolution of the Yalgoo Dome, Yilgarn Craton, Western Australia: a core perspective. Geological Survey of Western Australia, record 2015/1016.
- Foley, B.J., 1997. Reassessment of Archaean tectonics in the Yalgoo District, Murchison Province, Western Australia. Unpublished Thesis. Monash University, Melbourne, Australia.
- Fyson, W., 1984. Fold and cleavage patterns in Archean metasediments of the Yellowknife supracrustal domain, Slave Province, Canada. A. Kröner R. Greiling.-E. Schweizerbart'sche, pp. 281–293.
- Hickman, A.H., 2004. Two contrasting granite-greenstone terranes in the Pilbara Craton, Australia: evidence for vertical and horizontal tectonic regimes prior to 2900 Ma. *Precambrian Research*, pp. 131, 153–172.
- Hofmann, A., Kröner, A., Xie, H., Hegner, E., Belyanin, G., Kramers, J., Bolhar, R., Slabunov, A., Reinhardt, J., Horváth, P., 2015. The Nhlngano gneiss dome in south-west Swaziland – A record of crustal destabilization of the eastern Kaapvaal craton in the Neoproterozoic. *Precambrian Research*, 258, pp.109–132.
- Ivanic, T.J., Li, J., Meng, Y., Guo, L., Yu, J., Chen, S.F., Wyche, S. and Zibra, I., 2015. Yalgoo, WA Sheet 2241: Geological Survey of Western Australia. 1:100 000 Geological Series.
- Ivanic, T.J., Van Kranendonk, M.J., Kirkland, C.L., Wyche, S., Wingate, M.T.D., Belousova, E., 2012. Zircon Lu–Hf isotopes and granite geochemistry of the Murchison Domain of the Yilgarn Craton: evidence for reworking of Eoarchean crust during Meso-Neoproterozoic plume-driven magmatism. *Lithos*, 148, pp.112–127.
- Klein, C., 2005. Some Precambrian banded iron-formations (BIFs) from around the world: their age, geologic setting, mineralogy, metamorphism, geochemistry, and origin. *American Mineralogist*, 90, pp.1473–1499.
- Kloppenburg, A., White, S., Zegers, T., 2001. Structural evolution of the Warrawoona Greenstone Belt and adjoining granitoid complexes, Pilbara Craton, Australia: implications for Archaean tectonic processes. *Precambrian Research*, 112, pp. 107–147.
- Kruckenbergh, S.C., Vanderhaeghe, O., Ferré, E.C., Teyssier, C., Whitney, D.L., 2011. Flow of partially molten crust and the internal dynamics of a migmatite dome, Naxos, Greece. *Tectonics*, 30, pp. 1–24.
- Lana, C., Kisters, A., Stevens, G., 2010. Exhumation of Mesoproterozoic TTG gneisses from the middle crust: insights from the Steynsdorp core complex, Barberton granitoid-greenstone terrain, South Africa. *Bulletin of the Geological Society of America*, 122, pp.183–197.
- Myers, J.S., Watkins, K.P., 1985. Origin of granite-greenstone patterns, Yilgarn Block, Western Australia. *Geology*, 13, pp.778–780.
- Moyen, J-F. and O. Laurent, 2018. Archean tectonic systems: A view from igneous rocks. *Lithos*, 302–303, pp.99–125.

- Ramsay, J.G., 1989. Emplacement kinematics of a granite diapir: the Chindamora batholith, Zimbabwe. *Journal of Structural Geology*, 11, pp.191–209.
- Ramsay, J.G., 1962. Interference patterns produced by the superposition of folds of similar type. *Journal of Geology*, 70, pp.466–481.
- Rey, P.F., Philippot, P., Thébaud, N., 2003. Contribution of mantle plumes, crustal thickening and greenstone blanketing to the 2.75–2.65 Ga global crisis. *Precambrian Research*, 127, pp.43–60.
- Roger, F., Teyssier, C., Respaut, J.-P., Rey, P.F., Jolivet, M., Whitney, D.L., Paquette, J.-L., Brunel, M., 2015. Timing of formation and exhumation of the Montagne Noire double dome, French Massif Central. *Tectonophysics*, 640–641, pp.53–69.
- Schwerdtner, W.M., 1982. Salt stocks as natural analogues of Archaean gneiss diapirs. *Geol. Rundschau* 71, 370–379.
- Snowden, P., 1984. Non-diapiric batholiths in the north of the Zimbabwe Shield. *Precambrian Tectonics Illustrations*, 2, pp.189–214.
- Stephansson, O., 1975. Polydiapirism of granitic rocks in the Svecofennian of central Sweden. *Precambrian Research*, 2, pp.189–214.
- Symington, N.J., Weinberg, R.F., Hasalova, P., Wolfram, L.C., Raveggi, M., Armstrong, R. A., 2014. Multiple intrusions and remelting-remobilization events in a magmatic arc: the St. Peter Suite, South Australia. *Geological Society of the American Bulletin*, 126, pp.1200–1218.
- Talbot, C.J., Jackson, M.P.A., 1987. Internal kinematics of salt diapirs. *American Association of Petrology and Geology Bulletin*, 71, pp.1068–1093.
- Van Kranendonk, M.J., Collins, W.J., Hickman, A., Pawley, M.J., 2004. Critical tests of vertical vs. horizontal tectonic models for the Archaean East Pilbara granite-greenstone Terrane, Pilbara Craton, Western Australia. *Precambrian Research*, 131, pp.173–211.
- Van Kranendonk, M.J., Ivanic, T.J., Wingate, M.T.D., Kirkland, C.L., Wyche, S., 2013. Long-lived, autochthonous development of the Archean Murchison domain, and implications for Yilgarn craton tectonics. *Precambrian Research*, 229, pp.49–92.
- Van Kranendonk, M.J., Smithies, R.H., Griffin, W.L., Huston, D.L., Hickman, A.H., Champion, D.C., Anhaeusser, C.R., Pirajno, F., 2014. Making it thick: a volcanic plateau origin of Palaeoarchean continental lithosphere of the Pilbara and Kaapvaal cratons. *Geological Society of London, Special Publications*, 389, pp.83–111.
- Vearncombe, J.R., 1998. Shear zones, fault networks, and Archean gold. *Geology*, 26, pp.855–858.
- Weinberg, R.F., Mark, G., 2008. Magma migration, folding, and disaggregation of migmatites in the Karakoram Shear Zone, Ladakh, NW India. *Geological Society of the American Bulletin*, 120, pp.994–1009.
- Weinberg, R.F., Schmeling, H., 1992. Polydiapirs: multiwavelength gravity structures. *Journal of Structural Geology*, 14, pp.425–436.
- Weinberg, R.F., van der Borgh, P., 2008. Extension and gold mineralization in the Archean Kalgoorlie Terrane, Yilgarn Craton. *Precambrian Research*. 161, pp.77–88.
- Weinberg, R.F., Veveakis, E., Regenauer-Lieb, K., 2015. Compaction-driven melt segregation in migmatites. *Geology*, 43, pp.471–474.
- Wiedenbeck, M., Watkins, K.P., 1993. A time scale for granitoid emplacement in the Archean Murchison Province, Western Australia, by single zircon geochronology. *Precambrian Research*, 61, pp.1–26.

- Yin, A., 2004. Gneiss domes and gneiss dome systems, in: Special Paper 380: Gneiss Domes in Orogeny, pp. 1–14.
- Zegers, T.E., White, S.H., de Keijzer, M., Dirks, P.H., 1996. Extensional structures during deposition of the 3460 Ma Warrawoona Group in the eastern Pilbara Craton, Western Australia. *Precambrian Research*, 80, pp.89–105.
- Zibra, I., Gessner, K., Smithies, H.R., Peternell, M., 2014a. On shearing, magmatism and regional deformation in Neoproterozoic granite-greenstone systems: insights from the Yilgarn Craton. *Journal of Structural Geology*, 67, pp.253–267.
- Zibra, I., Smithies, R.H., Wingate, M.T.D., Kirkland, C.L., 2014b. Incremental pluton emplacement during inclined transpression. *Tectonophysics*, 623, pp.100–122.
- Zibra, I., Clos, F., Weinberg, R.F., Peternell, M., 2017. The c. 2730 Ma onset of the Neoproterozoic Yilgarn orogeny. *Tectonics*, 36, pp. 1787–1813
- Zibra, I., Peternell, M., Schiller, M., Wingate, M.T.D., Lu, Y., Clos, F., 2018. Tectono-magmatic evolution of the Neoproterozoic Yalgoo Dome (Yilgarn Craton). Diapirism in a pre-orogenic setting. Geological Survey of Western Australia, Report 176.

Supplementary material

Supplementary material 1: Major and trace elements chemistry of the five granite groups in the Yalgoo Dome.

Refer to electronic data file" Appendix 4.1.xls"

CHAPTER 5

Conclusion



1 Introduction

This thesis investigates the tectono-magmatic evolution of the Archean Yalgoo Dome in the Murchison Domain of the Yilgarn Craton (Western Australia). The project aimed at:

- Re-evaluate the structural and metamorphic evolution of the Yalgoo Dome.
- Reconstruct the processes that generated a stable continental crust towards the end of the Archean eon.

These points are addressed in Chapters 2–4 using a multidisciplinary approach combining field mapping, petrography, whole-rock major and trace element geochemistry, thermodynamic modeling and geothermobarometry. This final chapter brings the findings of the thesis together, drawing conclusions for the evolution of the Yalgoo Dome and evaluates future outlooks.

2 Reworking of crustal rocks and diapirism

Chapter 2 reassesses the structural evolution of the Yalgoo Dome by detailing the structures exposed in the migmatitic core of the dome. The core contains multi-scale domes and basins, previously interpreted as the result of superposed folds (Fig. 10 in Appendix A; Myers and Watkins, 1985).

The outcome of the structural mapping presented in Chapter 2 suggests that this interpretation is unlikely and shows that these structures are better interpreted as vertical sheath folds developed in a single, progressive deformation event (D_1). This deformation event was interpreted to be a result of the diapiric ascent of partially molten tonalites during the main dome-forming event associated with the intrusion of the Goonetarra Granodiorite at 2760–2740 Ma (Zibra et al., 2018; Chapter 2). These sheath folds forming the domes and basins, were later overprinted by D_2 folds during the last phases of diapirism. The youngest deformation event recorded in the area (D_3) includes shear zones with thrust-to-the-west kinematics that developed within a network of north-trending, c. 2707 Ma granitic dykes. This event is roughly coeval with a regional-scale EW shortening event, characterized by W-verging thrusts intruded by contemporaneous magmas recorded east of the Yalgoo Dome by the c. 2700 Ma Lakeside pluton (Zibra et al., 2014).

Chapter 3 estimates pressure, temperature and fluid conditions recorded in the migmatitic core of the Yalgoo dome during anatexis and diapirism at 2760–2740 Ma. Phase equilibria modelling and geothermobarometry on the high-grade tonalites and amphibolites suggest that melting of these rocks during D_1 – D_2 occurred at mid-crustal conditions of 3–9 kbar and 700–800 °C. Widespread melting and remobilization of mid-crustal rocks represented by migmatization in the core of the dome, occurred partly as a result of an external influx of LILE-rich fluids, possibly derived from the crystallization of the Goonetarra Granodiorite between 2760 and 2740 Ma. In this chapter I concluded that H_2O transfer through the crust assisted remobilization of mid-crustal rocks by enhancing melt production of old tonalites from <5 vol% to up to 15–30 vol%. The accumulation of the Goonetarra Granodiorite and the anatexis of these pre-existing mid-crustal rocks decreased both the density and viscosity of mid-crustal levels below a mafic-ultramafic overburden, causing diapirism in response to this crustal-scale gravitational instability.

The main findings of chapters 2 and 3 provide insights into the processes and mechanisms responsible for the 2760–2740 Ma crustal reworking episode in the Yalgoo Dome. The development of the dome-and-keel architecture was related to an intense mantle activity between 2825–2760 Ma, which created a crustal-scale gravitational instability with the deposition of thick packages of greenstones in the upper crust and by establishing the thermal conditions to weaken the crust. This thermal perturbation triggered a set of cascading reactions starting with the partial melting of the mafic lower crust, which lead to the formation of the 2760–2740 Ma Goonetarra Granodiorite, intruded into the middle crust, and causing melting of the 2970–2900 Ma tonalites and amphibolites in the core of the dome. The consequent mid-crustal decrease in bulk viscosity favored doming of the gravitationally unstable, low-density granitoids and sagduction of the dense, overlying greenstones. In essence, the evolution of crustal magmatism and diapiric rise of the Yalgoo dome records the transfer of heat and fluids waves through the crust.

3 Intermittent crustal reworking and development of continental crust

In the Yalgoo dome area, I identified five granitic groups, whose crystallizing ages spans a >350 Myr long evolution, between 2970 and 2600 Ma, recording a pulsed magmatic evolution (Chapter

4). Such evolution can be separated into four stages of granitic magmatism based on age, geochemical signature and structural position within the dome (Fig. 1a; Chapter 4). The oldest rocks are TTGs defining Stage 1 (2970–2900 Ma). This was followed by high-Mg granitic rocks and transitional TTGs of Stage 2 (2760–2740 Ma), and transitional TTG dykes were emplaced during Stage 3 (c. 2707 Ma) and the latest magmatism of Stage 4 comprise two suites: A-type and low-Ca (2640–2600 Ma; Fig. 1a; Chapter 4). These four phases are in turn tied in with three separate phases of mantle-derived, mafic-ultramafic magmatism. The first phase was coeval with Stage 1 TTGs and is recorded by greenstones of the Gossan Hill Formation (2963–2958 Ma) (Phase 1; Fig. 1a). After a magmatic hiatus lasting approximately 100 Myr, Phase 2 commenced with the eruption of the 2825–2805 Ma Norie Group followed by the 2800–2760 Ma Polelle Group (Ivanic et al., 2012; Van Kranendonk et al., 2013; Ivanic et al., 2015) and ended up with the diapiric emplacement of Stage 2 granitic rocks (Fig. 1a) described above (section 2.1). This episode of crustal reworking, lasting c. 20 Myr, was dominated by the buoyancy of granitic plutons and migmatitic bodies that led to the vertical re-arrangement of the crust and genesis of the dome-and-keel geometry (section 2.1). The onset of the third phase (Phase 3; Fig. 1a) is associated with a new stage of extrusion of mantle-derived komatiitic basalts such as those of the 2735–2710 Ma Yalgowra Suite and 2720 Ma Glen Group (van Kranendonk et al., 2013), outcropping only in the northern part of the Murchison Domain (Ivanic et al., 2012). Phase 3 coincided with shortening related to the Neoproterozoic Yilgarn Orogeny (2730–2640 Ma; Zibra et al., 2017), resulting in the emplacement of Stage 3 transitional TTG dykes (Fig. 1a). The final magmatic episode is not directly related to mantle-derived magmatism and occurred during the intrusion of post-orogenic A-type and low-Ca granites (stage 4). which mark the end of felsic magmatism in the Yalgoo Dome.

The Late-Archean evolution of the Yalgoo Dome derived in this thesis share a similar evolution with the domes in the East Pilbara Terrane (van Kranendonk et al., 2004; Pawley et al., 2004) and can be generalized by comparing it to the example of the Mt Edgar Dome (Fig. 1b), the best exposed and most studied dome-and-keel structure in the East Pilbara (Collins et al., 1989; Gardiner et al., 2017). The granitoids in the Mt Edgar Dome follow the same temporal trend from TTGs, to transitional TTGs and then to low-Ca magmatism as in the Yalgoo Dome, but displaced in time

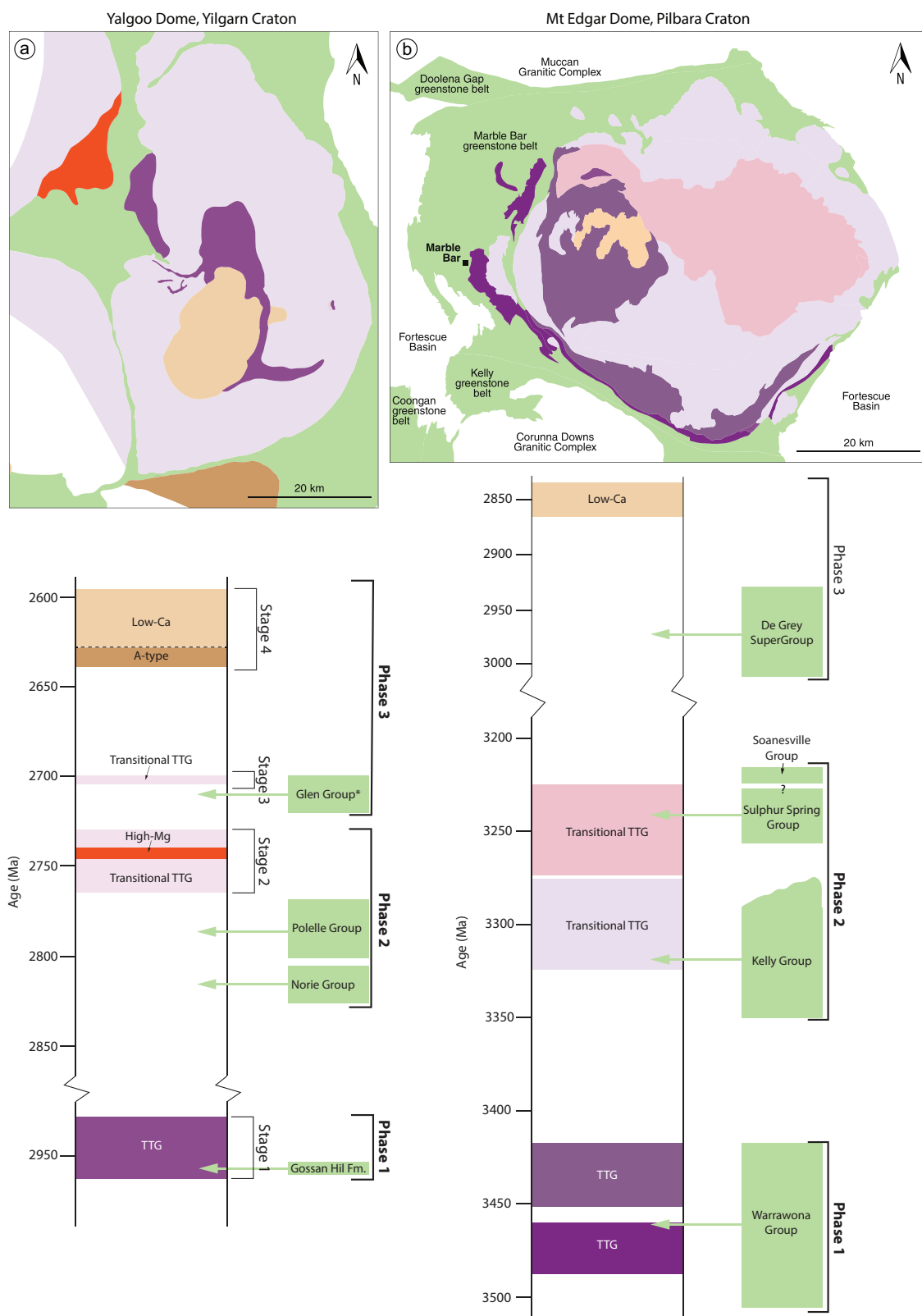


Figure 1: Simplified geological maps and stratigraphic columns in the Yalgoo Dome and Mt Edgar Dome in the East Pilbara Terrane. (a) In the Yalgoo Dome, three phases of mantle-derived greenstones (green boxes) are followed by crustal reworking and intrusion of granites, divided in four stages showing transition from TTGs to transitional TTGs and high-Mg granitoids, and finally to low-Ca and A-type magmatism (Chapter 4). The greenstones of the Glen Group* do not outcrop in the Yalgoo Dome but has been recognized in the NE section of the Murchison Domain. (b) This evolution is comparable with the three-phase evolution of the Mt Edgar Dome in the East Pilbara Terrane. Although the chemical evolution is similar, the Mt Edgar Dome lacks A-type magmatism and the high-Mg-granitoids present in the Yalgoo dome. Mafic and granitic groups are after van Kranendonk et al. (2007) (map modified after Gardiner et al., 2017).

(Figs 1, 2). Each major granitic intrusion was also pre-dated by the deposition of mafic-ultramafic sequences of greenstones, divided into three major phases. The first phase (Phase 1) involves the greenstones of the Warrawoona Group (3525–3426 Ma; van Kranendonk, 2006, 2007) partly overlapping in time with a series of TTG intrusions between 3484 and 3416 Ma (Fig. 1b; Champion and Smithies, 2007). A second phase (Phase 2) is associated with the deposition of mafic-ultramafic rocks between 3350 and <3240 Ma, which is followed by 3324–3223 Ma transitional TTGs (Champion and Smithies, 2007) (Figs 1b, 2b). The last magmatic phase (Phase 3) starts with the extrusion of the greenstones of the De Grey Supergroup (3020–2930 Ma; Van Kranendonk et al., 2007) followed nearly 70 Myr later by the intrusion of the K-rich granitic rocks of the Split Rock Supersuite

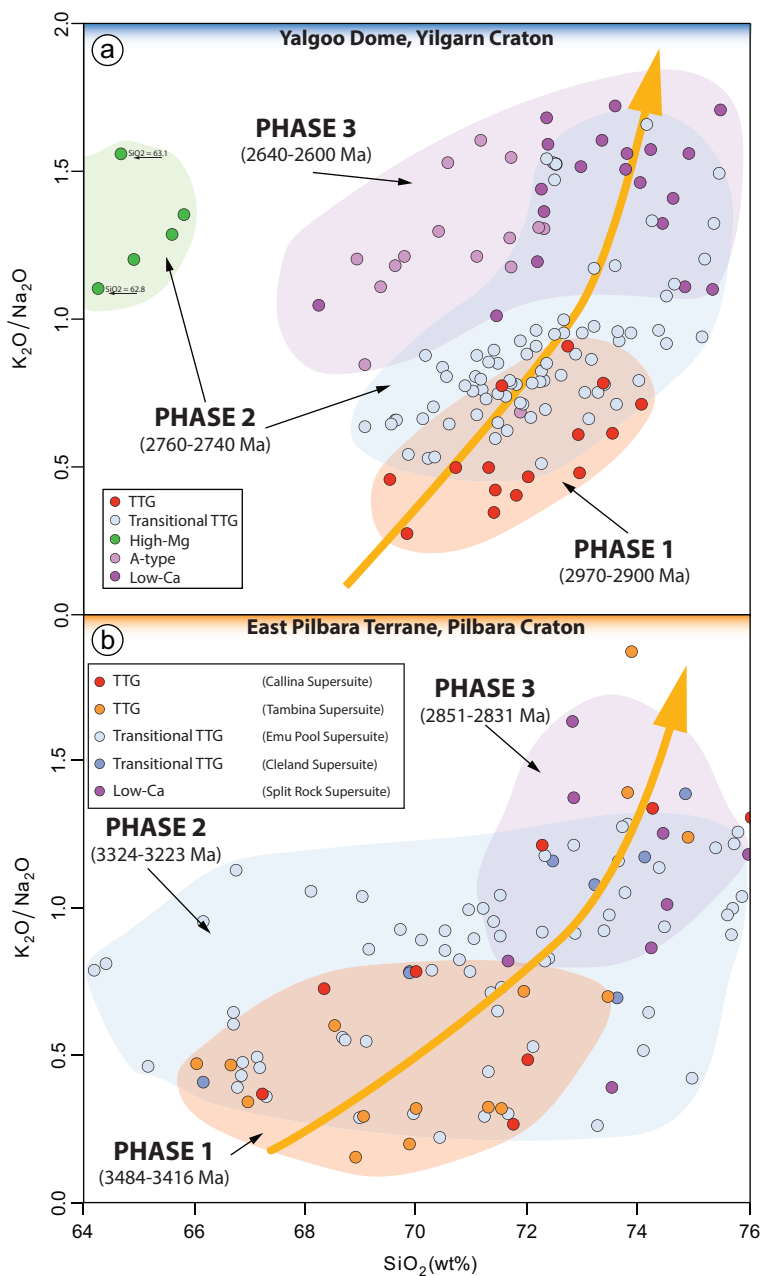


Figure 2: K_2O/Na_2O vs SiO_2 showing the evolution of magmatism in the Yalgoo Dome (a) and in the East Pilbara Terrane (b). The trends are comparable and record the transition from sodic to potassic granitoids as would be expected with intracrustal reworking causing chemical differentiation of the crust. Notice the different absolute times and duration of the evolution of the two regions. Whole-rock data from the Mt Edgar Dome and the other domes in the East Pilbara Terrane were extracted from the [Geological Survey of Western Australia's geochronology and geochemistry online databases](#).

(2851–2831 Ma) (Fig. 1b), which have a chemical composition akin to the low-Ca in the Yalgoo Dome (Fig. 2b).

The magmatic evolution of the Yalgoo Dome and of the domes of the East Pilbara Terrane reflects the process of stabilization of continental crust through intermittent episodes of enhanced magmatism. The first order driver for the evolution of the crust was the vigor and duration of phases of juvenile magmatic input accompanied by crustal reworking in the form of anatexis and granitic magmatism. The chemistry of granitoids records the secular shift from a sodic to potassic composition ($K_2O/Na_2O > 1$; Fig. 2), indicating a long-lived melting wave gradually migrating from deep basaltic sources of TTGs, to shallow granitic sources of low-Ca granites (van Kranendonk et al., 2015; Chapter 4). Each crustal reworking phase generated more evolved pulses of granitic magmas that intruded into the medium and upper crust amplifying the dome-and-keel architecture, in a fashion that has no equal on modern Earth. In the older East Pilbara Terrane (3550–2850 Ma), the duration and volume of mafic-ultramafic rocks for each phase was far greater than in the younger Yalgoo Dome (2970–2600 Ma; Fig. 1) and this might reflect secular cooling in the Archean mantle (Herzberg et al., 2010). This first order evolution is modified locally by the appearance of high-Mg granitoids and A-type granites in the Yalgoo Dome (Fig. 1a) and reflect the worldwide diversification of granitic magmatism during Late Archean (Laurent et al., 2014; Moyen and Laurent, 2018).

4 Future outlook

4.1 Origin of the high-Mg granitoids

High-Mg granitic rocks are described in other cratons as Archean sanukitoids and they are often related to a source component derived from a metasomatized lithosphere (Shirey and Hanson, 1984; Martin et al., 2005, 2009; Heilimo et al., 2010) or they are viewed as TTG melts which incorporated variable amounts of mantle rocks before crustal emplacement (Rapp et al., 1999, 2010). Given that the appropriate modern geodynamic environment capable of supplying sufficient volumes of hydrous and LILE-enriched metasomatic agents/melts to the upper mantle is a subduction zone, many authors contend that similar processes would have characterized the Archean (Heilimo et al., 2010; Farina et al., 2015). However, melts with sanukitoid signature might form in other geological

contexts, such as asymmetric drips of lower crustal rocks during regional delamination (Gao et al., 2009) or along transpressional lineaments, where continental crust is down-thrusted into the upper mantle (Campbell et al., 2014). The geodynamic significance of these Archean high-Mg granitic rocks remains to be refined in the future, but it is clear that they required a significant involvement of fluids (or melts) and mantle rocks (Moyen and Laurent, 2018) and their world-wide appearance in the Late Archean suggests they are related to a substantial change in mantle dynamics and plate tectonics at that time (Halla et al., 2017).

4.2 Archean crust and depleted mantle coupling?

In this Ph.D. thesis I used the Yalgoo Dome as a case study to infer the processes that lead to the development of the continental crust at the end of the Archean Eon. There is substantial evidence that multiple mantle-related thermal perturbations remobilized large sections of previously formed crust causing a cascade of crustal recycling episodes to generate the dome-and-keel structure in the Yalgoo Dome. This large-scale process of crustal growth required numerous stages in which the lithosphere was heated and softened, leading to melting and genesis of felsic magmas and triggered doming (Choukroune et al., 1995). Yet, the magnitude of these pulsed episodes seems incompatible with the presence of the thick and highly depleted mantle roots of Archean Cratons, which would shelter the crust from thermal events (Bédard et al., 2013; Bédard, 2017). This disparity raises a debate on how and when the sub-continental lithospheric mantle (SCLM) formed and coupled with the crust. On a global scale, a compilation of Re–Os model ages of sulphides from Archean mantle xenoliths and mantle wedge peridotites suggests that the bulk of the Archean is broadly synchronous with the peaks of crust formation in Archean terranes between 3300 and 2700 Ma (Griffin et al., 2014). However, on a craton-scale, the formation and coupling of Archean crust and SCLM is difficult to discern and several hypotheses have been proposed.

A first hypothesis is that crust and mantle share an allochthonous relationship. One example to back this assumption is the Vredefort structure in the Kaapvaal, where a Proterozoic meteorite impact exposed deep Archean crustal rocks. Moser et al. (2001) investigated these rocks and concluded that physical pairing of crust and mantle occurred 120 Ma after the major crust assembly. This implies

an allochthonous relationships between crust and depleted mantle keels, consistent with continental genesis models that portray crust and mantle lithosphere as components created in different tectonic settings before juxtaposition (Jordan et al., 1975; Halla et al., 2017). A second hypothesis involves in-situ formation of both SCLM and crust through multiple mantle melting that progressively created highly depleted lithospheric roots. When large sections of the upper mantle were depleted, the crust-mantle system could stabilize (Moyen and Martin, 2018) effectively leading to cratonization.

Although we favor the second hypothesis, because of the intermittent nature of magmatism in Archean terranes, a clear answer cannot be given and the nature of the relationship between Archean crust and SCLM remains largely undetermined. Future studies might refine the formation of the SCLM and connect it with the polycyclic evolution of the crust in Archean cratons. Yet, this challenge presents a serious obstacle as Archean SCLM can only be investigated indirectly through xenoliths in kimberlite and lamprophyres pipes and orogenic peridotites in collisional belts where correlations with Archean crust are complicated. Continental crust and SCLM are strange partners (Arndt et al., 2002) and unraveling how, when and why they coupled are part of future challenges along the path to understand the fundamental changes that occurred at the end of the Archean eon.

4.3 Which came first, subduction or continental crust?

Is it the onset of subduction processes that led to the eventual development and stabilization of the continents or is it the late Archean formation of continental lithosphere with a thick stable root that triggered the onset of plate tectonics and subduction? A model that is gaining ground amongst the scientific community explains the Late Archean geodynamic changes and stabilization of continents as a results of the global initiation of “modern-style” plate tectonics between 3000 and 2500 Ma (Laurent et al., 2014). The establishment of subduction–collision processes were the consequence of the first order Earth's cooling (Moyen and Martin, 2012), which in turn regulated the thickness, temperature, composition and rheology of the continental and oceanic crusts (Laurent et al., 2014). Second-order thermal attributes of each craton influenced the timing of this transition, but invariably within a limited time span (~500 Ma).

A challenging question to this mainstream model is how to resolve the sudden shift in Earth's geodynamics by slow, gradual cooling of the Earth. What if the survival of the SCLM triggered plate tectonics? Once assembled, buoyant and rigid continental plates could move, collide against nearby mafic crust and cause localized subduction (or the dripduction of Moyen and Laurent, 2018) of denser material at the edges of cratons, allowing metasomatism of mantle rocks and subsequent formation of high-Mg granitic rocks. Perhaps the Late Archean coupled formation and preservation of continental, that are the structural components of contemporary continental plates, might have been the trigger for subduction-like processes and plate tectonics.

4 Conclusion

The Yalgoo Dome is part of a large dome-and-keel structure exposed in the granite–greenstone terrane of the Yilgarn Craton. More than 350 Myr of tectono-magmatic evolution (2970–2600 Ma) is recorded by multiple granitoid intrusions cored by migmatitic bodies and flanked by a composite greenstone belt. In this thesis I recognized three phases of mantle-derived mafic–ultramafic magmatism accompanied by crustal reworking of older crust by anatexis and granite magmatism episodes that provoked the intrusion of a wide diversity of granitic rocks. The first phase of mantle magmatism includes greenstones accompanied by TTGs at 2970–2900 Ma. A second phase started with the deposition of thick mafic-ultramafic greenstones between 2825 and 2760 Ma. This major magmatic event caused an array of cascading reactions, tracking the migration of a heat and magma wave through the crust, beginning with partial melting of the mafic lower crust and underlying metasomatized mantle, forming the 2760–2740 Ma transitional TTGs and the c. 2747 Ma high-Mg suite (Archean sanukitoid). The third phase started with a renewed phase of mafic-ultramafic greenstones (2730–2710 Ma) and crustal reworking which gave rise to the c. 2707 Ma transitional TTGs dykes and two suites of K-rich granitic intrusions (the 2640–2600 Ma post-tectonic A-type and Low-Ca granites).

In this thesis I also investigated the initial conditions and processes that lead to anatexis and diapirism of the old migmatitic core (2970–2900 Ma) of the dome during phase 2. This area defines multi-scale domes-and-basins, formerly interpreted as the result of superposed folding. Structural

mapping demonstrates that these geometries result from vertical sheath folds developed in a single, progressive syn-anatectic deformation event (D_1) refolded by D_2 folds during the last phases of diapirism. D_1 and D_2 took place during the intrusion of the 2760–2740 Ma Goonetarra Granodiorite, which provided heat and LILE-rich fluids that induced water-fluxed melting of the older tonalites at mid-crustal conditions (3–9 kbar and 700–800 °C). This process softened the stiff mid-crustal levels allowing sagduction of the dense greenstone overburden and diapirism of hot migmatitic and magmatic bodies. The evolution of crustal magmatism and diapiric rise of the Yalgoo dome at 2760–2740 Ma is evidence of a large-scale crustal remobilization through the upward migration of a wave of heat and fluids mediated by crustal anatexis and magma migration.

In summary, the tectono-magmatic evolution of the Yalgoo Dome records the stepwise development of a felsic continental crust, in response to major phases of mantle-derived mafic-ultramafic magmatism accompanied by crustal reworking at 2970–2900 Ma, 2760–2740 Ma and 2707–2600 Ma. Granitic magmatism records a secular shift from sodic (i.e. TTG) to increasingly potassic compositions (transitional TTG and low-Ca suites), including the appearance of high-Mg granitoids (Archean sanukitoids) during the main-dome forming episode at c. 2750 Ma. Comparable evolution has been recorded in the older domes of the East Pilbara Terrane (3550–2850 Ma), but in the Yalgoo Dome the Late Archean appearance of A-type and high-Mg granitoids reflect the diversification of granitic magmatism during Late Archean, likely linked to the onset of a different tectonic regime.

References

- Arndt, N.T., Lewin, É. and Albarède, F., 2002. Strange partners: formation and survival of continental crust and lithospheric mantle. Geological Society, London, Special Publications, 199(1), pp.91–103.
- Bédard, J.H., Harris, L.B. and Thurston, P.C., 2013. The hunting of the snArc. *Precambrian Research*, 229, pp.20–48.
- Bédard, J.H., 2017. Stagnant lids and mantle overturns: implications for Archean tectonics, magma genesis, crustal growth, mantle evolution, and the start of plate tectonics. *Geoscience Frontiers*, 9, pp. 11–49.
- Campbell, I.H., Stepanov, A.S., Liang, H.Y., Allen, C.M., Norman, M.D., Zhang, Y.Q. and Xie, Y.W., 2014. The origin of shoshonites: new insights from the Tertiary high-potassium intrusions of eastern Tibet. *Contributions to Mineralogy and Petrology*, 167(3), pp.1–22.
- Champion, D.C. and Smithies, R.H., 2007. Geochemistry of Paleoproterozoic Granites of the East Pilbara Terrane, Pilbara Craton, Western Australia: implications for Early Archean Crustal Growth. *Developments in Precambrian Geology*, 15, pp.369–409.

- Choukroune, P., Bouhallier, H. and Arndt, N.T., 1995. Soft lithosphere during periods of Archean crustal growth or crustal reworking. *Geological Society, London, Special Publications*, 95(1), pp.67–86.
- Collins, W.J., 1989. Polydiapirism of the Archean Mount Edgar Batholith, Pilbara Block, Western Australia. *Precambrian Research*, 43(1–2), pp.41–62.
- Farina, F., Albert, C. and Lana, C., 2015. The Neoproterozoic transition between medium- and high-K granitoids: clues from the Southern São Francisco Craton (Brazil). *Precambrian Research*, 266, pp.375–394.
- Gao, S., Zhang, J., Xu, W. and Liu, Y., 2009. Delamination and destruction of the North China Craton. *Chinese Science Bulletin*, 54(19), pp.3367–3378.
- Gardiner, N.J., Hickman, A.H., Kirkland, C.L., Lu, Y., Johnson, T. and Zhao, J.X., 2017. Processes of Crust Formation in the Early Earth Imaged through Hf isotopes from the East Pilbara Terrane. *Precambrian Research*, 297, 56–76.
- Griffin, W.L., Begg, G.C. and O'Reilly, S.Y., 2013. Continental-root control on the genesis of magmatic ore deposits. *Nature Geoscience*, 6(11), pp.905–910.
- Halla, J., Whitehouse, M.J., Ahmad, T. and Bagai, Z., 2017. Archean granitoids: an overview and significance from a tectonic perspective. *Geological Society, London, Special Publications*, 449(1), pp.1–18.
- Heilimo, E., Halla, J. and Hölttä, P., 2010. Discrimination and origin of the sanukitoid series: geochemical constraints from the Neoproterozoic western Karelian Province (Finland). *Lithos*, 115(1), pp.27–39.
- Herzberg, C., Condie, K. and Korenaga, J., 2010. Thermal history of the earth and its petrological expression. *Earth and Planetary Science Letters*, 292, pp.79–88.
- Ivanic, T.J., Li, J., Meng, Y., Guo, L., Yu, J., Chen, S.F., Wyche, S. and Zibra, I., 2015. Yalgoo, WA Sheet 2241: Geological Survey of Western Australia, 1:100 000 Geological Series.
- Ivanic, T.J., Van Kranendonk, M.J., Kirkland, C.L., Wyche, S., Wingate, M.T.D. and Belousova, E.A., 2012. Zircon Lu–Hf isotopes and granite geochemistry of the Murchison Domain of the Yilgarn Craton: evidence for reworking of Eoarchean crust during Meso-Neoproterozoic plume-driven magmatism. *Lithos*, 148, pp.112–127.
- Jordan, T.H., 1988. Structure and formation of the continental tectosphere. *Journal of Petrology*, (1), pp.11–37.
- Laurent, O., Martin, H., Moyen, J.F. and Doucelance, R., 2014. The diversity and evolution of late-Archean granitoids: evidence for the onset of “modern-style” plate tectonics between 3.0 and 2.5 Ga. *Lithos*, 205, pp.208–235.
- Martin, H., Moyen, J.F. and Rapp, R., 2009. The sanukitoid series: magmatism at the Archean–Proterozoic transition. *Earth and Environmental Science Transactions of the Royal Society of Edinburgh*, 100(1–2), pp.15–33.
- Mikkola, P., Huhma, H., Heilimo, E. and Whitehouse, M., 2011. Archean crustal evolution of the Suomussalmi district as part of the Kianta Complex, Karelia: constraints from geochemistry and isotopes of granitoids. *Lithos*, 125(1), pp.287–307.
- Moser, D.E., Flowers, R.M. and Hart, R.J., 2001. Birth of the Kaapvaal tectosphere 3.08 billion years ago. *Science*, 291(5503), pp.465–468.
- Moyen, J.F. and Martin, H., 2012. Forty years of TTG research. *Lithos*, 148, pp.312–336.
- Moyen, J.F. and Laurent, O., 2018. Archean tectonic systems: A view from igneous rocks. *Lithos*, 302–303, pp.99–125.

- Myers, J.S. and Watkins, K.P., 1985. Origin of granite-greenstone patterns, Yilgarn block, Western Australia. *Geology*, 13(11), pp.778–780.
- Pawley, M.J., Van Kranendonk, M.J. and Collins, W.J., 2004. Interplay between deformation and magmatism during doming of the Archaean Shaw granitoid complex, Pilbara Craton, Western Australia. *Precambrian Research*, 131(3), pp.213–230.
- Rapp, R.P., Norman, M.D., Laporte, D., Yaxley, G.M., Martin, H., Foley, S.F., 2010. Continental formation in the Archean and chemical evolution of the cratonic lithosphere: melt–rock reaction experiments at 3–4 GPa and petrogenesis of Archean Mg–diorites (Sanukitoids). *Journal of Petrology*, 51, pp.1237–1266.
- Rapp, R.P., Shimizu, N., Norman, M.D. and Applegate, G.S., 1999. Reaction between slab–derived melts and peridotite in the mantle wedge: experimental constraints at 38 GPa. *Chemical Geology*, 160(4), pp. 335–356.
- Shirey, S.B. and Hanson, G.N., 1984. Mantle–derived Archaean monozodiorites and trachyandesites. *Nature*, 310, pp. 222–224.
- Van Kranendonk, M.J., Collins, W.J., Hickman, A. and Pawley, M.J., 2004. Critical tests of vertical vs. horizontal tectonic models for the Archaean East Pilbara granite–greenstone terrane, Pilbara craton, Western Australia. *Precambrian Research*, 131(3-4), pp.173–211.
- Van Kranendonk, M.J., Collins, W.J., Hickman, A. and Pawley, M.J., 2004. Critical tests of vertical vs. horizontal tectonic models for the Archaean East Pilbara granite–greenstone terrane, Pilbara craton, western Australia. *Precambrian Research*, 131(3), pp.173–211.
- Van Kranendonk, M.J., 2006. Volcanic degassing, hydrothermal circulation and the flourishing of early life on Earth: a review of the evidence from c. 3490–3240 Ma rocks of the Pilbara Supergroup, Pilbara Craton, Western Australia. *Earth-Science Reviews*, 74(3), pp.197–240.
- Van Kranendonk, M.J., Hugh Smithies, R., Hickman, A.H. and Champion, D.C., 2007. Secular tectonic evolution of Archean continental crust: interplay between horizontal and vertical processes in the formation of the Pilbara Craton, Australia. *Terra Nova*, 19(1), pp.1–38.
- Van Kranendonk, M.J., Smithies, R.H., Griffin, W.L., Huston, D.L., Hickman, A.H., Champion, D.C., Anhaeusser, C.R. and Pirajno, F., 2015. Making it thick: a volcanic plateau origin of Palaeoarchean continental lithosphere of the Pilbara and Kaapvaal cratons. *Geological Society, London, Special Publications*, 389(1), pp.83–111.
- Zibra, I., Gessner, K., Smithies, H.R., Peternell, M., 2014. On shearing, magmatism and regional deformation in Neoproterozoic granite-greenstone systems: insights from the Yilgarn Craton. *Journal of Structural Geology*, 67, pp.253–267.
- Zibra, I., Clos, F., Weinberg, R.F., Peternell, M., 2017. The c. 2730 Ma onset of the Neoproterozoic orogeny in the Yilgarn. *Tectonics*, 36, pp.1787–1813.
- Zibra, I., Peternell, M., Schiller, M., Wingate, M.T.D., Lu, Y., Clos, F., 2018. Tectono-magmatic evolution of the Neoproterozoic Yalgoo Dome (Yilgarn Craton). Diapirism in a pre-orogenic setting. *Geological Survey of Western Australia, Report 176*.

APPENDICES

APPENDIX A

Geological setting and literature review

This appendix starts with a review of the available geological, lithological and chemical knowledge for the Murchison Domain in the Yilgarn Craton of Western Australia (Fig. 1). The second part concentrates on the Yalgoo Dome, a prominent dome-and-keel structure located in the westernmost part of the Murchison Domain. We describe the older granite-greenstone classification and the structural characterization of the dome with data available before the start of this Ph.D. thesis. Structural and stratigraphic updates can be found in the work of Zibra et al. (in press) in Appendix B.

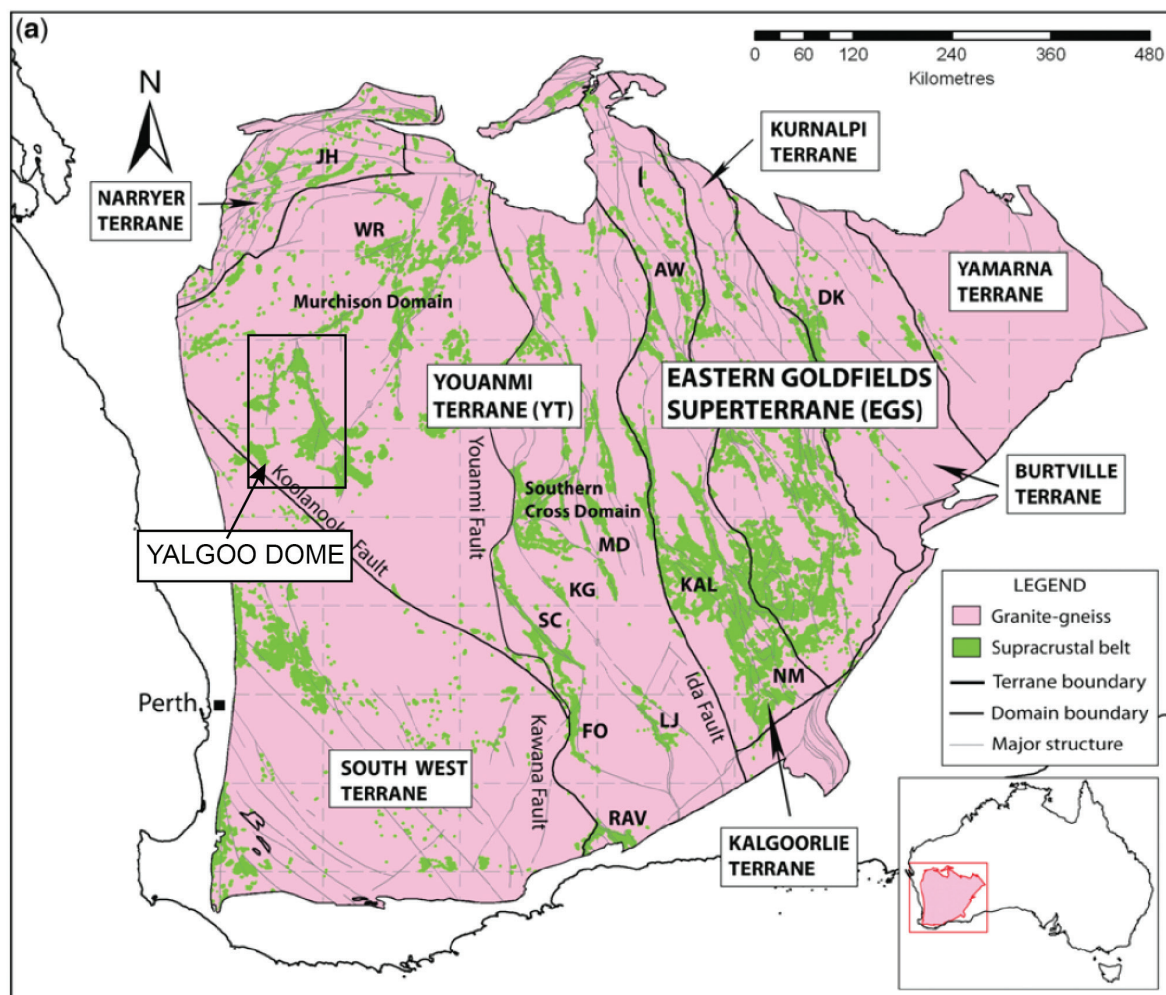


Figure 1: Lithotectonic map of the Yilgarn Craton and its terranes. The Yalgoo Dome is located in the westernmost part of the Murchison Domain of the Youanmi Terrane (modified after Mole et al., 2013).

1 Murchison Domain

1.1 Greenstones

The stratigraphy of the greenstones in the Murchison Domain has been recently updated by the work of van Kranendonk and Ivanic (2009) and Van Kranendonk et al. (2013). These authors identified four autochthonous volcano-sedimentary groups (Murchison Supergroup) based on mapping and geochronology in the NE part of the domain (Fig. 2). The older greenstones are collectively grouped as Mt Gibson Group and outcrop in the Golden Grove and Mount Gibson area, dated at 2960–2945 Ma and c. 2935 Ma respectively (Fig. 2; Yeats et al., 1996; Wang et al., 1998). These rocks are unconformably overlain by mafic volcanic rocks, felsic volcanoclastic sandstones and banded iron formation of the 2825–2805 Ma Norie Group (Van Kranendonk et al., 2013). On top of the Norie Group lies the voluminous 2800–2730 Ma Polelle Group, a continuous volcanic succession evolving from komatitic and tholeiitic basalts (c. 2.5 km Meekaharra Formation) to andesitic to rhyolitic volcanics and volcanoclastic rocks (c. 5 km Greensleeves Formation). The rocks

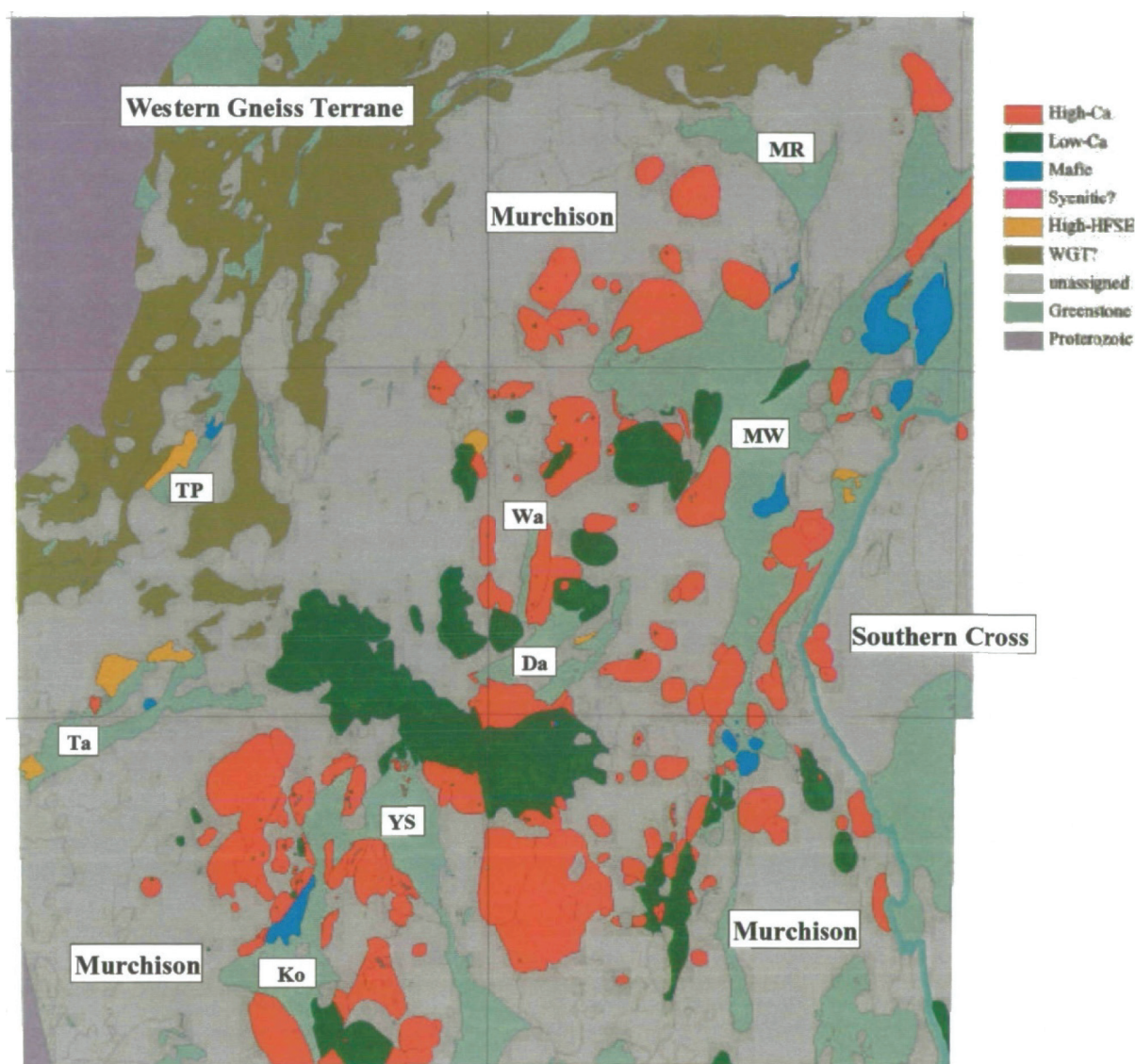


Figure 3: Granitoid suites in the northern part of the Murchison Domain and part of the Southern Cross Domain (from Champion and Cassidy, 2002).

1.2.2 Composite classification

This classification identifies seven granitic suites in the NW part of the Murchison Domain (Fig. 2):

- Unnamed Suite (>2900 Ma): the older granitoids in the Murchison Domain outcrop in the Mount Gibson area (c. 2935 Ma; Yeats et al., 1996) and in the migmatitic core of the Yalgoo Dome (c. 2912 Ma; Wiedenbeck and Watkins, 1990).
- Mount Kenneth Suite (2815–2800 Ma): these granitoids formed around large layered mafic-ultramafic intrusion (Ivanic et al., 2012).
- Annean Supersuite (2787–2733 Ma): the Culculli Suite includes tonalite-trondhjemite-granodiorite (TTG) with abundant mafic enclaves. The Eeylia Suite comprises the Peter Well Granodiorite, an intrusion with high field strength element enrichment (HFSE-group of Champion and Cassidy, 2002).

Group Area %	Lithologies	Field Characteristics	Geochemistry	Yonambi Terrane	Eastern Goldfields Superterrane	Comments
High-Ca >60%	granodiorite, granite, trondjemite. distributed both within and external to greenstone belts	strongly deformed to gneissic to mildly deformed; typically ovoid plutons (elongate parallel to structural grain); minor dykes/sills and small bodies; some allanite or sphene	high Na ₂ O, Na ₂ O/K ₂ O, low Th, LREE, Zr; mostly Y-depleted, Sr-undepleted; range of LILE, LREE and Th contents; younger rocks extend to more LILE-enriched compositions	>3.0 Ga-2.9? Ga, ca. 2.81 Ga, ca. 2.76 to 2.68 Ga; mostly 2.73-2.68 Ga	ca. 2.8 Ga (minor remnants); 2.74-2.65 Ga; majority 2.685 to 2.655 Ga; youngest members appear to occur within Kalgoorlie Terrane	high pressure partial melting of basaltic protoliths
Low-Ca >20%	granodiorite, granite mostly external to greenstone belts	mildly deformed to undeformed, locally strongly deformed; large intrusions (sheet-like) to small pods and dykes; biotite-dominant; allanite, sphene and fluorite-bearing	high K ₂ O, low Na ₂ O, high Rb, Th, LREE, Zr; moderately fractionated end-members	2.65-2.6? Ga; mostly 2.65 to 2.63 Ga; possibly also 2.685 Ga	2.655 to 2.63 Ga	partial melting of High-Ca type source rocks
High-HFSE 5-10%	granite, minor granodiorite mostly internal or marginal to greenstone belts	variably deformed, high-level intrusives, commonly spatially associated with volcanic rocks and volcanic complexes; presence of amphibole in a very felsic rock is diagnostic	distinctive combination of high FeO*, MgO, TiO ₂ , Y, Zr with low Rb, Pb, Sr, Al ₂ O ₃	3.01 to 2.92 Ga?, ca. 2.81 Ga, 2.76 Ga to 2.45 & younger?; also 2655-2620 Ma	>2.72 Ga to 2.665 Ga; 2.7 to 2.68 Ga most common; mostly geographically restricted to Kurnalpi Terrane & north-east Kalgoorlie Terrane	spatial association with VHMS mineral systems
Mafic 5-10%	diorite, granodiorite, granite, tonalite & trondjemite	variably deformed, distinctive dark-looking granites; form moderate to small sized plutons and common dikes and sills; common amphibole ± biotite ± pyroxene	low SiO ₂ (55-70+%), moderate to high Ni, Cr, MgO; range of LILE, LREE and Th; subdivided into high- and low-LILE	3.01 to 2.92 Ga?, ca. 2.81 Ga, 2.76 Ga to 2.10 Ga	>2.72 Ga to 2.65 Ga; possibly younger? LILE-enriched members tend to be ca. 2.665 and younger	common spatial association with gold mineralisation, especially high-LILE members
Syenitic <5%	syenite, quartz syenite internal or marginal to greenstone belt	commonly undeformed; distinctive red granites with green pyroxene (or amphibole); K-feldspar-rich, little or no quartz	high total alkalis (Na ₂ O + K ₂ O) 10-12%; commonly low MgO, FeO*, TiO ₂	none	ca. 2.65 Ga, and 2.655-2.645 Ga	some spatial association with gold mineralisation

Table 1: Summary of the main field and geochemical characteristic of the five granitoid suites (from Champion and Cassidy, 2007) identified by Champion and Cassidy (1997) in the Eastern Goldfields Superterrane, then extended to the whole Yilgarn Craton (Champion and Cassidy, 2002).

- Big Bell Suite (2735–2690 Ma): foliated tonalitic to monzogranitic rocks intruding the area between north of Meekatharra and south of Golden Grove (Schjøtte and Campbell, 1996).
- Tuckanarra and Jungar suites (2690–2640 Ma): strongly foliated granites emplaced in NS-trending transpressive shear zones (Zibra et al., 2014).

Bald Rock Supersuite (2640–2600 Ma): post-tectonic intrusion of undeformed biotite + muscovite monzogranites that intruded older granite-greenstone sequences.

1.3 Crustal evolution

In the Murchison Domain, the origin of granitoids and greenstones is linked. Figure 4 presents a frequency plot of granite magmatism, inherited zircons and greenstones age in the 2600–3200 Ma interval (Champion and Cassidy, 2002), pointing out several crustal formation and reworking episodes. The first magmatic peaks, marked by coeval development of greenstones and granites, took place at 3100–3000 Ma and 2970–2920 Ma. Following a hiatus of nearly 100 Myr, mafic-ultramafic

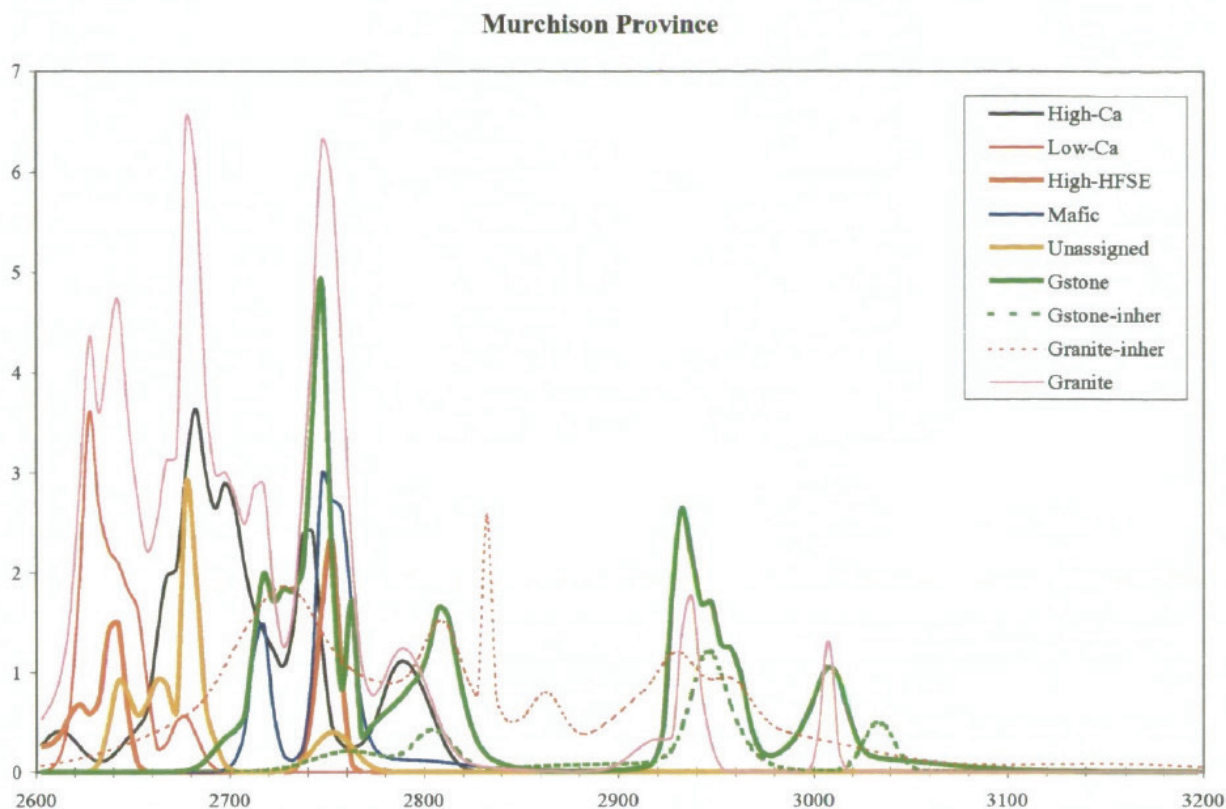


Figure 4: Frequency plot showing age of granite magmatism, inherited zircons and greenstones age in the 3200–2600 Ma interval for the Murchison Domain (after Champion and Cassidy, 2002).

magmatism resumed at c. 2825 Ma and culminated in 3 major episodes of crustal reworking and granite formation peaking at c. 2750 Ma, c. 2690 Ma and 2640–2620 Ma (Fig. 4).

These peak ages are corroborated by recent Lu-Hf isotopes data on zircons from granitic rocks, four felsic volcanics and two gabbro in the work of Ivanic et al. (2012). The diagram in figure 5a-b show three separate trends and a drastic change in the age of the source region for melts intruded in the Murchison Domain between c. 2970 and 2600 Ma. Early 2970–2900 Ma granitoids display a

vertical ϵHf array varying between -4 and +2 (Fig. 4a) and were explained as a juvenile input into a Meso-to-Paleoarchean crust (Fig. 4b; Ivanic et al., 2012). The second phase of juvenile magmatism at 2825–2760 Ma shows ϵHf from 0 to +3 and matured from a 3040 Ma source. A sudden change in the melting source occurred at 2760–2730 Ma, as the felsic volcanics of the Greensleaves and An-nean Supersuite granitoids show a wide vertical array of ϵHf , varying from 0 to -10 (Fig. 4a). The source of these granitoids could be old up to 3800 Ma (Fig. 4b). The ϵHf on c. 2720 and c. 2640 Ma granitoids indicates reactivation of a c. 3040 Ma source. The 2640–2600 Ma Bald Rock Suite is

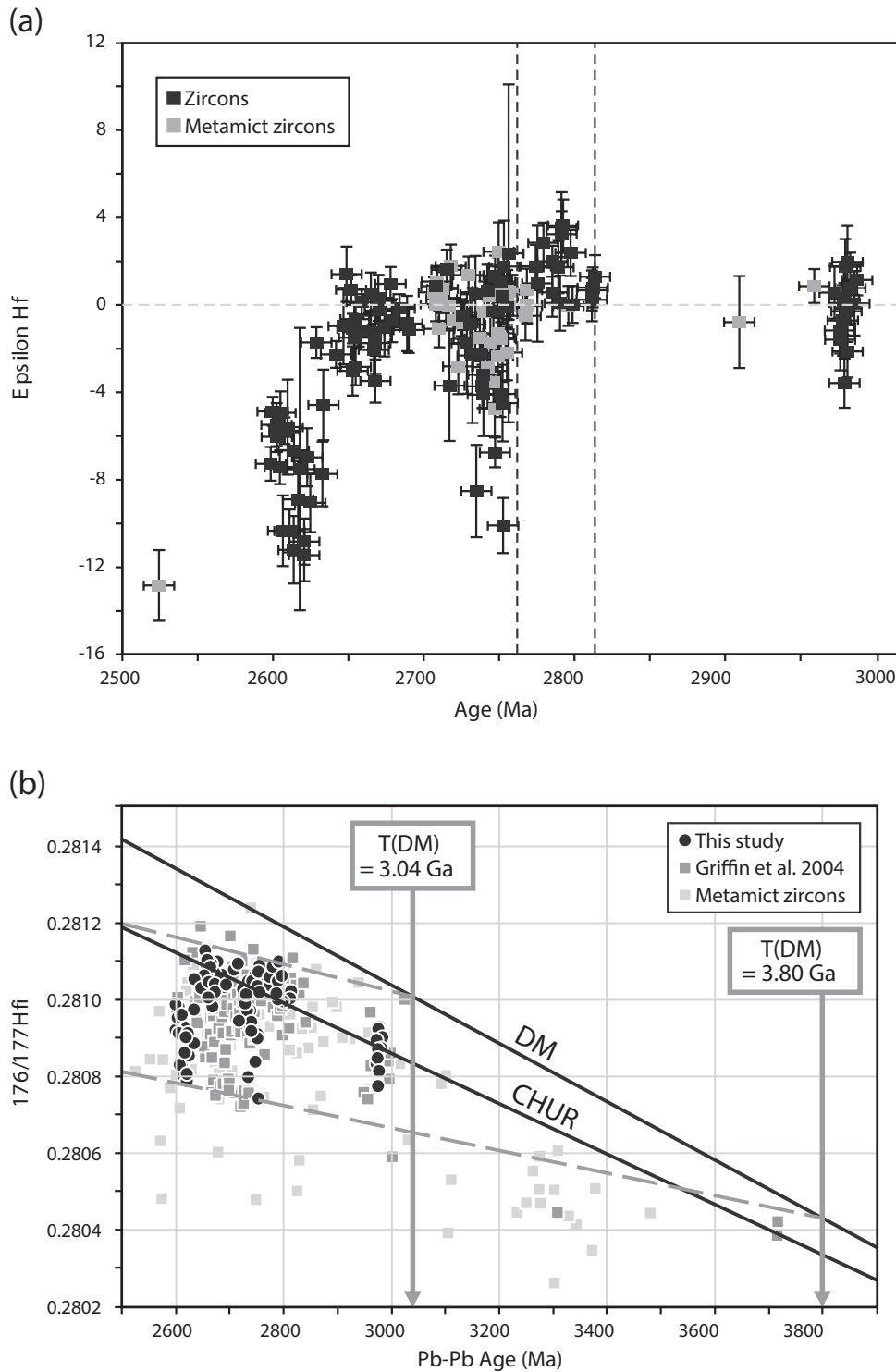


Figure 5: Diagrams showing Lu-Hf data for zircons of granitic rocks, felsic volcanics and few gabbro from the northern Murchison Domain (after Ivanic et al., 2012): (a) ϵHf vs ^{207}Pb - ^{206}Pb age (Ma) showing three major cycles of juvenile input (i.e. mafic greenstones) followed by crustal recycling and emplacement of granitic rocks; (b) $^{176}\text{Hf}/^{177}\text{Hf}$ initial vs. Pb-Pb age (Ma) showing depleted mantle (DM) and chondrite uniform reservoir (CHUR) evolution for reference. Dashed lines indicating the maximum and minimum depleted mantle model ages ($T_{(\text{DM})}$) in Ga to indicate the age of the source that generated the granitoids.

characterized by ϵ_{Hf} between -4 and -12 (Fig. 4a). Ivanic et al. (2012) explained this vertical array as melting of a source old up to 3800 Ma or by mixing of with a more juvenile component between 3000 and 2700 Ma.

Whole-rock Sm-Nd isotopes of granitoids in the Yilgarn Craton (Mole et al., 2013) yield similar results and distinguish four major magmatic episodes (Fig. 6): i) 2950–2920 Ma granitoids show Sm-Nd T_{DM}^2 ages ranging from 3000 to 3700 Ma, ii) 2760–2740 Ma granitoids have three distinct sources at 3000, 3200 and 3300 Ma, iii) the felsic magmatic events at 2700–2680 Ma reworked older and established crust, iv) 2640–2600 Ma granitoids derived from a 3200–3300 Ma source. One striking feature that materialize from the spatio-temporal distribution of Sm-Nd model ages for 2800–2600 Ma granitoids in the Murchison Domain is an NE–SW elongated section of relatively juvenile crust with T_{DM}^2 ages of c. 3000 Ma ($\epsilon_{\text{Hf}} = -1$ – -1.6) enveloped by 3000–3400 Ma rocks (Fig.

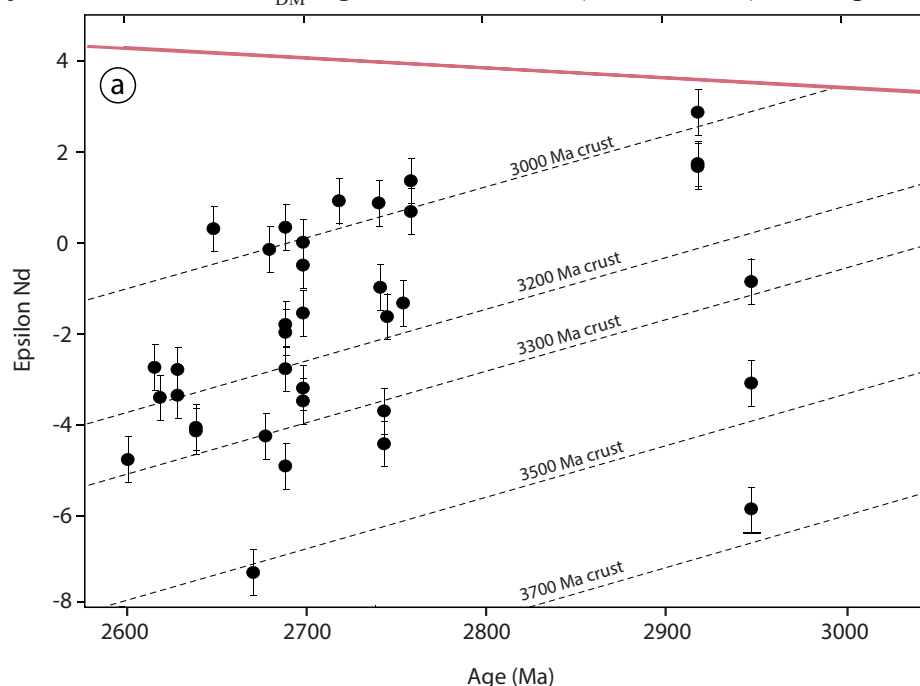


Figure 4: Sm–Nd isotope data (as ϵ_{Nd}) versus age for granitic rocks from the Murchison Domain (modified after Mole et al., 2013). The chondritic uniform depleted mantle (DM) reservoir is shown as a red line while later additions of juvenile or ancient crustal material and the subsequent mixed reservoirs are shown by black dotted lines.

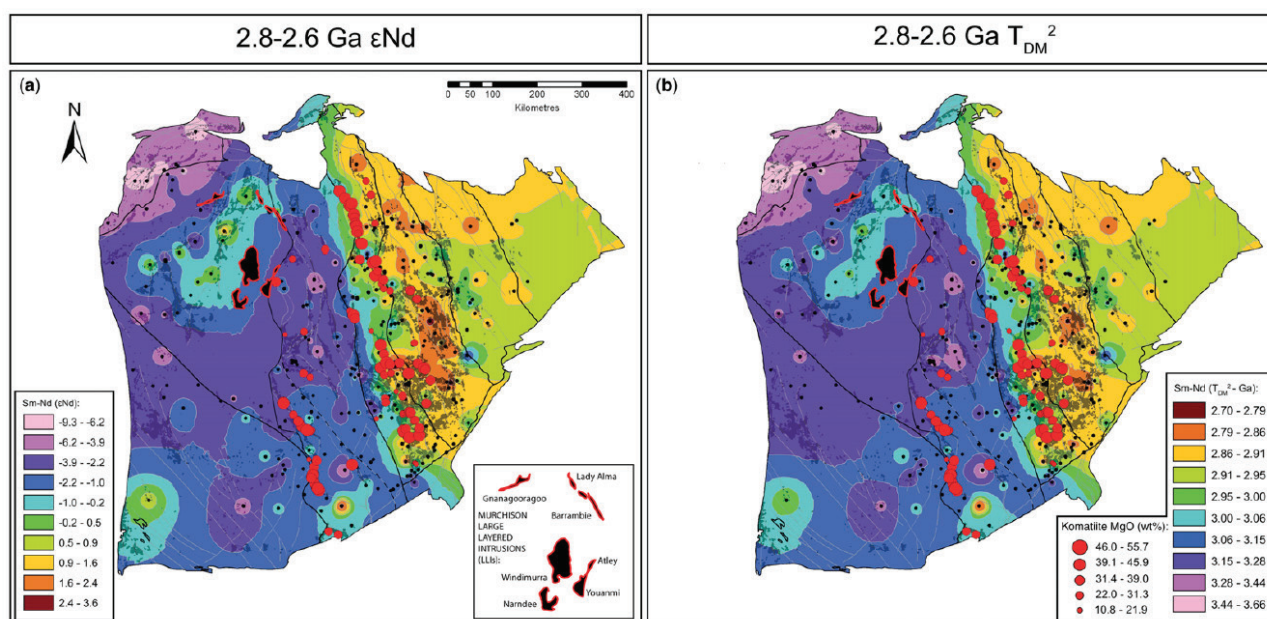


Figure 7: Sm–Nd isotopic contour maps displaying the spatial variation of ϵ_{Nd} (a) and T_{DM}^2 (b) for granitic rocks formed between 2800 and 2600 Ma in the Yilgarn Craton (after Mole et al., 2013). In the Murchison Domain, T_{DM}^2 model ages suggest that the large majority of granitic rocks formed from an unexposed and older crust, with ages varying between 3400 and 2950 Ma.

1; Cassidy et al., 2005; Cassidy et al., 2007; Ivanic et al., 2010, 2012; Mole et al., 2013). This band is bordered by large layered mafic intrusions and encloses the great majority of greenstones in the Murchison Domain, upholding the assumption it might represent a failed rift (Ivanic et al., 2010).

2 Yalgoo Dome

The Yalgoo Dome is located in the westernmost part of the Murchison Domain (Fig. 1) and is defined by a 100x50 km dome-and-keel with an NS oriented long-axis (Fig. 8). The new stratigraphic scheme proposed by van Kranendonk et al. (2013) was implemented in the Yalgoo area during the

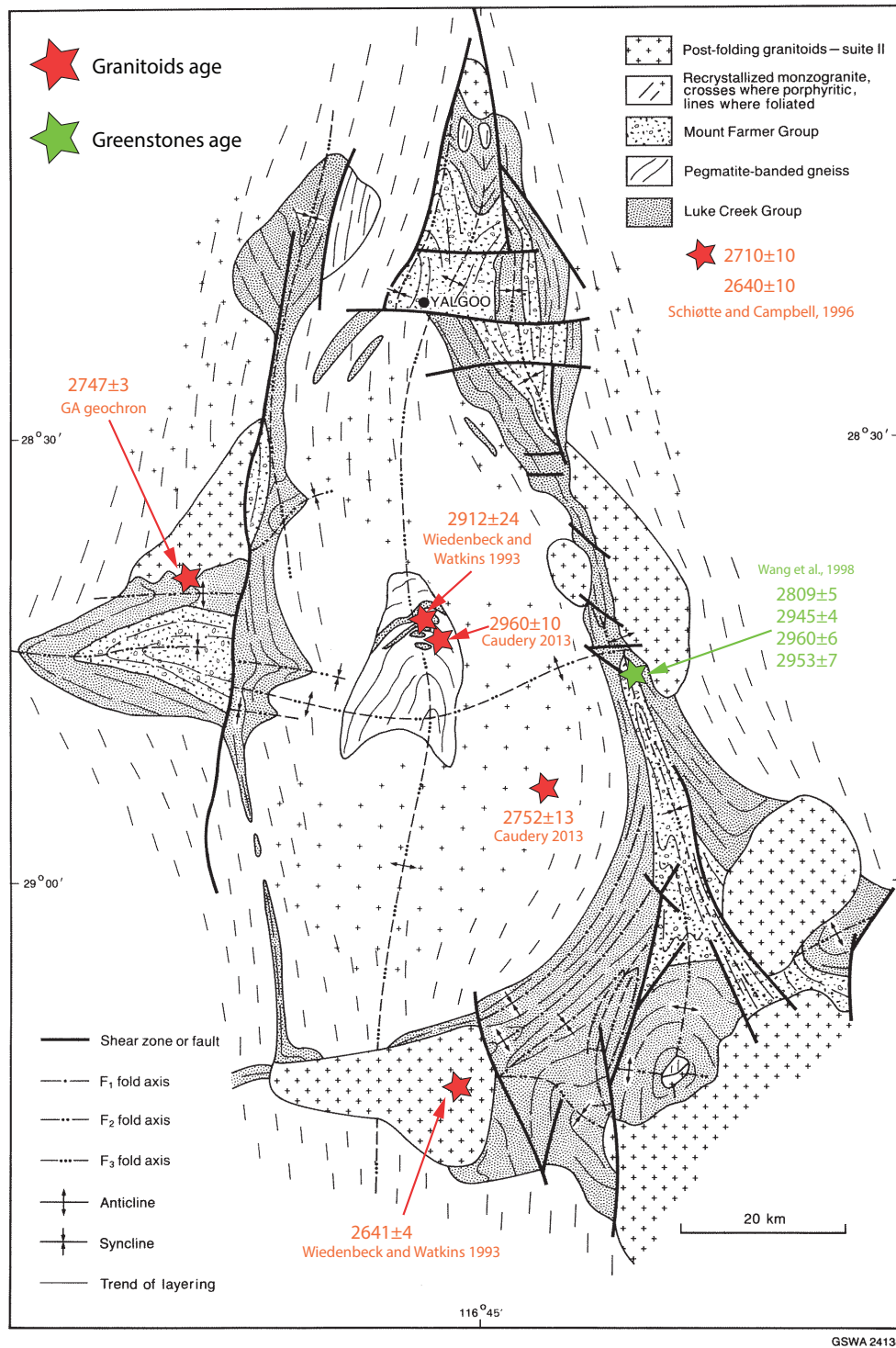


Figure 8: Simplified geological map of the Yalgoo Dome (modified after Watkins and Hickman, 1990) showing the distribution of granitoids and greenstones. Red and green stars represent age of granitoids and greenstones from the literature.

course of this Ph.D. and the geochronological and stratigraphic update can be found in the GSWA report of Zibra et al. (in press) in Appendix B. For the purpose of this literature review, the following sections summarize information available at the onset of this Ph.D. project, focusing on the older classification scheme of granitoids, greenstones, structures and tectonic models.

2.1 Greenstones

The first attempt to classify supracrustal assemblages in the Yalgoo Dome and Murchison Domain divided granite-greenstone terranes in an upper felsic–sedimentary and mafic association opposed to a lower felsic–sedimentary and a lower mafic association (Baxter and Lipple, 1985). Such interpretations were soon abandoned when Watkins and Hickman (1990) introduced the “Murchison Supergroup”, formally divided in two volcano-sedimentary groups, the Luke Creek Group and the Mount Farmer Group (Fig. 8). The Luke Creek Group comprise four laterally extensive lithostratigraphic formations (Fig. 9). In the lower part of the sequence thick mafic sequences of the Murrouli Basalts are topped by interlayered banded iron formations and mafic rocks of the Golconda Formation. The Gabanintha Formation comprises ultramafic-to-mafic sequences overlain by the banded iron formation, felsic volcanics and volcanoclastic rocks (rare basalts) of the Windaning Formation. The Mount Farmer Group always lies on top of the Windaning Formation and is divided in two subgroups and numerous formations. These formation have limited aerial extension and are interpreted to represent individual volcanic center. Only the Mougouderra Formation, an epiclastic sedimentary basin, outcrop throughout the Yalgoo Dome area (Figs 8, 9).

Mafic supracrustal rocks in the Yalgoo area were the subject of geochronological studies only in the work of Wang et al., (1998) near the Golden Grove mine (Fig. 8). SHRIMP U-Pb zircon dating of three samples from the Gabanintha Formation (Luke Creek Group) yield ages of 2960 ± 6 Ma, 2953 ± 7 Ma and 2945 ± 4 Ma, whereas the overlying Windaning Formation age is c. 2809 ± 5 Ma (Fig. 3). These results perfectly match ages from the same formations in the Murchison Province, identi-

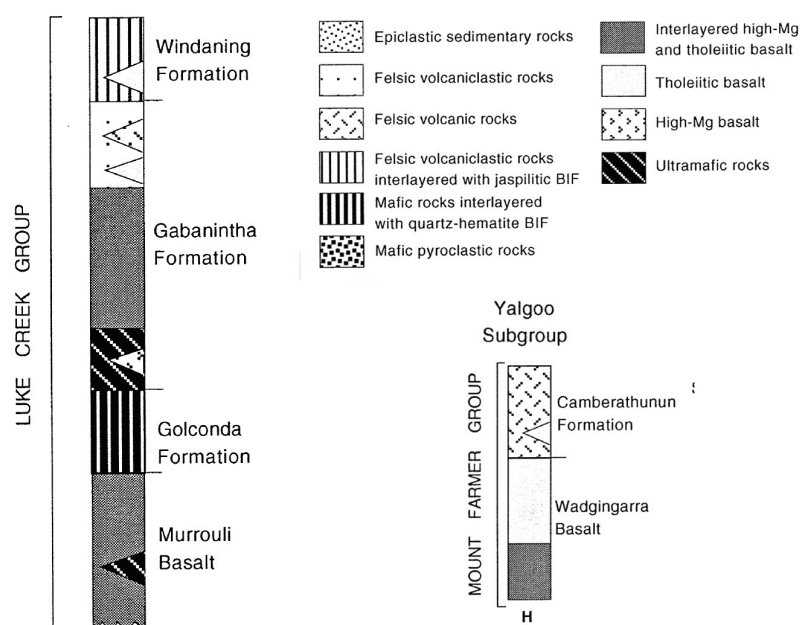


Figure 9: The Murchison Supergroup is divided into the voluminous Luke Creek Group and the Mount Farmer Group (after Watkins and Hickman, 1990).

fying a >100 Ma magmatic hiatus on a regional scale (Fig. 9).

For a more detailed description of the Murchison Supergroup, the reader is referred to chapter 2 of Watkins and Hickman (1990).

2.2 Granitic rocks

Most of the Yalgoo Dome area comprises granitic rocks outcropping between greenstones belts. Myers and Watkins (1985) and Watkins and Hickman (1990) recognized four groups on the basis of relative chronology and geochemical characteristics:

- Pegmatite-banded gneiss preferentially outcrops in the core of the dome and comprises cm-size layering of quartz-feldspar-rich and biotite-rich and layers parallel to gneissosity and several generations of cross-cutting pegmatite layers. In some outcrops this unit contains thick layers and lenses of amphibolite and banded iron formation (Fig. 10; Myers and Watkins, 1985) which closely resemble units of the Windaning Formation (Watkins and Hickman, 1990). Pegmatite-banded gneiss occurs also as cm-to-plurimetric enclaves in recrystallized monzogranite, in many cases as partially adsorbed xenoliths (patches of nebulous banding) or large fractured xenoliths intruded by hosting monzogranite (Caudery, 2014). SHRIMP U-Pb zircon ages indicate crystallization age of 2919 ± 12 Ma (Wiedenbeck and Watkins, 1993) and 2960 ± 10 Ma (Caudery, 2014).
- Recrystallized monzogranites are the most abundant of the four suites (> 60%). They include several generations of monzogranite, syenogranites and granodiorite with equigranular, porphyritic or sparsely porphyritic magmatic texture. Contacts between these granitic rocks are generally gradational, but in places cross-cutting relationships indicate that porphyritic monzogranites intruded equigranular monzogranites and were both intruded by the sparsely porphyritic variety. Recrystallized monzogranites display magmatic fabric, but the structural complexity increase towards the contacts with the overlying greenstone belt, where a solid state foliation overprints magmatic textures (Watkins and Hickman, 1990; Foley, 1997). Xenoliths of pegmatite-banded gneiss occurs in most of the internal batholith and show different degree of equilibrium with the host granites. In the southern part of the dome, recrystallized monzogranites have been dated at 2752 ± 13 Ma (Caudery, 2014).
- Two suites of post-folding granitoids characterize Murchison Domain (Fig. 8). Suite I post-folding granitoids include tonalite, granodiorite, monzogranite and trondhjemite while Suite II granitoids are typically quartz-rich monzogranite and syenogranites. Although some plutons are partially to completely recrystallized, the hosting rocks are not deformed. In the Yalgoo Dome, only Suite II granitoids are present and were dated at 2747 ± 3 Ma and 2641 ± 5 Ma (Fig. 8).

2.3 Structural Geology

The distribution of granite and greenstones in the Yalgoo Dome is controlled by 5 phases of deformation (Watkins and Hickman, 1990):

- D_1 horizontal structures: pegmatite-banded gneiss and greenstone is poorly preserved, but on a local scale Watkins and Hickman (1990) recognized a tectonic foliation parallel to isoclinal folds with subvertical axial plane. The authors interpreted these fabrics as sub-horizontal recumbent folds rotated vertically during deformation.
- D_2 EW folds: tight to isoclinal folds with EW-trending axes and weak axial plane foliation, mainly developed in recrystallized monzogranite, greenstones and pegmatite-banded gneiss. Fabrics are poorly preserved due to a strong, regional overprinting during D_3 .
- D_3 folds: upright tight to isoclinal folds with NNW-trending fold axes accompanied by a penetrative foliation which overprinted previous structures. Fold axial planes are vertical to subver-

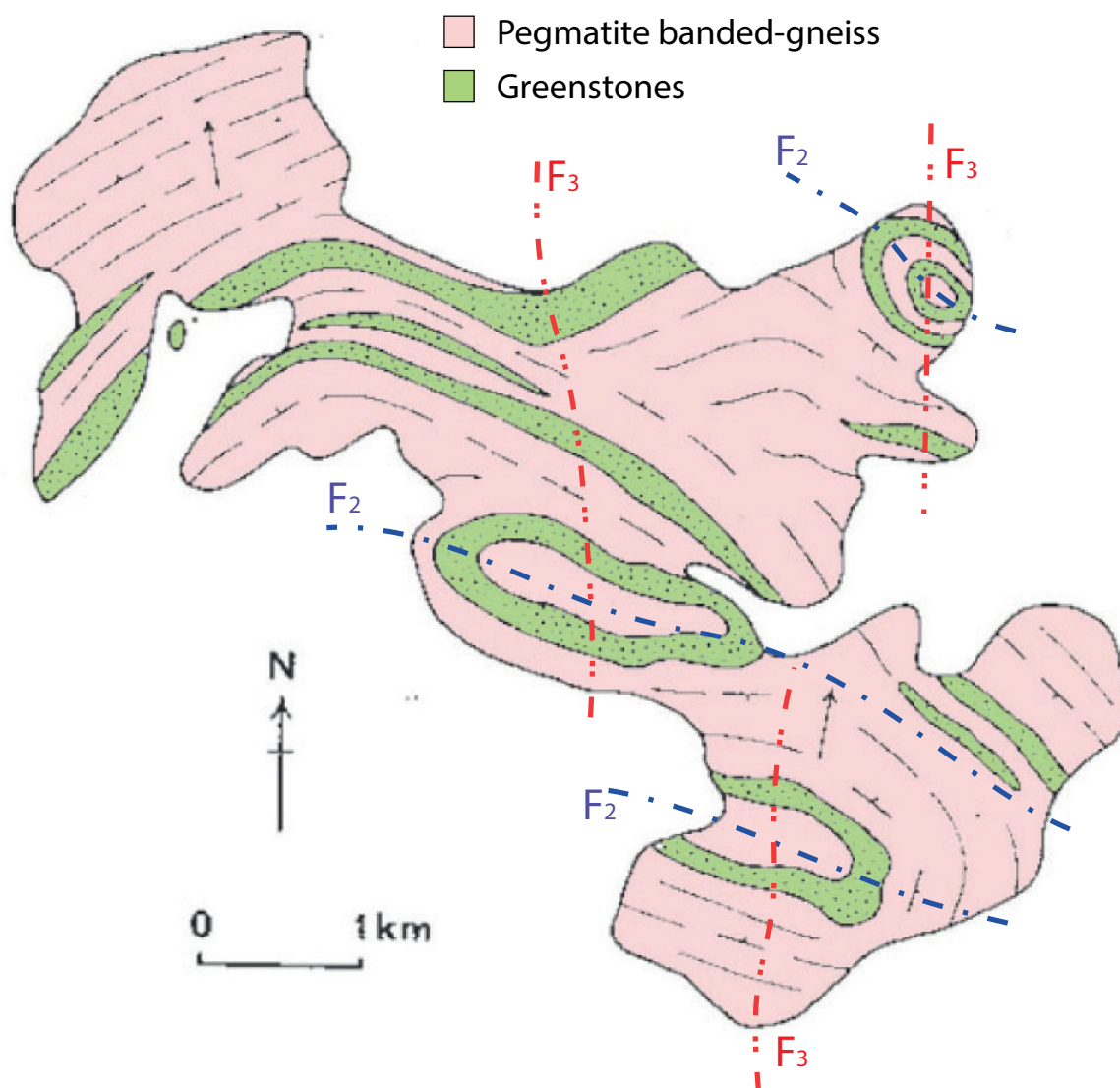


Figure 10: Simplified geological map of the structures outcropping in the migmatitic core of the Yalgoo Dome. Dome-and-basins patterns are defined by circular keels of greenstones within 2970–2900 Ma pegmatite banded gneiss (map modified after Myers and Watkins, 1985). According to Myers and Watkins (1985), these patterns formed by fold interference between two orthogonal deformation events with sub-horizontal fold axis and vertical axial planes. The same area was remapped during the course of this Ph.D. and is presented in Chapter 2.

tical with fold axis controlled by orientation of S_2 surfaces. In zones of high strain, sheath folds commonly develops. Intense shearing generates in fold limbs with little or no deformation in the core. In fact, S_3 is well developed within 50 m to 1 km from the granite-greenstone contact.

- D_4 – D_5 shear zones: extensive thrusting and shear zone development related to the development of an anastomosing network of shear zones and faults (>100 km in length) affecting the NW part of the Murchison Domain but were not recognized in the Yalgoo Dome.

2.4 Tectonic models

The formation of the dome-and-keel in the Yalgoo Dome has been object of a long-lived controversy. Gee et al. (1981) advocated that the granite-greenstone patterns were generated during diapirism by density inversion between buoyant granitic masses underneath dense and colder greenstones. Myers and Watkins (1985) then rejected this initial interpretation as the dome did not present a clear radial lineation and lacked concordant foliations at the granite-greenstone interface, typical in gneiss dome (Teyssier and Whitney, 2002) and salt diapir (Talbot and Jackson, 1987). Three distinct (D_1 – D_3) episodes of deformation define the final geometry of the dome. In particular, D_2 and D_3 fold interference generated the elliptical shape of the dome (Fig. 8). This model is reinforced by the

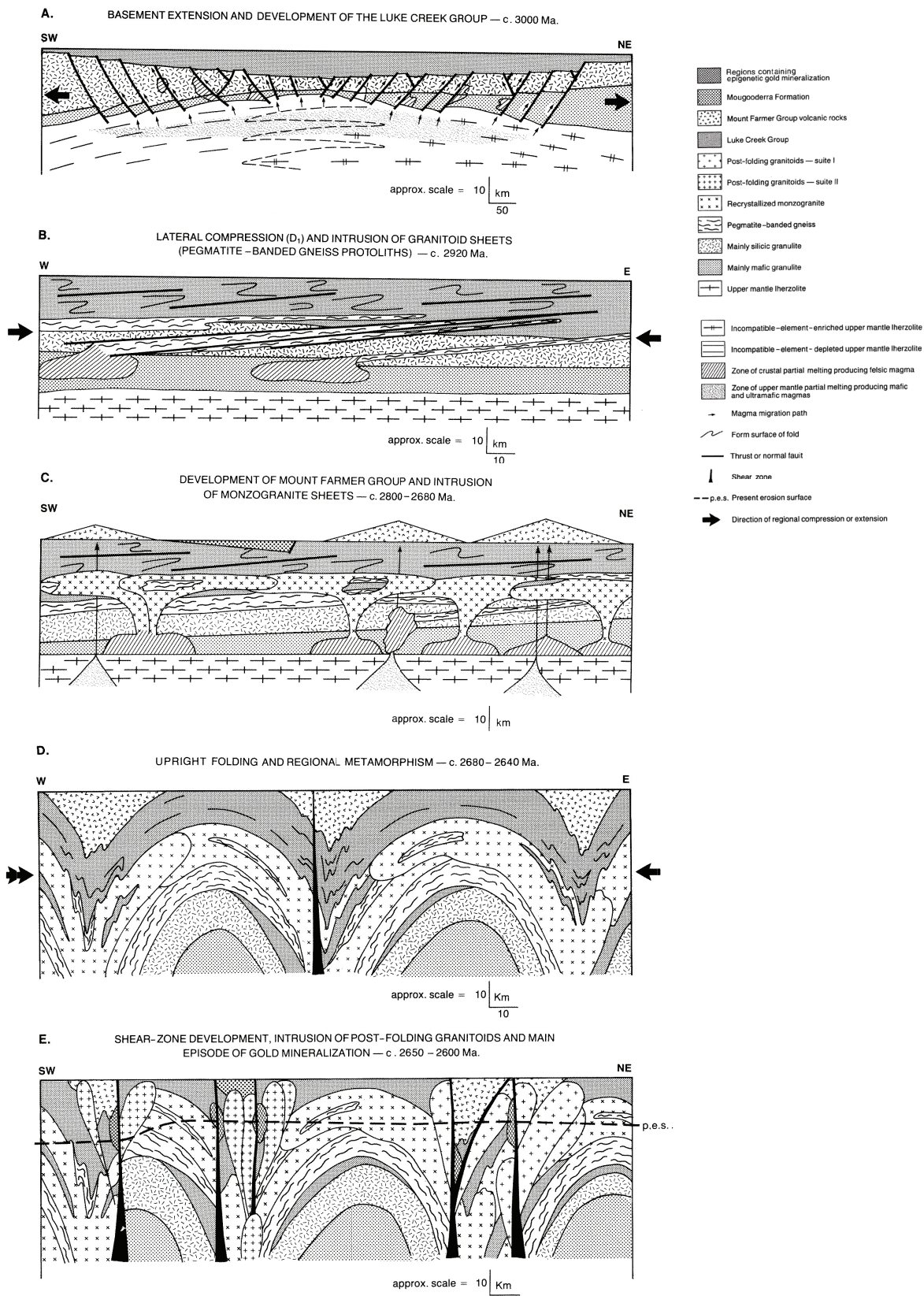


Figure 11: Cartoons illustrating the five stage tectonic evolution of the Murchison Domain and Yalgoo Dome area (after Watkins and Hickman, 1990).

occurrence of dome-and-basin in the migmatitic core of the dome (Fig. 10). On a map-view these structures are defined by interlayered pegmatite-banded gneiss and greenstones interpreted to form from the superimposition of F_2 and F_3 (Myers and Watkins, 1985).

The fold interference model in the Yalgoo Dome was part of a tectonic model for the crustal evolu-

tion in the Murchison Domain. Watkins and Hickman (1990) proposed 5 stages model largely based on externally imposed compressive and extensional events, presumably linked to large-scale tectonic processes:

- A) Basement extension and development of the Luke Creek Group at c. 3000 Ma (Fig. 11a).
- B) Lateral compression and intrusion of the granitoid sheet (pegmatite-banded gneiss protoliths) at c. 2920 Ma (Fig. 11b).
- C) Development of the Mount Farmer Group and intrusion of monzogranite sheets at 2800–2680 Ma (Fig. 11c).
- D) Upright folding and regional metamorphism at 2680–2640 Ma causing the formation of fold interference patterns (Fig. 11d).
- E) Shear zone development, intrusion of post-folding granitoids and gold mineralization at 2650–2600 Ma

In the late 90's, a new geological campaign intending to re-investigate the Yalgoo district revealed all shortcomings of the fold interference model for the Yalgoo Dome. In the Ph.D. thesis of Foley (1997), field observations were largely incompatible with superimposition of two deformation event:

- Granitoids show magmatic fabric, overprinted by a solid state foliation only at the contact with the greenstones. These over-imposed fabric is parallel to the granite-greenstone contacts and display clear granite up–greenstone down kinematics (Figs 12, 13),
- Dome is cored by migmatites and granites with clear magmatic and sub-magmatic flow structures
- Absence of pervasive axial planar foliations in the “dome and basins” structures described by Myers and Watkins (1985).

Hence, the work of Foley (1997) preferably support the diapiric model, as formerly suggested by (Gee et al., 1981), but with significant variations. The presence of a sinistral strike/slip sense of movement at the granite-greenstone boundaries implies horizontal interferences during the diapiric, vertical displacement of the granitoids. Further, the author speculates about the crustal emplacement of the Yalgoo Dome not as a single pluton, but as a series of smaller magmatic injections in a rather brief time interval (Fig. 12).

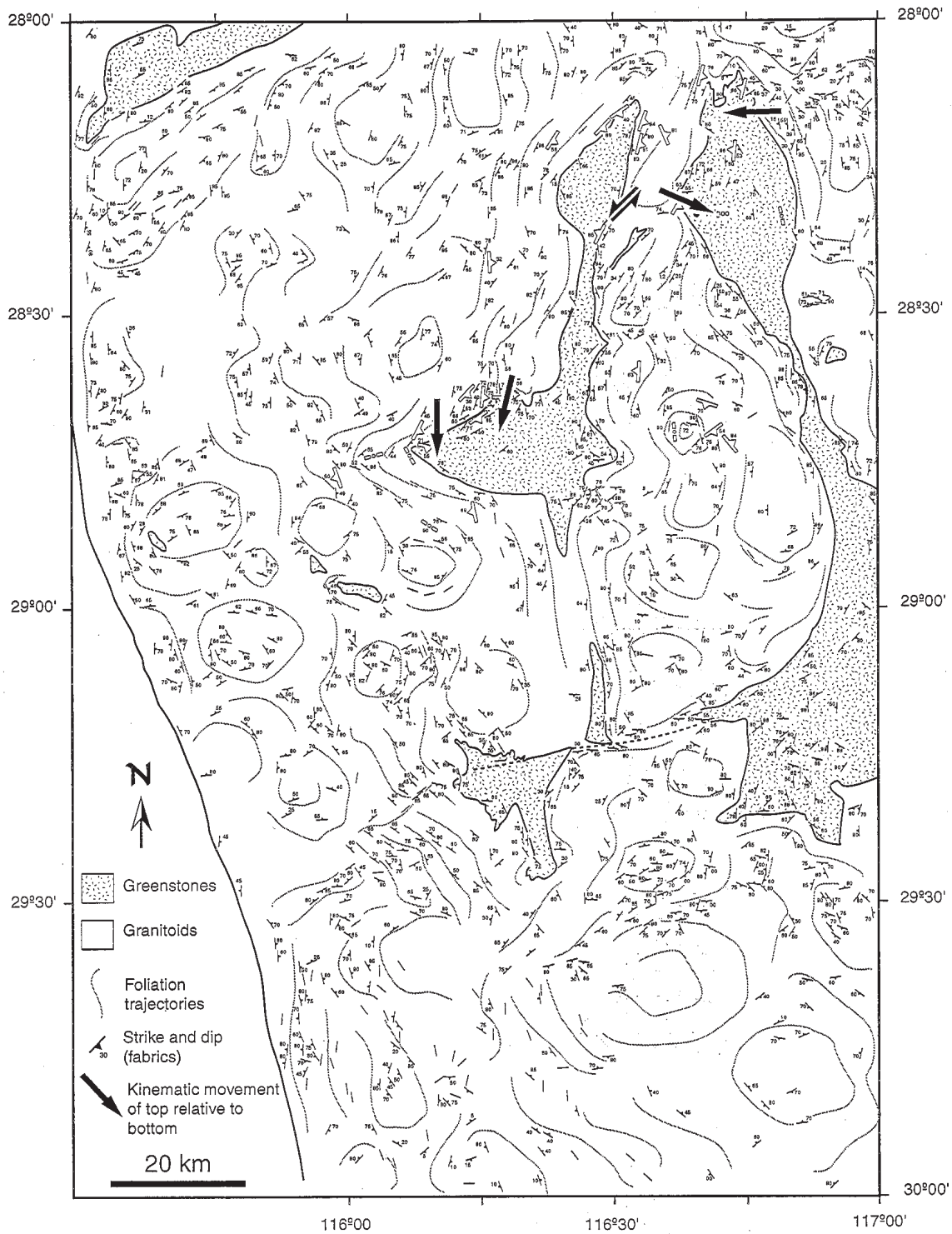


Figure 12: Interpretative map of regional foliation trajectories in the Yalgoo Dome area. Black arrows consistently shows granite up-greenstone down kinematics (after Foley, 1997).

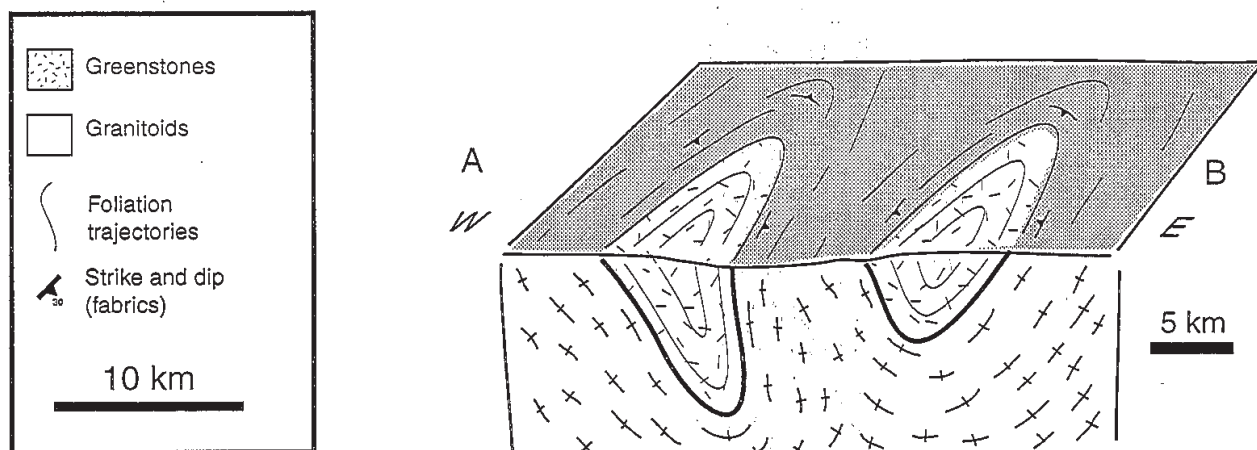


Figure 13: Interpretative cross-section of foliation trajectories in greenstones and granites (after Foley, 1997).

References

- Baxter, J.L. and Lipple, S.L., 1985. Perenjori, Western Australia, 1: 250 000 geological series-explanatory notes. Geological Survey of Western Australia.
- Cassidy, K.F., Champion, D.C. and Huston, D.L., 2005. Crustal evolution constraints on the metallogeny of the Yilgarn Craton. In *Mineral Deposit Research: Meeting the Global Challenge*, Springer Berlin Heidelberg, pp.901–904.
- Caudery, J.N. 2014. Structural evolution of the Yalgoo Dome, Yilgarn Craton, Western Australia. Geological Survey of Western Australia, Record 2014/4, pp.89.
- Cassidy, K.F., Champion, D.C., McNaughton, N.J., Fletcher, I.R., Whitaker, A.J., Bastrakova, I.V. and Budd, A.R., 2002. Characterisation and metallogenic significance of Archaean granitoids of the Yilgarn Craton, Western Australia. Minerals and Energy Research Institute of Western Australia (MERIWA), Report 222, pp.514.
- Champion, D.C. and Cassidy, K.F., 2007. An overview of the Yilgarn Craton and its crustal evolution. *Geoscience Australia Record* 14, pp.8–13.
- Champion, D.C. and Sheraton, J.W., 1997. Geochemistry and Nd isotope systematics of Archaean granites of the Eastern Goldfields, Yilgarn Craton, Australia: implications for crustal growth processes. *Precambrian Research*, 83(1-3), pp.109–132.
- Foley, B.J., 1997. Reassessment of Archaean tectonics in the Yalgoo District, Murchison Province, Western Australia. Unpublished B. Sc. Thesis. Monash University, Melbourne, Australia.
- Gee, R.D., Baxter, J.L., Wilde, S.A. and Williams, I.R., 1981. Crustal development in the Archaean Yilgarn Block, Western Australia. *Special Publication Geological Society Australia*, 7, pp.43–56.
- Ivanic, T.J., Wingate, M.T.D., Kirkland, C.L., Van Kranendonk, M.J. and Wyche, S., 2010. Age and significance of voluminous mafic–ultramafic magmatic events in the Murchison Domain, Yilgarn Craton. *Australian Journal of Earth Sciences*, 57(5), pp.597–614.
- Ivanic, T.J., Van Kranendonk, M.J., Kirkland, C.L., Wyche, S., Wingate, M.T. and Belousova, E.A., 2012. Zircon Lu–Hf isotopes and granite geochemistry of the Murchison Domain of the Yilgarn Craton: evidence for reworking of Eoarchean crust during Meso-Neoproterozoic plume-driven magmatism. *Lithos*, 148, pp.112–127.
- Mole, D.R., Fiorentini, M.L., Cassidy, K.F., Kirkland, C.L., Thebaud, N., McCuaig, T.C., Doublier, M.P., Durning, P., Romano, S.S., Maas, R. and Belousova, E.A., 2013. Crustal evolution, intra-cratonic architecture and the metallogeny of an Archaean craton. Geological Society, London, Special Publications, 393, pp.SP393–8.
- Myers, J.S. and Watkins, K.P., 1985. Origin of granite-greenstone patterns, Yilgarn block, Western Australia. *Geology*, 13(11), pp.778–780.

- Schiøtte, L. and Campbell, I.H., 1996. Chronology of the Mount Magnet granite-greenstone terrain, Yilgarn Craton, Western Australia: implications for field based predictions of the relative timing of granitoid emplacement. *Precambrian Research*, 78(4), pp.237–260.
- Talbot, C.J. and Jackson, M.P.A., 1987. Internal kinematics of salt diapirs. *AAPG Bulletin*, 71(9), pp.1068–1093.
- Teyssier, C. and Whitney, D.L., 2002. Gneiss domes and orogeny. *Geology*, 30(12), pp.1139–1142.
- Van Kranendonk, M.J. and Ivanic, T.J., 2009. A new lithostratigraphic scheme for the northeastern Murchison Domain, Yilgarn Craton. Geological Survey of Western Australia, Perth, pp.35–53.
- Van Kranendonk, M.J., Ivanic, T.J., Wingate, M.T., Kirkland, C.L. and Wyche, S., 2013. Long-lived, autochthonous development of the Archean Murchison Domain, and implications for Yilgarn Craton tectonics. *Precambrian Research*, 229, pp.49–92.
- Wang, Q., Schiøtte, L. and Campbell, I.H., 1998. Geochronology of supracrustal rocks from the Golden Grove area, Murchison Province, Yilgarn Craton, Western Australia. *Australian Journal of Earth Sciences*, 45(4), pp.571–577.
- Watkins, K.P. and Hickman, A.H., 1990. Geological evolution and mineralization of the Murchison Province, Western Australia. Geological Survey of Western Australia, Bulletin 137.
- Yeats, C.J., McNaughton, N.J. and Groves, D.I., 1996. SHRIMP U-Pb geochronological constraints on Archean volcanic-hosted massive sulfide and lode gold mineralization at Mount Gibson, Yilgarn Craton, Western Australia. *Economic Geology*, 91(8), pp.1354–1371.
- Zibra, I., Gessner, K., Smithies, H.R. and Peternell, M., 2014. On shearing, magmatism and regional deformation in Neoproterozoic granite-greenstone systems: Insights from the Yilgarn Craton. *Journal of Structural Geology*, 67, pp.253–267.
- Zibra, I., Peternell, M., Schiller, M., Wingate, M.T.D., Lu, Y., Clos, F., in press. Tectono-magmatic evolution of the Neoproterozoic Yalgoo Dome (Yilgarn Craton). Diapirism in a pre-orogenic setting. Geological Survey of Western Australia, Report 176.

APPENDIX B

Tectono-magmatic evolution of the Neoproterozoic Yalgoo Dome (Yilgarn Craton). Diapirism in a pre-orogenic setting.

- Refer to electronic data file" Appendix B.zip"
- Status: in press at the Geological Survey of Western Australia

APPENDIX C

Badja 1:100,000 Geological Map

- Refer to electronic data file" Appendix C.pdf"
- Status: published at the Geological Survey of Western Australia

APPENDIX D

The ~2730 Ma onset of the Neoproterozoic Yilgarn Orogeny

- Refer to electronic data file" Appendix D.pdf"
- Status: published on Tectonics (2017)

